University of Southampton

Faculty of Engineering and Physical Sciences

School of Electronics and Computer Sciences

Electrokinetic biased Deterministic Lateral Displacement for particle separation

by

Victor Calero Martin

ORCID ID 0000-0002-8971-7301

Thesis for the degree of Doctor of Philosophy

March 2021

University of Southampton

Abstract

Faculty of Engineering and Physical Sciences

School of Electronics and Computer Sciences

Thesis for the degree of Doctor of Philosophy

Electrokinetic biased Deterministic Lateral Displacement for particle separation

by

Victor Calero Martin

Microfluidics will lead to a revolution in the field of sample analysis and to the development of Lab-on-a-Chip platforms capable to perform complete analytical processes cheaper and faster than the current methods inside single tiny chips. Many biomedical and diagnostic analytical processes require micro/nanoparticle separation which means there is an increasing need for reliable particle separation techniques, suitable for integration within Lab-on-a-Chip systems.

This thesis introduces a novel microfluidic sorting technique that combines a well-established size-based microfluidic separation technique known as Deterministic Lateral Displacement (DLD) with electrokinetic particle manipulation. This new approach to particle sorting expands the spectrum of potential applications and delivers precise, high-resolution and label-free separation and fractionation of particles in the range of micro and nanometres.

Coplanar parallel electrodes were integrated into a DLD microfluidic device in order to generate electric fields orthogonal to the fluid flow. These electrical forces enable fine tuning of particle trajectories within the DLD microchannels depending on particle structural and electrical properties. This turns a simple size-based separation DLD into a tunable technique capable of targeting a range of particle properties other than size, including particle polarisability and electrical charge. Proof-of-principle experiments demonstrate the potential of this new separation technique and investigate its working principles.

Characterisation experiments were performed to identify the scaling laws that govern behaviour under the action of alternating electric fields. The results were compared with a theoretical model together with numerical simulations to achieve a full understanding of the physical mechanisms that lead to particle sorting. The results showed two distinct working regimes that depend on the frequency of the applied AC electric field. At high frequencies (above 500 Hz), Dielectrophoresis (DEP) was identified as the force driving the separation. When a low frequency field is applied (below 500 Hz), the physical mechanism differs significantly, and experiments indicated the existence of new electrokinetic phenomena that drive the separation process.

Finally, the thesis also describes a refined design of a device that is capable of separation of nanoparticles. The experimental results demonstrate the potential of this technique for the extraction and purification of a wide range of micro and nanoparticles.

List of Contents

Acknowledgements

To everyone who supported me during this amazing experience.

Firstly, I would like to thank Pablo and Antonio who not only offered me this project but also who have shared with me all their knowledge and have guided me along this scientific journey in the most kind and supportive way. Secondly, I would like to thank my supervisor, Hywel Morgan for giving me this opportunity, who has been the best of the mentors and from whom I have learnt so much about science and this world of academic research.

Also, I must thanks all members of the CHB (old and new) who are not only work colleagues but also friends and who have helped and supported me every time I needed (which was quite often): Roel, Anna, Josh, Kri, Nikita, Jon B, Yuetao, Marios, Joao, Fernando, Fabrizio, Antonio, Dan, Ying, Laila, Katie, Miguel, Catarina, Sybil, Prameen, Summit and many others. Specially to Carlos, who introduced me to the PhD life and showed me how to deal with almost every aspect of lab work, and Raul and Ric with whom I have shared many hours working in the lab and discussing protocols and results and who have contributed significantly to the work presented in this thesis. I cannot think of better people I could have shared this experience with. I will never forget the nights at Stags (with or without karaoke), followed by some nice food (not from Hong Kong Chef) nor the Friday brunches, transitioning from Fish and Chips to spicy noodle soups and baps.

I must thank the rest of my friends in Southampton (at the Futsal Club and the Oasis Academy) with whom I have shared so many hours of football, burgers and beers. Also, to my friends back in Spain, who made me feel as I never left every time I went back, who came to visit and even moved to Southampton for a little while to enjoy the experience of changing the sun of Spain for the rain and greenness of England.

To Chari for all the time and experiences we have enjoyed together during these years and, finally, to my family who I have missed so much during the time abroad, whose care and love gave me the strengths to accomplish this project and who certainly will be the strongest support I will have in my entire life, I could not be writing these words without you.

Research Thesis: Declaration of Authorship

Print name: Victor Calero Martin

Title of thesis: Electrokinetic biased Deterministic Lateral Displacement for particle separation

I declare that this thesis and the work presented in it are my own and has been generated by me as the result of my own original research.

I confirm that:

1. This work was done wholly or mainly while in candidature for a research degree at this University;
2. Where any part of this thesis has previously been submitted for a degree or any other qualification at this University or any other institution, this has been clearly stated;
3. Where I have consulted the published work of others, this is always clearly attributed;
4. Where I have quoted from the work of others, the source is always given. With the exception of such quotations, this thesis is entirely my own work;
5. I have acknowledged all main sources of help;
6. Where the thesis is based on work done by myself jointly with others, I have made clear exactly what was done by others and what I have contributed myself;
7. Parts of this work have been published as:
   I. Calero V., Garcia-Sanchez P., Honrado C., Ramos A. & Morgan H. (2019). AC electrokinetic biased deterministic lateral displacement for tunable particle separation. Lab on a Chip, 19(8), 1386-1396
   II. Calero V., Garcia-Sanchez, P., Ramos A. & Morgan H. (2019). Combining DC and AC electric fields with deterministic lateral displacement for micro- and nano- particle separation. *Biomicrofluidics*, *13*(5), 054110
   III. Calero V., Garcia-Sanchez P., Ramos A. & Morgan H. (2020). Electrokinetic biased Deterministic Lateral Displacement: Scaling Analysis and Simulations. *Journal of Chromatography A*, 461151.
   IV. Calero V., Garcia-Sanchez P., Ramos A. & Morgan H. (2018). Electrokinetic induced lateral displacement in deterministic lateral displacement microfluidic devices. Dielectrophoresis 2018.
   V. Calero V., Garcia-Sanchez P., Ramos A. & Morgan H. (2018). AC Electrokinetic biased Deterministic Lateral Displacement separation systems. NanoBioTech 2018.

VI. Calero V., Garcia-Sanchez P., Ramos A. & Morgan H. (2019). AC Tuning Deterministic Lateral Displacement separation with AC electrokinetics. MicroTAS 2019.

VII. Calero V., Fernandez-Mateo R., Garcia-Sanchez P., Ramos A. & Morgan H. (2020). Rectified AC Electroosmosis Induced by Surface Conductance Around Insulating Posts. MicroTAS 2020.

Signature: ..... Date: .....

List of Tables

List of Figures

List of Abbreviations

EVs – Extracellular Vesicles

LoC – Lab-on-a-Chip

PoC – Point-of-Care

DLD – Deterministic Lateral Displacement

AC – Alternating Current

DC – Direct Current

SAWs – Surface Acoustic Waves

EP – Electrophoresis

DEP – Dielectrophoresis

nDEP – negative Dielectrophoresis

pDEP – positive Dielectrophoresis

CE – Capillary Electrophoresis

ITP – Isotachophoresis

EFGF – Electric Field Gradient Focusing

PFF – Pinched Flow Fractionation

EK – Electrokinetics

EHD – Electrohydrodynamics

EDL – Electrical Double Layer

CM factor – Clausius-Mossotti Factor

ROT – Electrorotation

EOr – Electroorientation

EO – Electroosmosis

ACEO – Alternating Current Electroosmosis

ICEK – Induced-Charge Electrokinetics

ICEO – Induced-Charge Electroosmosis

IDL – Induced Double Layer

CP – Concentration Polarisation

iDEP – Insulator-based Dielectrophoresis

FFE – Free Field Electrophoresis

PDMS - Polydimethylsiloxane

KCl – Potassium Chloride

DI water – Deionized water

List of Symbols

$\boldsymbol{u}, \boldsymbol{v}_f$ – fluid velocity

ρ – fluid density

p – pressure

η – dynamic viscosity

$\boldsymbol{f}$ – external body force

$\boldsymbol{F}$ – force

m – mass

$\boldsymbol{a}$ – acceleration

U – typical fluid velocity

L – characteristic length scale of the system

Re – Reynolds number

$\boldsymbol{F}_D$ – drag force

$\boldsymbol{v}_p$ – particle velocity

$\boldsymbol{F}_{ext}$ – external force

D – diffusion constant

x_{diff} – unidimensional diffusion average displacement

k_B – Boltzmann constant

T – temperature

a – particle radius

t – time

R_h – hydraulic resistance

Q – flow rate

w – channel width

h – channel height

$\Delta\lambda$ – DLD row lateral shift

D_c – DLD critical diameter

θ – DLD tilt angle

λ – centre to centre post spacing

D_p – pillar diameter

G – DLD gap between the posts

N – DLD periodicity

$\mathbf{p}$ – dipole moment

$\mathbf{P}$ – dipole moment density

n – number density

$\boldsymbol{E}$ – electric field

E_0 – electric field magnitude

ε – electric permittivity

ε_0 – vacuum permittivity

α – polarisability

σ – electrical conductivity,

ω – angular frequency

i – imaginary unit

$\tilde{f}_{\mathrm{CM}}$ – Clausius-Mossotti factor

τ – characteristic relaxation time

ϕ – electrostatic potential

λ_D – Debye length

q – ion charge

K_s – surface conductance

μ_{EP} – electrophoretic mobility

μ_{DEP} – dielectrophoretic mobility

ζ – zeta potential

Du – Dukhin number

V – particle volume

f – frequency

$\mathbf{\Gamma}$ – torque

μ_{EO} – electroosmotic mobility

$\boldsymbol{r}$ – particle position

Chapter 1 Introduction and motivation

1.1 The importance of particle separation

Almost every biological, chemical or environmental sample intended to be analysed consists of a mixture of different components, many of them containing valuable information that can be extracted during the analytical process. Many of these components are micrometric or even nanometric particles which often need to be extracted prior to subsequent specific testing. Therefore, particle separation is a key aspect of a large proportion of the analytical methods carried out in many different fields (medicine and diagnostics, nutrition and food industry, environmental sciences, biology, biomedical sciences, chemistry, engineering, etc)[1,2]. The development of new effective and reliable particle separation techniques is thus extremely important to sustain and support the development of these different fields.

Any new technique needs to address a wide range of different problems due to the variety and complexity of the samples. Some sample components, especially in the case of biomedicine, are often found in extremely low concentrations that would be practically invisible in most assays; this is the case for some rare blood cells, parasites or Circulating Tumour Cells (also known as CTCs)[3], cells shed by tumours which are one of the main vias of metastasis and are found in concentrations around 10^3-10^2 cells/L in blood. Other components are more common but so small that their presence in the samples is negligible; this is the case for Extracellular Vesicles (EVs) and exosomes which, in general, range in size from 10 to a few hundred nanometres in diameter[4,5]. These particles would be outside the scope of most assays but by exploiting particle separation techniques, their concentration can be enormously enriched so that they can be included in the analytical processes.

In addition, the separation of particles is not only useful for extraction of specific sample components for analysis, but often is part of the analysis itself. In many cases the separation process provides information about the sorted particles and allows identification of each of the components as well as quantification of the physicochemical characteristics that the separation mechanisms rely on.

A huge variety of physical properties can be exploited to distinguish particles in a mixture and thus perform separation, including size, density, shape, electric charge, deformability, etc. However, many samples often have components with very similar mechanical properties (for example similarly sized cells) so that these properties cannot be the sole basis of discrimination. In such cases, the particles must be specifically labelled using for example, magnetic or fluorescent tags, in

order to establish a source of discrimination that allows different forces to be exerted on different particles for efficient particle sorting[6–8].

1.2 Advantages of a microfluidic approach for particle separation

Microfluidics is a novel research field that uses tiny amounts of fluid constrained into microscopic channels for diverse application mainly focused on processing and analysis[9,10]. Although the dimensions of microfluidic devices are commonly a few centimetres with channels that are often thinner than a human hair, these devices are capable of outperforming current lab machinery, executing the same analytical processes cheaper and quicker with high precision and resolution.

Nowadays, most separation techniques are lengthy, costly, complex and require substantial pieces of equipment with large amounts of sample and reagents. Nevertheless, microfluidic approaches will bring several advantages for particle separation with respect to current methods. The fact that only simple, tiny and relatively easy to fabricate devices are used, reduces drastically the costs, the duration and the volume of sample and reagents needed for the separation[1,11].

Microfluidic particle sorting is not often characterised by throughputs larger than those of the traditional techniques due to the small dimensions of the devices. However, most microfluidic separation techniques are intended to be combined with microfluidic analytical devices which require tiny amounts of processed samples to produce conclusive and accurate outcomes, so very high-throughputs are not necessary. In the case where large volumes of sample need to be processed, microfluidic separation devices require parallelisation, so that many devices can be run at the same time in order to multiply throughput[12].

Another advantage of microfluidics for micro- and nano-particle sorting is that the forces acting on the particles inside the microchannels are managed at a microscopic level, i.e. the magnitude and direction of the forces can be controlled at a very small scale within the range of micro and even nanometres[13]. This increases enormously the specificity of the separation and enables discrimination of particles by exploiting slight differences in their properties, resulting in a high level of precision and resolution.

Finally, the majority of existing microfluidic sorting methods are label-free, which means that particles do not need specific labelling for separation[14]. Particle labelling is a powerful approach but has some significant handicaps since most labelling methods are complex, expensive and time consuming. In addition, where biological particles are involved, labels have side effects on their viability and limit the post-separation utility. Nonetheless, the intrinsic characteristics of

microfluidics are suitable for the development of label-free separation techniques, which exploit only the physical properties of the particles.

1.3 Lab-on-a-Chip platforms and Point-of-Care testing

The development of microfluidic sample preparation and analysis is leading to major breakthroughs in the fields of biomedicine and diagnostics, mainly thanks to the development of Lab-on-a-Chip (LoC) systems[15–19]. Microfluidics enables most analytical steps to be miniaturised, so that they can be combined and integrated within the same microfluidic device to perform a complete analytical process. These are the Lab-on-a-Chip platforms and eliminate the need for big pieces of lab equipment and trained users.

The main advantage of LoC platforms is the possibility of Point-of-Care (PoC) testing and diagnostics[20]. The term Point-of-Care means that the diagnostic tests are run rapidly and close to the patients with no need for expensive and long laboratory testing[21,22]. This allows for fast and early detection of health problems and easy constant monitoring of health states and chronic disease, improving the life quality of the patients. The development of reliable PoC tests is of great importance in developing countries where these cheap and portable diagnostic devices could mitigate the lack of high-tech lab equipment.

There are some well-known and familiar PoC tests such as pregnancy, HIV and blood glucose tests, but research in microfluidics will bring much more powerful devices capable to detect and monitor a much wider range of biophysical parameters much more precisely.

Lab-on-a-Chip systems intended for Point-of-Care testing integrate and execute full analytical processes within a single microfluidic chip. Since most of these processes include particle separation steps, there is a growing demand for reliable and high-quality microfluidic particle separation methods able to target diverse particle populations and easy to integrate within LoC platforms.

1.4 Project aim

The main goal of this research project is to develop and characterise a novel microfluidic particle separation technology that combines classic Deterministic Lateral Displacement (DLD) continuous flow size-based separation with particle electrical manipulation. DLD utilises arrays of offset microposts specifically arranged so that the rows are tilted at a small angle (typically smaller than 6°). Particles smaller than a given size threshold, called the critical diameter, travel in straight trajectories through the array, zigzagging around the posts. On the contrary, particles bigger than

the threshold, bump on the posts and displace following the tilting angle. This enables particle separation.

Although DLD has shown a lot of promising results in terms of separation quality, it has some drawbacks such as the lack of tunability and applicability. Nevertheless, combining DLD with electrokinetics, adds extra forces on the particles that provide a means of tuning their trajectories inside the microchannels. Particles smaller than the critical diameter can be forced to bump on the posts and deviate depending on their electrical response. This expands the range of potential applications and turns DLD into a tunable technique where separation can be actively controlled by regulating the electrical signals applied to the system.

This project focuses on the characterisation of this technique in terms of the parameters that govern particle behaviour as they move inside the DLD (electric field, suspending medium and particle properties, flow rate, device geometry). It also aims to identify the optimal separation regimes for several types of particles. The device had a pair of electrodes placed along the microchannel walls to generate electric fields orthogonal to the fluid flows. This enables to study the effect of the electric field on the trajectories of different types of particles. The results outline the advantages of combining DLD devices with electric fields and depict the potential sorting applications for real-world samples containing biologically relevant particles.

1.5 Thesis outline

Chapter 1 illustrates the aim of the project and provides a brief background on the importance of particle separation and the advantages of using a microfluidic approach.

Chapter 2 and **Chapter 3** introduce the central theoretical concepts of microfluidics and electrokinetics, respectively, and depict the most relevant techniques related to micro and nanoparticle manipulation and separation.

Chapter 4 describes the experimental methods, the designs of the devices used in the experiments and the software used for the data analysis and the numerical simulations.

Chapter 5 and **Chapter 6** include a full experimental characterisation of the particle behaviour inside DLD devices under the action of AC electric fields applied orthogonal to the fluid flow. These results are then compared to the existing theory together with numerical simulations.

Chapter 7 explore the effects of including a DC component to the alternating electric fields and how this enables to achieve further improved particle separation inside DLD devices.

Chapter 8 presents a refined design of the DLD microfluidic devices to reduce the minimum particle size that can be targeted by this technique in order to address the problem of nanoparticle separation.

Chapter 9 concludes the thesis with a summary of the main research outcomes of the project and a discussion on the direction for future research.

Chapter 2 Microfluidics

Microfluidics is a research field that studies the behaviour of small amounts of fluid (of the order of nanolitres) constrained in micron-sized channels, often thinner than a human hair. The physics of fluids in such small dimensions differs enormously from that in the macroscale[23,24], the inertial effects vanish, and the fluids behave as composed by several laminae that do not mix with each other. This regime is called laminar flow. This characteristic behaviour of the fluids and the microscopic dimensions of the microfluidic systems have strong implications from a practical point of view.

The main applications of microfluidics are in sample analysis in many different areas, from biology to chemistry but most importantly for medicine. The ability to manipulate reduced volumes of samples and reagents shortens the analysis costs and duration maintaining a high precision and resolution. It also allows control of the forces at a microscopic level. This fact is especially relevant for biological samples since the cells, bacteria and other biological particles can be studied one by one, in a variety of techniques with different applications termed single-cell analysis[25–27].

Nevertheless, the biggest potential of microfluidics lies in the possibility to miniaturise and combine different analytical techniques within the same platform. This allows development of microfluidic systems that integrate every analytical step and automate the whole process. These microscopic systems, capable of performing a complete analysis, are termed Lab-on-a-Chip and will eliminate the need for huge pieces of lab equipment and trained users, providing fast and accurate results wherever the patients are (Point-of-Care diagnosis).

Lab-on-a-Chip platforms will have profound implications in healthcare: improving significantly the life quality of those patients that need routine test and providing quick results for those in critical conditions. However, microfluidics is still a research field, not widely used for analytical purposes yet. At the beginning of every emerging technology there are challenges that need to be addressed, mainly in terms of standardisation and commercialisation. Before it turns into a major worldwide technology, microfluidic systems must become easy to use for the non-expert user, financially profitable for the companies and its components and tests must be standardised[28,29].

This chapter includes a short introduction to the physics of fluids on the microscale and provides a background on microfluidic particle separation, a very important area of microfluidics and the most relevant for this thesis.

2.1 Fluids in the microscale

2.1.1 The Navier-Stokes equation and the Reynolds number

Matter in the universe is typically found in three phases: solid, liquid or gas. Solids are made of packed atoms bound to each other forming resistant rigid structures. In liquids and gases, the atoms can move with respect to each other so that the bodies deform continuously under shear stress and external forces. Liquids and gases are yet different. While gases expand to adopt the shape of the container and can deform under pressure, liquids are almost uncompressible and keep a constant volume. Microfluidics focuses mainly on the manipulation of liquids in the microscale (although the term fluid is often used).

The nature of fluids forces them to be described in terms of continuous quantities. The behaviour of incompressible fluids is governed by two equations. First, the continuity equation accounts for a basic principle of physics, the conservation of mass:

$$\nabla \cdot \boldsymbol{u} = 0 \tag{2.1}$$

where $\boldsymbol{u}$ is the fluid velocity field. Second, the Navier-Stokes equation describes the motion of incompressible fluids. This set of partial derivative equations results from the application of Newton's Second Law:

$$\rho\left(\frac{\partial \boldsymbol{u}}{\partial t} + (\boldsymbol{u} \cdot \nabla)\boldsymbol{u}\right) = -\nabla p + \eta\nabla^{\boldsymbol{2}}\boldsymbol{u} + \boldsymbol{f} \tag{2.2}$$

where ρ is the fluid density, p the pressure, η the dynamic viscosity and $\boldsymbol{f}$ an external body force. In this equation, as in Newton's second law ($m\boldsymbol{a} = \boldsymbol{F}$), the inertial terms, on the left, are separated from the forces, on the right. The internal forces are ∇p, the pressure gradient over the fluid body and $\eta\nabla^{\boldsymbol{2}}\boldsymbol{u}$, the viscous term which accounts for the friction within the fluid. The term $\boldsymbol{f}$ can be any external force applied to the fluid.

In the absence of external forces ($\boldsymbol{f} = 0$), the pressure gradient is balanced by a sum of the inertial effects and the viscous forces. The contribution of both can be quantified in terms of a typical fluid velocity U and the characteristic length scale of the system L:

$$Inertia \sim \rho\frac{U^2}{L} \tag{2.3}$$

$$Viscous \sim \eta\frac{U}{L^2} \tag{2.4}$$

The ratio between the inertial and the viscous contributions is known as the Reynolds number[30]:

$$Re = \frac{\rho L U}{\eta} \tag{2.5}$$

This dimensionless quantity defines the behaviour of the fluid. If $Re \gg 1$, then inertial effects dominate, and the viscosity does not affect the fluid motion. On the contrary, if $Re \ll 1$ inertia is negligible, and the pressure gradient is balanced solely by the viscous forces. In this case the time dependence is lost, the fluid responds instantaneously to any external perturbation and the Navier-Stokes equation becomes linear:

$$\eta \nabla^2 \boldsymbol{u} - \nabla \mathrm{p} + \boldsymbol{f} = 0 \tag{2.6}$$

This is the Stokes equation and the resulting fluid flow is creeping flow, also called Stokes flow. For microfluidic systems the length scales are very small so that Re is typically very low. For Reynolds numbers lower than 200 the flow profile is free of turbulence and the fluid behaves as if it were composed of several laminae that do not mix in the so-called laminar flow. This is the governing behaviour in microfluidics. An important characteristic of this flow is that the fluid velocity is zero at the contact points with the walls of the microchannels. This generates a parabolic flow profile where the velocity is maximum at the mid-point between the walls.

2.1.2 Particles in microfluidics

As mentioned above, microfluidic systems are characterised by low Reynolds numbers and the flow profile in the microchannels is defined by the Stokes flow. Particles suspended in the liquid experience a fluid drag force which is proportional to the relative velocity of the particle and the fluid. For a spherical particle of a radius a, this force is given by:

$$\boldsymbol{F}_D = 6\pi\eta a(\boldsymbol{v}_p - \boldsymbol{v}_f) \tag{2.7}$$

where $\boldsymbol{v}_p$ is the velocity of the particle, and $\boldsymbol{v}_f$ the fluid velocity. When the steady-state is reached:

$$\boldsymbol{F}_D = 0 \rightarrow (\boldsymbol{v}_p - \boldsymbol{v}_f) = 0 \rightarrow \boldsymbol{v}_p = \boldsymbol{v}_f \tag{2.8}$$

i.e. the particle has the same velocity as the fluid and flows following the fluid streamlines. The absence of turbulence in the Stokes flow imply a predictable fluid profile where the streamlines can be easily calculated. Thus, the paths of the particles within the microchannels are fully determined by the channel geometry.

However, additional forces exerted on the particles modify their paths through the microfluidic channels. Under the action of a continuous force field $\boldsymbol{F}_{ext}$ the particle velocity is given by:

$$\boldsymbol{F}_D + \boldsymbol{F}_{ext} = 0 \rightarrow \boldsymbol{v}_p = \boldsymbol{v}_f + \frac{\boldsymbol{F}_{ext}}{6\pi\eta a} \tag{2.9}$$

The combination of specific channel geometries with forces exerted to single particles at a microscopic scale enables a precise particle manipulation with applications in many different areas.

2.1.3 Diffusion

Although the deterministic particle trajectories are well defined by the microchannel geometry and the external forces, the role of diffusion needs to be considered due to the small dimensions of the microfluidic systems. Diffusion refers to the movement of particles from high to low concentration regions caused by Brownian motion, i.e. the random movement arising from collision with the fluid molecules[31]. The particle average displacement in one direction caused by diffusion is given by:

$$\langle x_{diff} \rangle = \sqrt{2Dt} \tag{2.10}$$

where t is the time and D the diffusion constant, which for a spherical particle of radius a:

$$D = \frac{k_B T}{6\pi\eta a} \tag{2.11}$$

This is the Stokes-Einstein equation[31,32], where k_B is the Boltzmann's constant and T the absolute temperature. According to this equation, the smaller the particle, the bigger the effect of diffusion on the particle's trajectories. Thus, the addition of the diffusion stochastic component to the deterministic particle motion has important implications in microfluidics where microscopic particles are manipulated, primarily with particles of the order of ~1 μm and below. This causes, for example, the widening of particle streams and the spread of particles in stagnant fluids (often used for microfluidic devices operating in batch mode).

2.1.4 Fluidic resistance

An important specification that defines the performance of a microfluidic device is the throughput of sample, i.e. the amount of sample it can process within a given time. In some cases, a high sample throughput is not required because only tiny sample volumes need to be treated to produce meaningful results. However, some devices need to process relatively large sample volumes to be effective. This is the case of some microfluidic separation devices, which need to process enough sample for the subsequent analysis.

The throughput of sample of a microfluidic device is largely (although not exclusively) affected by its fluidic resistance, also known as hydraulic resistance R_h. This is a parameter that relates the pressure difference applied to a channel Δp to the resulting flow rate Q:

$$R_h = \frac{\Delta p}{Q} \tag{2.12}$$

It is possible to derive an analytical expression for R_h in the laminar flow regime for simple channel geometries. For example, in the case of a channel of length L with a rectangular cross-section of w width and h the height ($w > h$)[24]:

$$R_h = \frac{12\eta L}{wh^3(1 - 0.63h/w)} \tag{2.13}$$

where η is the fluid dynamic viscosity. Nevertheless, for most microfluidic devices the channel geometries are too complex for a similar expression to be derived and R_h needs to be experimentally characterised.

2.2 Microfluidics for particle separation

Almost every analytical process requires a step of particle separation and therefore it is important for many different areas[15,33,34]. Sometimes, separation is part of the analysis and gives crucial information about the components of the samples. Other times, separation is a preliminary step that allows analysis of each constituent independently.

Advances in microfluidics have enabled the development of sorting techniques that bring several advantages over the classic techniques[1,35]. In general, microfluidic based separations are cheaper, quicker, require smaller amounts of sample and reagents and are capable of precise separations with a high resolution. In addition, they are essential for Lab-on-a-Chip platforms that perform full in-situ analysis of samples for Point-of-Care diagnosis. Also, in case large sample volumes need to be processed, high throughput separations are possible by means of device parallelization enabled by the low fabrication costs and the small sizes of microfluidic devices.

Another significant fact is that label-free separation is simplified in microfluidic systems due to the precise control of the forces at a microscopic level. This eliminates the need for specific tags, such as antibodies, and binding procedures allowing targeting of the physical properties of the particles in the sample.

In the last decades, several microfluidic separation techniques have been reported exploiting a vast number of phenomena and forces[11,36,37]. They can be divided into two classes. Passive techniques[38]

only use the characteristic microscale fluid behaviour together with specific microchannel geometries to carry out the separation, mainly based on the mechanical properties of the particles (size, deformability, density, …). On the other side, active techniques include external forces, such as electric or acoustic forces, to control the particle trajectories as they flow through the microchannels[39–41].

Active techniques address a wider range of physical properties (such as electrical, magnetic or chemical) compared with passive techniques that only target the particle's mechanical properties for separation. However, active techniques are in general more complex since they need extra external equipment to apply and control the fields and more complicated working procedures. In passive techniques, the separation is solely determined by the characteristics of the microfluidic setup, simplifying enormously the working procedures.

2.2.1 Active techniques

2.2.1.1 Magnetic

External fields, such as electric or magnetic, applied within the microfluidic channels exert additional forces that enable a more precise control of particle trajectories and add extra parameters for particle discrimination.

Separation of magnetically susceptible particles can be achieved applying inhomogeneous magnetic fields perpendicular to the direction of the fluid flow. Non-magnetic particles follow the unaltered trajectories while magnetic particles are attracted to the magnets with the separation depending on the particle volume and magnetisation and the magnitude of the magnetic fields (see Figure 2-1a). This technique is called magnetophoretic sorting[40,42].

In free-flow magnetophoresis[43,44], the microfluidic devices have multiple outlets so that not only are magnetic particles separated from non-magnetic particles, but particles with different magnetic susceptibility can be fractionated from each other, see Figure 2-1b.

However, most of separation techniques focus on biological particles which, in general, do not exhibit intrinsic magnetism. To overcome this problem, the particles can be labelled using magnetic particles, mainly via antibody binding techniques[8]. Thus, when the magnetic field is applied, the labelled particles will experience a magnetic force and will be separated from the unlabelled particles[45].

Besides the requirement for labels, the other great disadvantage of magnetophoretic separations is that the magnetic forces are usually very small, significantly limiting the operation flow rates and thus the separation throughput.

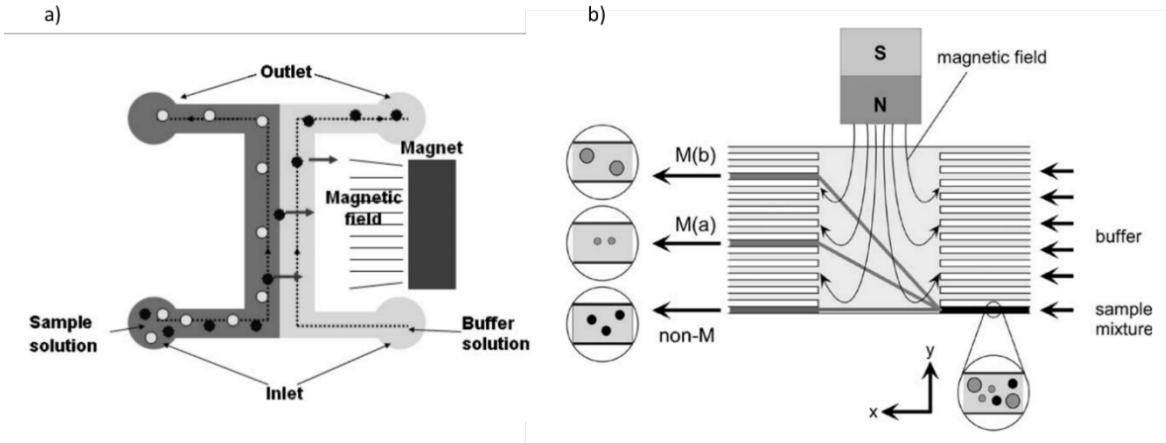

Figure 2-1. Principles of magnetophoretic microfluidic separation. a) Sorting of magnetic from non-magnetic particles within a non-uniform magnetic field (adapted from Kim & Park, 2005[45]). b) Free-flow magnetophoretic particle fractionation (adapted from Pamme et al., 2006[44]).

2.2.1.2 Acoustic

Acoustic forces can also be used to perform particle separation in microfluidic systems[46], known as acoustophoretic separation. This is often achieved using Surface Acoustic Waves (SAWs) created via piezoelectric transducers to generate acoustic force fields over the microchannels cross-section[47]. The particles within the force field are then pushed towards the nodes or the anti-nodes of the sound waves (see Figure 2-2a). The force magnitude and direction, either towards the nodes or the anti-nodes, depend on the characteristics of the sound wave (amplitude and frequency) and the properties of the particles and the suspending medium[48,49]. As a result, particles are separated based on their size, density and deformability without needing previous labelling.

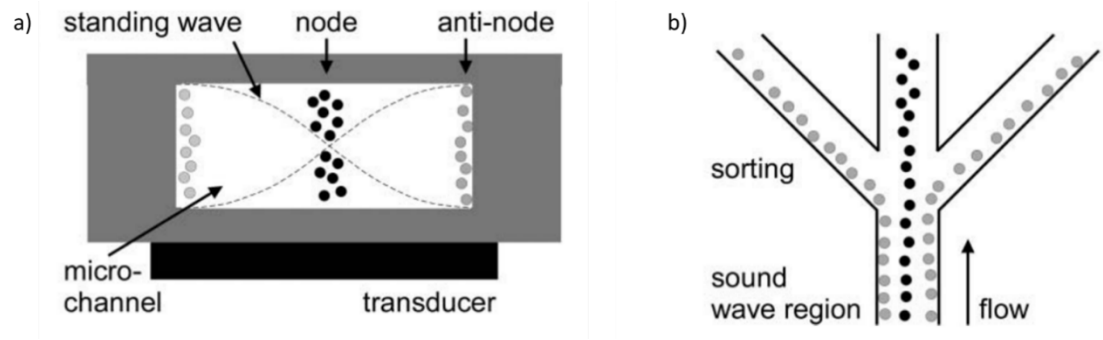

Figure 2-2. Principles of continuous flow acoustophoretic separation. a) Particles with different physical properties are pushed towards either the nodes or the anti-nodes of the sound waves created by the piezoelectric transducer. b) The sample components are focused and sorted into different streams that are then directed to different outlet channels. Adapted from Pamme 2007[50].

So far, acoustic forces combined with microfluidics have been used for the separation of a wide range of particles of very different sizes, from cells[51–53] to extracellular vesicles (EVs) in the range of nanometres[41,54,55]. The most common approach in acoustic microfluidic separation implies focusing different sample components into different streams that are then directed to different outlets[49,56], as shown in Figure 2-2b.

2.2.1.3 Electric

The utilisation of electric fields for particle sorting has attracted a huge interest in the past decades, given that most of the biologically relevant particles exhibit characteristic electrical properties that can be exploited for separation. Many different electrical phenomena have been used in combination with microfluidics for this purpose[57]. The two main forces arising when an electric field is applied to a suspension of particles are Electrophoresis (EP) and Dielectrophoresis (DEP). EP refers to the force exerted on particles suspended in an electrolyte when an electric field is applied due to an intrinsic electric charge. DEP is the movement of polarisable particles under the action of a spatially non-uniform electric field. Contrary to EP, DEP acts on neutral particles because the force is exerted on the electrical induced dipole. A more detailed explanation of these forces is provided in Chapter 3.

EP has been widely used to separate charged particles, primarily biomolecules but also biological particles like cells, based on their migration velocities under an electric field. For example, Capillary Electrophoresis (CE) in microfluidics uses long microchannels filled with an electrolyte to separate different ionic species along the microchannel length[58] (see Figure 2-3a). Other approaches such as Isotachophoresis (ITP)[59] or Electric Field Gradient Focusing (EFGF)[60–62] utilise electric field gradients to concentrate particles into different regions depending also on their migration velocity.

The DEP force moves the particles towards the high electric field gradients if the particles are more polarisable than the medium (positive DEP - pDEP) or away from these regions if they are less polarisable (negative DEP - nDEP)[63]. These two directions make DEP a very versatile technique. Particles with different electrical properties polarise differently and thus can be selectively trapped or directed to different places and sorted from each other[64]. Originally, most DEP sorting techniques operate in batch mode, i.e. target particles are trapped by DEP and separated from the rest of the sample[65,66]. They are then released when the field is turned off and collected. Recent developments in microfluidics have led to the development of continuous flow DEP separation techniques where particles experience DEP as they flow through the microfluidic channels. The DEP modifies the particle trajectories and directs them towards different collection outlets depending on their electrical properties[67–69] (see Figure 2-3b).

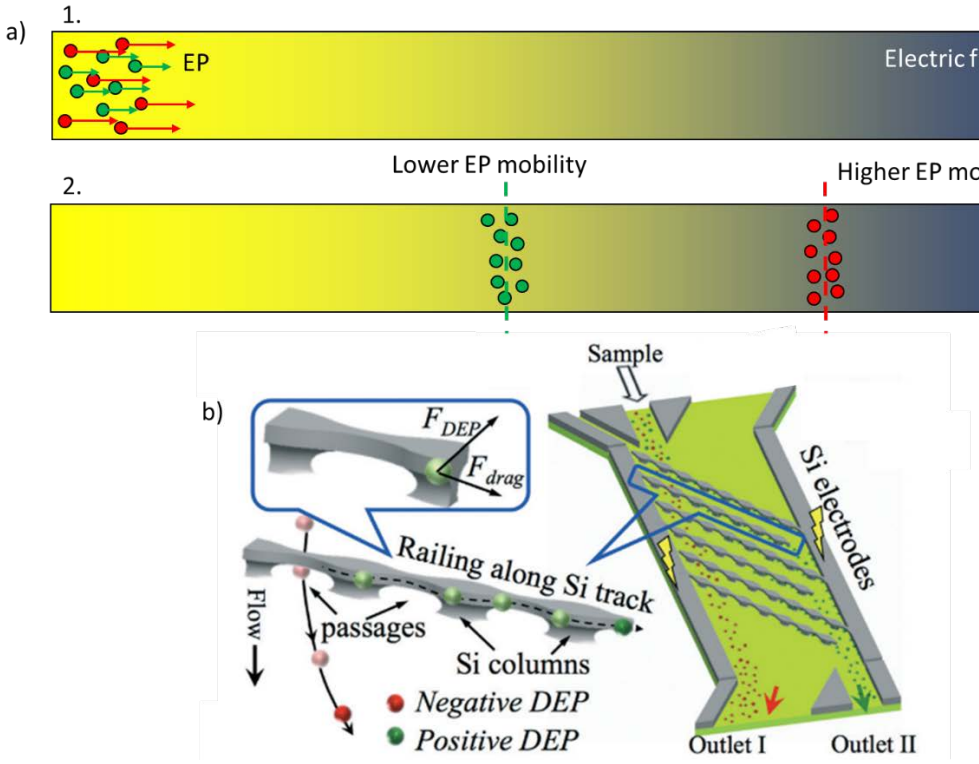

Figure 2-3. Examples of electrically assisted microfluidic separations. a) Electric field gradient electrophoretic particle separation. Red particles (high EP mobility) are separated from the green particles (low EP mobility) in a linear electric field gradient. b) Example of continuous flow DEP microfluidic separation. The green particles experiencing pDEP cannot penetrate the railing tracks and are directed to a different collection outlet, separated from the red particles that undergo nDEP. Reprinted from Xing *et al.*[67].

2.2.2 Passive techniques

2.2.2.1 Pinched flow fractionation (PFF)

In PFF[70,71], samples composed by different types of particles are pinched against one of the sidewalls of a narrow microchannel using a particle-free sheath flow. In the channel, particles flow straight and are aligned along the direction of the flow, touching the wall. They then arrive at an expansion channel where the flow broadens. When the particles get to that region they spread together with the flow and separate depending on their size and the particles are collected at different outlets.

Separation occurs due to the slightly different position of the particles in the alignment channel due to their size. The centre of mass of the smaller particles is closer to the wall than the centre of mass of the bigger particles. Moreover, the device performance depends on the flow rate ratio between the sample and sheath inlets and the geometrical parameters, mainly the broadening angle between the alignment channel and the spreading region and the alignment channel width.

2.2.2.2 Inertial and viscoelastic

As mentioned above, in passive separation techniques the particles are expected to always follow the fluid streamlines given the laminar behaviour of fluids in microsystems. However, under certain conditions the inertial effects become significant, for example at very high flow rates, forcing the suspended particles to migrate across streamlines. Recent research has shown that several different mechanisms give rise to the inertial forces[72–74]: flow disturbances around particles near the channel walls, shear gradient, particle rotation, curvature induced secondary flows, etc.

Based on the understanding of these physical phenomena, it is possible to control the inertial forces acting on the particles and thus modify their trajectories in a predictable manner. The fact that these forces also depend on the particle mechanical properties (size, shape, deformability and density) means that they can be exploited for particle manipulation and separation[75–77].

The use of viscoelastic fluids[78,79] also adds extra elastic forces to the inertial lifts expanding the separation possibilities, for example, reducing the minimum size that the separation can address[80]. These forces can also be coupled with existing separation techniques to improve the performance and range of applications[81,82].

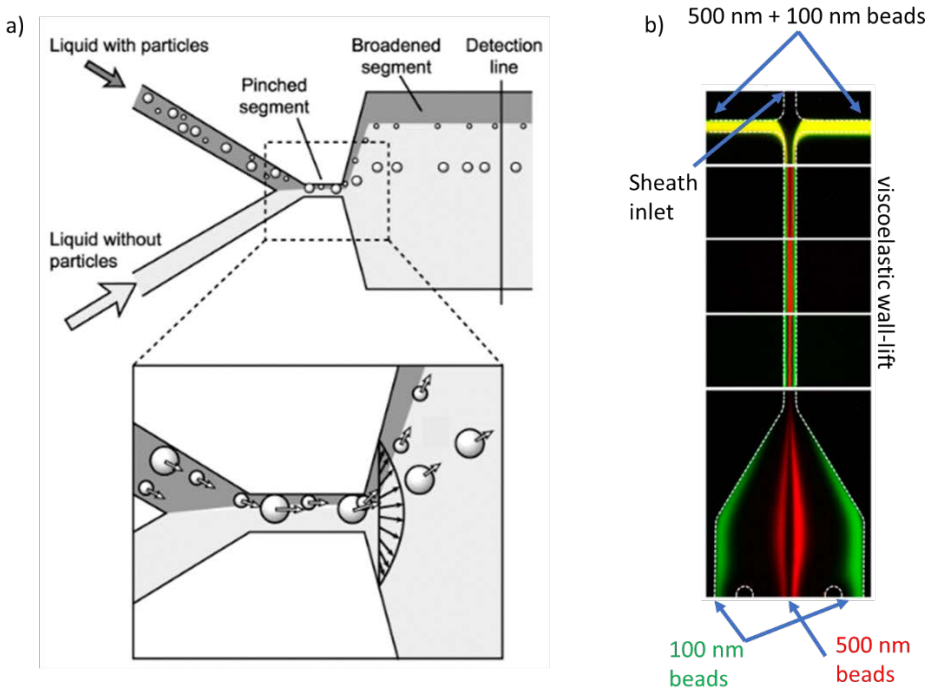

Figure 2-4. Examples of passive microfluidic separations. a) Pinched Flow Fractionation (PFF). Reprinted from Yamada *et al.*[70]. b) Viscoelastic size-based nanoparticle separation in a straight channel. Adapted from Liu *et al.* [80]

2.2.2.3 Deterministic Lateral Displacement (DLD)

Deterministic Lateral Displacement (or DLD) is an example of a passive microfluidic technique that is used for micro and nano-particle size-based separation in a continuous flow. DLD has attracted a huge interest since first reported by Huang *et al.*[83] in 2004, due to its simplicity, robustness and high precision and resolution. DLD has evolved over the last years thanks to the work of many research groups, significantly improving separation quality, possibilities and understanding of the underlying physical mechanisms[84,85].

DLD utilises a specific arrangement of micrometre-sized pillars to separate particles depending on size. Arrays of posts are placed inside a microfluidic channel so that each column of posts is shifted a given lateral distance $\Delta\lambda$ with respect to the previous column (see Figure 2-5a). This particular geometry defines a critical particle size, the critical diameter (D_c). Particles bigger than the D_c bump on the posts following the tilt angle θ (also termed deviation angle) in the so-called displacement mode, whilst particles smaller than the D_c flow straight zigzagging around the posts (see Figure 2-5b). Thus, the larger particles reach the end of the channel having been displaced laterally with respect to the smaller particles, resulting in a size-based binary separation (Figure 2-5c).

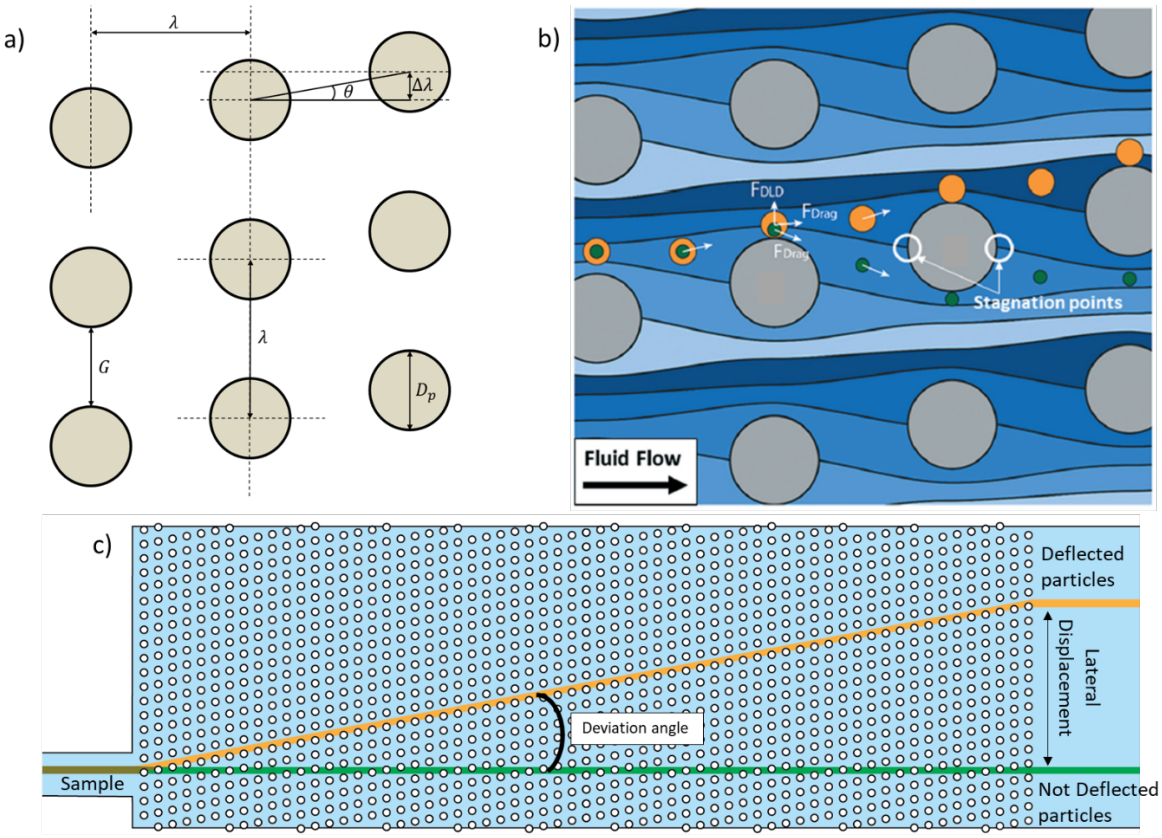

Figure 2-5. DLD separation principles a) Geometry of a DLD array of posts and structural parameters. b) Streamlines inside the DLD post array and separation mechanism. Particles bigger than the critical diameter (orange) bump on the posts and are separated from the smaller particles (green). c) Overall particle trajectories throughout the DLD channel. Big particles (orange) follow the tilt angle of the posts and reach the outlet being laterally displaced with respect to the small particles (green) that flow straight.

In a symmetric DLD array, each column is separated from the previous by a distance λ which is the sum of the pillar diameter D_p and the gap between the posts G. θ is then given by:

$$\theta = \operatorname{atan}\frac{\Delta\lambda}{\lambda} \tag{2.14}$$

Due to the column shifting, the DLD geometry is periodic with a periodicity N given by:

$$N = \frac{\lambda}{\Delta\lambda} = \frac{1}{\tan\theta} \tag{2.15}$$

DLD exploits the laminar nature of the flow on the microscale. The number of fluid laminae into which the flow is divided between two adjacent posts of the same column equals N. Each streamline that separates two fluid laminae starts in a stagnation point on the downstream side of

a post and ends in a stagnation point on the upstream side of the post located N columns further (see Figure 2-5b).

For a given post (see black post on Figure 2-6), the separatrix is the streamline that separates the portion of fluid that passes above the post from the fluid that passes below the post and ends at the stagnation point on its upstream side. This is the streamline responsible for the separation. When particles bigger than the D_c hit the previous post, they cross the separatrix and are pushed to the fluid that passes above the post. Particles smaller than the D_c, instead, remain in the portion of fluid that passes below the post following the fluid laminae. The mechanism is diagrammatically described in Figure 2-6. This process is repeated every time the particles encounter a post and is amplified throughout the DLD array, resulting in a significant lateral deflection of the bigger particles from the smaller particles and thus in a binary size-based separation.

According to this mechanism, the D_c corresponds to twice the minimum distance between the separatrix and the previous post, which is completely determined by the channel geometry. Some models such as that by Inglis *et al*.[86] have been proposed to estimate the value of the D_c, but they fail to provide an accurate estimation. Currently, the most accepted manner to calculate the D_c is the equation experimentally derived by Davis[87], assuming cylindrical posts and spherical particles:

$$D_c = 1.4GN^{-0.48} \tag{2.16}$$

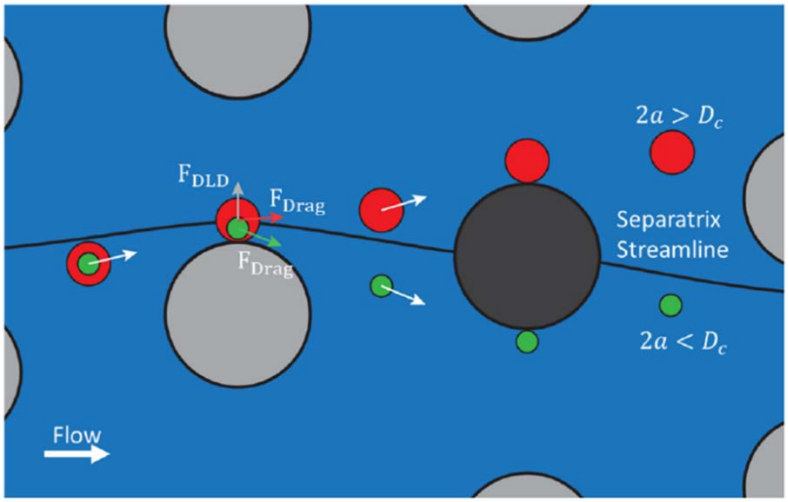

Figure 2-6. DLD separation mechanism and the role of the separatrix streamline. Particles bigger than the critical diameter (red) interact with the previous post and cross the separatrix to the portion of fluid that passes above the next post (black). The small particles (green) are not pushed to cross the separatrix and continue within the portion of fluid that passes below the next post (black).

So far, DLD has been used to separate and concentrate many different types of particles within a wide range of sizes, mainly biological particles like cells[88–90], Extracellular Vesicles (EVs)[12,91,92] and

microorganisms[93–95]. The fact that cells are not perfectly round rigid particles means that other mechanical properties such as deformability[90,96] or shape[97] can be exploited for discrimination in DLD systems.

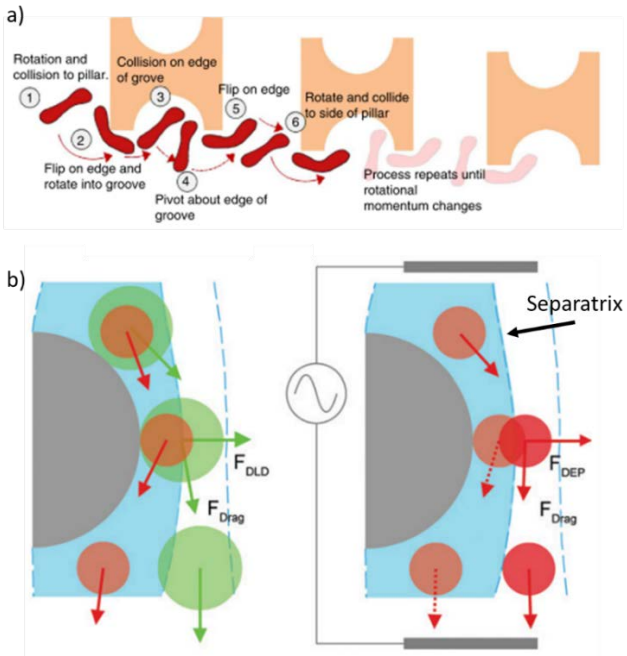

Figure 2-7. Examples of improved DLD separation. a) Rotational induced bumping mode of RBCs with I-shaped posts. Adapted from Zeming *et al.*[98]. b) DEP induced bumping mode using an external electric field. Adapted from Beech *et al.*[99].

Changes in device geometry can lead to improved separation. Although most DLD devices use circular posts, other post shapes such as triangular[89,100] or I-shaped posts[98,101] enhance the device efficiency and sorting of non-spherical particles[102,103] (see Figure 2-7a). In addition, the use of different horizontal and lateral gaps between the posts can improve the efficiency and throughput of this technique[104].

Finally, DLD devices can be coupled with additional forces (electric[99,105], electrostatic[106], viscoelastic[82], gravity[107], …) to modify the particle trajectories (see Figure 2-7b). This adds extra tunability to the separation and allows other particle properties to be targeted for separation, significantly increasing the range of potential applications.

2.3 Summary

Microfluidics describes the behaviour of fluids inside microscopic channels. The developments in microfluidics have led to new techniques that significantly improve the way samples are processed and analysed. This has implications in many research fields, especially in medicine with the

development of Lab-on-a-Chip systems, portable devices capable of rapidly performing an entire analytical process using reduced amounts of sample and reagents for Point-of-Care diagnosis.

The fact that most of the analytical techniques include a sorting step means that there is a need of reliable and precise microfluidic separation techniques. Amongst all reported microfluidic separation techniques, Deterministic Lateral Displacement has shown promise for particle size-based separation. The addition of external fields adds extra control over particle separation and turns DLD into a tunable technique capable to target a wider range of particle properties.

This thesis discusses a novel microfluidic separation technology that combines DLD with electric fields. The following chapters include a detailed description of the technique, a full characterisation of the separation mechanisms and promising experimental results. First, a short theoretical introduction to Electrokinetics is provided, together with a discussion about the applications of electrokinetics to particle separation and its combination with microfluidics.

Chapter 3 Electrokinetics

Electrokinetics (EK) is the research field that explores the behaviour of particles suspended in an electrolyte under the action of an electric field. When the electric field is applied, the combined action of different mechanisms gives rise to a net particle motion. The deep understanding of these physical mechanisms achieved over the last decades[108–110] enabled to use electric fields to manipulate the particles in a precise and controlled manner[111] for many applications, including particle sorting.

Not only are the electrical forces acting directly on the particles important, but in addition other phenomena must be considered. The ion concentration around a charged surface is altered due to the attraction of counterions and the repulsion of co-ions. An ionic double layer is then formed, which is central to most electrokinetic phenomena[112]. Furthermore, electric fields induce fluid movement in the liquid bulk, or electrohydrodynamic flows, which significantly influence the net particle motion[113,114].

In general, biological particles possess distinct electrical properties, such as surface charge or conductivity and permittivity of membrane and cytoplasm, which are particular to each particle type. The particle electrical response is determined by these properties together with other structural and mechanical properties like particle size or the membrane and/or wall structure. This fact, combined with the strong forces generated by the electric fields, makes electrokinetics a powerful tool to discriminate between different sample components and target specific subpopulations[115,116].

The field of micro and nano-particle manipulation with electric fields has experienced a huge growth over the past decades thanks to the development of microfabrication techniques[117]. The fabrication of microelectrode structures enables strong electric fields to be created at a microscopic scale which are easy to control. This growth is also related to developments in microfluidic technologies. The integration of electrokinetics with microfluidic systems enables electric forces to be applied directly at a microscopic level as particles flow within channels and electrically manipulate the fluid flows, combining the advantages of microfluidics with the versatility and robustness of electrokinetics[118,119].

This chapter starts with an introduction to the theory of electrokinetics and other relevant related phenomena, such as electrohydrodynamics (EHD), the electrical double layer (EDL) and induced charge electrokinetics (ICEK)[120], followed by a description of the most important electrokinetic techniques used for particle manipulation and separation, mainly in combination with microfluidics.

3.1 Dielectric polarisation and the Electrical Double Layer (EDL)

3.1.1 Dielectric polarisation

A dielectric is an electrically insulating material which polarises under the action of an electric field. These materials have bound charges which can move a small distance from their equilibrium position when a field is applied[121]. Opposite charges move in opposite directions creating induced electric dipoles inside the material, proportional to the electric field magnitude:

$$\mathbf{p} = \alpha \boldsymbol{E}' \tag{3.1}$$

where $\mathbf{p}$ is the dipole moment, $\boldsymbol{E}'$ the local electric field and α the proportionality constant called polarisability. All these microscopic induced dipoles produce a net dipole moment density $\mathbf{P} = n\mathbf{p}$, with n being the number of dipoles ($\mathbf{p}$) per unit volume. For linear and isotropic dielectrics, $\mathbf{P}$ is proportional to the applied field $\boldsymbol{E}$ and can be calculated in terms of the electric permittivity ε:

$$\mathbf{P} = \varepsilon_0 \left(\frac{\varepsilon}{\varepsilon_0} - 1 \right) \boldsymbol{E} \tag{3.2}$$

where the constant ε_0 is the vacuum permittivity. There are different dielectric polarisation mechanisms, electronic, atomic, orientational, ionic and interfacial, and the average polarisation results from their combined action: $\alpha = \alpha_{el} + \alpha_{at} + \alpha_{or} + \alpha_{io} + \alpha_i$[109,122]. The electronic, atomic, orientational and ionic polarisations occur at a molecular level (see Figure 3-1) while the interfacial polarisation refers to a longer-range polarisation due to the accumulation of charge at the interfaces where the dielectric is inhomogeneous (Figure 3-2).

There is a delay between the application of the electric field and the polarisation of the dielectric due to the time the charges take to move and form the electric dipoles. The rate of charge movement differs for each polarisation mechanism so that each has a characteristic time, which accounts for the time period necessary to achieve maximum polarisation. In particular, the time related to the interfacial relaxation is bigger than the times associated with the other mechanisms because the moving charges need to cover longer distances.

In electrokinetics, AC electric fields are often used so that the polarisation is thus frequency dependent. At frequencies below the characteristic time, the mechanism has enough time to achieve maximum polarisation whilst at higher frequencies the maximum polarisation is no longer achieved. At much higher frequencies the material does not respond to the field and polarisation is no longer observed. The frequency dependence of the polarisation is given by the complex permittivity:

$$\tilde{\varepsilon} = \varepsilon - i\frac{\sigma}{\omega} \tag{3.3}$$

where σ is the electrical conductivity, ω the angular frequency of the electric field and i the imaginary unit, with the polarisability now also complex:

$$\mathbf{P} = \varepsilon_0\left(\frac{\tilde{\varepsilon}}{\varepsilon_0} - 1\right)\boldsymbol{E} = n\tilde{\alpha}\boldsymbol{E} \tag{3.4}$$

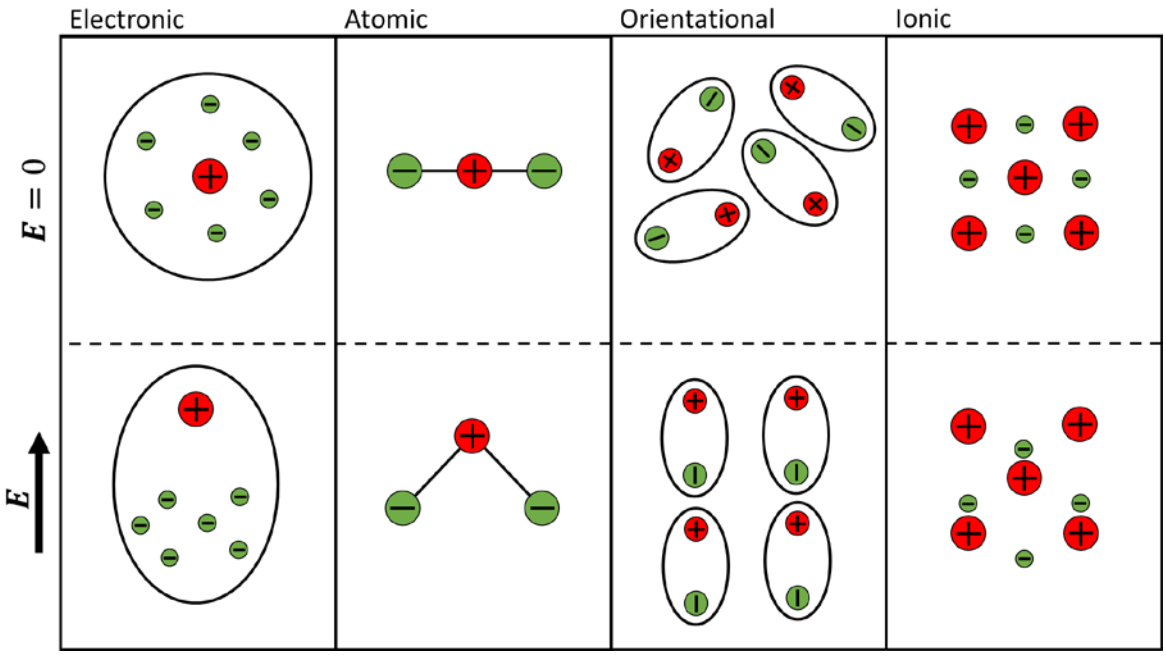

Figure 3-1. Diagram of the dielectric polarisation mechanisms. In the electronic polarisation, when an electric field is applied, electrons arrange themselves around the atomic nucleus to form a dipole across the atom. The atomic polarisation consists of a modification of the structure of the molecules so that positive and negative charges are separated, giving rise to a net dipole moment. In the orientational polarisation pre-existing dipoles in the material (originally randomly orientated), re-orientate in the direction of the external electric field, leading to a non-zero effective dipole moment. The ionic polarisation occurs in ionic crystals when the ions are displaced due to the action of an electric field.

3.1.2 Maxwell-Wagner polarisation and the effective dipole of particles

Interfacial polarisation is the most important polarisation mechanism in electrokinetics since, in general, the system consists of a suspension of dielectric particles in a dielectric liquid. Upon the application of an electric field, charge accumulates at the interfaces between the particles and the

suspending medium due to differences in the polarisability between both dielectrics, as shown in Figure 3-2.

This accumulation of charges has opposite sign on opposite sides of the particles. When the polarisabilities of the medium and the particle are different, the net charge is different on either side of the particle-electrolyte interface, giving rise to an induced dipole moment that depends on both the properties of the particle and the suspending medium. As depicted in Figure 3-2, if the polarisability of the particle is greater than the electrolyte, more charges accumulate inside the interface than outside, creating an induced dipole aligned with the direction of the field. Conversely, if the polarisability of the particle is smaller than the electrolyte, less charge accumulates inside the interface and more charge accumulates outside, giving rise to an induced dipole aligned opposite to the field direction. For AC electric fields, the polarisability also depends on the field frequency, and as a result the surface charge accumulated at the surfaces and the induced dipole moment depends on the field frequency. This polarisation mechanism is called the Maxwell-Wagner interfacial polarisation. A full theoretical description of these phenomena together with detailed mathematical analysis can be found in the literature[110,123].

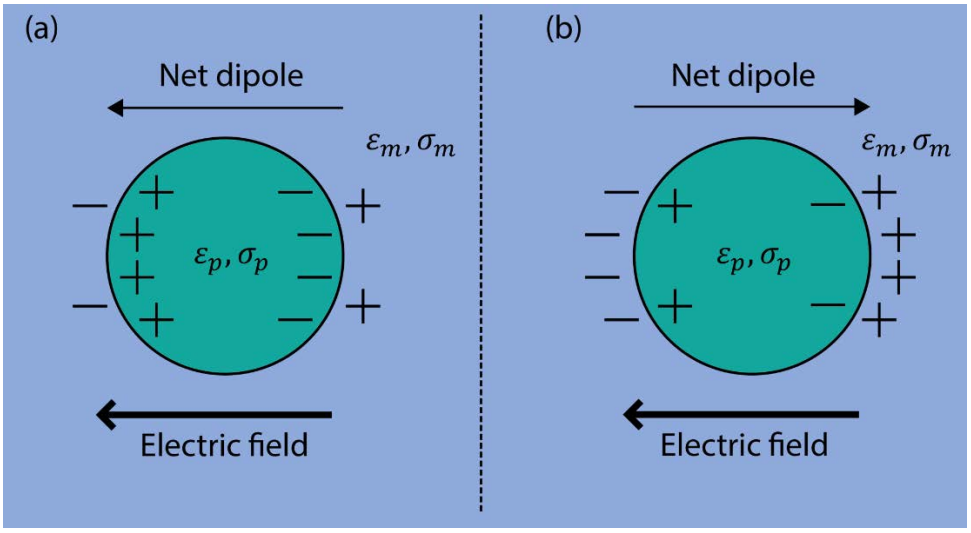

Figure 3-2. Diagram of particle interfacial polarisation due to the differences in the electrical properties of the two dielectrics, particle and suspending medium ($\varepsilon_p \neq \varepsilon_m, \sigma_p \neq \sigma_m$) . (a) Particle more polarisable than the medium – induced dipole aligned with the field. (b) Particle less polarisable than the medium– induced dipole aligned opposite to the field.

For a spherical dielectric particle of radius a the induced dipole moment is given by:

$$\tilde{\mathbf{p}} = 4\pi\varepsilon_m \tilde{f}_{\mathrm{CM}} a^3 \boldsymbol{E} \tag{3.5}$$

where the $\tilde{f}_{\mathrm{CM}}$ is the Clausius-Mossotti factor which accounts for the dipole frequency dependence:

$$\tilde{f}_{\mathrm{CM}} = \frac{\tilde{\varepsilon}_p - \tilde{\varepsilon}_m}{\tilde{\varepsilon}_p + 2\tilde{\varepsilon}_m} \tag{3.6}$$

the index p refers to the particle and the index m to the suspending medium. The CM factor of a spherical particle describes a single relaxation with a time (τ_{MW}) and angular frequency (ω_{MW}):

$$\tau_{\mathrm{MW}} = \frac{\varepsilon_p + 2\varepsilon_m}{\sigma_p + 2\sigma_m} = \frac{1}{\omega_{\mathrm{MW}}} \tag{3.7}$$

At low frequencies the CM factor reaches the limit:

$$\tilde{f}_{\mathrm{CM},\omega\to 0} \approx \frac{\sigma_p - \sigma_m}{\sigma_p + 2\sigma_m} \tag{3.8}$$

also valid in case DC electric fields are used. At high frequencies the limiting value is:

$$\tilde{f}_{\mathrm{CM},\omega\to \infty} \approx \frac{\varepsilon_p - \varepsilon_m}{\varepsilon_p + 2\varepsilon_m} \tag{3.9}$$

The Maxwell-Wagner polarisation mechanism is dominated by conductivity at low frequencies and by permittivity at high frequencies.

A rigid dielectric sphere is the simplest case; however, the CM factor depends on the particle shape and internal characteristics. For example, biological particles have a complicated internal structure due to the presence of cell membranes and walls. A good approximation is to consider the cell to be composed of concentric shells (shell-model)[124–127]. For the case of a single shell that is different from the internal environment the CM factor is[109,128]:

$$\tilde{f}_{\mathrm{CM,single\ shell}} = \frac{\tilde{\varepsilon}_{cell} - \tilde{\varepsilon}_m}{\tilde{\varepsilon}_{cell} + 2\tilde{\varepsilon}_m} \tag{3.10}$$

with $\tilde{\varepsilon}_{cell}$ the complex permittivity of the cell (or other single-shelled particles) given by:

$$\tilde{\varepsilon}_{cell} = \tilde{\varepsilon}_{mem} \frac{\gamma^3 + 2\left(\frac{\tilde{\varepsilon}_{cyt} - \tilde{\varepsilon}_{mem}}{\tilde{\varepsilon}_{cyt} + 2\tilde{\varepsilon}_{mem}}\right)}{\gamma^3 - \left(\frac{\tilde{\varepsilon}_{cyt} - \tilde{\varepsilon}_{mem}}{\tilde{\varepsilon}_{cyt} + 2\tilde{\varepsilon}_{mem}}\right)} \tag{3.11}$$

where $\tilde{\varepsilon}_{cyt}$ and $\tilde{\varepsilon}_{mem}$ are the complex permittivitites of the cell cytoplasm and membrane respectively and $\gamma = a_{cell}/a_{cyt}$, where a_{cell} is the cell radius and a_{cyt} the cytoplasm radius. Single-shelled particles have two characteristic relaxation times, one for each of the interfaces. This model can be extended to more shells to accommodate better the internal structure of more complex particles.

3.1.3 The Electrical Double Layer (EDL) and surface conductance

The Electrical Double Layer (EDL) is a layer of ions that builds up at the interface between a charged surface and an electrolyte. In general, most surfaces either are or become charged when immersed in an electrolyte either by ion adsorption or ionisation of groups in the surface. A surface carrying a net charge creates an electrostatic surface potential ϕ_0 local to the interface. When the surface is immersed in an electrolyte, the surface electric potential attracts ions of opposite charge and repels ions of the same charge. As a result, the region of liquid close to the charged surface has a higher density of counter-ions and a lower density of co-ions, depending on the distribution of the electric potential over the surface. The counter-ions screen the surface charge making the overall charge zero on a global scale. This ion redistribution forms the EDL which is a central concept to most electrokinetic phenomena and has been extensively studied over the last decades[129–134].

The Electrical Double Layer which can be divided in two different parts. The closest region to the surface is called the Stern layer and consist of a thin layer of bound counter-ions that do not move. The outer region of the double layer is referred as the diffuse layer and is the region of liquid near the surface which possesses an excess of counter-ions and a reduced density of co-ions (see Figure 3-3), where the ions can move. The characteristic thickness of the EDL is quantified using a parameter named Debye length λ_D, which is the distance over which the electric potential of the surface falls to $1/e$ of its maximum value (see Figure 3-3). For a monovalent electrolyte with a charge q and a density of ions n_0, this is:

$$\lambda_D = \sqrt{\frac{\varepsilon_m k_B T}{2q^2 n_0}} \tag{3.12}$$

where k_B is the Boltzmann's constant and T the temperature. Figure 3-3 shows a diagram of the structure of the Double Layer where ζ is the zeta potential, i.e. the potential at the slip plane between the Stern and the diffuse layer. λ_D varies enormously depending on the electrolyte concentration, from a few nanometres for relatively concentrated electrolytes (λ_D ≈ 3 nm for 10 mM KCl) to tens of nanometres for very diluted electrolytes (λ_D ≈ 30 nm for 0.1 mM KCl). The relationship between the surface charge density q_s and ζ is given by the Gouy-Chapman equation[135]: $q_s = 2\sqrt{2c\varepsilon e\phi_{ther}}\sinh(\zeta/2\phi_{ther})$ where ϕ_{ther} is the thermal voltage ($\phi_{ther} = k_B T/e$, where e is the eletron charge).

The EDL that forms around the surface of particles in suspension has a strong effect on their electrokinetic behaviour. The presence of the Double Layer gives rise to a particle surface conductance K_s which is the sum of the components from the Stern and the diffuse layer[134]:

$$K_s = K_{s,S} + K_{s,d} \tag{3.13}$$

The magnitude of K_s is a function of the charge density of the surface in contact with the electrolyte which depends on both the properties of the surface material and the liquid. Typical experimentally measured values reported in the literature are found within the range of 0.1-10 nS[136,137]. The existence of a surface conductance affects the interfacial polarisation of dielectric particles. The contribution of the EDL can be described by considering a dipole moment with the particle conductivity as the sum of the particle bulk $\sigma_{p,b}$ and the surface conductance term $\sigma_{p,s}$ given by[137]:

$$\sigma_{p,s} = \frac{2K_s}{a} \tag{3.14}$$

For most solid dielectric particles, the particle bulk conductivity can be neglected and $\sigma_{p,b} \approx 0$ so that the conductivity is determined solely by the surface conductance attributed to the Double Layer.

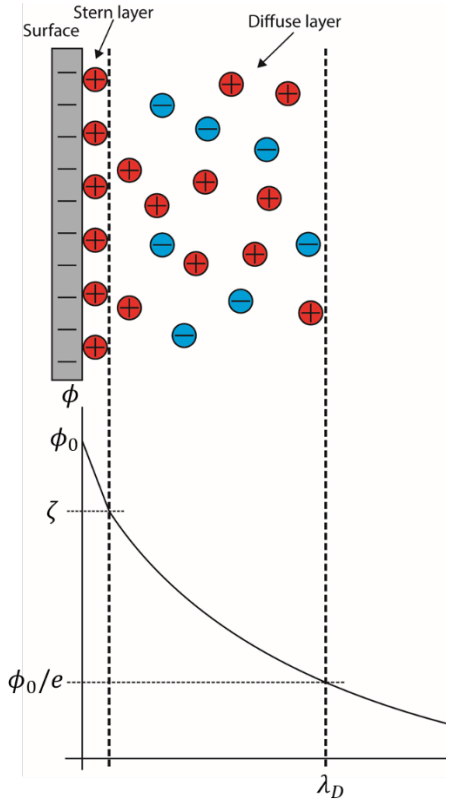

Figure 3-3. Structure of the EDL close to a charged surface.

3.1.3.1 EDL polarisation

Apart from its effect on the interfacial polarisation of particles, the EDL itself also polarises[138–140]. When an electric field is applied, the unbound ions of the diffuse layer move and accumulate at the poles of the particle, modifying the particle overall dipole. This effect has been observed via

dielectric spectroscopy measurements[129,141–143] and is reflected as an extra relaxation that occurs at much lower frequencies, the α-relaxation. According to the work by Schwarz and Schurr[141,144] , who extended O'Konski's model to account for the role of the surface conductance on the EDL polarisation, the characteristic relaxation time of the α-relaxation can be calculated as:

$$\tau_\alpha = \frac{a^2}{2D} \tag{3.15}$$

where a is the particle radius and D is the effective diffusion coefficient of the counterions in the EDL. The characteristic frequency of the α-relaxation is thus $\omega_\alpha = 2\pi f_\alpha = 1/\tau_\alpha$. Typically for KCl solutions in water (at 298 K) $D \sim 10^{-9}$ m^2/s, so that in the case of a 1 nm diameter particle $f_\alpha \sim 660$ MHz whereas for a 1 µm particle $f_\alpha \sim 660$ Hz..

The polarisation of the EDL has been the subject of thorough analysis and discussion over the last decades. In 1995, Lyklema[134] presented a consistent theory and derived a parameter $\tilde{d}_e$ equivalent to the CM factor in the Maxwell-Wagner interfacial polarisation, to account for the induced dipole around a spherical particle of radius a linked to the EDL polarisation:

$$\tilde{d}_e = -\frac{1}{2} + \frac{3\mathrm{Du}^d}{2(1 + \mathrm{Du}^d(\gamma + 1))} \tag{3.16}$$

where the parameter γ is defined as:

$$\gamma = 1 - \frac{(\omega\tau_\alpha)^{2/3} - i\omega\tau_\alpha}{(1 + \sqrt{\omega\tau_\alpha})(1 + \omega\tau_\alpha)} \tag{3.17}$$

and where Du^d is a parameter known as the Dukhin number associated to the diffuse and which is given by the equation:

$$\mathrm{Du}^d = \frac{2\lambda_D}{a}\left(1 + \frac{3m}{z^2}\right)\left[\cosh\left(\frac{zq|\zeta|}{2k_BT}\right) - 1\right] \tag{3.18}$$

with m:

$$m = \frac{2}{3}\frac{\varepsilon}{\mu\eta}\left(\frac{k_BT}{q}\right)^2 \tag{3.19}$$

where μ is the mobility of the ions. A more detailed explanation of this derivation is beyond the scope of this thesis but can be found in the literature[109,134,145].

3.2 Electrokinetic forces on particles

3.2.1 Electrophoresis (EP)

Electrophoresis (EP) is defined as the movement of charged particles suspended in an electrolyte in the presence of an applied electric field[123]. When a charged particle is immersed in an electrolyte, the EDL surrounding the particle effectively screens the charge so that electroneutrality is maintained. As a result, the electric field exerts no net Coulomb force on the particle.

Nonetheless, charged particles move due to the action of the field on the ions in the double layer. The excess charge in the double layer is equal to the charge of the particle but with opposite sign. The Coulomb force moves the mobile ions in the diffuse layer in the direction opposite to that which the charged particle would move. The ions drag the liquid around the particle (this fluid motion is called electroosmosis and is discussed later in this thesis) so that the moving fluid pushes the particle in the opposite direction, the same direction the particle would move through Coulomb force.

As explained in Chapter 2, particles suspended in a fluid reach a constant velocity under the action of an external force. In the case of Electrophoresis, the velocity in the steady state is proportional to the electric field and the proportionality constant is called the electrophoretic mobility μ_{EP}:

$$\boldsymbol{v}_{\mathrm{EP}} = \mu_{\mathrm{EP}} \boldsymbol{E} \tag{3.20}$$

The electrophoretic mobility is thus dependent on the characteristics of the EDL, in particular on the thickness of the EDL with respect to the particle radius, described in terms of the ratio a/λ_D. For $a/\lambda_D \gg 1$, the EDL is thin compared to the particle radius and appears flat on the scale of the Debye length. This case is known as the Helmholtz-Smoluchowski limit where μ_{EP} is given by[146]:

$$\mu_{\mathrm{EP}} = \frac{\varepsilon \zeta}{\eta} \tag{3.21}$$

On the contrary, if the EDL is thick compared to the particle radius, i.e. $a/\lambda_D \gg 1$, the situation is analogous to a point charge. Although the charge is screened by the EDL, the excess of charge on the overall system equals the particle charge. Thus, the net force is then given by the difference between the Coulomb force and the viscous fluid drag with the zeta potential being the potential of a point charge. Then the electrophoretic mobility is[146]:

$$\mu_{\mathrm{EP}} = \frac{2\varepsilon \zeta}{3\eta} \tag{3.22}$$

This is the case for very small particles or very dilute electrolytes and is referred to as the Hückel-Onsager limit.

The model described above is known as the linear regime of electrophoresis. When high electric fields are applied, the influence of the field on the EDL is very significant and the dependence of the EP force becomes non-linear with the electric field. High electric fields change the ion distribution surrounding the particle and disturb the electroneutrality of the system. This mechanism is called concentration polarisation and on a local scale gives rise to regions of enhanced and decreased concentration around the particles. Non-linearity can also appear when the particle surface conductance is high with respect to the medium conductivity. This factor is quantified by a dimensionless parameter, the particle Dukhin number[147,148]:

$$Du = \frac{K_s}{\sigma_m a} \tag{3.23}$$

A detailed description of non-linear electrophoresis and the role of concentration polarisation are complicated, however many excellent papers on non-linear electrophoretic behaviour can be found in the literature[147,149,150].

Many techniques that use EP for particle manipulation and separation have been developed, exploiting charge differences to discriminate between sample components[136,151–154]. However, there is a lack of versatility intrinsic to EP. The fact that most biologically relevant particles have very similar values of the zeta potential has directed efforts to exploration of other electrokinetic forces, mostly Dielectrophoresis (DEP).

3.2.2 Dielectrophoresis (DEP)

Dielectrophoresis (DEP) refers to the movement of polarisable particles suspended in an electrolyte in response to a non-uniform electric. This motion is caused by the action of the electric field on the induced dipole of the particle and does not require the particles to be charged[155]. As explained in the previous section, when an electric field is applied to a suspension of particles, the charges that build up at the interface between the particle and the electrolyte give rise to an effective dipole moment on the particle. The electric field then exerts a force on the dipole. In the case of a uniform electric field, the force acting on each of the poles is the same so that the net force acting on the particle is zero. However, if the applied electric field is spatially non-uniform, the force on each of the poles is different, producing a net force on the particle called Dielectrophoresis. The force can be calculated from the particle effective dipole moment[123]:

$$\boldsymbol{F}_{\mathrm{DEP}} = (\mathbf{p} \cdot \nabla)\boldsymbol{E} \tag{3.24}$$

This expression is only valid if the size of the particle is much smaller than the dimensions of the non-uniformity of the electric field, i.e. if the field does not change significantly at the scale of the particle. This is the dipole approximation[63,156].

Under the action of an AC electric field, the DEP force acting on the particle has a non-zero time average ($\langle \boldsymbol{F}_{\mathrm{DEP}} \rangle \neq 0$), in opposition to the EP force ($\langle \boldsymbol{F}_{\mathrm{EP}} \rangle = 0$). As a result, the net electrically induced particle motion is solely determined by DEP. This time-averaged AC-DEP force is:

$$\langle \boldsymbol{F}_{\mathrm{DEP}} \rangle = \frac{1}{4} V \mathrm{Re}[\tilde{\alpha}] \nabla |\boldsymbol{E}|^2 \tag{3.25}$$

where V is the particle volume and E the electric field magnitude. This expression shows that the frequency dependence is given by the real part of the particle polarisability. For the specific case of a spherical particle:

$$\langle \boldsymbol{F}_{\mathrm{DEP}} \rangle = \pi \varepsilon_m a^3 \mathrm{Re}\left[\tilde{f}_{\mathrm{CM}}\right] \nabla |\boldsymbol{E}|^2 \tag{3.26}$$

with:

$$\tilde{f}_{\mathrm{CM}} = \frac{\tilde{\varepsilon}_p - \tilde{\varepsilon}_m}{\tilde{\varepsilon}_p + 2\tilde{\varepsilon}_m} \tag{3.27}$$

There are two possible directions for the DEP force depending on whether the particle is more polarisable than the medium or less. If the particle is more polarisable than the medium, the net dipole aligns with the field so that the particle moves towards regions of high electric field gradient; called positive DEP (pDEP). In contrast, negative DEP (nDEP) occurs if the particle is less polarisable than the medium; the dipole is aligned opposite to the field and the particle is repelled from regions of high field gradient. This is diagrammatically shown in Figure 3-4. The direction of the DEP force is governed by the previous equation for the real part of the CM factor: $\mathrm{Re}\left[\tilde{f}_{\mathrm{CM}}\right] > 0$ for pDEP and $\mathrm{Re}\left[\tilde{f}_{\mathrm{CM}}\right] < 0$ for nDEP. Since $\mathrm{Re}\left[\tilde{f}_{\mathrm{CM}}\right]$ is frequency dependent, in general it is possible to switch from pDEP to nDEP simply by changing the frequency of the field.

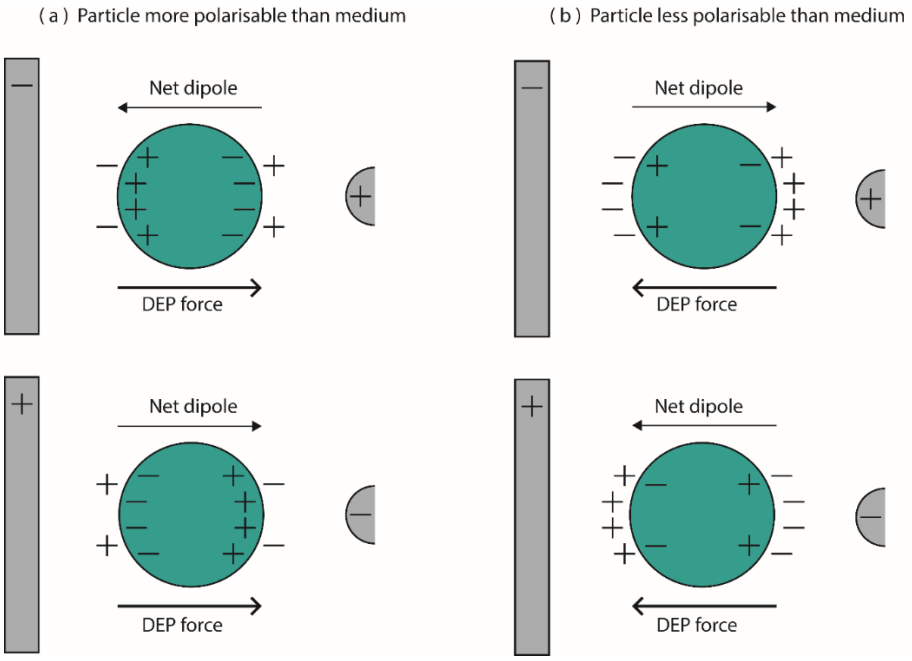

Figure 3-4. DEP force direction for particles (a) more polarisable or (b) less polarisable than the suspending medium. (a) pDEP: particle moves towards high gradient field regions. (b) nDEP: particle is repelled from high gradient field regions.

The frequency at which $\boldsymbol{F}_{\mathrm{DEP}} = 0$ is the crossover frequency f_0 and separates the nDEP from the pDEP behaviour[157]. For a homogeneous solid dielectric sphere:

$$f_0 = \frac{1}{2\pi}\sqrt{-\frac{(\sigma_p - \sigma_m)(\sigma_p + 2\sigma_m)}{(\varepsilon_p - \varepsilon_m)(\varepsilon_p + 2\varepsilon_m)}} \tag{3.28}$$

Note that f_0 does not exist for all situations but only when the particles exhibit at least one large enough relaxation so that the induced dipole changes direction (Figure 3-5).

The DEP force acting on the particles suspended in the electrolyte is balanced by the fluid viscous drag, resulting in a steady state with a constant particle velocity which is proportional to the gradient of the electric field squared, with the proportionality constant being the dielectrophoretic mobility (μ_{DEP}):

$$\boldsymbol{v}_{\mathrm{DEP}} = \mu_{\mathrm{DEP}} \nabla |\boldsymbol{E}|^2 \tag{3.29}$$

with:

$$\mu_{\mathrm{DEP}} = \frac{\varepsilon_m a^2 \mathrm{Re}\left[\tilde{f}_{\mathrm{CM}}\right]}{6\eta} \tag{3.30}$$

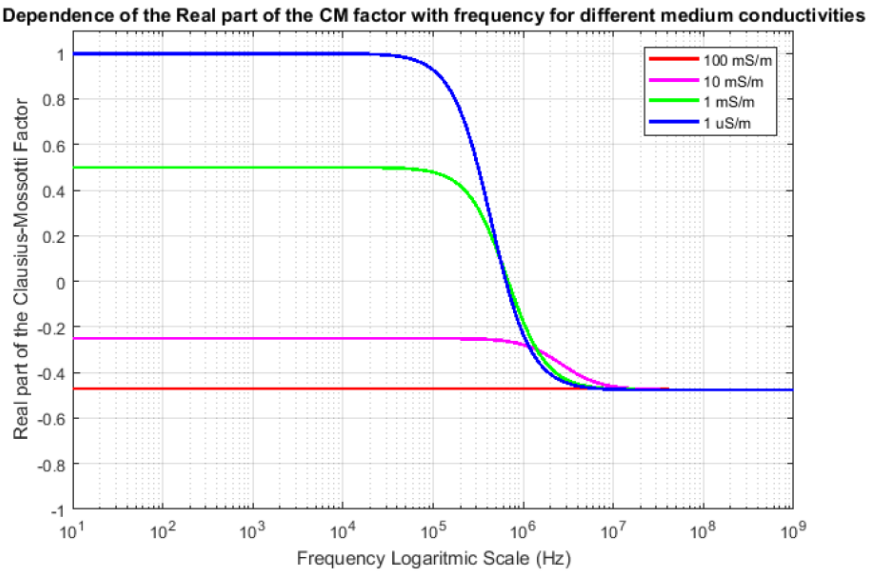

Figure 3-5. Frequency dependence of $\mathrm{Re}\left[\tilde{f}_{\mathrm{CM}}\right]$ for 1 µm diameter spheres for different medium conductivities assuming $K_s = 1$ nS and a medium permittivity of $\varepsilon_m = 80\varepsilon_0$ (permittivity of water).

Furthermore, it is now consistent to consider the contribution of the EDL polarisation on the overall dipole around the particle and thus on the magnitude and direction of the DEP force. Given that the characteristic frequency of the EDL polarisation is much lower than that of the Maxwell-Wagner mechanism, the effects of the α-relaxation are expected to be relevant only in the low frequency limit (in frequencies of the order of ω_α).

Nevertheless, the induced dipole moment associated to the EDL polarisation does not change the net dipole direction and is thus not capable of switching from pDEP to nDEP, or vice-versa[138]. When the frequency of the applied AC field is reduced, the induced dipole of particles experiencing nDEP increases in magnitude because of the α-relaxation, making the nDEP slightly stronger. On the contrary, for particles undergoing pDEP the magnitude of the induced dipole is reduced due to this mechanism but, nevertheless, the dipole does not change direction, regardless the strength of the EDL polarisation. Therefore, the EDL polarisation does not predict a change in the DEP behaviour, i.e. it is not capable of switching between pDEP and nDEP.

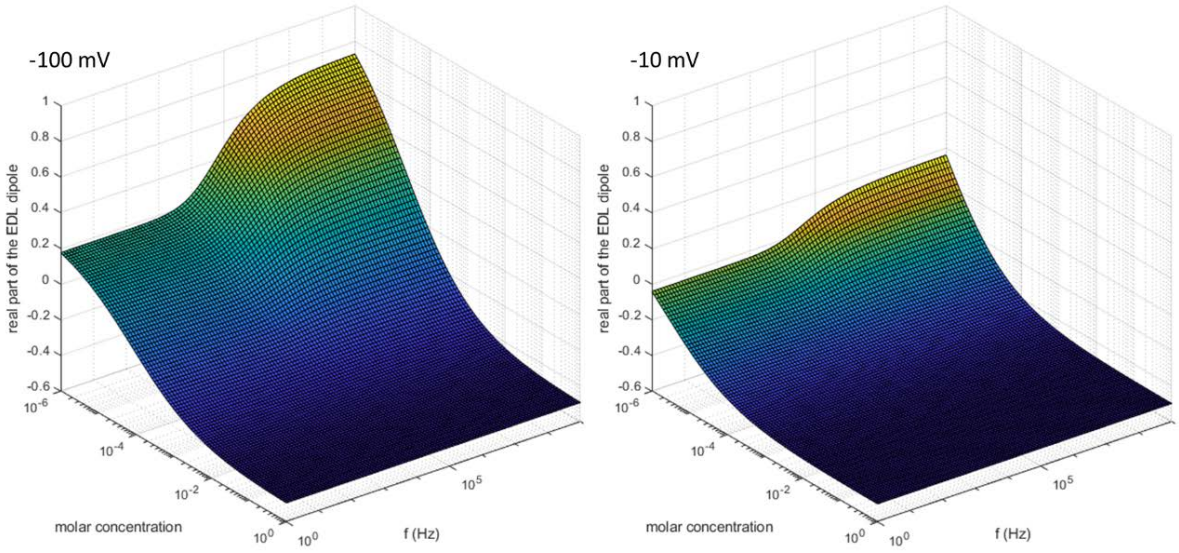

Figure 3-6. Dependence of the real part of the function $\tilde{d}_e$, the dipole coefficient associated to the EDL polarisation, as a function of the frequency of the electric field and the electrolyte molar concentration for KCl at 298 K for a 500 nm diameter sphere and two different zeta potentials, -100 mV and -10 mV.

Figure 3-6 shows the dependence of the real part of the function $\tilde{d}_e$ (the equivalent to the Clausius-Mossotti factor for the EDL polarisation) with the frequency of the electric field and the electrolyte concentration for a 500 nm particle with two different zeta potentials (-10 mV and -100 mV). Further developments on the role of the EDL polarisation on the DEP particle behaviour can be found in the literature[140,158].

DEP particle manipulation has many advantages due to the inherent characteristics of the DEP force and its dependence on particle polarisation. A wide range of tunable parameters (field magnitude and geometry, frequency, waveform, phase and medium conductivity) can be used to precisely control the force on different types of particles. Moreover, the DEP behaviour depends on a great variety of electrical and structural particle parameters, making DEP very powerful for discriminating subpopulations within mixtures and for particle characterisation and separation.

These characteristics have led to the development of many applications for DEP. It has been successfully used to separate particles with different electrical properties from a mixture[39,159–162] like bacteria[163] and colloidal particles[157], to trap particles for later analysis[164], to assemble particles to form microstructures[165,166] for example for miniaturized biosensors[167], to purify and concentrate samples[168] or for particle characterization[169]. It is also used for the manipulation of droplets and biomolecules[170,171] like different length DNA molecules[172,173]. Many other applications, together with a detailed analysis of DEP, can be found in a review by Pethig[63].

3.2.3 Electrorotation (ROT)

When a particle sits in a uniform electric field, the DEP force on the induced dipole is zero so there is no net particle motion. However, the fact that each pole (with opposite charges) experience a force of the same magnitude but opposite direction generates a torque on the particle that tends to align the induced dipole with the applied electric field. This torque is given by:

$$\boldsymbol{\Gamma} = \mathbf{p} \times \boldsymbol{E} \tag{3.31}$$

In electrokinetics, this mechanism is known as electro-orientation (EOr). Nonetheless, the alignment is not instantaneous and there is a delay between the field being stablished and the dipole alignment. If the field then changes direction, the dipole realigns causing particle rotation, termed electrorotation (ROT). The time averaged first order electrorotation torque can be calculated as[174]:

$$\boldsymbol{\Gamma} = \frac{1}{2}\mathrm{Re}[\mathbf{p} \times \boldsymbol{E}^*] \tag{3.32}$$

The torque depends on the induced dipole of the particle and hence on the particle polarisation. Therefore, inspection of the ROT behaviour provides information of the particle electrical properties. The most common ROT techniques apply a rotating electric field created using four 90° shifted signals using an electrode configuration such as that shown in Figure 3-7. This rotating field creates a constant torque on the particle which makes it rotate asynchronously[128]:

$$\boldsymbol{\Gamma} = -V\ \mathrm{Im}[\tilde{\alpha}]|\boldsymbol{E}|^2 \tag{3.33}$$

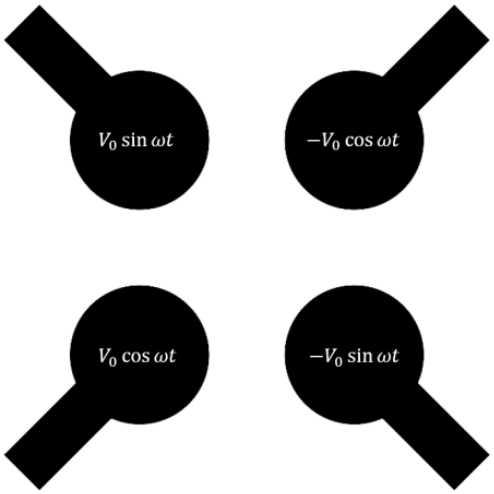

Figure 3-7. ROT electrode configuration. The four 90° shifted signals create a rotating field vector with a uniform electric field region in the centre of the four electrodes.

As for to EP and DEP, particles reach a stationary state where the ROT torque is balanced by the fluid viscous drag. However, the ROT torque depends on the imaginary part of the complex polarisability, in contrast to DEP. This means that if $\mathrm{Im}[\tilde{\alpha}] > 0$ the particle rotates counter-field while if $\mathrm{Im}[\tilde{\alpha}] < 0$ the particle rotates co-field, and that the rotation velocity has a peak corresponding to the peak of $\mathrm{Im}[\tilde{\alpha}]$ at the polarisation relaxation frequency. These characteristics make ROT a very useful technique to explore the polarisation mechanisms and very powerful in combination with DEP for particle characterisation[128,137,175–178].

3.3 Other electrokinetic phenomena

3.3.1 Electrohydrodynamics (EHD)

Electrically induced fluid flow often plays an important role in electrokinetic systems, and the understanding of this phenomena is therefore necessary before developing electrokinetic techniques for particle separation, manipulation and characterisation. Also, understanding of EHD flow has led to specific applications for these flows which are relatively easy to control by tuning the electrical signal, the geometry of the channels and the characteristics of the fluid and the surfaces.

3.3.1.1 Electroosmosis (EO)

In general, any surface carries a net charge which when submerged in an electrolyte leads to the formation of an EDL and a non-zero zeta potential. In the case of a cell, typical values for this surface charge are in the range of 10^{-11}∼10^{-12} C/m whereas popular microfluidics substrates such as glass and PDMS normally carry surface charge densities of the order of 10^{-3} C/m. The magnitude of the net surface charge, and thus the zeta-potential, depends on the properties of the material and the medium, mainly on the electrolyte concentration and the pH. For example, in the common case when the ions that determine the surface charge are H^+/OH^-, the pH at which the groups on the surface in contact with the medium do not ionise, and therefore the surface do not carry a net charge, is known as the isoelectric point[179,180].

An applied electric field with a component tangential to the surface pulls the charges in the EDL which drag the fluid and set it into motion. This is called Electroosmosis (EO) and it is the mechanism behind electrophoretic particle motion.

The electrical forces are balanced by the viscous friction of the fluid, producing a constant flow velocity proportional to the field magnitude, which can be calculated from the Stokes equation by considering a Coulomb force acting on the fluid:

$$\boldsymbol{v}_{\mathrm{EO}} = \mu_{\mathrm{EO}} \boldsymbol{E}_t \tag{3.34}$$

where μ_{EO} is the proportionality constant called electroosmotic mobility, given by:

$$\mu_{\mathrm{EO}} = -\frac{\varepsilon \zeta}{\eta} \tag{3.35}$$

The resulting EO fluid velocity is zero at the slip plane and maximum at the limit of the EDL, with a high spatial gradient of the velocity in distances of the order of the Debye length. Inside channels, the EO flow produces a plug flow such as that shown in Figure 3-8a, constant across the channel section.

The previous equations show that an AC electric field produces a zero-time average electroosmotic flow. However, AC induced electroosmotic flows (ACEO) have been reported around microelectrode structures when non-uniform electric fields are applied[114,181,182]. These ACEO flows are related to the charging of the double layer around the electrodes and are described in Figure 3-8b. When a voltage is applied, charge of opposite signs accumulates at the interface between the electrode and the electrolyte, creating an induced EDL. The electric field acts on this excess charge moving the ions and thus the fluid. When the polarity of the AC field changes, the field changes direction and the induced charge changes sign, resulting in an induced flow in the same direction.

The dependence on the charging of the EDL means that the effects of ACEO flows become predominant in the low frequency range[114]. At higher frequencies the ions do not have enough time to move and form the EDL. A more detailed description of the ACEO mechanisms can be found in the literature [109,114,181,182].

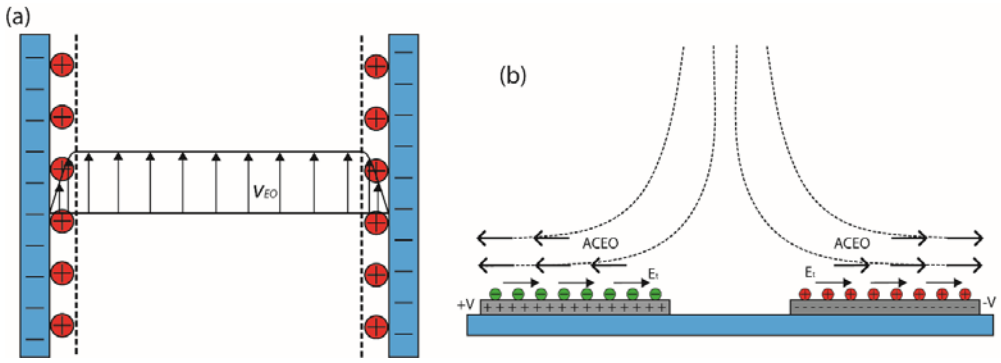

Figure 3-8. (a) EO flow profile inside a channel. (b) ACEO profile around two planar microelectrodes. Every half period of the AC signal, the charges in the diagram switch sign but the direction of the ACEO remains unchanged.

Although the effects of electroosmosis on particle behaviour are unspecific and can sometimes be inconvenient for particle sorting, EO has been successfully used for other applications. The

characteristics of EO flows and the ability to integrate electrodes within microchannels enable an easy and precise control of the electrically induced flows in the microscale. Thus, many microfluidic techniques utilise EO flows, for example for pumping and mixing of samples and reagents[183–189].

3.3.1.2 Electrothermal flow

The electrothermal flow is the dominant mechanism when high frequency AC electric fields are applied. This flow arises from the interaction of the electric field with gradients in the fluid conductivity and permittivity caused by a temperature gradient. A temperature gradient is in general caused by a non-uniform Joule heating of the fluid although it can also arise from external sources of heat, such as light. More detailed explanations of this mechanism can be found in the literature[190,191] together with specific technological applications[192,193].

3.3.2 Induced charge electrokinetics (ICEK)

The concept of Induced charge Electrokinetics was first introduced by Bazant and Squires[120] to describe several Electrokinetic phenomena observed mainly in the vicinity of metallic structures and particles arising from the interaction of the field with an induced charge.

The difference between ICEK phenomena and classic electrokinetics lies on the origin of the diffuse layer charge. In traditional electrokinetics the surfaces become charged by adsorption and/or dissociation of specific groups or atoms. In ICEK, instead, the EDL is induced by the electric field. When a perfectly polarisable particle (i.e. a conducting particle) is placed in an electric field, the free-moving charges in the particle material move to opposite poles of the particle resulting in a zero net electric field in the inside, as shown in Figure 3-9a. In this situation, the electric field lines intersect the particle surface perpendicularly (see Figure 3-9a). If such particle is immersed in an electrolyte, the ions in solution are driven along the field lines and, since perfectly polarisable surfaces pass no current, these charges accumulate at the interface between the metal and the electrolyte, building up an Induced Double Layer (IDL) that screens the local charge so that, when the steady-state is reached, the electric field lines do not intersect the surface and the particle behaves as an insulator (see Figure 3-9b). The time the ions in solution need to move and create the double layer is known as the charging time of the IDL and can be calculated as:

$$\tau_c = \frac{\lambda_D a}{D} \tag{3.36}$$

where a is the particle radius, λ_D the Debye length and D the ion diffusivity ($D \approx 2{\cdot}10^{-9}$ for KCl in water at 25°C). For AC electric fields, the characteristic frequency of this polarisation mechanism (ω_c) corresponds to the inverse of the charging time, τ_c^{-1}. For frequencies higher than ω_c, the ions

in solution do not have sufficient time to form the IDL before the field changes polarity and the particle behaves as a conductor. At lower frequencies, the IDL has enough time to build up and the particle behaves as an insulator[175,194–196]. The dependence of τ_c with λ_D means that this mechanism is strongly dependent on the electrolyte conductivity (for KCl at 25ºC : 1M - λ_D ≈ 0.3 nm, 10 mM - λ_D ≈ 3 nm). Equation (3.36) also implies a linear dependence with the particle size: a 1 nm radius particle in a 10 mM KCl solution has a relaxation frequency of around 100 MHz whereas for 1 µm radius this frequency is around 100 kHz.

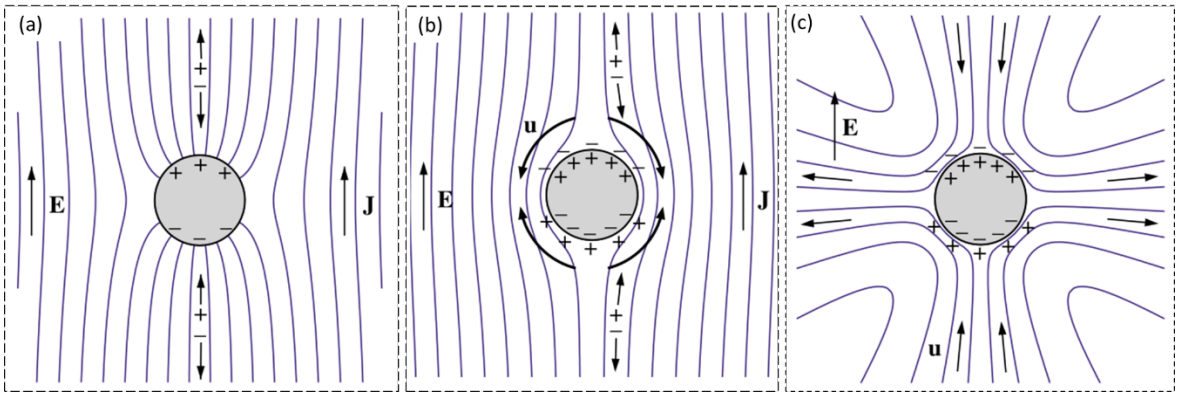

Figure 3-9. Adapted from Bazant and Squires[120]. (a) Electric field lines around a conducting particle. (b) Electric field lines after the IDL forms at the interface between the conductor and the electrolyte. The field lines bend around the particle and the behaviour is analogous to an insulator. (c) ICEO flow profile around a conducting particle. The field acts on the induced charges creating a net quadrupolar flow.

The ICEK phenomena arise from the interaction of the external field with the induced charges in the IDL. The electric field drags the mobile ions in the IDL and generates an electroosmotic flow, termed Induced Charge EO or ICEO[197]. Since opposite charges accumulate on opposite sides of the particle, the ICEO flow is generated in opposite directions producing the quadrupolar flow profile shown in Figure 3-9c. For an AC field, when the polarity changes, both the direction of the electric field and the sign of the induced charges switch. As a result, the net ICEO flows always in the same direction and thus has a non-zero time average. This mechanism is very similar to ACEO and opposite to classic EO flows which have a zero-time average in AC electric fields.

This description is perfectly valid for other types of conducting particles and structures. Depending on the shape and the characteristics of the surface the flow profile differs from the quadrupolar flows shown in Figure 3-9c[198]. For example, in the case of Janus particles where one half of the particle is metallic and the other half is a dielectric, the ICEO flows generated on the conducting side propel the particle in the direction the dielectric side is facing[199,200]. In addition, fixed metallic structures can have different applications, especially in combination with microfluidics[201], that

include generating vortices for mixing[202,203] and also pumping using asymmetric structures to create a net ICEO flow in one direction[204–206].

3.3.3 Concentration Polarisation (CP)

The structure of the EDL was described in a previous section assuming an equilibrium state. Nevertheless, external influences, such as the application of an external electric field, lead to a non-equilibrium situation in the EDL. Typically, low electric field strengths are used, so that these effects are not significant. However, at high electric fields, the characteristics of the EDL are modified considerably. This leads to several related phenomena which are studied by the field of non-linear electrokinetics, including Concentration Polarisation (CP)[150].

CP refers to the appearance of a concentration gradient at the local scale, around a surface, often caused by an applied electric current which drives the ions. Since electroneutrality is maintained in the bulk, at the regions where the ions accumulate the electrolyte concentration increases, whilst the depleted regions correspond to regions of reduced conductivity. CP is often accompanied by a deviation from electroneutrality beyond the EDL that gives rise to regions of induced space charge. This generates additional electroosmotic flows around the surface, and therefore electrophoretic motion in the case of particles, that reshape the classical EO and EP behaviour and are known as second kind EO[207,208] and EP[147,209].

Although CP is more pronounced and relevant for ion-exchange membranes and particles[210,211], which are selectively conductive for one species in solution, it can also be influential for non-conducting particles with a high surface conductance ($Du \gg$)[212,213]. In this case, the surface current moves the ions from one side of the particle to the opposite, creating regions of increasing and decreasing concentration around the particle (see Figure 3-10a). Induced space charge also arises from this mechanism and produces second kind EO and EP for non-conducting particles.

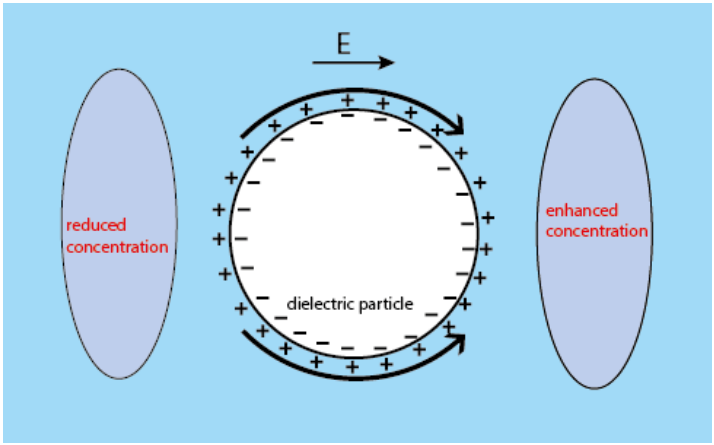

Figure 3-10. Concentration polarisation mechanism around a non-conducting particle.

Not only is the surface conductivity important, but other factors also play a relevant role such as the number of mobile counterions and electromigration of ions. In addition, the surface conductivity is also affected by CP, complicating the development of a complete theory that fully explains all aspects of CP and second kind EO and EP.

CP has a strong influence (beyond Electrokinetics) on the physics of a wide range of interfacial phenomena[214–216]. Furthermore, CP has shown a great potential for the development of new technologies[217–221], including particle separation techniques[222–224].

3.4 Electrokinetics for particle separation

Electrokinetics is a wide research field with innumerable capabilities, great utility and far-reaching applications. The influential role electrokinetics in the development of separation techniques is therefore not surprising. Nowadays, a considerably high percentage of all new techniques use electric fields to achieve separation. When electrokinetics is combined with microfluidics the separation potential is magnified. The position and trajectories of particles are precisely determined and constrained within the microchannels while electric fields can be applied to tune and control the separation.

3.4.1 Insulator based DEP (iDEP)

DEP and EP are the two main forces responsible for particle electrokinetic behaviour. However, EP depends only on the particle charge which is a characteristic that does not vary much amongst the particles targeted by most separation techniques. The charge differences between cells, bacteria or vesicle populations are minimal meaning that EP is not the best way of discriminating different sample components. In contrast, DEP depends on a wider and more variable set of properties. The strong dependence with particle size allows precise size-based DEP separation, and the dependence with the particle polarisability can be exploited to discriminate particles with different electrical and structural features. Despite the fact that DEP needs relatively high electric fields to generate a strong enough force on the particles, the fact that it has a non-zero time average eliminates the EP and EO side effects which have a zero time average and are negligible at high frequencies.

The first DEP separation techniques used microelectrodes patterned onto glass to create non-uniform electric fields[225–229]. However, the microelectrodes are expensive and costly to fabricate and are often accompanied by some unwanted effects, such as ACEO or Joule heating of the fluid (and therefore electrothermal flows) which affect particle motion and make separation difficult.

Over the last decades, microfluidics has led to the development of new techniques that significantly improved DEP separation. A very promising approach consists of using insulating structures placed within uniform electric fields to create the field gradients necessary for DEP. This is called insulator-based DEP (iDEP) and has several advantages over electrode-based DEP, mainly in terms of device fabrication and reduction of the costs.

iDEP was firstly introduced by Masuda *et al.*[230] in 1989. They reported a technique to induce cell-fusion via pDEP using a small gap between two insulators placed between two electrodes. Since then, the field of iDEP has experienced a huge growth and devices with a great variety of channel shapes, in-channel geometries and modes of operation have been developed[231].

iDEP techniques have two main modes of operation for particle sorting. Batch mode iDEP uses DEP to trap target particles as they flow through microchannels and hence separate them from the sample which continues to flow (see Figure 3-11a). Once the whole sample has been processed, the trapped particles are released by turning off the field and washing them away[65,168]. These devices often use arrays of fixed insulating structures placed inside the channel to constrain the electric field and provide enough trapping locations for all the particles in the sample[232–235].

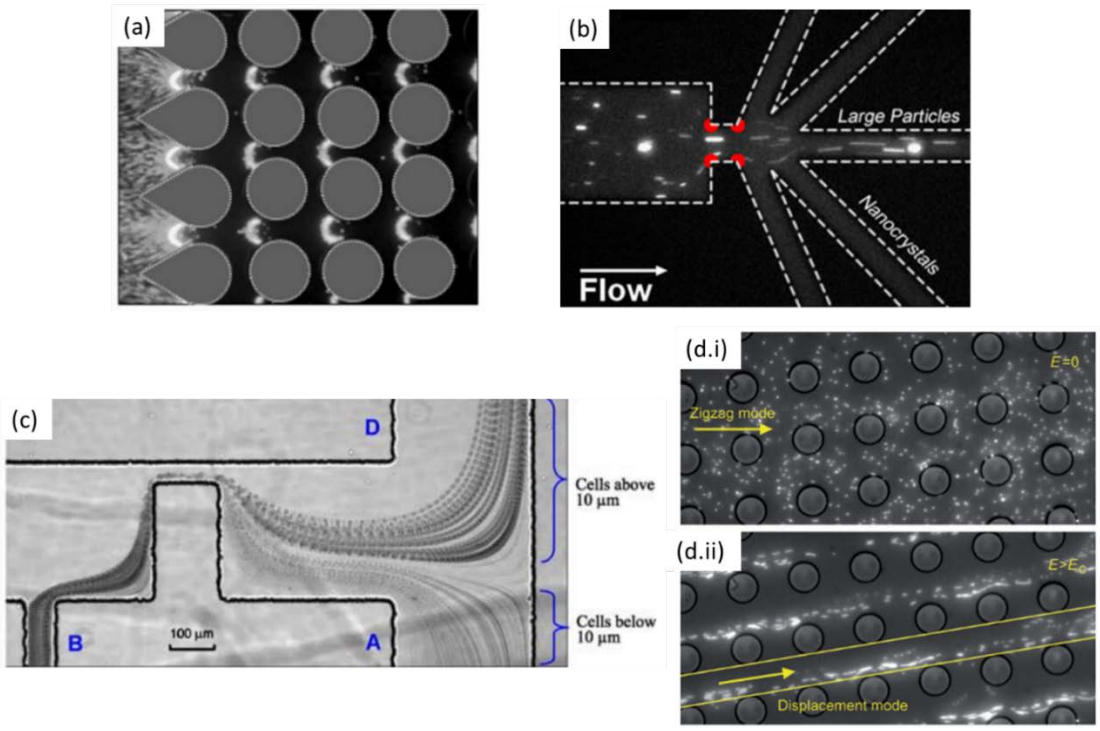

Figure 3-11. Examples of iDEP techniques. (a) nDEP trapping of 1 µm diameter particles with micron-sized insulating cylindrical posts. Copied from Lalonde *et al.*[236] (b) Continuous iDEP separation around insulating corners. Copied from Abdallah *et al.*[237] (c) Continuous iDEP cell sorting using an insulating constriction. Copied from Kang *et al.*[238] (d) Combination of DLD with DEP for tunable separation. Copied from Beech *et al.*[99].

The second mode of operation uses DEP to modify the particle trajectories and discriminate between the different sample components as they flow. This continuous flow approach is usually more convenient since the operating protocols are simpler, throughputs are higher, and the risks of contamination are reduced. Furthermore, the field magnitudes are in general lower, since the particles only need to be deflected slightly from their microfluidically determined trajectories and not completely stopped against the flow. These iDEP devices use ridges, curved channels and constrictions to create the field gradients[68,69,237,238] (see Figure 3-11b and c). Nevertheless, the iDEP continuous flow separation technique that is most relevant for this thesis consists of a combination of DEP and DLD which was first reported by Beech *et al.*[99] in 2009. They placed electrodes at the inlet and the outlet of a DLD device and argued that the DLD posts (which are typically made of insulating polymers) perturbed the electric field lines creating field gradients which then gave rise to DEP that acted on the flowing particles and altered their trajectories (see Figure 3-11d). Subsequent investigations demonstrated that this behaviour is much more complicated than was explained in the paper and this thesis develops a significant number of these.

3.4.2 Free Flow EP and Field Gradient EP and CP

Electrophoretic separation is also a very common approach for particle sorting and many methods have been reported. These techniques exploit the small differences in the electrophoretic mobility between particles to separate the sample. As mentioned above, bioparticles show little variations in charge or zeta potential and thus electrophoretic mobility. This is the reason why most EP techniques focus on the separation of analytes and biomolecules.

Some techniques use uniform electric fields to perform the separation. Capillary Electrophoresis (CE) use electric fields applied along a capillary where the sample is flowing[239]. The different sample components are separated along the capillary length depending on their electrophoretic mobility and collected at different times. In Free Flow Electrophoresis (FFE) the electric fields are applied perpendicularly to the fluid flow, so the particles displace across the channel section as they flow and separate depending, again, on their electrophoretic mobilities[240]. FFE enables continuous flow separation but has some drawbacks, principally band broadening along the channels, caused by mechanisms such as diffusion or lateral EO flow.

EP based separations can be improved using electric field gradients to increase the resolution and precision of the techniques, enhancing the quality of the separation. In general, electric field gradients are created by means of conductivity gradients created by precisely controlled electrolyte concentration gradients. The most common technique that uses electric field gradients is Isotachophoresis (ITP)[241]. In ITP self-correcting conductivity gradients are established using two

electrolytes with different electrophoretic mobilities, the leading and the trailing electrolytes. The sample components concentrate between the two electrolytes within the conductivity gradient region and separate according to their EP mobilities. The nature of ITP makes it perfect for combining with CE[58,242].

Other electric field gradient techniques have also been reported[60,61,243], some in combination with FFE[244]. A very interesting approach consist of using Concentration Polarisation through an ion selectively permeable membrane to create a conductivity gradient and control the EP force acting on particles[223,224].

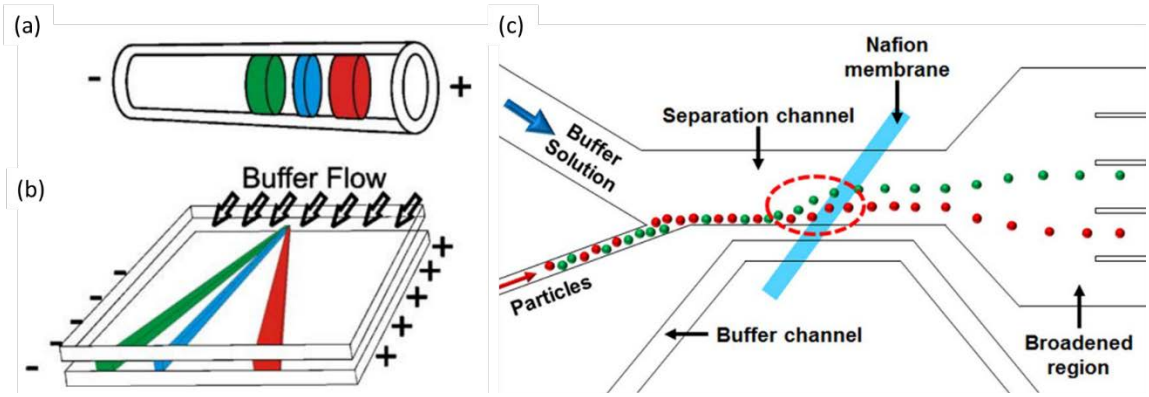

Figure 3-12. Examples of electrophoretic separations. (a) Capillary Electrophoresis and (b) Free Flow Electrophoresis. Copied from Turgeon *et al.*[240]. (c) Electrophoretic separation using Concentration Polarisation. Copied from Jeon *et al*.[223].

3.5 Summary

This chapter provided a very short and general introduction to the vast research field that is Electrokinetics. The most important theoretical concepts were introduced and the relevance of electrokinetics to particle sorting discussed. The enormous potential that a combination of microfluidics and electrokinetics has for particle separation was also discussed.

In the following chapters a technique that combines microfluidics and electrokinetics is described and analysed in detail. This is an electrokinetically tunable DLD technology which has shown a great potential for the separation of a wide range of particles based on several structural and electrical particle properties. The physics behind the separation are presented together with hints of new electrokinetic phenomena that might play a role in controlling the spectrum of particle behaviour observed within these systems.

Chapter 4 Methods, fabrication and experimental setup

This thesis describes a combined microfluidics and electrokinetics device for particle separation. Specifically, the technique consists of classical DLD sorting which is tuned using electrokinetics. For this purpose, parallel planar electrodes were integrated within traditional DLD devices. The electrodes were placed along the channel edges to create electric fields perpendicular to the fluid flow. This chapter provides a description of the design and fabrication process of these devices, together with a summary of the experimental methods that were used to collect and analyse the data presented throughout this thesis.

4.1 Device design

4.1.1 Design A – Microparticle Electrokinetic DLD separation

Two different kinds of DLD devices were designed for this research project. The objective of the first type of devices (Design A) was to conduct proof-of-principle experiments, study the separation mechanisms and characterise the technique as a function of different experimental parameters.

Devices with different DLD array geometries were designed, all of them with cylindrical posts and a symmetric arrangement, i.e. equal lateral and horizontal gaps, which were also equal to the post diameter. The values of the parameters are found in Table 4-1 (the parameters are defined in Chapter 2).

Table 4-1. Design A - DLD array geometric parameters.

Device	$\boldsymbol{\lambda}$ (μm)	$\boldsymbol{\Delta\lambda}$ (μm)	$\boldsymbol{N}$	$\boldsymbol{\theta}$ (°)	$\boldsymbol{G = D_p}$ (μm)	$\boldsymbol{D_c}$ (μm)
#1	36	2	18	3.18	18	6.3
#2	30	1.5	20	2.86	15	5.0
#3	21.6	1.2	18	3.18	10.8	3.8
#4	16	0.8	20	2.86	8	2.7

A diagram of the device design is shown in Figure 4-1a. The microfluidic channels were 2.6 mm wide and 31.6 mm long and had a concentration region at the top to avoid particles from touching the electrode. This consisted of a section of posts with no offset (zero tilt angle) where all particles follow straight trajectories (see Figure 4-1b). The transition from tilted to straight posts was achieved using stretched posts with modified lateral gaps to avoid perturbed flow patterns around the neighbouring posts; following the method of Inglis[245]:

$$G_n = \sqrt{2 - n/N} \tag{4.1}$$

where n is the post index which goes from 1 to N.

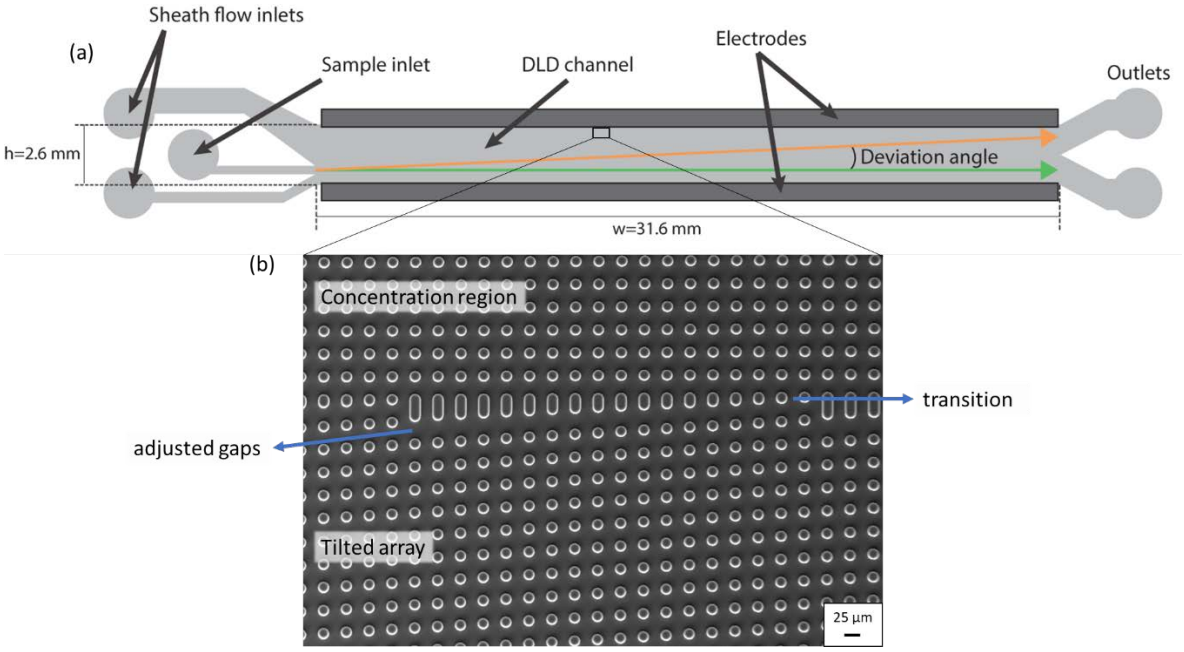

Figure 4-1. Design A. (a) Device design. (b) SEM picture of the transition between the sorting and the concentration regions.

These devices had three different inlets, two for sheath flow (top and bottom in Figure 4-1a) and another to introduce the sample. The sheath flow allowed focusing of the sample into a tight stream simply controlling the flow rate on each inlet, enabling measurement of the deviation angle by comparison of the entry and exit positions of the sample. Two outlets placed at the end of the channels served to collect the zigzagging (bottom outlet) and the displacing (top outlet) particles separately.

Two parallel planar electrodes were placed along the channels at the edges to apply electric fields perpendicular to the fluid flow. The electrodes were 31.2 mm long with a gap of 2.2 mm so that they invaded the channel approximately 200 µm on each side.

4.1.2 Design B – Nanoparticle Electrokinetic DLD separation

The second type of DLD devices (Design B) had an optimized design for separation of nanoparticles. For that purpose, the width of the channels was reduced in order to place the electrodes closer together and thus increase the electric field magnitude. The parameters of the DLD array were also modified to improve the device performance and reduce the size of the particles that could be targeted, based on previous experimental results and numerical simulations. The posts were also

cylindrical but had a special arrangement: the lateral gap between the posts (G_L) was different from the horizontal gap (G_H). In particular, G_L was kept the same as D_p while G_H was reduced a third of that value ($D_p/3$) (see Figure 4-2b). Details of the design process are given in a following chapter. Again, different devices with different array geometries were designed to increase the range of particles that could be studied and investigate the dependence of the separation on the geometry (see Table 4-2).

Table 4-2. Design B - DLD array geometric parameters.

Device	$\boldsymbol{\lambda_L}$ (μm)	$\boldsymbol{\lambda_H}$ (μm)	$\Delta\boldsymbol{\lambda}$	$\boldsymbol{N}$	$\boldsymbol{\theta}$ (°)	$\boldsymbol{D_p}$ (μm)
#1	24	16	0.5	48	1.19	12
#2	24	16	0.6	40	1.43	12
#3	18	12	0.4	45	1.27	9
#4	18	12	0.5	36	1.59	9
#5	18	12	1.0	18	3.18	9
#6	12	8	0.3	40	1.43	6
#7	12	8	0.5	24	2.39	6

The channel width was reduced to 1.3 mm while the length was kept almost the same at 30.5 mm. These devices also had a section of posts with zero offset at the top to concentrate the particles in displacement mode, similar to the DLD Design A shown in Figure 4-1b. The inlet was very similar to the previous design, with three channels, two for the sheath flow and one thinner channel to introduce the sample. However, the outlet design was modified. The outlet consisted of 24 channels 35 μm wide uniformly distributed across the channel section separated 20 μm from each other. All these channels were then connected to the same outlet reservoir. This outlet design enabled quantification of deflection as a function of the outlet channel number. The experiments performed with these devices did not aim for real sample separation and analysis but only for the characterisation of the separation technique, therefore additional outlet reservoirs were not necessary and not included for simplicity. A diagram of the design of these devices can be found in Figure 4-2.

The two parallel planar electrodes were both 29 mm long with a gap that was reduced to 1.1 mm so that each was placed approximately 100 μm inside the channel.

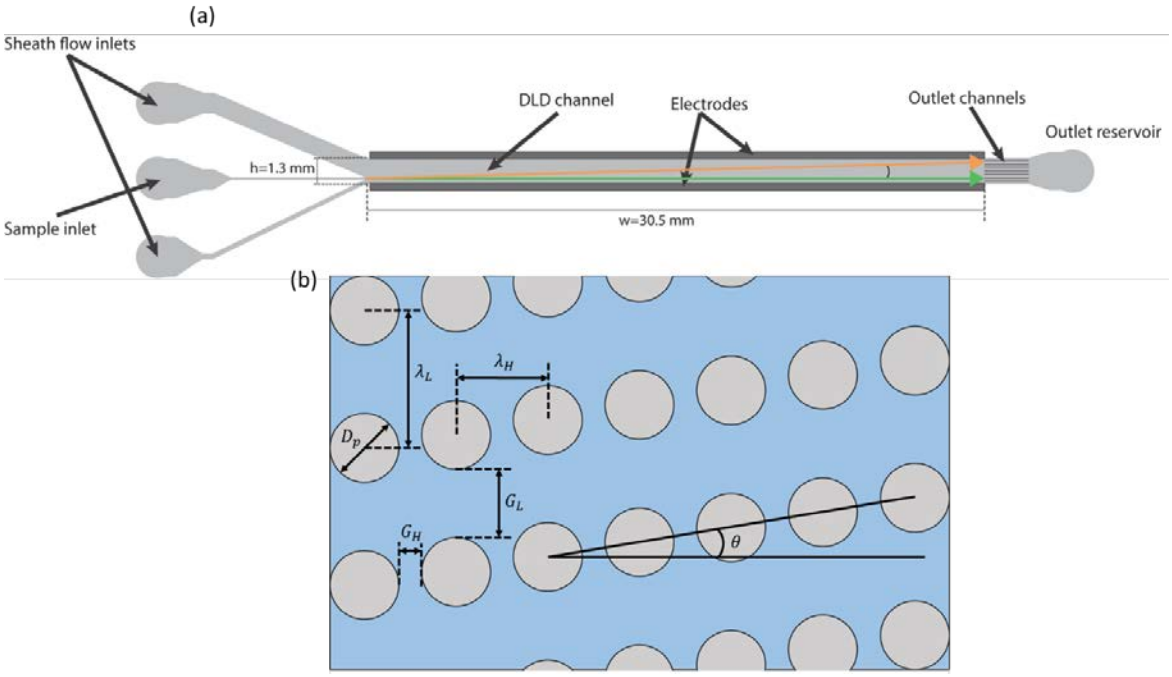

Figure 4-2. Design B. (a) Device design. (b) Diagram of the asymmetric DLD array with $G_L > G_H$.

4.1.3 EK flow devices – fluid behaviour in the vicinity of insulating posts

As discussed later in the thesis, experiments in the DLD devices revealed new interesting low frequency AC EK phenomena arising in the vicinity of the insulating DLD pillars; specially electrokinetic quadrupolar flows similar to those reported for ICEO around conducting pillars. Hence, a new set of devices was designed to simplify the experiments and study in detail the physics underlying these phenomena (see Figure 4-3), focusing on particle motion induced by the electric field near insulating structures.

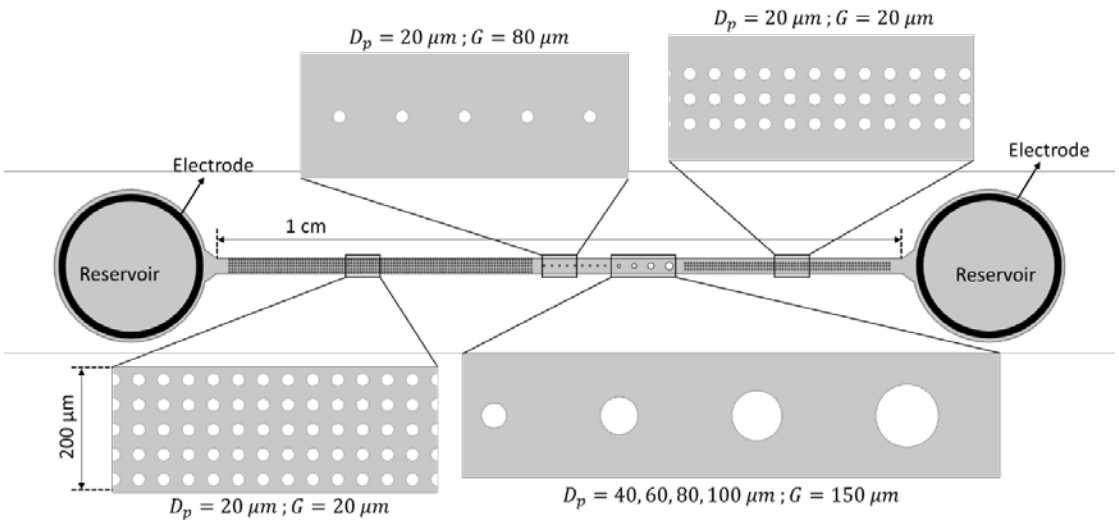

Figure 4-3. Diagram of the devices used to study the electrokinetic behaviour in the vicinity of insulating pillars.

The new devices consisted of a 1 cm long and 200 µm wide straight channels with a reservoir on each of the two ends; both acting as inlet or outlet depending on the applied pressure. The channels were divided into different sections, filled with insulating posts of different sizes and arrangements (see Figure 4-3). Electrodes placed at the reservoirs served to apply electric fields along the channels.

4.2 Fabrication

All devices were made from polydimethylsiloxane (PDMS), cast from a master fabricated using standard photolithography. A mask with the designs was placed above a silicon wafer, which was previously coated with a layer of photoresist of the desired thickness. The wafer was then exposed to UV light. The negative photoresist SU-8 was used (Microchem SU-8 3000 series to fabricate the master. The wafer was developed to wash away the non-cross-liked excess photoresist. The height of the PDMS features was determined by the thickness of the photoresist layer. The devices were fabricated with different heights depending on their design and their future applications (see Table 4-3).

Table 4-3. Average device heights for the different designs.

Design	Photoresist	Average device height
DLD Design A	SU-8 3005	8 – 9 µm
DLD Design B	SU-8 3005	4 – 5 µm
EK flows design	Su-8 3050	50 – 60 µm

The final step was to bond the PDMS to a glass slide patterned with two parallel platinum electrodes. For that, the PDMS and glass surfaces were exposed to O_2 plasma for 30 seconds and then brought into contact and baked at 60°C for at least 2 hours creating covalent Si-O-Si permanent bonds between both surfaces[246,247]. The alignment of the microfluidic channel and the electrodes was done manually. In order to reuse the electrodes after the experiments, the devices were soaked in pure Ethanol for more than 48 hours to break the bond. A diagram of the complete fabrication process can be found in Figure 4-4.

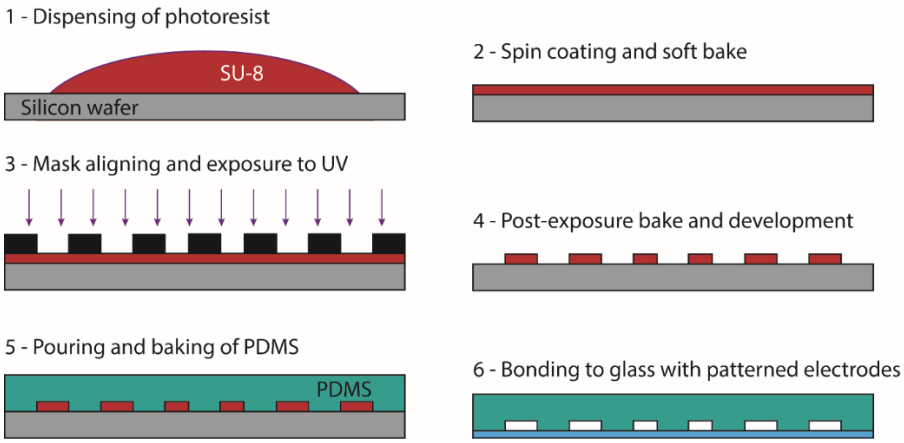

Figure 4-4. Diagram of the fabrication process of the PDMS devices with SU-8 photolithography.

4.3 Methods

4.3.1 Experimental setup

4.3.1.1 DLD devices

For both types of devices, the fluid flow was controlled independently at each of the inlets to focus the sample into a tight stream with approximately the same width as the inlet channel. This was achieved using a pressure controller with 3 independent channels (Elveflow OB1 MK3) that delivers up to 1000 mbar using a pressure-driven pump with an accuracy of ± 0.5 mbar. The outlet reservoirs were left open with no pressure applied.

A signal generator (TTi, Inc TGA12104) in series with a 50x voltage amplifier (Falco Systems High Voltage Amplifier WMA-300) was connected to the planar electrodes delivering up to 320 Vpp at frequencies up to 500 kHz. For the experiments where only AC fields were desired, a 10 µF capacitor was connected in series with the amplifier to filter out any possible residual DC offset that could affect particle behaviour. The applied electric signal was always monitored using an oscilloscope (Agilent Technologies DSO3202A) with a 100x probe.

4.3.1.2 EK flows devices

A different pressure controller was used for the experiments with the EK flows devices; a much more precise controller with an accuracy of ± 0.01 mbar but with a maximum pressure of 20 mbar (Fluigent MFCS-4C). These channels were much taller and shorter than the DLD devices, resulting in a significantly reduced fluidic resistance. Thus, 20 mbar was enough to achieve high flow rates. Also, a high precision of applied pressure was necessary since experiments with these devices needed a stagnant flow, no flow was needed to explore the EK behaviour near the insulating posts.

To achieve this, both reservoirs were connected to two independent channels of the pressure controller and the applied pressure on both was adjusted until no net fluid flow was observed.

Cylindrical hollow electrodes placed at the end of silicone tubes were used to both introduce the sample and apply the electric fields along the channels. They were connected in series to the same signal generator connected, in this case, to a high voltage amplifier (Trek Model PZD700A) delivering up to 2000 Vpp with frequencies up to 50 kHz. The signal was also continuously monitored with the oscilloscope.

4.3.1.3 Measuring equipment

Particle behaviour during the experiments was monitored using an inverted microscope (Zeiss Axiovert 200) and videos were recorded using a camera (Hamamatsu ORCA-ER C4742-95) for later analysis. In most of the experiments, fluorescent particles were used to image the particle tracking; the fluorescence was excited via a mercury lamp that provided illumination in a wide frequency spectrum (HBO 100 Mercury Arc Lamp).

4.3.2 Device preparation and samples

All the PDMS devices were primed with a non-ionic PEG based surfactant, Pluronics F-127 (0.1 % w/v in DI water), before the experiments for at least an hour to avoid particle adhesion to the channel walls and the surfaces of the posts; this is a very common practice in microfluidic research[248]. Surfactants are molecules with long aliphatic carbon chains and a hydrophilic head. When the microfluidic devices are exposed to the surfactant, the heads attach to the surfaces of the channels leaving the tails pointing outwards[247]. The interaction between the tails and the particles in suspension prevents the particles from sticking to the surfaces via the DLVO mechanism.

The surface passivation had another important effect on the electrokinetics of the systems. As previously reported in the literature, a pre-treatment with Pluronics F-127 significantly reduces the EO mobility by damping down the fluid slip velocity at the interface between the surface and the electrolyte[249,250].

The suspending medium used for the experiments was KCl diluted in deionized (DI) water at different concentrations (and thus conductivities). To study the EK behaviour, polystyrene microspheres of different sizes and surface charges (mostly fluorescent) were used; a list of all particles can be found in Table 4-4.

4.3.2.1 Zeta potential measurements

The zeta potential (ζ) of some particles used for the experiments was measured using a Zetasizer (Malvern Panalytical, Zetasizer NanoZS) at a medium conductivity of 6.6 mS/m. The results are summarized in Table 4-4.

Table 4-4. List of particles used on the experiments. The zeta potential (ζ) was measured at 6.6 mS/m diluted KCl at a pH of ~5.5 (the pH of non-buffered DI water in contact with air).

Diameter	Manufacturer	Fluorescence	Surface charge	Zeta potential
100 nm	Fluoresbrite	Yellow - Green	Carboxylate	−49 ± 7 mV
200 nm	Fluoresbrite	Yellow - Green	Carboxylate	−52 ± 7 mV
500 nm	Fluoresbrite	Yellow - Green	Carboxylate	−63 ± 6 mV
1 µm	Fluoresbrite	Yellow - Green	Carboxylate	−71 ± 4 mV
1.5 µm	Sigma Aldrich	None	None - Plain	
2 µm	Sigma Aldrich	Red	Carboxylate	
3 µm	Fluoresbrite	Yellow - Green	Carboxylate	−78 ± 6 mV
3 µm	Sigma Aldrich	None	None - Plain	−15 ± 3 mV

4.3.3 Software tools

Most of the data processing consisted of analysis of the videos of the particle behaviour recorded during the experiments. In particular, in the DLD experiments the EK induced deflection had to be quantified from particle lateral position at the outlet, while in the EK flows experiments, the induced flows had to be characterised from particle motion around the insulating posts. For this purpose, two software tools were used: ImageJ[251] and MATLAB R2017a (The MathWorks Inc, Natick, Massachusetts, USA).

This thesis also presents numerical simulations of particle behaviour inside the described microfluidic systems, performed using the commercial finite element solver COMSOL Multiphysics v5.3a (COMSOL AB, Stockholm, Sweden). The following packages were used: Single Phase Flow to solve the Stokes equation (creeping flow) and calculate fluid velocity fields, Electric Currents to calculate field distributions and Mathematical Particle Tracing to compute particle trajectories. In

all simulations the mesh refinement level was improved, and the time stepping was reduced until the simulation results converged.

Chapter 5 AC electrokinetic biased Deterministic Lateral Displacement: Frequency characterisation

5.1 Introduction

In the last years, Deterministic Lateral Displacement has been highlighted as one of the most promising microfluidic approaches for particle separation. However, like every other separation technique, DLD is not "definitive" and has some deficiencies that limit its utility and applicability.

The most fundamental drawback of DLD is linked to the fact that the critical diameter depends only on the geometry of the device. Once a DLD device has been designed and fabricated, it can only be used to separate particles bigger or smaller than a fixed size threshold that cannot be modified. This means that a given DLD device is only useful for processing the sample it was specifically designed for; or at most, a very short range of very similar samples.

Another important limiting factor of DLD is that, in principle, it only allows for size-based separation whereas many samples contain particles of similar sizes that need to be sorted (for example different bacteria populations or Circulating Tumour Cells and some White Blood Cells). Although separation based on other mechanical properties such as deformability or shape has also been reported[90,96,97], the proficiency of DLD to target particle properties other than size for separation is still very narrow.

Clogging is also a common problem in DLD[100]; the maximum particle size that can be processed is equal to the lateral gap between the posts. If a sample contains particles which are bigger than G_L they get stuck between the posts leading to device clogging. Since the D_c is linked to the geometry too, it is often necessary to introduce a previous separation stage to get rid of all particles bigger than G_L before processing the sample with the DLD devices[88].

DLD separation techniques are restricted to a low throughput[252], usually 1-100 µL/h. This is because of the very high hydrodynamic resistance that these devices offer due to the presence of thousands of posts within the channels separated by narrow gaps and the fact that the channel height is limited by the post diameter since the fabrication of high aspect ratio posts is hard to achieve. This makes it difficult to consider DLD alone as a feasible technique for nanoparticle separation[92].

Combining DLD with additional forces can overcome some of these drawbacks. To date DLD devices have been effectively coupled with several different forces (gravity, electric, magnetic, viscoelastic, electrostatic, magnetic …)[82,99,106,107,253]. The inclusion of EK forces that act on the particles in a DLD

device enables particle paths to be modified as they pass through the post array, controlling separation by inducing a deflection of particles smaller than D_c. This thesis describes a technique that incorporates electrokinetic particle manipulation within a classical DLD system to achieve tunable sorting.

5.1.1 Electrokinetically biased

The combination of DLD with AC electrokinetics was first reported by Beech *et al.*[99] in 2009. The authors placed electrodes at the inlet and the outlet of a DLD device to generate electric fields along the channels, parallel to the fluid flow. They observed induced deviation of particles smaller than the D_c with 100 Hz AC signals and attributed it to the DEP forces arising around the insulating PDMS posts. The DLD array acts as an iDEP system, where the pillars perturb the electric field distribution giving rise to high and low electric field gradients and therefore to DEP, although in this case the DEP force is not used to trap the particles but to modify their paths resulting in a continuous separation.

When the electric field is applied parallel to the fluid flow, the high electric field gradients are created between the posts of the same column (see colour map in Figure 5-1a). When the particles pass close to the posts, those that experience a strong enough nDEP are pushed away and forced to cross the separatrix streamline towards the portion of the fluid that passes above the next post. As depicted in Figure 5-1a, even if the particle is smaller than the D_c, the nDEP force has the same effect as the hydrodynamic interaction with the post, forcing it to enter displacement mode. Every time a particle encounters a post the nDEP force deviates it from the original trajectory, resulting in a continuous electrically induced deflection.

In the work presented here, two coplanar electrodes are placed along the DLD channel length (see page 47, Device design) to create AC electric fields perpendicular to the fluid flow. In this system the electrodes can be placed close together, increasing the magnitude of the electric field. This also means that the range of frequencies can be expanded. The frequency range of commercial voltage amplifiers (like used in this thesis) is limited by the applied voltage. If the electrodes are placed at the channel inlet and outlet (as in Beech *et al.*[99]), the large distance between the electrodes requires thousands of volts to exert a significant force on the particles, limiting the working frequencies to a few hundred hertz. Thus, in this configuration the electric field lines are perpendicular to the fluid flow and the high electric field gradients are created between the posts of the same row (see Figure 5-1b).

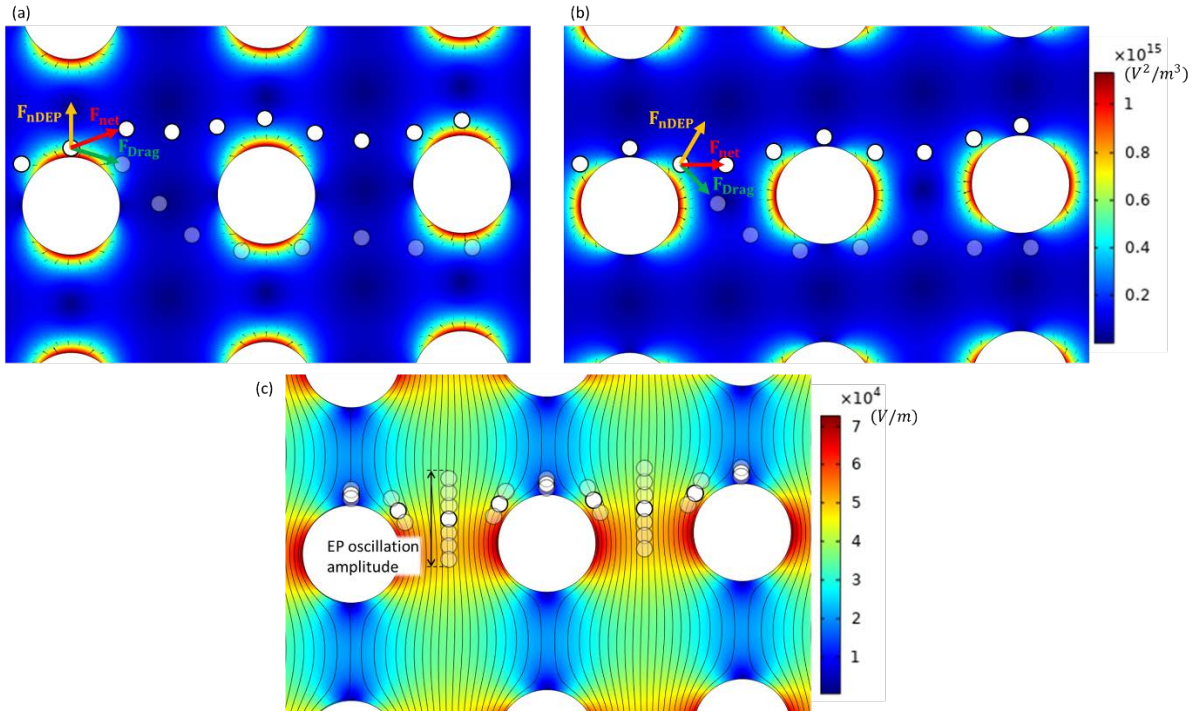

Figure 5-1. Diagrams of the Electrokinetic induced deflection in DLD systems. (a) Electric field parallel to fluid flow – nDEP forces the particles to cross the streamline. The colour map represents the $\nabla|\boldsymbol{E}|^2$. (b) Electric field perpendicular to the fluid flow – nDEP force prevents the particles from passing between two posts of the same row. The colour map represents the $\nabla|\boldsymbol{E}|^2$. (c) Electric field perpendicular to the fluid flow – At low frequencies the particles undergo an electrophoretic oscillation along the electric field lines and, at the same time, are forced to bump on the posts. The colour map and the black lines represent the magnitude of the electric field and the electric field lines respectively. The magnitude of the electric field in all figures is 40 kV/m).

The experiments presented here show a much richer behaviour than reported previously indicating that EP and other EK phenomena must be considered when low frequency AC fields are applied. The research in this thesis identified two distinct frequency regimes. At high frequencies the particle behaviour and deflection are governed solely by the dielectrophoretic response. For particles smaller than the critical diameter to travel in a straight line without deflection, they must follow the fluid flow, zigzagging around the posts. However, if a particle experience a strong enough nDEP force, which is orthogonal to the Stokes force, it overcomes the fluid drag and is prevented from passing between the posts of the same row (and thus from zigzagging); as a result the particle starts bumping on the DLD pillars deviating with the row tilt angle on the displacement mode. This mechanism is diagrammatically described in Figure 5-1b.

At low frequencies (below 1 kHz), the behaviour changes completely (see Figure 5-1c). The combination of electrophoretic oscillation along the perturbed electric field lines, together with

other EK phenomena arising at low frequencies, dominates particle motion. In this regime, a transition from zig-zag to bumping mode induced by the electric field was observed. This transition is independent of the direction of the DEP (particles experiencing both pDEP and nDEP are forced to deviate) and occurs at a lower field magnitude threshold. These facts led to the conclusion that a different physical mechanism, which is not fully understood, is responsible for the deviation at low frequencies

Both mechanisms change the dynamics of the DLD separation and bring several advantages over classic DLD systems. First, it allows control over the effective critical diameter by regulating the applied electrical signal. Thus, size-based separation is no longer determined by the geometry of the device.

Second, it allows the electrical properties of the particles to be exploited, such as the surface charge or the electrical polarisability. This enables, for example, separation of subpopulations of particles with similar size in the same sample by exploiting differences in their electrokinetic response.

In addition, combining DLD with electrokinetics means that the dimensions of the microfluidic channels and the DLD arrays can be enlarged with respect to the sizes of the particles in the samples, increasing the throughput of the separation and reducing the risk of clogging in the devices.

This chapter describes proof-of-principle experiments to investigate particle EK behaviour inside DLD devices and how this leads to an induced deflection of the particles smaller than the critical diameter.

5.2 Experimental methods

The DLD devices and the experimental methods are described in Chapter 4 (page 47). For the experiments presented in this chapter, only devices from DLD Design A were used (section 4.1.1, page 47). Experiments with and without pressure driven flow were performed to study both particle EK behaviour near the insulating DLD pillars and electrically induced deflection.

For the experiments in the absence of pressure driven flow, first particles were introduced in the channel and then the flow was stopped by reducing the applied pressure with the controller. Afterwards, the electric field was applied for short time (up to 1 minute) while particle motion was monitored with the microscope. Before applying different electrical signals, the channel was flushed with fresh electrolyte to ensure any ionic species from Faradaic reactions produced at the electrodes when the voltage was applied were washed away; so the medium conductivity remained stable and consistent in all cases.

When a pressure driven flow was established, the induced lateral deflection of 500 nm, 1 µm and 3 µm diameter fluorescent carboxylate particles inside a device was characterised as a function of different parameters: medium conductivity, applied voltage and AC frequency. The calculated values of $\mathrm{Re}[\tilde{f}_{\mathrm{CM}}]$ of 1 and 3 µm particles as a function of the frequency for the medium conductivities used in the experiments are given in Figure 5-2. The effects of the Double Layer polarisation and the α-relaxation on the particles overall dipoles have not been considered for this calculation. This mechanism appears at frequencies of the order of the characteristic relaxation frequency $f_\alpha = D/2\pi a^2$ (for 1 µm and 3 µm diameter particles $f_\alpha \sim 10 - 100$ Hz). However, the α-relaxation is not expected to play a relevant role in this study since it has a negligible effect on particles with a negative polarisability and it only predicts a small decrement of the induced dipole magnitude of particles with positive polarisabilities for frequencies lower than f_α (see discussions in Chapter 3).

The pressure applied to each of the inlet channels was adjusted so that the samples were focused to a tight stream of a width approximately equal to that of the sample inlet. In addition, the pressure was always the same resulting in an almost identical flow velocity for all the experiments presented in this chapter.

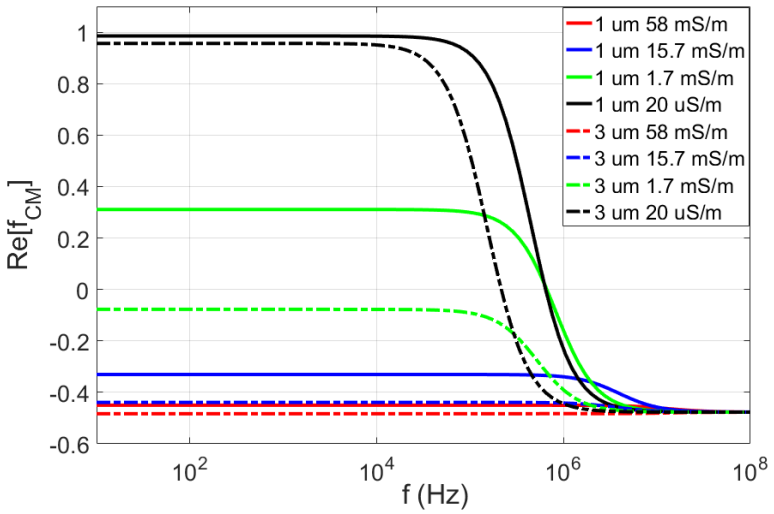

Figure 5-2. Real part of the CM factor of 1 and 3 µm spherical particles at the medium conductivities used in the experiments. A surface conductance of 1 nS was assumed for both types of particles (note that the α-relaxation was not taken into account for this plot).

Figure 5-3 shows the deviation angle measured experimentally. Given that the channel length is known, the induced deviation angle could be calculated from the average lateral displacement at the outlet with respect to the position at the inlet. Particles travelling in full displacement mode reached the top of the channels (and concentrated in the concentration region of the devices)

before arriving at the outlet. This meant that the experimentally measured deviation angle θ_{exp} was always smaller than the angle imposed by the DLD array geometry θ_{geom} ($\theta_{exp} < \theta_{geom}$) and that there was a small range of angles that could not be discerned; from the maximum value of θ_{exp}, corresponding to a maximum lateral deflection, to θ_{geom}.

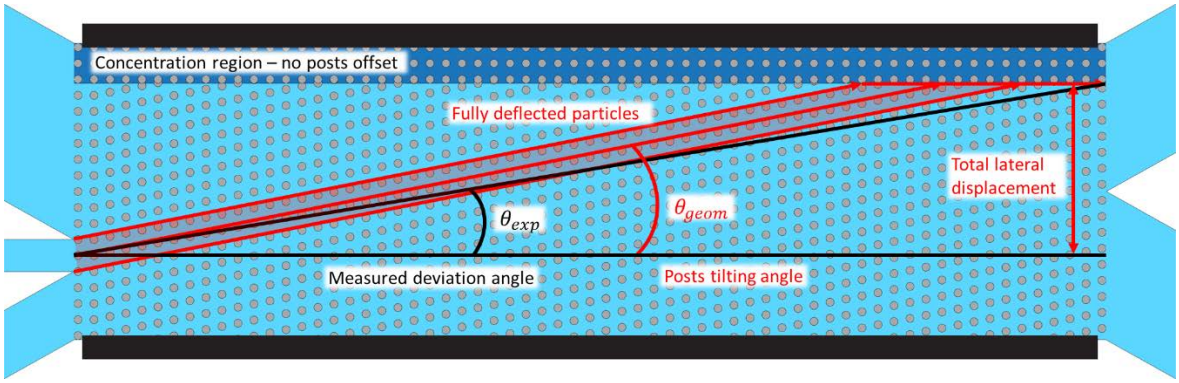

Figure 5-3. Diagram of the deviation angle measured experimentally θ_{exp} compared to the tilt angle of the post array θ_{geom} and the particle trajectories in full displacement mode through the DLD devices. The maximum angle that could be measured corresponds to a maximum lateral displacement at the outlet and was always smaller than θ_{geom}.

The moment the electric field was applied some particles were forced to switch to the bumping mode. Particles that were already inside the channel when the field was applied were only partially deflected. Thus, before the measurements, the electric field was applied for long enough to ensure that only the deflection of particles that had travelled the whole channel length was measured.

5.2.1 Data analysis

In order to measure the deviation angle, videos were recorded for long enough, so the number of studied particles was significant (usually 2 minutes). The light intensity from the fluorescence emission was collected and measured as a function of the lateral position. The amount of fluorescence light collected during the videos for a given position was directly proportional to the number of fluorescent particles that reached the outlet at that position. The average outlet lateral position and thus the deviation angle could be calculated from this data. Video analysis was implemented using image analysis packages in MATLAB. Each frame of a video was digitally filtered to remove the background and all fluorescent spots that did not correspond to the particle size (such as aggregations of particles and dust or PDMS fragments). A diagram of the video analysis process is provided in Figure 5-4.

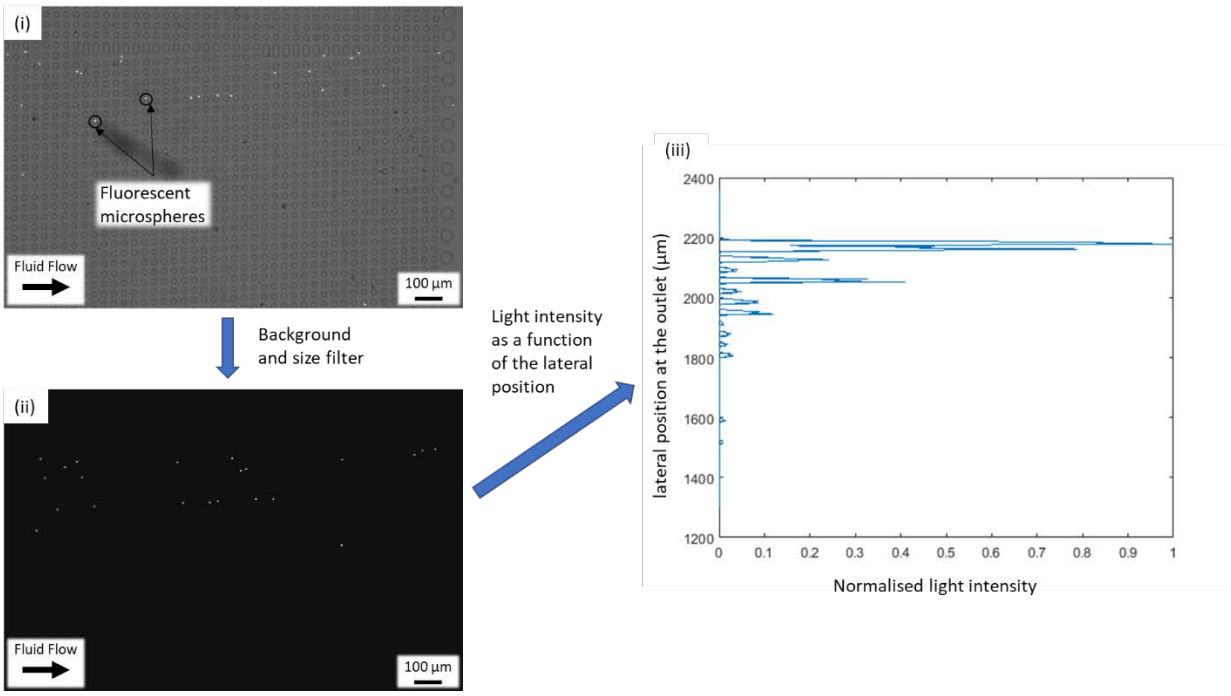

Figure 5-4. Diagram of the video analysis procedure. (i) Videos were recorded for at least 2 minutes with the field of view focused at the outlet. (ii) Each frame was processed so that only the light from the fluorescent particles was considered – a digital filter was applied to remove the background and any object bigger than the particles. (iii) The light intensity was summed as a function of the lateral position of particles at the exit.

5.3 Results and discussion

5.3.1 Electrokinetic behaviour in absence of pressure-driven flow

Experiments were performed in the absence of hydrodynamic flow in order to study the EK forces acting on particles inside the microchannels, and also to characterise their behaviour as a function of the field frequency. Images of particle equilibrium positions for different frequencies and conductivities are shown in Figure 5-5. Significant differences in particle behaviour were noted between a low frequency field (50 - 500 Hz) and a high frequency field (above 500 Hz). The DEP behaviour at high frequencies and its dependence on the medium conductivity was generally in agreement with Maxwell-Wagner interfacial polarisation theory.

Similar to iDEP devices, the DLD pillars are made from PDMS (an insulating polymer) and are positioned in the channels to create a spatially non-uniform electric field with two coplanar parallel electrodes. This structure creates regions of high and low electric field gradient that generates a DEP force on the particles, which in turn governs their behaviour at high frequencies, above 500 Hz. A diagram of the spatial dependence of the DEP force around the DLD posts is shown in Figure 5-5a,

where the colour map represents the magnitude of the electric field gradient squared ($\nabla|\boldsymbol{E}|^2$ – proportional to the DEP force). Thus, the red areas on the sides of the posts correspond to high electric field gradients, where particles experiencing pDEP concentrate. The particles experiencing nDEP are repelled from these areas (see black arrows in Figure 5-5a) and concentrate in the regions of minimum field gradient, the dark blue areas at top and bottom of the posts.

As observed in the experiments, for a high frequency and in the absence of a pressure driven flow, particles less polarisable than the medium ($\mathrm{Re}\left[\tilde{f}_{\mathrm{CM}}\right] < 0$ - nDEP) are repelled from the high electric field gradient regions and concentrate at the low electric field gradient regions located between the posts of the same column (see Figure 5-5c). Conversely, particles more polarisable than the medium ($\mathrm{Re}\left[\tilde{f}_{\mathrm{CM}}\right] > 0$ - pDEP) are attracted towards high field gradient regions and concentrate there, between the posts of the same row (see Figure 5-5e). In this frequency regime (above 500 Hz), the DLD arrays function as iDEP trapping systems.

In iDEP systems, the AC fields are at high enough frequency so that the effects of EP and EO are negligible – EP and EO have a zero-time average so that at high frequencies the direction of these forces changes too quickly to produce any observable effect. However, at low frequencies these forces can lead to a measurable effect, a particle oscillation along the direction of the electric field lines at the frequency of the electric field. In other words, the particles have sufficient time to move before the electric field switches direction. This particle oscillation was observed in the DLD channels when low frequency AC electric fields were applied (below 500 Hz). The distortion of the electric field by the posts, as shown in Figure 5-5b where the colour map represents the field magnitude, means that the amplitude of this oscillation is dependent on the particle position with respect to the posts.

Although electrophoretic oscillation of particles is the predominant effect at low frequencies, the movement is superimposed on a non-zero DEP force. Particles undergoing nDEP are pushed away from the high electric field gradient regions while they oscillate. These particles reached the same equilibrium as for the high frequency case and also oscillated, but with a much smaller amplitude due to the fact that in these positions the magnitude of the electric field is minimum (see Figure 5-5d).

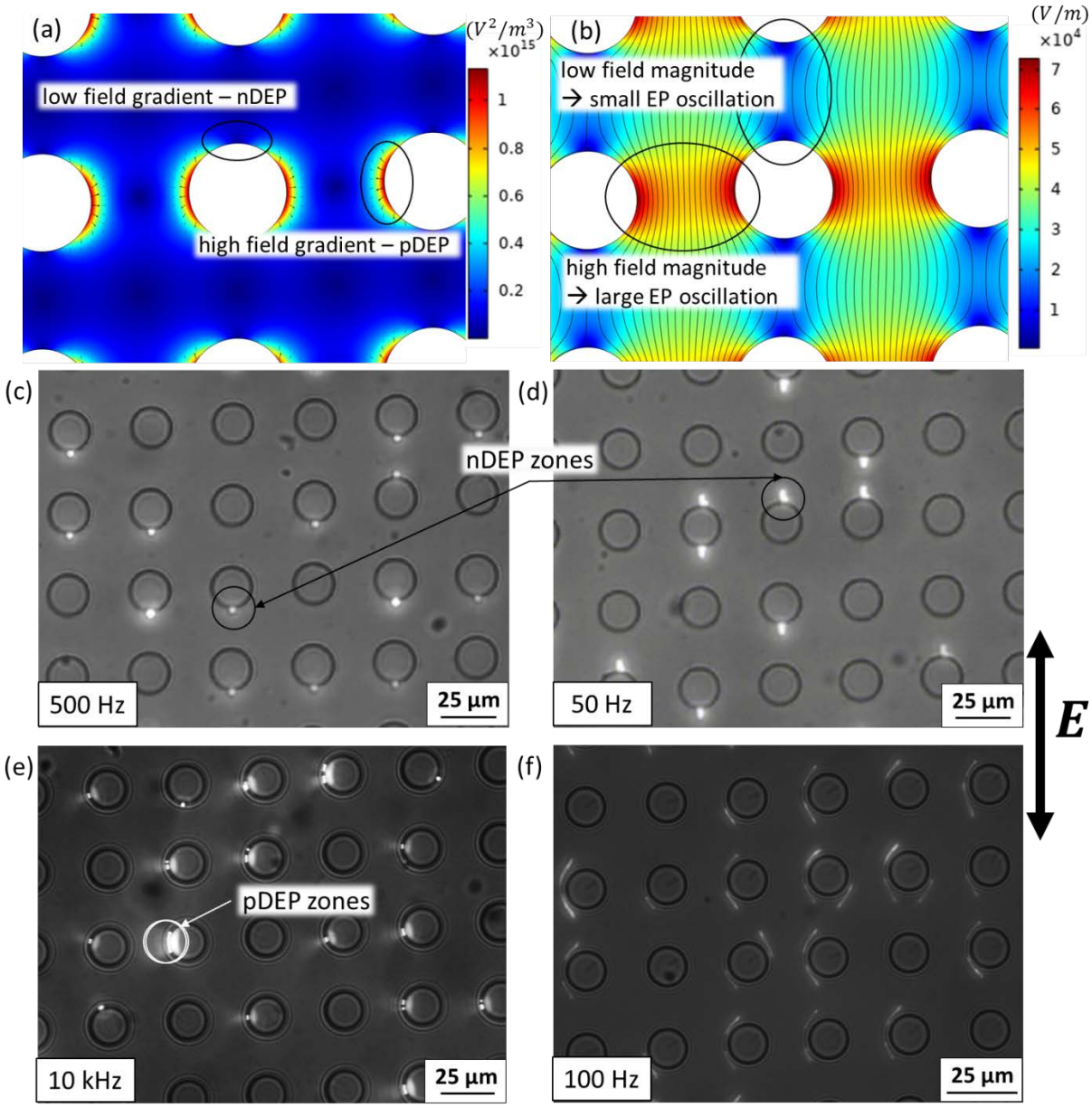

Figure 5-5. Electrokinetic particle behaviour in the vicinity of the DLD insulating posts in the absence of pressure driven flow for an applied voltage of 320 Vpp. (a) Diagram of the spatial dependence of $\nabla|\boldsymbol{E}|^2$ – proportional to the DEP force. The colour map represents the magnitude of $\nabla|\boldsymbol{E}|^2$ while the black arrows correspond to the direction of a nDEP force. (b) Diagram of the electric field distribution around the insulating posts. (c) nDEP trapping of 3 µm particles suspended in 15.7 mS/m KCl in the low electric field gradient regions for an applied signal of 500 Hz. (d) Same nDEP trapping but for an applied signal of 50 Hz – The particles show a small electrophoretic oscillation caused by the low frequency electric field. (e) pDEP trapping of 1 µm particles suspended in DI water (≈ 20 µS/m) in the high electric field gradient regions for an applied signal of 10 kHz. (f) When a low frequency signal is applied (100 Hz in this case), the trapping positions change and, at the same time, the particles oscillate along the electric field lines.

A similar behaviour might be expected for particles experiencing pDEP, however, the particles behaviour did not accord with classical EK theory. It was observed that pDEP force attracted particles to the high gradient regions where the electric field magnitude and thus the low frequency EP oscillation was maximum. Nevertheless, the final equilibrium position was not located in the high electric field gradient regions but at an intermediate position between the high and the low gradient regions, in the "corners" of the posts as if they were square shaped (compare Figure 5-5f to Figure 5-5a and Figure 5-5b).

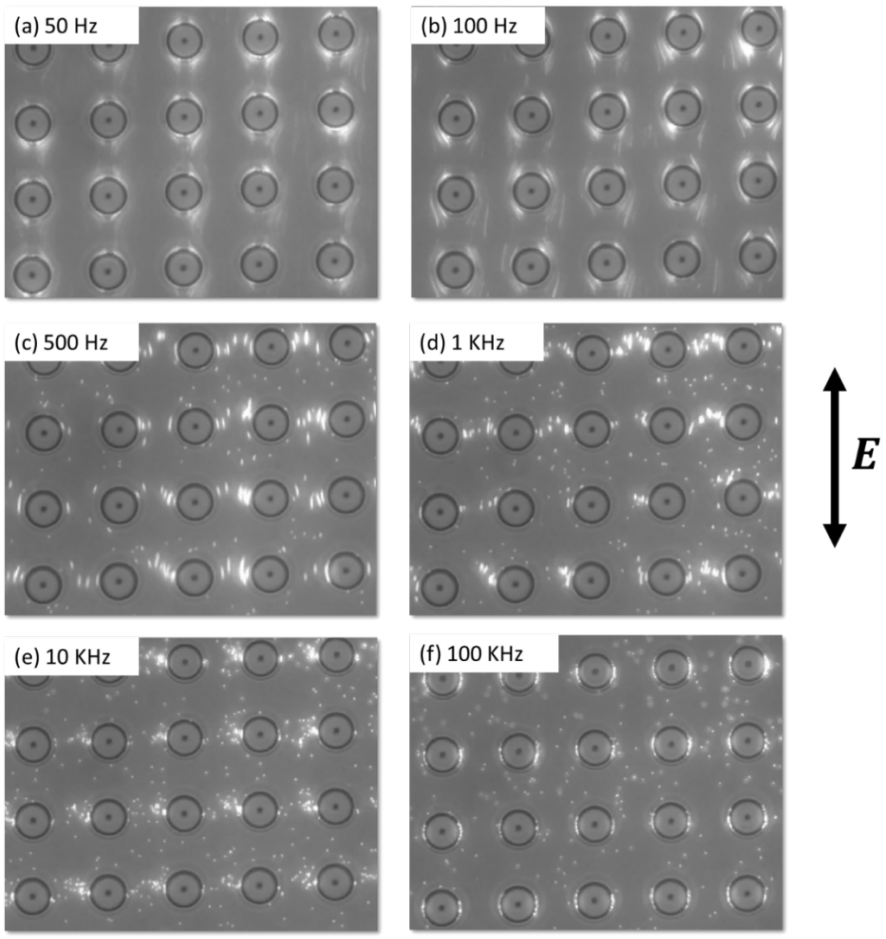

Figure 5-6. Series of images of the no-flow EK behaviour of 500 nm particles suspended in a low conductivity medium (1.7 mS/m KCl) for an applied voltage of 320 Vpp at different electric field frequencies. The experiments show a change in the pDEP trapping positions as the frequency of the electric field increases.

Figure 5-6 shows images of the frequency dependence of the equilibrium position of 500 nm diameter particles experiencing pDEP. It shows how this position changes with the frequency, from the "corners of the posts" at low frequencies when the oscillation amplitude is very large, to the expected pDEP trapping positions at the highest frequencies. The transition is not abrupt but occurs gradually as the frequency increases.

In addition, examination of the low frequency particle behaviour did not show a sign of the effect of the EDL polarisation mechanism and the α-relaxation. A reduction of the dipole magnitude of particles experiencing pDEP would only lead to a weaker trapping force with the same equilibrium positions, located at the high electric field gradient regions. On the other hand, the particles subjected to a nDEP force did not show any change in the behaviour when electric fields of frequencies of the order of f_α were applied.

These low frequency observations are probably linked to quadrupolar electrokinetic flows arising in the vicinity of the insulating posts as described in Chapter 6. These flows have not been previously reported in the literature and are caused by a rectified EO. They are most significant at low frequencies and low conductivities, coinciding with the observations of these unexpected equilibrium positions.

5.3.2 Electrokinetic biased DLD separation – frequency dependence

5.3.2.1 Qualitative behaviour

In the presence of a hydrodynamic flow, the EK forces are added to the Stokes drag force modifying the particle trajectories through the DLD device resulting, under the right conditions, in an induced deflection of particles smaller than the D_c. This mechanism is diagrammatically described in Figure 5-7a. For particles smaller than the critical diameter to flow without lateral deflection, they must follow the fluid laminae zigzagging around the DLD posts. However, when an orthogonal electric field is applied, high electric field gradient regions arise between the posts of the same row. If the particles experience a strong enough nDEP, they are prevented from zigzagging around the posts and thus forced to switch to the displacement mode.

Figure 5-7b shows the behaviour of 1 µm diameter particles in a 6.3 µm D_c DLD in the absence of an external perturbation. Such particles are smaller than the D_c and thus move by zigzagging around the posts, not crossing the separatrices streamlines and always follow the same stream lamina with an overall straight trajectory.

However, when an AC electric field is applied orthogonal to the fluid flow, high electric field gradient regions are created between the posts of the same row. If a particle is less polarisable than the medium it experiences a nDEP force which acts mainly orthogonal to the fluid drag. If this force is strong enough, particles are prevented from passing between the posts and thus from zigzagging, switching their behaviour to displacement mode, being deflected at the DLD deviation angle (Figure 5-7c). This behaviour differs from that originally reported by Beech *et al.*[99], the particles follow the displacing trajectories because they cannot pass between the posts of the same row, not because

they are pushed away from them and forced to cross the separatrix (as in the paper by Beech *et al*.[99]).

On the contrary, experiments showed that a pDEP force did not result in a significant diversion from the zig-zag mode for particles smaller than the critical diameter. An increase in the electric field eventually leads to particle trapping in the high electric field gradient regions, but no induced deviation was observed.

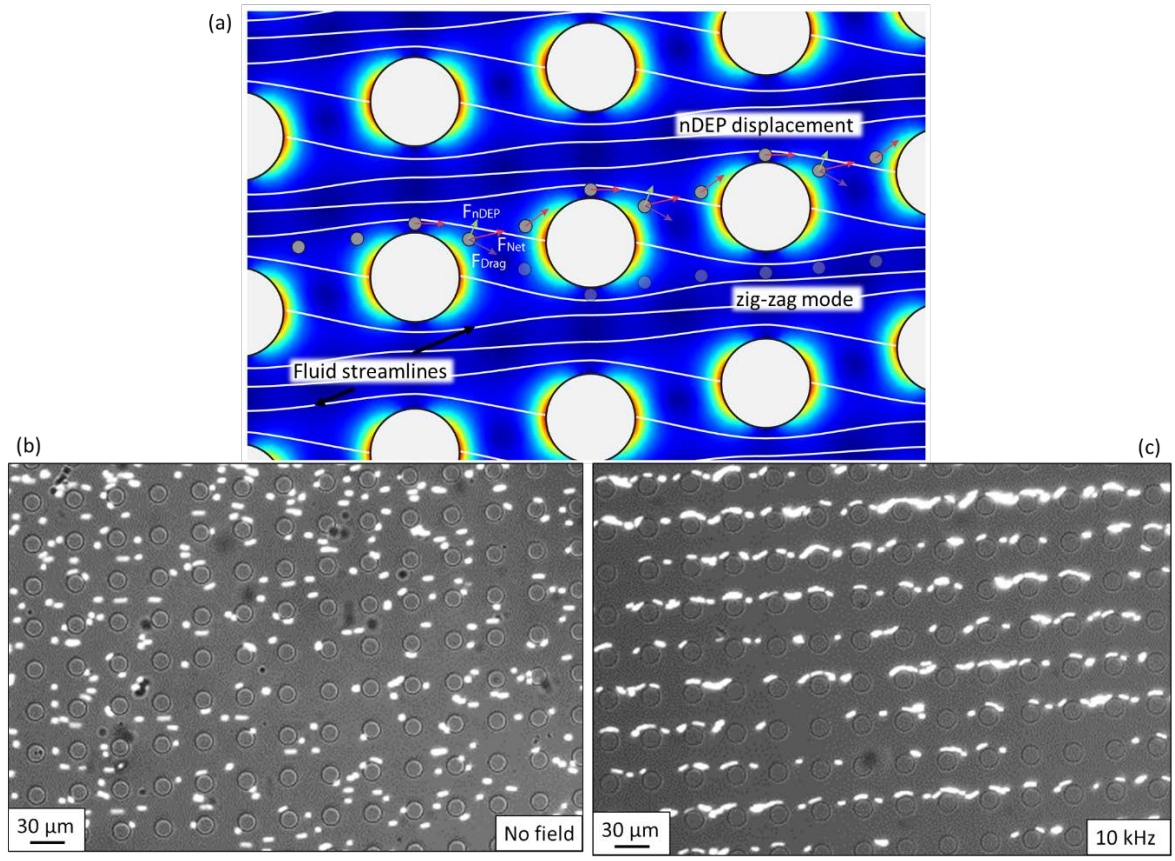

Figure 5-7. Images of electrokinetically induced deflection of 1 µm particles in a 6.3 µm D_c DLD device suspended in a 50 mS/m medium conductivity. (a) Diagram comparing zig-zag mode trajectories to nDEP induced deviation. (b) Particles zigzagging in the absence of electric field. (c) nDEP induced deviation caused by a 10 kHz 320 Vpp signal.

In the low frequency range below 500 Hz, the mechanisms of particle deviation is completely different and particles oscillate along the electric field lines while forced to bump on the posts as shown in Figure 5-8. For the same conditions (same particle size and flow rate), and at low frequencies the transition from zig-zag to displacement mode occurs at a much lower electric field magnitude than in the high frequency regime, where the induced deviation is attributed solely to nDEP. In addition, particles that experience either nDEP or pDEP deviate when a low frequency field is applied – although a pDEP force does not prevent the particles from following the zigzagging trajectories. Furthermore, a change in the particle induced dipole magnitude caused by the

polarisation of the EDL cannot successfully explain why particles experiencing pDEP are deflected or why there is a lower field magnitude required to induce deviation at low frequencies. These results lead to the conclusion that a mechanism other than DEP must be the origin of the induced deviation at low frequencies.

This induced deflection was initially attributed to an increase in the effective particle diameter due to the oscillation that was predominantly perpendicular to the fluid flow. However, further experiments discussed later in Chapter 6 of this thesis invalidated this hypothesis.

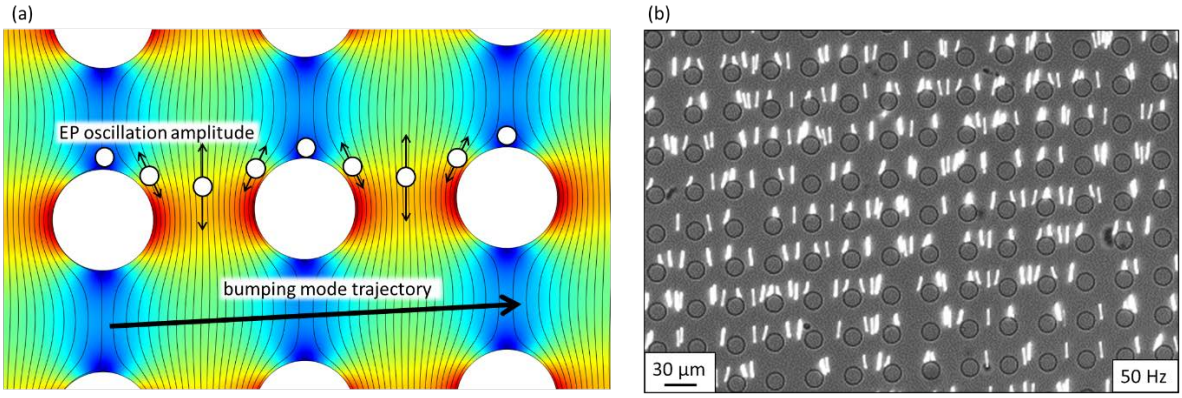

Figure 5-8. Low frequency induced deviation. (a) Diagram of low frequency deviation of particles while oscillating along the perturbed electric field lines. (b) 1 µm particles in a 6.3 µm D_c DLD device suspended in a 50 mS/m medium conductivity caused by a 50 Hz 320 Vpp signal – the particles oscillate along the electric field lines while bumping on the posts.

5.3.2.2 Separation characterisation

To characterise the system, the electrokinetically induced deviation angle of 1 and 3 µm diameter microspheres was measured as a function of the frequency of the applied signal for different medium conductivities. A 6.3 µm D_c DLD device was used so that, in the absence of an applied electric field, both particle populations move in the zig-zag mode. The results are summarised in Figure 5-9.

Figure 5-9a and Figure 5-9b show data for the 3 µm particles for three different electrolyte conductivities 1.7 mS/m, 6.6 mS/m and 15.7 mS/m, for which the particles always experience nDEP, $\mathrm{Re}\left[\tilde{f}_{\mathrm{CM}}\right] < 0$, in a frequency range from 50 Hz to 500 kHz (see Figure 5-2). For an applied voltage of 320 Vpp (Figure 5-9a) the deviation was maximum for all frequencies for the three conductivities. The deviation at low frequencies was maximum and the nDEP was always strong enough to force the particles to bump on the posts. As a result, there was no observable difference in the deviation angle between the two frequency regimes.

Figure 5-9b shows the deviation angle for a lower voltage of 120 Vpp. In this case, the low frequency mechanism was capable of inducing maximum deflection. However, when the frequency was increased, the induced deflection disappeared; nDEP was too weak to overcome the fluid drag force and prevent the zigzagging motion.

A comparison between Figure 5-9a and Figure 5-9b clearly illustrates the difference between both mechanisms and show that the low frequency induced deviation is independent of the nDEP induced deviation. In current electrokinetic theory, the DEP frequency dependence is given by the value of $\mathrm{Re}[\tilde{f}_{\mathrm{CM}}]$ which, for the medium conductivities studied here, is constant throughout the whole range of experimental frequencies. A constant nDEP cannot explain the difference between the data shown in Figure 5-9a and Figure 5-9b. This difference clearly indicates that another mechanism is responsible for the deviation observed at low frequencies, which also has a lower electric field magnitude threshold.

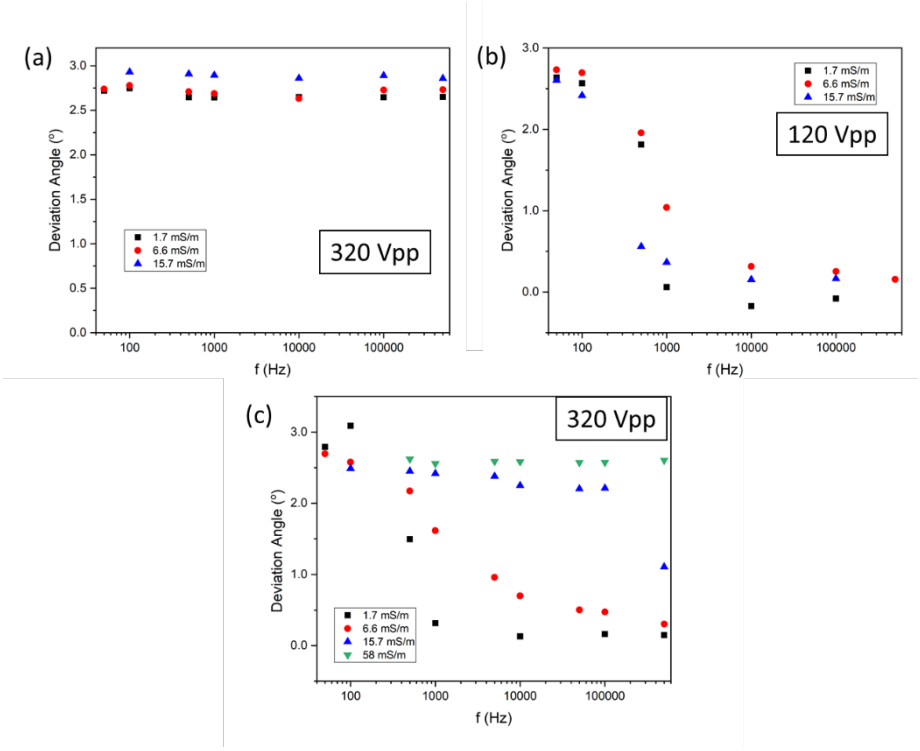

Figure 5-9. Measurements of the EK induced deviation angle of 1 and 3 µm diameter microspheres in 6.3 µm D_c DLD devices as a function of the frequency of the AC electric field perpendicular to the fluid flow for different medium conductivities. (a) 3 µm and 320 Vpp, (b) 3 µm and 120 Vpp and (c) 1 µm and 320 Vpp.

It is necessary here to consider the role of the α-relaxation and the fact that it could increase the induced dipole magnitude of the particles, making the nDEP stronger in the low frequency regime. However, the 3 µm diameter microspheres studied for the data in Figure 5-9a and Figure 5-9b already had the minimum value of the dipole factor $\mathrm{Re}[\tilde{f}_{\mathrm{CM}}] \sim -0.5$, according to the theory of the

Maxwell-Wagner and EDL polarisation (see Chapter 3), and thus the DEP force was as negative as possible. The polarisation of the EDL is therefore not expected to further increase the magnitude of the nDEP at low frequencies and thus cannot be responsible for the lower field magnitude deviation threshold at low frequencies.

Figure 5-9c shows deviation data for 1 µm particles suspended in an electrolyte with conductivities of 1.7 mS/m, 6.6 mS/m, 15.7 mS/m and 58 mS/m for an applied voltage of 320 Vpp as a function of frequency. This figure shows the difference in the behaviour of these particles when they experience pDEP or nDEP. For 1.7 mS/m, they undergo pDEP ($\mathrm{Re}\left[\tilde{f}_{\mathrm{CM}}\right] > 0$), and thus the induced deflection was only observed at low frequencies. At higher frequencies, where DEP dominates the behaviour, the particles are not forced to bump by the pDEP but stay in the zig-zag mode as expected. For 6.6 mS/m, $\mathrm{Re}\left[\tilde{f}_{\mathrm{CM}}\right]$ was only slightly negative so the nDEP was not strong enough to induce a significant deviation at high frequencies whilst a low frequency electric field was capable of inducing maximum deflection. For the two highest medium conductivities (15.7 mS/m and 58 mS/m), the nDEP was maximum and strong enough to make the particles switch from zigzagging to bumping, and the maximum deviation was achieved for the entire range of frequencies.

Figure 5-10 illustrates how this technique can be used to tune classical DLD separation and achieve selective control of particle behaviour. This sample was composed by a mixture of 500 nm, 1 µm and 3 µm diameter microspheres suspended in a 1.7 mS/m conductivity electrolyte, introduced into a 6.3 µm critical diameter DLD. The four pictures in each of the three series (Figure 5-10a, Figure 5-10b and Figure 5-10c) were taken in the downstream direction along the length of the microchannel in steps of 5 mm and illustrate the overall particle trajectories throughout the entire DLD channel. These images demonstrate the gradual selective separation driven by electrokinetic forces. Figure 5-10a show the case in the absence of an electric field where all the particles move in the direction of the fluid flow with zero deflection in the zig-zag mode, as expected because they are all smaller than D_c.

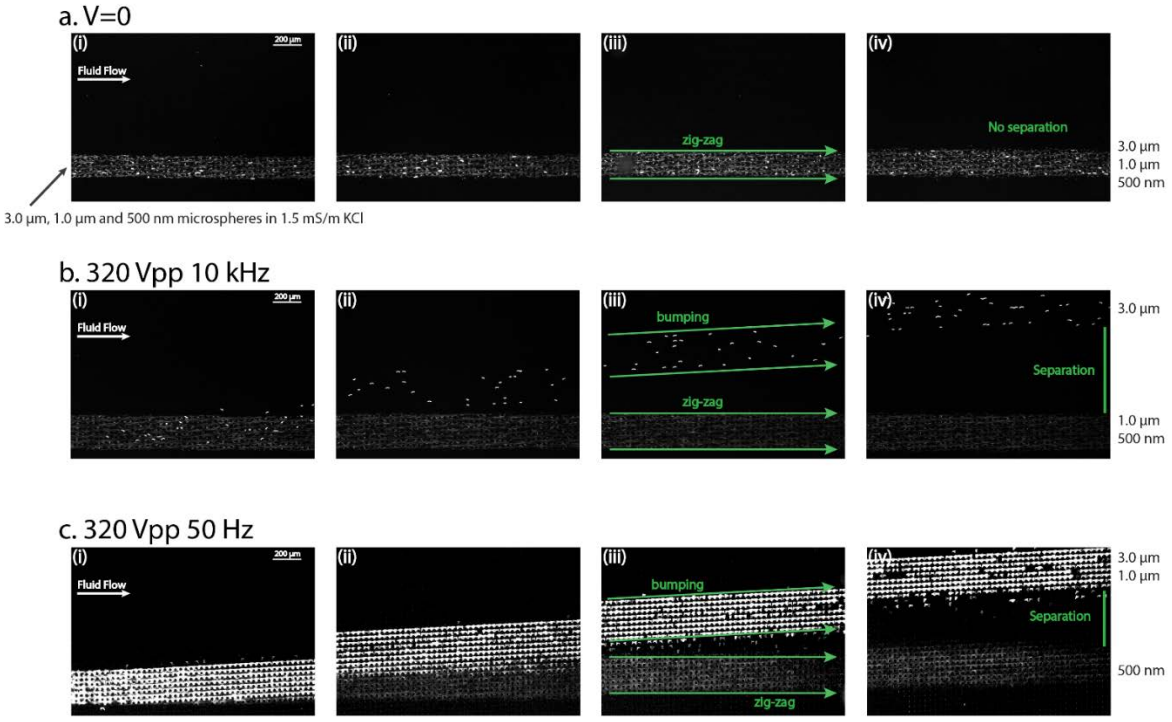

Figure 5-10. AC electrokinetic selective DLD separation of 500 nm, 1 µm and 3 µm diameter microspheres in a 6.3 µm critical diameter DLD device for an electrolyte conductivity of 1.7 mS/m using electric fields applied orthogonal to the fluid flow. Each of the three series of images was obtained by scanning the microchannels in the downstream direction and taken pictures in steps of 5 mm. (a) All particles move in straight trajectories parallel to the fluid flow in the absence of an applied electric field since they are smaller than the D_c. (b) Applied signal of 320 Vpp and 10 kHz: 3 µm particles are forced to switch to displacement mode and separate from the other two populations by nDEP. (c) Applied signal of 320 Vpp and 50 Hz: 1 and 3 µm particles are forced to deviate with the tilting angle of the array by a low frequency electric field and are laterally displaced from the 500 nm particles.

For this electrolyte conductivity, only the 3 µm particles experience nDEP. Therefore, in the presence of a high frequency electric field (10 kHz 320 Vpp) these particles switched to displacement mode resulting in separation from the 500 nm and 1 µm particles. When the frequency was reduced to 50 Hz, the 1 µm particles also changed their behaviour and started to deviate, bumping on the posts while the 500 nm particles continued to zig-zag around the posts showing that the mixture can be successfully separated (Figure 5-10c). These observations are in accordance with the experimental data shown in Figure 5-9 and demonstrates the separation potential of this technology for continuous flow particle separation.

5.4 Conclusions

This chapter described proof-of-principle experiments and the basic theory for a new microfluidic sorting technique that combines Deterministic Lateral Displacement with electrokinetics to achieve enhanced tunable continuous flow separation. Electric fields applied orthogonal to the fluid flow exert forces on the flowing particles that allow active control of their trajectories through the DLD array. This brings several advantages over classical DLD separation such as control of the effective critical diameter with separation based on the particle electrokinetic response.

The experimental results presented in this chapter showed two distinct regimes of particle behaviour. At high frequencies, nDEP is responsible for induced particle separation while at low frequencies the behaviour is governed by other electrokinetic phenomena (EP, rectified EO quadrupolar flows around the PDMS pillars, …) but the full separation mechanism is not yet fully understood.

This technology exhibits promising results for rapid and high throughput microparticle separation, and in particular for nanoparticle sorting in a continuous flow. The next chapter describes experiments used to further investigate the underlying scaling laws of both separation mechanisms. The induced deflection is characterised as a function of the fluid velocity and the applied electric field magnitude. For the high frequency deviation, the results are compared with theory and numerical simulations. For the low frequency mechanism, new insights into particle behaviour are presented.

Chapter 6 AC electrokinetic biased Deterministic Lateral Displacement: Numerical simulations and scaling laws

6.1 Introduction

In the previous chapter, a technique combining DLD separation with Electrokinetics was presented. Proof-of-principle experiments showed the possibility of inducing deviation of particles smaller than the critical diameter by applying an AC electric field perpendicular to the fluid flow as a way to achieve tunable particle separation. Two distinct regimes depending on the AC electric field frequency were identified. At high frequencies, the induced deflection is attributed to nDEP that prevents the particles form zigzagging around the posts. At low frequencies the mechanism behind the induced deflection is still not fully understood.

This chapter provides further experimental characterisation of the behaviour of particles in DLD devices, as a function of the magnitude of the electric field and the fluid flow velocity. From the experimental results, scaling laws that govern the induced deviation for both mechanisms are derived and compared to the basic theory.

The experimental data at high frequencies discussed in Chapter 5 agrees qualitatively with the hypothesis that nDEP induces deflection; the particles only move to bumping mode when they experience a strong enough nDEP force. However, this theory still needed to be quantitatively tested. The experimental data presented in this chapter matches the theory perfectly and provides a much stronger and quantitative support to the hypothesis that nDEP is responsible for the deviation. A new numerical model is developed, and the predictions compared to the experiments. This model is in excellent agreement with the results and should be a powerful tool for the design of new devices for separation of specific particle sub-populations. Nonetheless it is only restricted to the high frequency regime where nDEP is dominant.

The low frequency data presented in the previous chapter indicated that the mechanism behind deflection was different at low and high frequencies. This inference is reinforced by the experiments presented in this chapter which provide further insights into the physical mechanism responsible for the deviation of particles smaller than the critical diameter at low frequencies. Although a final and complete explanation remains to be done, basic scaling laws are derived and analysed together with new observations of the low frequency EK behaviour of particles in the DLD devices. Significantly new quadrupolar EK flows were observed around the insulating PDMS pillars

only at low frequencies, and these are postulated to play a central role in the low frequency induced deflection of particles.

6.2 Theoretical analysis

6.2.1 High frequency – nDEP induced deviation

As explained in Chapter 2, the velocity of a particle in a moving fluid under the action of an external force is given by:

$$\boldsymbol{v}_p = \boldsymbol{v}_f + \frac{\boldsymbol{F}_{ext}}{6\pi\eta a} \tag{6.1}$$

If the force acting on the particle is DEP, then:

$$\boldsymbol{v}_p = \boldsymbol{v}_f + \frac{\varepsilon_m a^2 \mathrm{Re}\left[\tilde{f}_{\mathrm{CM}}\right]}{6\eta} \nabla |\boldsymbol{E}|^2 \tag{6.2}$$

A dimensionless form of this equation can be derived using the following parameters as references: the DLD posts radius (R), a typical fluid flow velocity (U) and a typical electric field magnitude (E_0).

$$\begin{gathered} U\tilde{\boldsymbol{v}}_p = U\tilde{\boldsymbol{v}}_f + \frac{\varepsilon_m R^2 \tilde{a}^2 \mathrm{Re}\left[\tilde{f}_{\mathrm{CM}}\right] E_0^2 \tilde{\nabla} \left|\tilde{\boldsymbol{E}}\right|^2}{6\eta R^3} \rightarrow \\ \rightarrow \tilde{\boldsymbol{v}}_p = \tilde{\boldsymbol{v}}_f + \mathrm{sgn}\left(\mathrm{Re}\left[\tilde{f}_{\mathrm{CM}}\right]\right) \frac{\varepsilon_m \tilde{a}^2 \left|\mathrm{Re}\left[\tilde{f}_{\mathrm{CM}}\right]\right| E_0^2 \tilde{\nabla} |\tilde{\boldsymbol{E}}|^2}{6\eta R U} \end{gathered} \tag{6.3}$$

Defining γ as:

$$\gamma = \frac{\varepsilon_m \tilde{a}^2 \left|\mathrm{Re}\left[\tilde{f}_{\mathrm{CM}}\right]\right| E_0^2}{6\eta R U} \tag{6.4}$$

Then:

$$\tilde{\boldsymbol{v}}_p = \tilde{\boldsymbol{v}}_f + \mathrm{sgn}(\mathrm{Re}\left[\tilde{f}_{\mathrm{CM}}\right]) \gamma \tilde{\nabla} \tilde{\boldsymbol{E}}^2 \tag{6.5}$$

The tilde indicates dimensionless magnitudes and $\mathrm{sgn}(\mathrm{x})$ is the sign function. For a particle smaller than the critical diameter of the DLD array to be forced to bump on the posts by DEP and thus follow the deviation angle, two conditions need to be met. First, $\mathrm{sgn}\left(\mathrm{Re}\left[\tilde{f}_{\mathrm{CM}}\right]\right) = -1$ so that the particle experiences a nDEP force against the fluid drag which pushes the particle to zig-zag around the pillars. Second, the contribution to the total particle velocity $\tilde{\boldsymbol{v}}_p$ from the DEP force must be large

enough to overcome the contribution of the drag force $\widetilde{\boldsymbol{v}}_f$. As shown in the previous equation (6.5), this contribution scales with the parameter γ. Therefore, the induced experimentally measured deviation is expected to scale with γ if deflection is caused by nDEP.

6.2.2 Low frequency

As the frequency decreases, the EP force becomes more important and its contribution to the net particle velocity must be considered as follows:

$$\boldsymbol{v}_p = \boldsymbol{v}_f + \boldsymbol{v}_{\mathrm{DEP}} + \boldsymbol{v}_{\mathrm{EP}} \tag{6.6}$$

with $\boldsymbol{v}_{\mathrm{DEP}} = \mu_{\mathrm{DEP}} \nabla |\boldsymbol{E}|^2$ and $\boldsymbol{v}_{\mathrm{EP}} = \mu_{\mathrm{EP}} \boldsymbol{E}$ as defined in Chapter 3. With $\boldsymbol{E}$ an alternating field of the form $\boldsymbol{E} = E_0 \sin(\omega t)$, $\boldsymbol{v}_{\mathrm{EP}}$ oscillates with a frequency ω which drives the particles to oscillate along the electric field lines with an amplitude proportional to E_0/ω. Inside the DLD, the presence of insulating pillars gives rise to a spatially non-uniform electric field. Hence, the EP oscillation amplitude of the particles depends on position relative to the posts.

Furthermore, the influence of EO should be also considered at low frequencies. However, in all experiments performed for this thesis, the microfluidic devices were primed with a PEO based surfactant (Pluronics F-127) to avoid particle adhesion to the channel surfaces. This significantly minimises the EO flow which is then assumed to be negligible with respect to the contribution to $\boldsymbol{v}_p$ (see page 53, section 4.3.2, Device preparation and samples).

6.3 Methods

6.3.1 Experimental

The DLD devices used for the experiments in this chapter were devices #1 from DLD Design A, with $D_c = 6.3\ \mu\mathrm{m}$. The experimental methods used to measure and quantify the induced deviation angles, as well as the data analysis process were identical to the methods explained in Chapter 5.

Fluorescent carboxylate polystyrene microspheres with diameters of 1, 2 and 3 µm (see Table 4-4) were used for characterisation experiments. These particles were suspended in KCl of different conductivities (2.8 mS/m, 3.1 mS/m, 6.1 mS/m 15.7 mS/m and 50 mS/m).

6.3.2 Numerical simulations

A 2D numerical model was developed to predict the EK induced deviation, test the theory and compare with experimental results. This was done using the finite element method with the solver

COMSOL Multiphysics v5.3a (COMSOL AB, Stockholm, Sweden). A 2D model is a good enough approximation to the physics of fluids inside microfluidic devices, including DLD[254], and reduces significantly the computation times with respect to a 3D model.

For the simulations the partial derivative equations of the Stokes flow and the electric field were solved within a DLD unit cell to calculate the 2D spatial distribution of each of the velocity fields ($\boldsymbol{v}_f$, $\boldsymbol{v}_{\mathrm{DEP}}$ and $\boldsymbol{v}_{\mathrm{EP}}$) and therefore the value of the particle instant velocity, $\boldsymbol{v}_p$ (Equations (6.5) and (6.6)). Given the small dimensions of the particles, inertial effects were ignored, meaning that the particle velocity was always given by $\boldsymbol{v}_p$.

The particle trajectories were computed by particle tracing, i.e. in every time step the initial position is set to be the final position of the previous step and the particle velocity to the calculated value of $\boldsymbol{v}_p$ at that specific point:

$$\boldsymbol{r}^{(n)}(x,y) = \boldsymbol{r}^{(n-1)} + \boldsymbol{v}_p(x,y) \cdot (t^{(n)} - t^{(n-1)}) \tag{6.7}$$

where $\boldsymbol{r}$ is the particle position, n the step index and the time step $\Delta t = t^{(n)} - t^{(n-1)}$ was set to be a constant value for which the simulation results converged, i.e. Δt was reduced gradually until the results did not change when Δt was reduced even further. The computed trajectories were then post-processed using MATLAB R2017a.

Since the physical mechanism underlying the low frequency induced deviation is not fully understood, the simulations focus mainly on the high frequency regime and the nDEP induced deviation.

6.3.2.1 High frequency simulations: nDEP induced deviation

6.3.2.1.1 Unit cell and basic equations

To model the nDEP induced deviation, the simulation domain was narrowed down to a single DLD unit cell (see Figure 6-1a). Following the method by Kim *et al.*[255], the particle trajectories through the unit cell were used to derive a transfer function that related the initial and final positions which then allow calculation of the deviation angle. The unit cell had exactly the same geometrical parameters as the unit cell of the devices used for the experiments (#1 from DLD Design A) with a symmetric arrangement ($D_p = G_x = G_y$) and 18 μm diameter circular posts with an offset angle of $\theta = 3.18°$.

Inside the DLD microfluidic channels the Reynolds number is very low; for a typical flow rate of $U = 100\ \mu\mathrm{m/s}$ the estimated value is $Re \sim 10^{-3}$. Hence, the fluid velocity profile was calculated by solving the 2D Stokes equation in the simulation domain:

$$\nabla \cdot \boldsymbol{v}_f = 0 \tag{6.8}$$

$$\eta \nabla^2 \boldsymbol{v}_f - \nabla p = 0 \tag{6.9}$$

A no-slip boundary condition was set on the walls of the pillars while periodic boundary conditions were used in pairs on boundaries H-A and D-E and boundaries B-C and F-G of the domain shown in Figure 6-1a, resulting in the same pressure and velocity profile for both. To simulate a net flow from left to right, a pressure difference Δp was imposed between boundaries H-A and D-E. Symbolically:

$$\begin{gathered} \boldsymbol{v}_{f,A-B} = \boldsymbol{v}_{f,C-D} = \boldsymbol{v}_{f,E-F} = \boldsymbol{v}_{f,G-H} = 0 \\ \boldsymbol{v}_{f,H-A} = \boldsymbol{v}_{f,D-E}\,;\boldsymbol{v}_{f,B-C} = \boldsymbol{v}_{f,F-G} \\ p_{H-A} = p_{D-E} + \Delta p\,;p_{B-C} = p_{G-F} \end{gathered} \tag{6.10}$$

The fact that the boundary D-E is slightly displaced with respect to boundary H-A, results in a non-zero fluid flow in the lateral y direction. This is valid for an ideally infinite DLD array; however, DLD devices in real situations are of finite length and have enclosing walls which do not permit a net flow orthogonal to the main flow direction. To solve this problem and create a more realistic model, a second flow component was solved under almost the same conditions but with a pressure difference set between walls B-C and F-G. Then, both components were added together so that the resulting flow profile had a zero net fluid flow in the lateral y direction. The final fluid flow distribution is shown in Figure 6-1b.

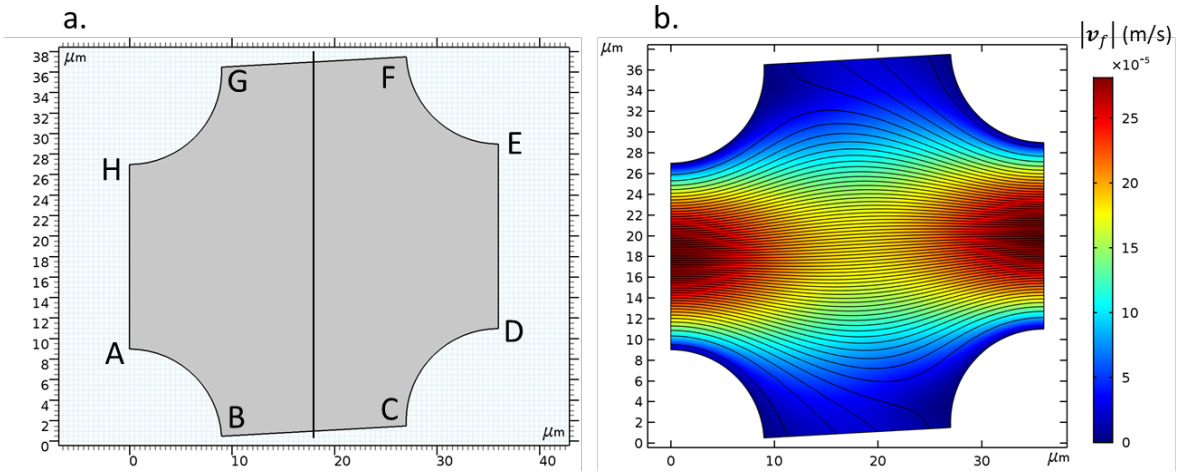

Figure 6-1. (a) Model domain used for the high frequency simulations corresponding to a single DLD unit cell with the same geometry as that of the DLD devices used for the experiments. (b) Stokes flow velocity field – the black lines correspond to the fluid streamlines.

Finally, the resulting average velocity was calculated along the central line of the unit cell (black line in Figure 6-1a) and adjusted to the typical values of U estimated for the experiments. In mathematical terms:

$$\boldsymbol{v}_f = B(\boldsymbol{v}_f' + B_c\boldsymbol{v}_f'') \tag{6.11}$$

$\boldsymbol{v}_f'$ is the flow component with the pressure difference set in the x direction, $\boldsymbol{v}_f''$ is the flow component with the pressure difference set in the y direction, B_c is the constant adjusted to achieve a zero net flow in the y direction and B a constant to adjust the average flow velocity to the estimated experimental values of U.

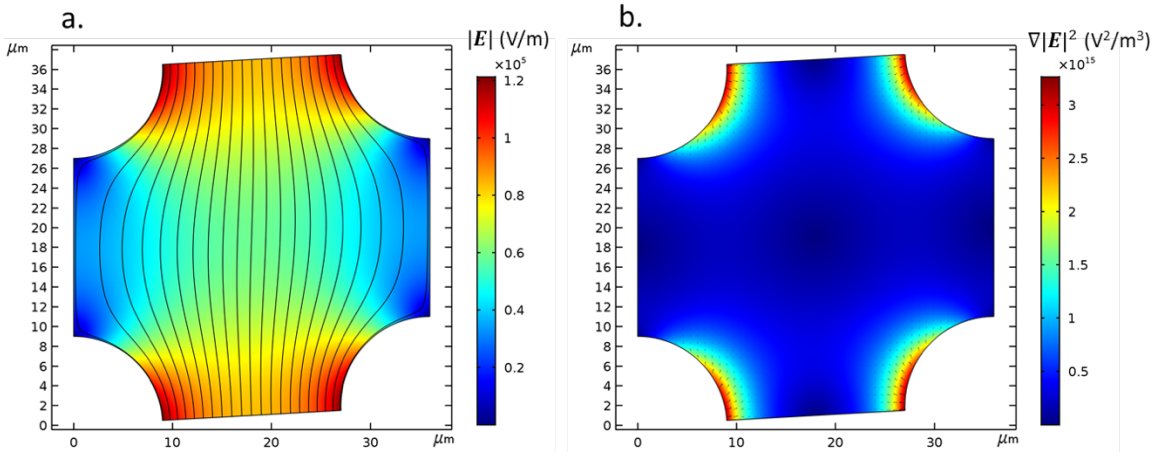

Figure 6-2. (a) Electric field magnitude distribution – the black lines represent the electric field lines bent by the presence of the insulating posts. (b) Calculations of $\nabla|\boldsymbol{E}|^2$ from the electric field distribution; this is proportional to the magnitude of the DEP force – the black arrows correspond to the direction of the nDEP force.

A net electric field $\boldsymbol{E}$ in the y direction, perpendicular to the fluid flow (x direction), was established with a magnitude E_0 equal to that of the field applied in the experiments. The field distribution was calculated as the sum of the uniform field of magnitude E_0 in the y direction and a perturbation $\boldsymbol{E}'$ created by the insulating posts:

$$\boldsymbol{E} = \boldsymbol{E}' + E_0\boldsymbol{u}_y \rightarrow \phi = \phi' - E_0 y \tag{6.12}$$

where $\boldsymbol{u}_y$ is the unit vector in the y direction, ϕ the total electric potential and ϕ' the electric potential corresponding to $\boldsymbol{E}'$. To calculate the spatial dependence of $\boldsymbol{E}'$, the Laplace equation for ϕ' was solved with periodic conditions in pairs on boundaries H-A and D-E and boundaries B-C and F-G:

$$\nabla^2\phi' = 0 \tag{6.13}$$

The pillars were modelled as perfect insulators, with a zero normal current density on the walls:

$$\frac{\partial \phi}{\partial n} = 0 \rightarrow \frac{\partial \phi'}{\partial n} = E_0 n_y \tag{6.14}$$

Figure 6-2a shows the resulting field $\boldsymbol{E}$ for $E_0 = 70\ \mathrm{kV/m}$ inside the DLD unit cell and Figure 6-2b shows the resulting spatial dependence of $\nabla|\boldsymbol{E}|^2$, which is proportional to the DEP force.

6.3.2.1.2 Particle trajectories and transfer function. Predicted critical diameter.

From the calculated $\boldsymbol{v}_f$ and $\boldsymbol{E}$, the particle trajectories could be easily computed using particle tracing. Consider first the case of point-like particles in a classical DLD without an applied electric field, where $\boldsymbol{v}_p = \boldsymbol{v}_f$, i.e. the particles follow the fluid streamlines (see Figure 6-3a). The trajectories entering the unit cell through boundary H-A leave either through wall D-E or wall B-C. The particle trajectories that end at wall B-C correspond to particles that, in a real array zig-zag and move to the unit cell placed below. To take these trajectories into account, they are correlated to the trajectories starting at wall F-G that then also end at wall D-E. It is possible to define a transfer function f, that relates the initial vertical coordinate y_i where the trajectories start at wall H-A and the final vertical position y_f at wall D-E. In this model, y_i and y_f the distances to the posts, i.e. the distance to points A and D in Figure 6-1a respectively. Using the dimensionless coordinate $h = y/G$:

$$h_f = f(h_i) \tag{6.15}$$

The particles enter the adjacent unit cell at the exit position of the previous unit cell:

$$h_{i+1} = h_f = f(h_i) \tag{6.16}$$

This means that the transfer function f fully determines the trajectories throughout the entire DLD array – the final position after crossing a given number n of unit cells can be calculated by applying n times the function f to the starting position:

$$h_{i+n} = f^n(h_i) \tag{6.17}$$

For a symmetric DLD array of periodicity N:

$$h_{i+N} = f^N(h_i) = h_i \tag{6.18}$$

This allows calculation of the net lateral displacement Δy predicted by the numerical model after a particle has passed through n unit cells simply by applying this function n times:

$$\Delta y = n\Delta\lambda + G\sum_{k=i}^{n+i}(h_{k+1} - h_k) \tag{6.19}$$

In the previous expression the difference $h_{k+1} - h_k$ is negative when the particle zig-zags in the unit cell k and enters the unit cell $k+1$ via wall F-G. The predicted deviation angle θ is calculated from Δy:

$$\theta = \text{atan}\left(\frac{\Delta y}{n\lambda}\right) \tag{6.20}$$

In Figure 6-3a, $y_s = h_s G$ indicates the point that divides the trajectories of point-like particles that pass below and above the next post. Therefore y_s corresponds to the distance from the post to the separatrix streamline and hence the D_c predicted by the model is equal to $2y_s$. Particles entering with $y_i < y_s$ leave through wall B-C (zig-zag). In the model, these particles are then reintroduced through wall F-G by means of interpolation of their exit position at B-C to the entry position at F-G. This serves to associate an initial position with $y_i < y_s$ to a final position at wall D-E. In a real situation, particles leaving through wall B-C would travel to a different unit cell and follow trajectories parallel to the fluid flow. This zigzagging behaviour produces the part of the transfer function located at the top left corner in Figure 6-3b; the trajectories with $y_i < y_s$ are related to the higher values of y_f located in the top part of the boundary D-E.

Assuming non-elastic hard-wall particle-post interactions, the transfer function for finite sized particles can be derived from that of point-like particles. Considering particles of radius a, trajectories with $y_i < a$ are prohibited since they cannot approach the posts by a distance smaller than the radius. Thus these trajectories are removed from the calculations. In addition, trajectories with $y_f < a$ or $y_f > G - a$ are corrected to have $y_f = a$ and $y_f = G - a$ respectively. These corrections account for the particle size in the model as shown in Figure 6-3c.

As a result, if $y_s < a$, i.e. the simulated particles are bigger than the calculated D_c; the zigzagging part of f disappears and the function cuts the line $h_{i+1} = h_i$, which is plotted as a red line in Figure 6-3b and Figure 6-3c. This means that the particles entrance and exit positions in the DLD unit cell become eventually the same and equal to $h_{i+1} = h_i = a/G$, which corresponds to a distance of one particle radius away from the posts (see Figure 6-3c). This characterises the bumping trajectories of particles bigger than the critical diameter. After applying the transfer function N times, all simulated particles converge to the bumping trajectories, leaving the unit cell in the same position as they enter.

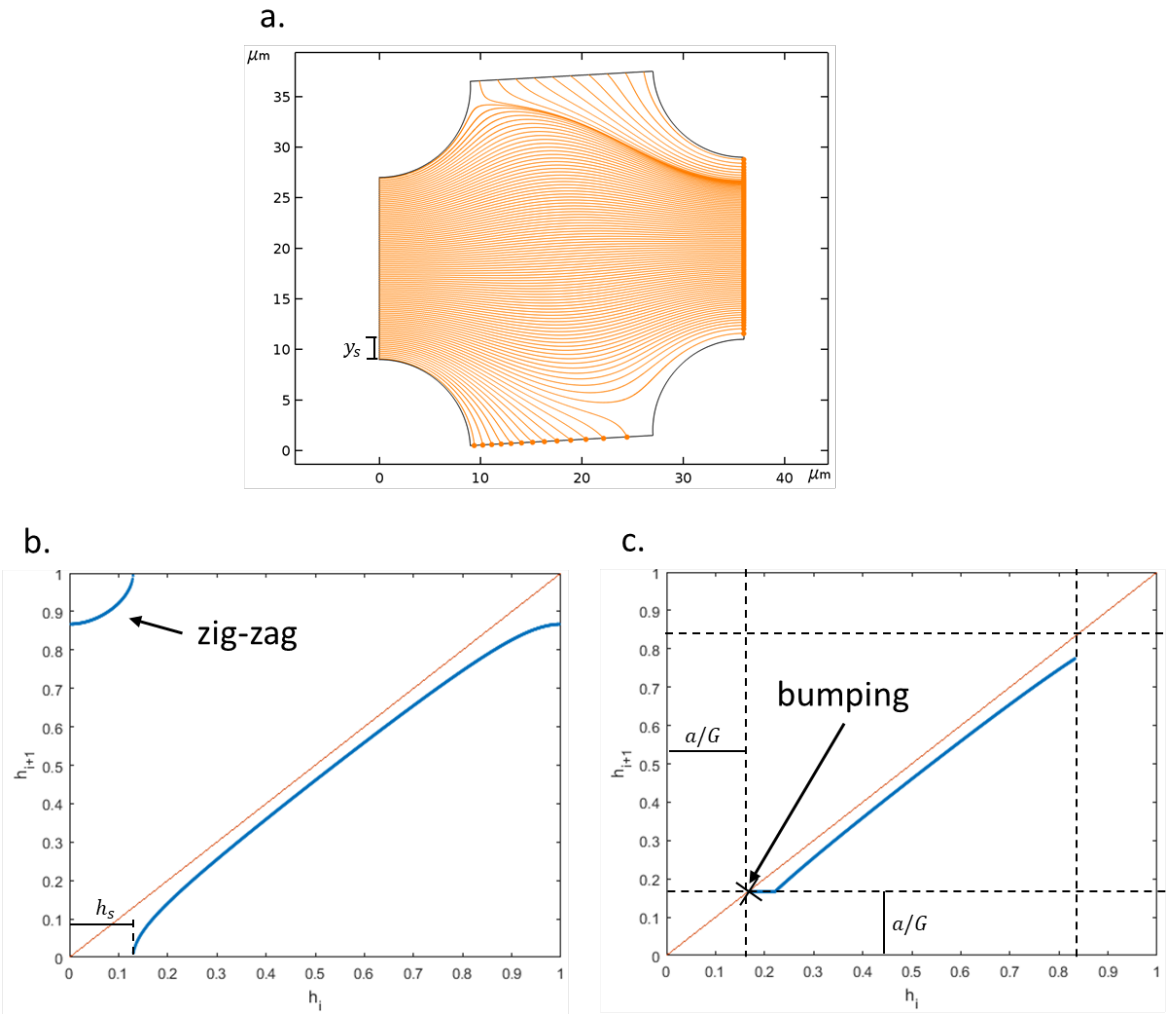

Figure 6-3. (a) Simulated trajectories of point-like particles through the DLD unit cell in the absence of electric field; y_S corresponds to the point dividing the zigzagging trajectories from those that pass above the next post, i.e. it indicates the distance from the post to the separatrix. (b) Transfer function corresponding to the trajectories in Figure 6-3a – associated with zig-zag mode trajectories. (c) Transfer function of 6 µm diameter particles derived by truncating the function in Figure 6-3b – associated with bumping mode trajectories.

This model predicts a critical diameter of 4.86 µm for Device #1 from DLD design A, which is lower than the value of 6.3 µm estimated using the equation derived experimentally by Davis[87] (see section 2.2.2.3 Deterministic Lateral Displacement (DLD)) but nevertheless in good agreement by the values predicted with the 2D analytical models in the literature such as those derived by Inglis[86] or Beech[256]. Figure 6-4 shows the dependence of the predicted D_c with the periodicity of the array in comparison with the aforementioned estimations. The D_c of this geometry was experimentally found to be between 6 µm and 7 µm, in good agreement with the empirical estimation of Davis and

indicating that there is still some physics missing in the analytical models, possibly the interaction of particles with the DLD pillars, which is probably not as simple as a non-elastic hard-wall interaction. However, this error in the model is not relevant for this case where the deviation is driven by electrokinetic forces and not by an interaction with the pillars of the array.

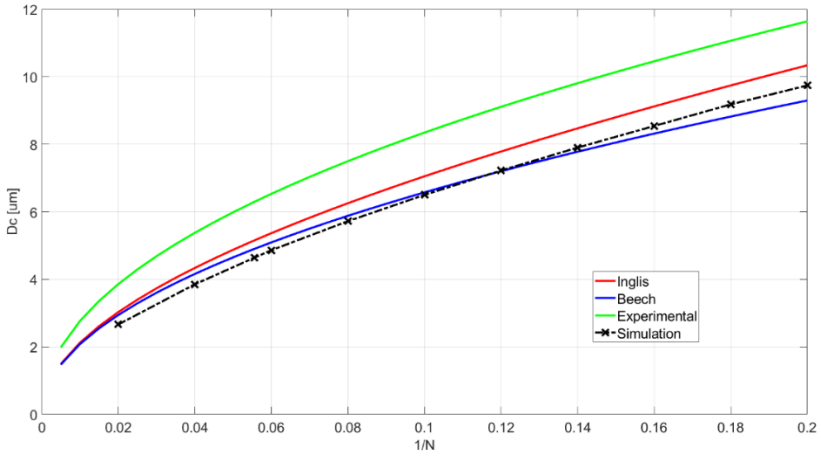

Figure 6-4. Values of the critical diameter predicted by the numerical model as a function of the periodicity of a symmetric DLD array ($D_p = G_x = G_y$) of 18 µm diameter posts in comparison to the analytical models developed by Inglis[86] and Beech[256], and the empirical expression derived by Davis[87].

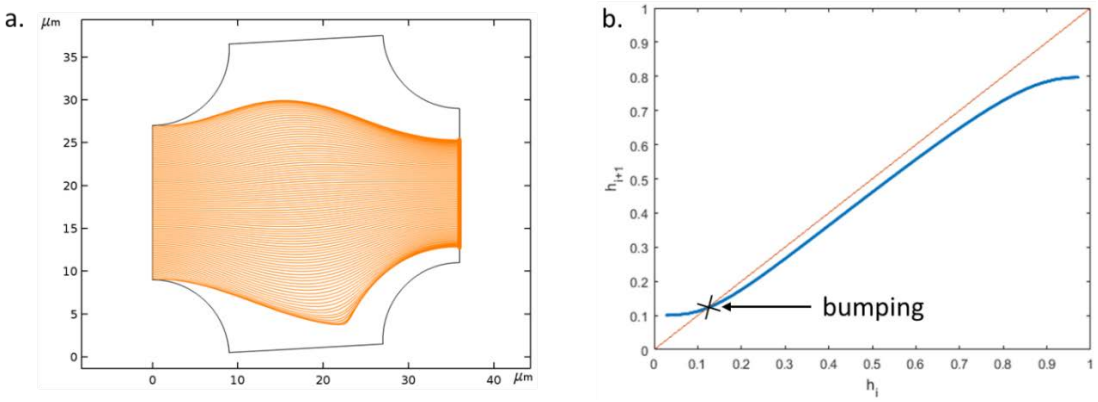

Figure 6-5. (a) Trajectories of point-like particles modified by a nDEP force – the particles are no longer allowed to zig-zag even if they enter the unit cell with $y_i < y_s$. (b) Transfer function corresponding to nDEP modified trajectories; the function crosses the $h_{i+1} = h_i$ indicating that the simulated particles move in the bumping mode.

When a nDEP force is included in the simulations, v_p is no longer equal to v_f but is given by the sum of v_f and v_{DEP}, resulting in a change in particle trajectories and thus the transfer function, as shown in Figure 6-5. In this situation, an induced bumping behaviour can also be predicted, and the deviation angle calculated in the same way. If the resulting transfer function cuts the line $h_{i+1} = h_i$, all simulated particles converge to a trajectory where they enter the DLD unit cells in the same

position as they leave, i.e. they are forced to move in displacement mode by the action of the electric field.

6.3.2.2 Low frequency simulations

To numerically simulate the low frequency behaviour, an electrophoretic oscillation was added to the particle motion together with an oscillatory component to the DEP force. However, in this case, the oscillation was often large enough to make the particle motion span over more than a single unit cell. To explore the complete trajectories, the simulation domain was extended to two cells in the vertical direction. As a result, the analysis of the overall trajectories in a DLD array had to be approached differently. The simulation domain was extended to a number of horizontal unit cells equal to the periodicity of the array N (which in this case was 18) so that the predicted trajectories within this domain fully defined the trajectories through a complete DLD.

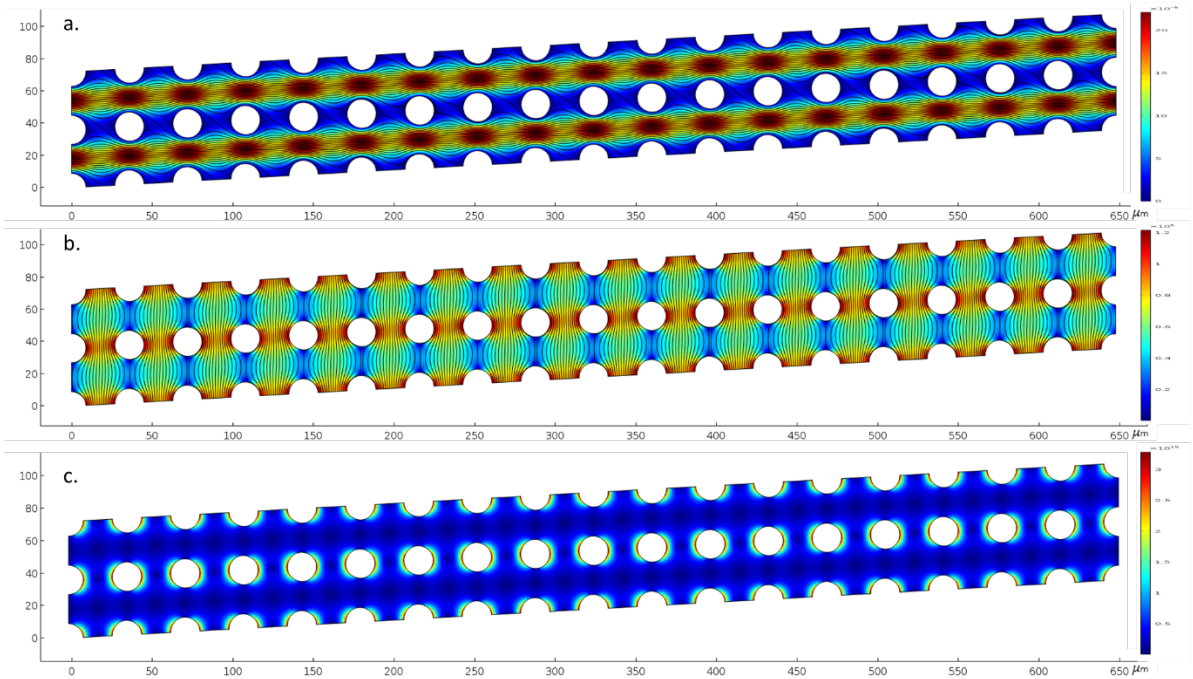

Figure 6-6. Extended domain for the low frequency simulations. (a) Fluid flow profile. (b) Electric field distribution. (c) $\nabla|\boldsymbol{E}|^2$ calculated from the electric field distribution – proportional to the magnitude of the DEP force.

The fluid flow and electric field inside this domain were calculated in the same manner as in the single DLD unit cell case, by simply adjusting the boundary conditions and correction factors. The results are shown in Figure 6-6. Since in this case a transfer function was not used, a virtual wall around the pillars located at one particle radius distance away from the pillar surface was incorporated into the calculations to account for a particle size. These walls did not allow the simulated particles to approach the posts closer than a distance equal to their radius but did not affect the flow or field profiles.

6.4 Results and discussion

6.4.1 High frequency induced deviation

6.4.1.1 Experimental results

The high frequency induced deviation of 1, 2 and 3 µm diameter carboxylate microspheres was measured at a fixed frequency of 50 kHz as a function of the magnitude of the electric field for different flow rates. This frequency was chosen because it was high enough for the low frequency effects to be negligible (DEP dominated the EK behaviour), but low enough for an optimal performance of the voltage amplifier. The suspending medium conductivity was chosen so that the particles had an estimated value for $\mathrm{Re}[\tilde{f}_{\mathrm{CM}}]$ of approximately -0.5, i.e. the particles always experienced the maximum strength of nDEP.

The magnitude of the applied electric field E_0 was calculated from the voltage applied to the electrodes and the gap between them (2.2 mm). A typical value of the fluid velocity U was indirectly estimated from the pressure drop Δp along the channel. For this purpose, the fluidic resistance R_h of the devices was determined by measuring the fluid outlet rate at a fixed pressure difference of 100 mbar (shown in Figure 6-7). A linear regression of the data in Figure 6-7 allowed to calculate the flow rate Q and then the fluidic resistance from $Q = \Delta p / R_h$; the final measured value was $R_h = 170.6\ \mathrm{mbar \cdot min/\mu L}$.

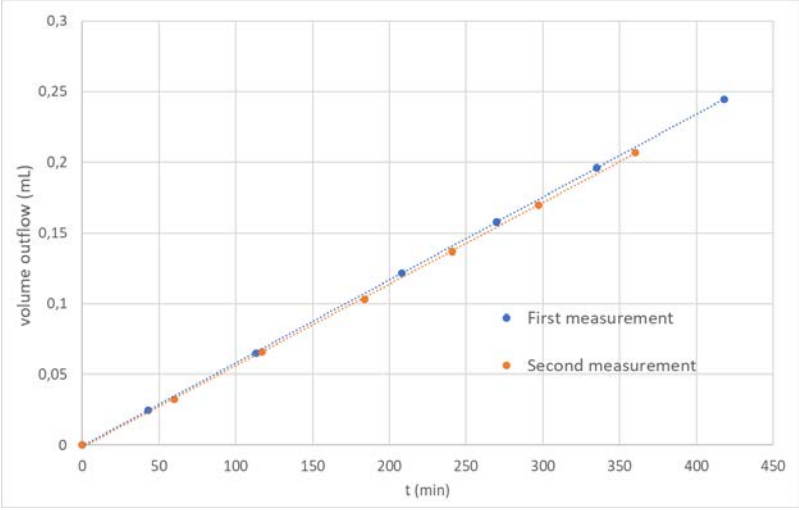

Figure 6-7. Volume outflow rate of devices #1 from DLD design 1 ($D_c = 6.3\ \mu\mathrm{m}$) for a fixed pressure drop of 100 mbar. The plot shows two indepedent data sets obtained under the same conditions.

In our model, U refers to the average fluid velocity in the channel cross-section in the middle of the gap between two columns of posts (in the numerical model this corresponds to the vertical black

line in Figure 6-1a). Knowing R_h and the cross-sectional area of the channels $w \times h$ (where w is the channel width and h is the channel height), U can be estimated from the applied Δp according to the relation:

$$U = \frac{\Delta p}{whR_h} \tag{6.21}$$

The plots in Figure 6-8 summarise the experimental data of the dependence of the high frequency induced deviation of 3 µm and 2 µm particles with the magnitude of the applied field for different flow rates. The suspending electrolyte had an electrical conductivity of 15.7 mS/m, so that $\mathrm{Re}[\tilde{f}_{\mathrm{CM}}] \sim -0.5$. The error in these measurements (see error bars in Figure 6-8a) was estimated from the sample stream width (similar to the width of the inlet channel), and it was assumed to be approximately the same for all the experimental data points in the plots of this chapter (for the sake of simplicity, the error bars are only included in one figure).

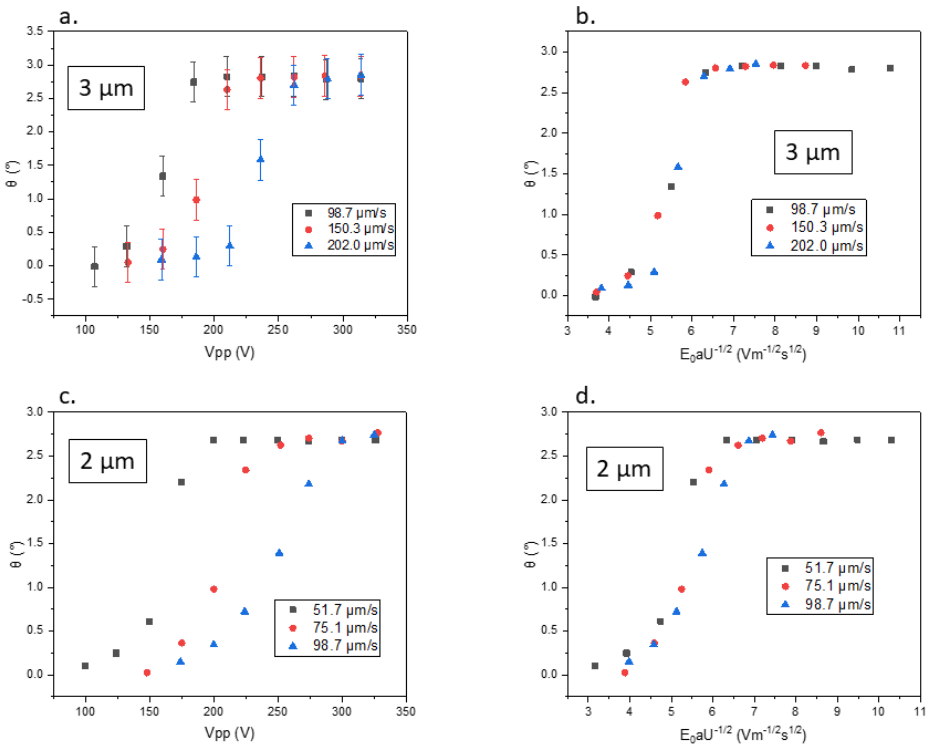

Figure 6-8. Induced deviation of 3 µm and 2 µm diameter microspheres with an applied AC electric field of 50 kHz and a suspending electrolyte conductivity of 15.7 mS/m. (a) 3 µm microspheres as a function of the applied voltage. (b) 3 µm microspheres as a function of $E_0 a/\sqrt{U}$; proportional to $\sqrt{\gamma}$. (c) 2 µm microspheres as a function of the applied voltage. (d) 2 µm microspheres as a function of $E_0 a/\sqrt{U}$. The figure legends indicate the values of U, constant for each curve.

Figure 6-8a and Figure 6-8c show the dependence of the induced deflection of 3 µm and 2 µm microspheres respectively with the voltage applied to the electrodes for different values of U. For high electric fields, the deviation angle reaches a maximum that corresponds to the maximum lateral deflection that can be achieved in the devices. When the field magnitude is reduced below a given threshold, there is an abrupt drop in the deviation angle. This threshold depends on the average fluid velocity; the faster the fluid flow, the higher the field magnitude needed to force the particles to switch to bumping mode, as expected.

In Figure 6-8b and Figure 6-8d, the deviation angle is plotted as a function of $E_0 a/\sqrt{U}$, a quantity which is proportional to $\sqrt{\gamma}$. These two figures show that the curves corresponding to different values of U collapse into a single curve when plotted as a function of $E_0 a/\sqrt{U}$. These results agree with the scaling laws that predict that nDEP is the force causing the induced deflection.

The size dependence of the high frequency induced deflection is summarised in Figure 6-9, where the deviation angle for three different particle sizes is plotted as a function of $E_0 a/\sqrt{U}$. The figure shows that the curves for the 3 µm and 2 µm particles collapse, in agreement with scaling laws for the nDEP induced deviation. However, the smaller 1 µm particles do not follow this trend and show a slightly different response. An explanation for this result is given in the next section.

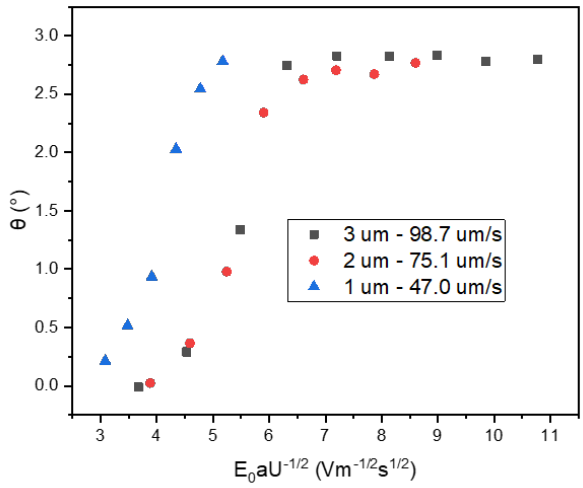

Figure 6-9. Measurements of the deviation angle of 3, 2 and 1 µm diameter microspheres as a function of $E_0 a/\sqrt{U}$ for a high frequency AC field of 50 kHz. The conductivity of the suspending electrolyte was adjusted so that $\mathrm{Re}[\tilde{f}_{\mathrm{CM}}] \sim -0.5$ in all cases with 15.7 mS/m for the 3 µm and 2 µm particles and 50 mS/m for the 1 µm particles.

6.4.1.2 Comparison of experiments vs simulations

The experimental results were compared to the values of deviation angle predicted using the numerical model previously presented (see section 6.3.2.1. High frequency simulations: nDEP induced deviation). The parameters U and E_0 of the model were adjusted to the experimental conditions whilst $\mathrm{Re}[\tilde{f}_{\mathrm{CM}}]$ was set to -0.5 and ε and η where set to those of water ($\varepsilon = 80\varepsilon_0$ and $\eta = 1.0042\ \mathrm{mPa \cdot s}$). The trajectories of at least 2000 particles experiencing a nDEP force were calculated and from these trajectories the transfer function f was derived by linear interpolation; this function then enabled calculation of the deviation angle.

The dependence of the simulated induced deflection with $E_0 a/\sqrt{U}$ is shown in Figure 6-10a, for the same particle sizes studied experimentally (3, 2 and 1 µm). Since the particle size is significantly smaller than the critical diameter predicted by the model, the particle-wall interaction with the posts can be neglected and the deflection is assumed to be caused solely by nDEP. As a result, the values of the deviation angle predicted for the different particle diameters are expected to collapse to the same curve, as observed in Figure 6-10a. The model also shows a trend very similar to the experiments, with a threshold value of the electric field magnitude below which no induced deflection is observed. Above this threshold, the deviation angle rapidly reaches a maximum value, in this case corresponding to the tilting angle of the posts in the DLD array (unlike the experimental case where it corresponds to the maximum lateral displacement inside the DLD devices, see section 5.2 Experimental methods).

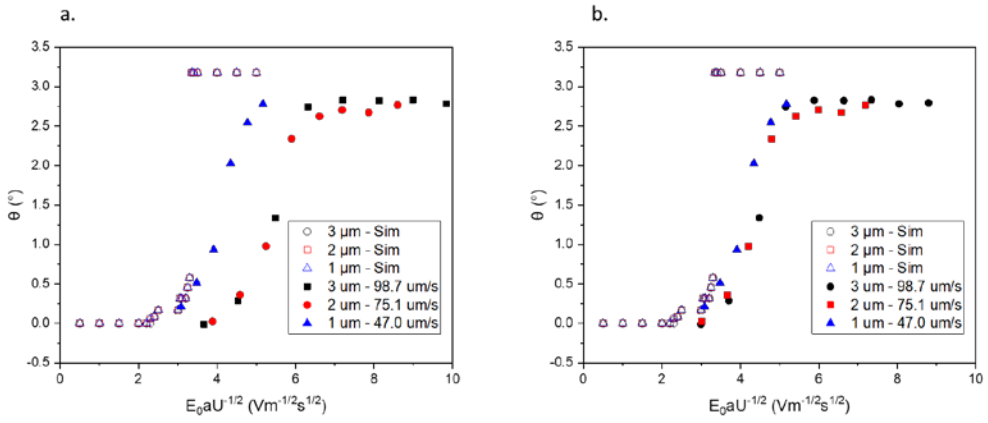

Figure 6-10. (a) Comparison of the numerically predicted values of the nDEP induced deviation angle of 3, 2 and 1 µm diameter particles with the experimental data as a function of $E_0 a/\sqrt{U}$. (b) Comparison of simulations-experiments with the corrected values of the deviation angle for the 3 µm and 2 µm diameter particles assuming a different fluid average velocity $U' = \alpha U$ with the correction factor $\alpha = 1.5$ which accounts for the increase in the average particle velocity in the centre of the parabolic flow profile.

A direct comparison between the experimental data and the model (Figure 6-10a), shows that the predicted values are much closer to the experimental data for the 1 µm particles. This indicates that the larger size of the 3 µm and 2 µm particles could be responsible for this mismatch and the difference in the behaviour of these larger particles with respect to the smaller 1 µm particles.

In the experiments, the 3 µm and 2 µm particles were observed to speed up significantly the moment the electric field was applied, whilst the 1 µm particles maintained the same average velocity. Given that the DLD channels were very narrow, only 8 µm tall, a moderate electrostatic wall repulsion from the top and bottom walls of the channels would focus these larger particles into the centre of the parabolic flow profile, in the mid plane of the channel. There the fluid flow velocity is 1.5 times faster than the average measured value U. A faster speed U' implies that a stronger electric field is needed to achieve the same induced deflection, i.e. a stronger nDEP force is necessary to overcome the increased Stokes drag. Because this effect is not considered in the simulations, the best agreement happens for particles that are unaffected by this repulsion, i.e. the smaller 1 µm particles.

Theoretically, the time the particles take to travel from near the wall to the centre of the channel can be calculated as a dipole-dipole repulsion using the method of images. The electrostatic repulsion force of a dipole from an insulating wall is given by:

$$F_{\mathrm{rep}} = \frac{3p^2}{4\pi\varepsilon z^4} \tag{6.22}$$

Where p is the dipole moment and z is the distance to the wall. Thus, for a dielectric particle immersed in an electrolyte:

$$F_{\mathrm{rep}} = \frac{3\pi\varepsilon a^6\left(\mathrm{Re}\left[\tilde{f}_{\mathrm{CM}}\right]E_0\right)^2}{4z^4} \tag{6.23}$$

This expression has a very strong dependence of force with particle radius a. For a sphere enclosed between two walls separated a distance g, as in the case of the DLD ($g = 8\ \mu\mathrm{m}$):

$$\begin{aligned} F_{\mathrm{rep}} = \frac{3\pi\varepsilon a^6\left(\mathrm{Re}\left[\tilde{f}_{\mathrm{CM}}\right]E_0\right)^2}{4z^4} - \frac{3\pi\varepsilon a^6\left(\mathrm{Re}\left[\tilde{f}_{\mathrm{CM}}\right]E_0\right)^2}{4(g-z)^4} = \\ = \frac{3\pi\varepsilon a^6\left(\mathrm{Re}\left[\tilde{f}_{\mathrm{CM}}\right]E_0\right)^2}{4g^4}\left(\frac{1}{s^4} - \frac{1}{(1-s)^4}\right) \end{aligned} \tag{6.24}$$

with $s = z/g$. Integration of the equation of motion, i.e. $v_p = F_{\mathrm{rep}}/6\pi a\eta$, gives the time for the particles to travel a given distance (from z_1 to z_2) due to this repulsion force:

$$t = 6\pi a\eta \int_{z_1}^{z_2} \frac{dz}{F_{\text{rep}}} = \frac{8\eta}{\varepsilon a^5 \left(\text{Re}\left[\tilde{f}_{\text{CM}}\right] E_0\right)^2} \int_{z_1}^{z_2} \frac{dz}{z^{-4} - (g-z)^{-4}} = \\ = \frac{8\eta g^5}{\varepsilon a^5 \left(\text{Re}\left[\tilde{f}_{\text{CM}}\right] E_0\right)^2} \int_{s_1}^{s_2} \frac{ds}{s^{-4} - (1-s)^{-4}} \tag{6.25}$$

This equation implies a strong dependence with g and a. Table 6-1 summarises the calculated migration times for different particle sizes from either the top or the bottom wall of the DLD channel, $z_1 = a$, to a central region of the channel cross-section, around 1 μm wide, where the fluid is 1.5 faster than the average due to the parabolic flow profile, $z_2 = 3.5\ \mu\text{m}$.

Table 6-1. Theoretical values of particle migration time from the top or the bottom walls to the centre of the DLD channel cross-section due to an electrostatic wall-repulsion force for different particle sizes and field strengths.

	$\boldsymbol{a = 1.5\ \mu\text{m}}$	$\boldsymbol{a = 1.0\ \mu\text{m}}$	$\boldsymbol{a = 0.5\ \mu\text{m}}$
320 Vpp	0.26 s	2.03 s	65.1 s
210 Vpp	0.59 s	4.57 s	146.5 s
150 Vpp	1.2 s	9.3 s	300 s

A diffusion force also acts against this repulsion force which tends to spread the particles over the channel section (see section 2.1.3 Diffusion). Table 6-2 contains the calculated diffusion times corresponding to a distance equal to the gap between the top and bottom wall of the DLD, i.e. the time the particles take to spread uniformly over the channel cross-section due to Brownian motion.

Table 6-2. Particle diffusion times over the DLD channel cross-section.

	$\boldsymbol{a = 1.5\ \mu\text{m}}$	$\boldsymbol{a = 1.0\ \mu\text{m}}$	$\boldsymbol{a = 0.5\ \mu\text{m}}$
Diffusion	225 s	150 s	75s

A comparison between Table 6-1 and Table 6-2 shows that diffusion is much weaker than the repulsion force for the 3 μm and 2 μm particles but it is comparable and more relevant for the 1 μm particles. For a better comparison, it is possible to calculate the particle concentration c as a function of position z due to the influence of these two contributions:

$$\frac{\partial c}{\partial t} + \frac{\partial cv}{\partial z} - D\frac{\partial^2 c}{\partial z^2} = 0 \tag{6.26}$$

with $v = F_{\mathrm{rep}}/6\pi a\eta$ and D being the particle diffusion constant. When steady-state is reached:

$$\frac{\partial cv}{\partial z} - D\frac{\partial^2 c}{\partial z^2} = 0 \rightarrow cv - D\frac{\partial c}{\partial z} = 0 \tag{6.27}$$

The integration constant is zero due to the channel symmetry. Integration gives the distribution of c over the channel section:

$$\frac{\varepsilon a^5 \left(\mathrm{Re}[\tilde{f}_{\mathrm{CM}}]E_0\right)^2}{8\eta D g^3}\left(\frac{1}{s^4} - \frac{1}{(1-s)^4}\right)c = \frac{\partial c}{\partial s} \tag{6.28}$$

$$\frac{\varepsilon a^5 \left(\mathrm{Re}[\tilde{f}_{\mathrm{CM}}]E_0\right)^2}{8\eta D g^3}\int\left(\frac{1}{s^4} - \frac{1}{(1-s)^4}\right)ds = \ln c + Cst \tag{6.29}$$

$$\begin{gathered}\ln(c/c_0) = -\alpha\left(\frac{1}{3(1-s)^3} + \frac{1}{3s^3}\right) + \alpha\frac{16}{3} \rightarrow \\ \rightarrow c/c_0 = \exp\left[\alpha\left(\frac{16}{3} - \frac{1}{3(1-s)^3} - \frac{1}{3s^3}\right)\right]\end{gathered} \tag{6.30}$$

with c_0 the particle concentration at the centre of the channel and α given by:

$$\alpha = \frac{3\pi\varepsilon a^6 \left(\mathrm{Re}[\tilde{f}_{\mathrm{CM}}]E_0\right)^2}{4k_B T g^3} \tag{6.31}$$

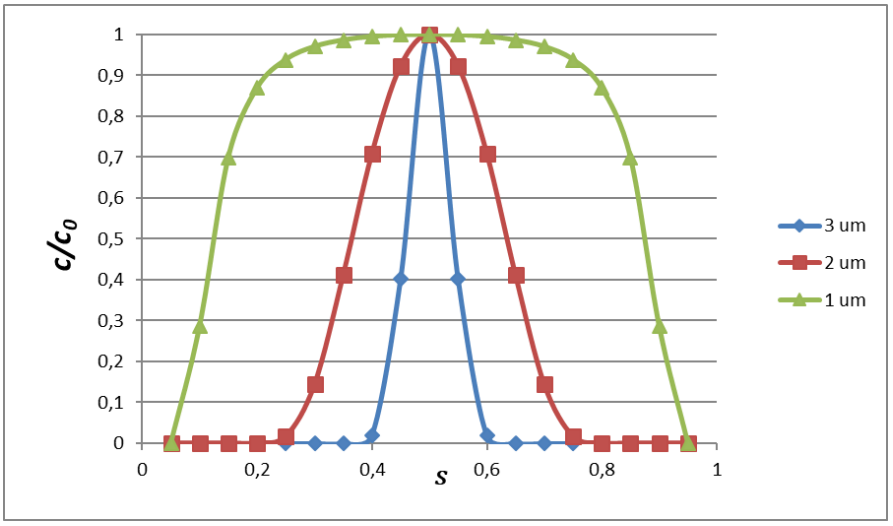

Figure 6-11. Dependence of particle concentration in the DLD microchannel cross-section under the influence of an electrostatic repulsion from the top and bottom walls for the three different particle sizes studied experimentally and with an electric field of $E_0 = 48\ \mathrm{kV/m}$.

Therefore, considering that the 3 µm and 2 µm particles are focused at the centre of the parabolic flow profile, the values of the deviation angle as a function of $E_0 a/\sqrt{U}$ can be corrected using an increased average speed of $U' = \alpha U$ with the correction factor $\alpha = 1.5$. This corrected data is shown in Figure 6-10b, where agreement with simulation and experiments is much better. This provides a firm support to the theoretical model presented here which assumes nDEP to be responsible for the induced deflection observed at high AC electric field frequencies, and which scales with the parameter γ.

6.4.2 Low frequency induced deviation

6.4.2.1 Experimental results

The previous chapter explains that the deviation observed at low frequencies has a different behaviour and currently unknown origin. When the frequency is reduced below 500 Hz, DEP is no longer the dominant force and other electrokinetic phenomena must be considered. DEP is a second order force and arises from the interaction of the non-uniform electric field with the effective dipole induced on the particles. EP and EO are first order forces which arise directly from the interaction of the field with the charges on the surfaces of particles and channels. At high frequencies the influence of this on particles is negligible since the forces have a zero-time average. Nevertheless, at low frequencies the oscillatory component created by these forces have a significant effect on the electrokinetic behaviour and overcomes the DEP (second order force). In addition, non-linear electrokinetic phenomena becomes more important at low AC electric field frequencies and may affect the particle behaviour in this regime, playing a role in the low frequency induced deviation.

The most evident amongst the low frequency effects is electrophoretic oscillation where particles move along the electric field lines, perturbed by the presence of insulating posts, at the frequency of the electric field. As the particles oscillate, they are forced to switch from zig-zag to displacement mode if the electric field magnitude is increased above a given threshold. This depends on particle size, medium conductivity, electric field frequency and flow rate.

As explained previously, two main results led to the conclusion that nDEP is not causing this deviation. First, under the same experimental conditions, the field magnitude threshold above which induced deflection is observed is significantly lower at low frequencies than at high frequencies where no EP oscillation is observed. Second and more important, particles experiencing pDEP are also forced to bump on the posts and follow the tilting angle when a low frequency AC electric field is applied, even though pDEP points in the opposite direction to nDEP, i.e. it attracts the particles to the gaps between the posts of the same row, and in theory, would not prevent them

from crossing a gap. In fact, if the frequency is increased, particles experiencing pDEP stop deflecting and eventually get trapped at the high electric field gradient regions. Both observations do not match with a mechanism that attributes the induced deviation to DEP.

The polarisation mechanism of the EDL and its effect on the net induced dipole of the particles is also not capable of explaining the low frequency behaviour. As explained in Chapter 3, the α-relaxation only affects the dipole magnitude and not its direction[138]. A particle experiencing pDEP at high frequencies, would experience pDEP also at low frequencies but weaker due to the reduction of the dipole moment caused by the α-relaxation. On the contrary, a particle experiencing nDEP experiences a is expected undergo a stronger nDEP in the low frequency regime, but with a limit set at a dipole factor of -0.5 (either governed by the Maxwell-Wagner polarisation or by the polarisation of the EDL). This mechanism is therefore not satisfactory to explain the low frequency deflection of particles experiencing pDEP nor can explain why particles with $\mathrm{Re}\left[\tilde{f}_{\mathrm{CM}}\right] = -0.5$ need lower electric field magnitude to switch to the bumping mode at low frequencies.

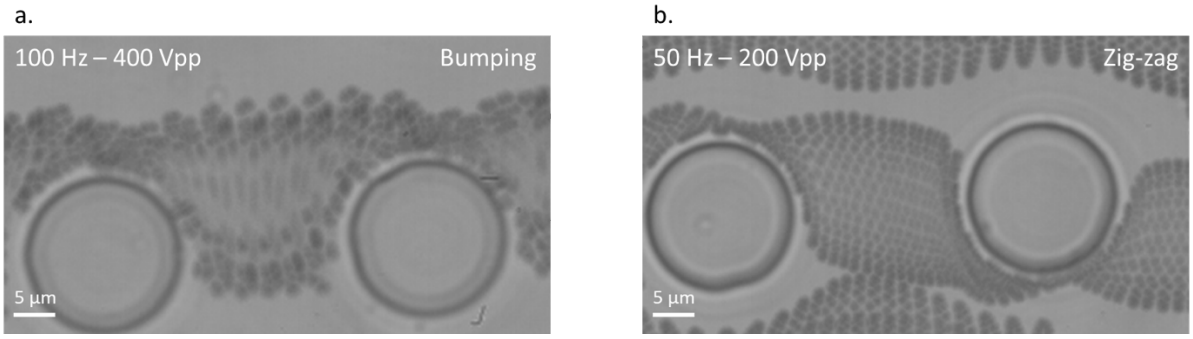

Figure 6-12. Trajectories followed by 1 µm particles around the DLD posts when a low frequency AC electric field is applied orthogonal to the fluid flow. (a) Signal of 100 Hz and 400 Vpp – bumping behaviour; image was created by superposition of 200 frames. (b) Signal of 50 Hz and 200 Vpp – zigzagging behaviour; image was created by superposition of 500 frames. The particles where suspended in a 1.8 mS/m electrolyte. Note that the oscillation amplitude is equal in both cases.

Although EP oscillation is the most obvious behaviour at low frequencies, it alone cannot explain the induced deviation. An oscillation-based deflection would be proportional to the oscillation amplitude. Figure 6-12 shows the paths followed by 1 µm particles through the DLD array under the influence of an orthogonal low frequency electric field. In both pictures the oscillation amplitude is the same. In Figure 6-12a the voltage signal was 100 Hz and 400 Vpp whilst in Figure 6-12b the signal was 50 Hz and 200 Vpp. The measured particle EP velocity was 6 mm/s in the case of Figure 6-12a which was double the measured velocity corresponding to Figure 6-12b, i.e. 3 mm/s, but the AC field changed direction twice as fast, leading to the same net EP displacement. However,

the observed behaviour was different. Figure 6-12a shows bumping trajectories, the opposite of Figure 6-12b where particles are observed to zig-zag around the posts.

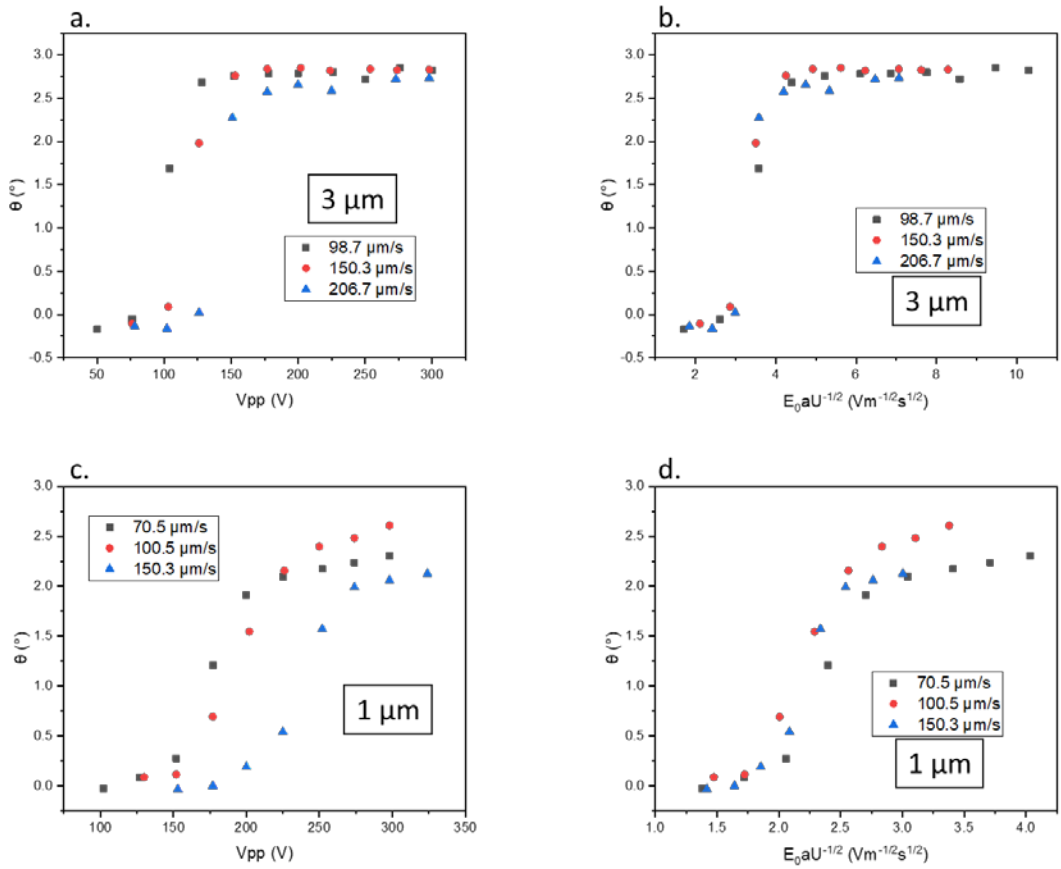

Figure 6-13. Induced deviation of 3 µm and 1 µm diameter microspheres with an applied AC electric field of 50 Hz and a suspending electrolyte conductivity of 2.8 mS/m. (a) 3 µm microspheres as a function of the applied voltage. (b) 3 µm microspheres as a function of $E_0 a/\sqrt{U}$; proportional to $\sqrt{\gamma}$. (c) 1 µm microspheres as a function of the applied voltage. (d) 1 µm microspheres as a function of $E_0 a/\sqrt{U}$. The figure legends indicate the values of U, constant for each curve.

Measurements of the deviation angle as a function of the electric field magnitude, at a fixed AC frequency of 50 Hz for different flow rates and particle sizes helped to bring more insight into the mechanism behind the low frequency induced deviation (see Figure 6-13). The dependence of the deviation angle of 3 µm and 1 µm microspheres with applied voltage is shown in Figure 6-13a and Figure 6-13c respectively. The suspending medium had a conductivity of 2.8 mS/m. The plots in these figures show a trend very similar to that obtained at high frequency but with one key difference, the deviation threshold was found a significantly lower voltages (compare Figure 6-13a with Figure 6-9a).

When this data is plotted as a function of the parameter $E_0 a/\sqrt{U}$, the curves also collapse, as for the nDEP induced deviation. This means that although the qualitative behaviour indicates that the DEP force is not responsible for the deflection, the underlying mechanism competing with the fluid drag must also scale with E_0^2. This result also proves that the EP oscillation amplitude is not the crucial aspect since it scales with E_0.

Figure 6-14 shows the trend for the low frequency deviation of 1 µm particles at a higher medium conductivity (15.7 mS/m). The behaviour is very much alike the case with a higher conductivity and the curves corresponding to different flow rates also collapse when plotted with respect to $E_0 a/\sqrt{U}$ (see Figure 6-14b). Nevertheless, the field magnitude at which maximum deflection is observed is significantly higher for this increased conductivity. This result supports the hypothesis that nDEP is not causing this deflection (it becomes stronger at greater conductivities) and reveals that the low frequency deflection is stronger at lower conductivities. This dependence neither can be attributed to the EDL polarisation since this mechanism predicts less negative dipole moments at lower conductivities ($\mathrm{Re}[\tilde{d}_e]$ decreases as the medium conductivity increases) and more negative dipole moments at high conductivities. Thus, according to the EDL polarisation, stronger nDEP is expected at higher conductivities and therefore a larger induced deflection, in opposition to the experimental observations.

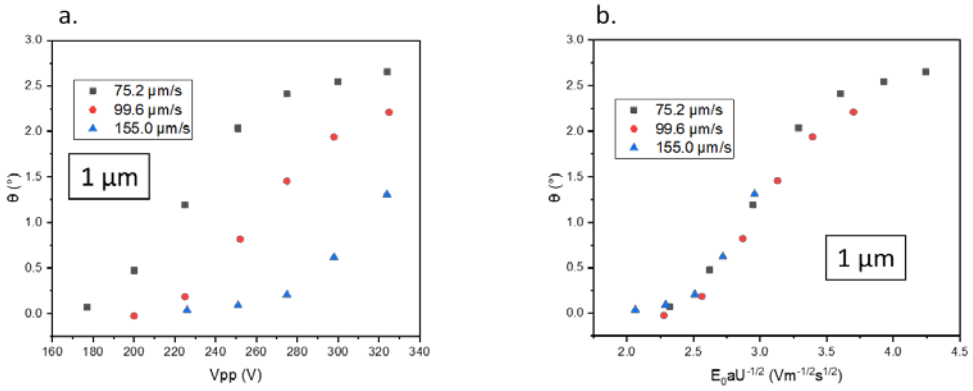

Figure 6-14. Induced deviation of 1 µm diameter microspheres using an applied AC electric field of 50 Hz with a suspending electrolyte of increased conductivity, 15.7 mS/m. (a) As a function of the applied voltage. (b) As a function of $E_0 a/\sqrt{U}$; proportional to $\sqrt{\gamma}$.

In Figure 6-15, the low frequency deviation angle for three different particles sizes (3, 2 and 1 µm diameter) is plotted as a function of $E_0 a/\sqrt{U}$. In this plot, the 1 µm particles also exhibit a behaviour which differs slightly from the larger particles. The curves of the 3 µm and 2 µm particles collapse almost perfectly, suggesting that the low frequency mechanism could scale with a^2 as well. If this assumption is right, the offset of the 1 µm particles data could have the same origin as for nDEP

induced deflection at high frequencies, i.e. the larger particles are focused to the centre of the parabolic flow profile where the fluid velocity is higher, which in turn requires a stronger electric field to be overcome.

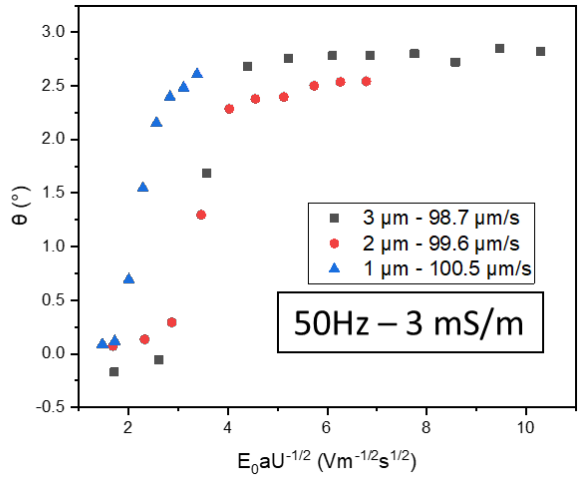

Figure 6-15. Measurements of the deviation angle of 3, 2 and 1 µm diameter microspheres as a function of $E_0 a/\sqrt{U}$ for a low frequency AC field of 50 Hz. The conductivity of the suspending electrolyte was 2.8 mS/m.

6.4.2.2 Simulation results

As explained above, simulations for the low frequency regime could not be performed in a single DLD cell mainly because the electrophoretic oscillation was often larger than the unit cell dimensions. Also, the oscillating particle trajectories in a unit cell depend on the electric field phase at which they enter the cell, adding an extra degree of freedom and therefore significantly complicating the numerical analysis.

The solution was to expand the simulation domain (see Figure 6-6), adding an extra cell in the lateral direction to avoid the oscillating particles from exiting the domain and computing the low frequency perturbed trajectories through a complete DLD period, i.e. through a number of consecutive unit cells that is equal to the periodicity of the DLD array. The resulting trajectories thus contain all the information necessary to infer the overall trajectories inside the real devices. If the particles cross the row of tilted posts inside this domain, they are expected to zig-zag periodically around the posts following a non-deflected trajectory. If instead, the particles do not zig-zag and bump on the posts through a whole DLD period, they are expected to stay in the displacement mode throughout the whole channel giving rise to a laterally deflected trajectory.

Simulations were performed using the fluid velocity field and the electric field distributions shown in Figure 6-6 under different conditions. Figure 6-16 contains two examples to account for the main

conclusions from the low frequency numerical analysis. Virtual walls were used to account for the particle size.

When only an EP oscillatory component of force was added, the particles described an oscillatory motion along the electric field lines at the frequency of the field, but they did not show any induced lateral deflection at any combination of field frequency and magnitude, i.e. they always zigzagged around the posts at some point within the DLD period. An example is given in Figure 6-16a, where the trajectories are simulated for an electric field of 70 kV/m magnitude and 100 Hz frequency (and an average fluid velocity of 100 µm/s). Under these conditions, an induced deflection is expected from the experimental results, but it is not predicted by the numerical model. This numerical analysis supports the experimental results and serves as an ultimate demonstration that the electrophoretic oscillation is not responsible for the induced deviation observed at low frequencies.

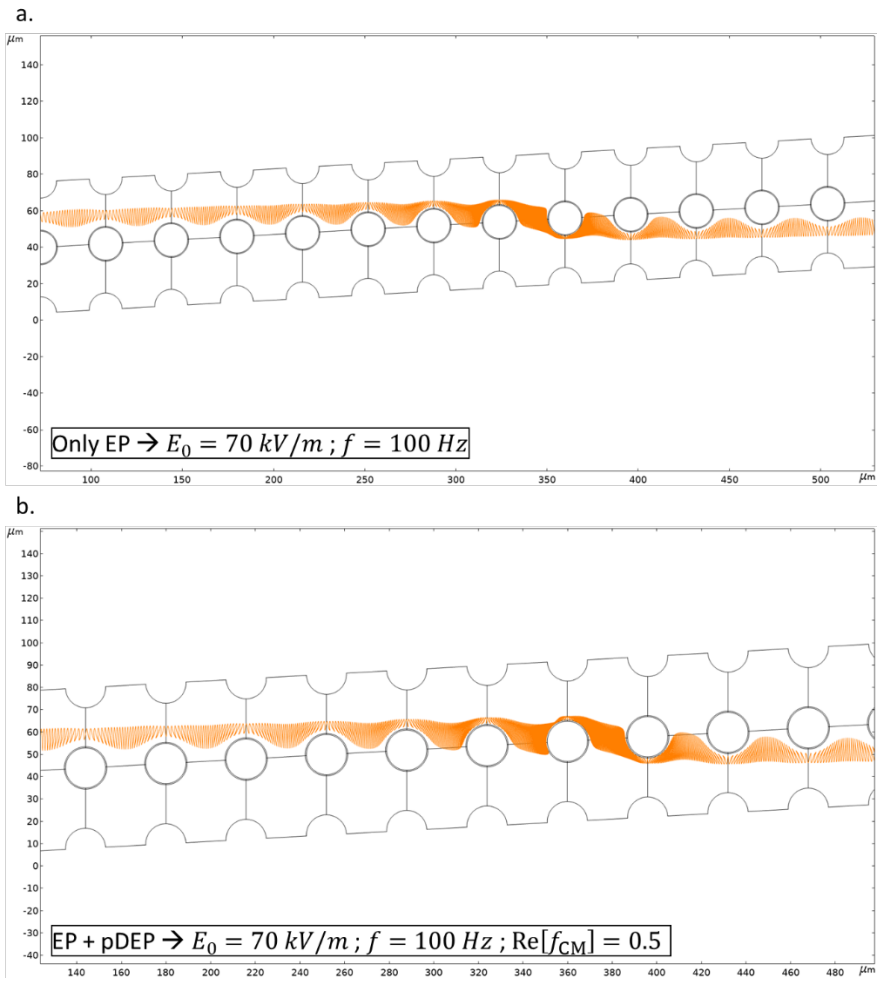

Figure 6-16. Simulated particle trajectories through a period of the DLD array under a low frequency AC electric field of 70 kV/m magnitude and 100 Hz frequency and an average fluid flow velocity of 100 µm/s. (a) Only the EP force is exerted on the particles leading to an oscillation along the electric field lines. (b) Both EP and pDEP act on the particles. A low frequency induced deflection is not predicted in none of the two cases.

Moreover, the model showed that EP in combination with pDEP did not lead to lateral deflection for any combination of simulation parameters (field frequency and magnitude, particle radius and CM factor) as exemplified in Figure 6-16b and contrary to the experimental results where low frequency induced deflection of particles experiencing pDEP was measured. In addition, EP did not alter the nDEP induced deviation since the electric field magnitude threshold (for nDEP) needed to prevent the particles from zigzagging around the posts did not change when an EP oscillation was added to the particle motion. Additionally, this analysis indicates that the α-relaxation is not playing a relevant role in the low frequency induced deviation - this mechanism would only increase or decrease the magnitude of the DEP force but it cannot account for the reduced electric field threshold needed to induce deviation at low frequencies with respect to the high frequency regime, where DEP is the dominant mechanism.

6.4.3 Quadrupolar EO Flows around insulating posts

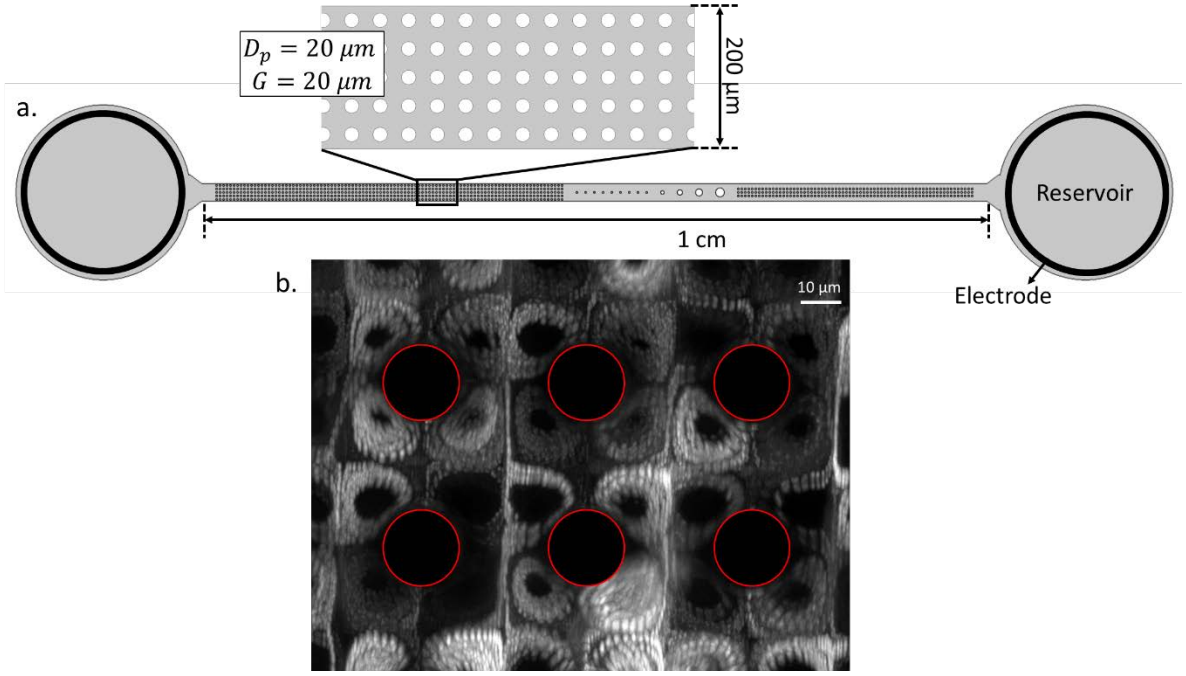

Figure 6-17. (a) Diagram of the devices used to experimentally explore the rectified Electroosmosis around insulating pillars. (b) Electroosmotic quadrupolar rectified flow pattern arising around the insulating PDMS pillars upon the application of a low frequency AC electric field (70 Hz). The white paths correspond to the trajectories of 500 nm spheres acting as flow tracers. The image was created by superposition of 300 frames.

Despite the fact that the scaling laws were identified, the ultimate origin of the low frequency deviation remains uncertain. Preliminary experiments of the low frequency EK phenomena in the vicinity of insulating structures have helped to identify further possible explanations. These

experiments were performed using the devices described in section 4.3.1.2 EK flows devices, consisting of a straight microfluidic channel containing different arrays of different sized insulating posts (with zero tilt angle) with electrodes placed at the inlet and outlet of the channel (see Figure 6-17a). Experiments were performed in the absence of pressure driven flow to explore only the electrically generated particle movement.

The observation of particle motion revealed the existence of quadrupolar electroosmotic flows in the vicinity of the insulating posts which occurred only when low frequency AC electric fields were applied (below 500 Hz). These rectified EO flows had very similar patterns to those arising from ICEO around conducting surfaces. Figure 6-17b shows the paths followed by 500 nm spheres (used as flow tracers) due to the quadrupolar rolls. These rectified EO flows were only found at low frequencies and qualitative observations showed a rapid decay with increasing frequency and electrolyte conductivity, the same as found for the low frequency induced deviation in the AC biased DLD systems suggesting that these rolls could be playing an important role in defining the particle behaviour.

6.4.3.1 Experimental characterisation

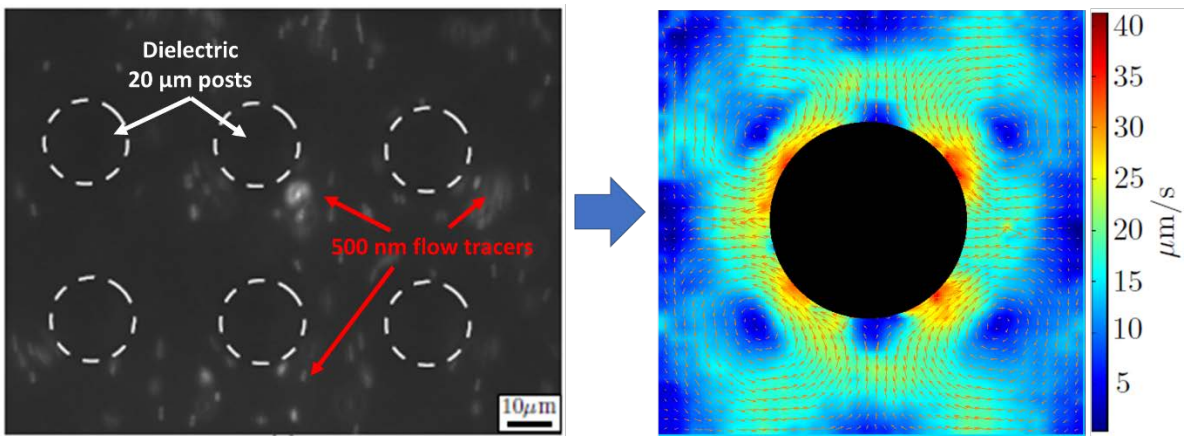

Figure 6-18. Summary of the µPIV analysis of the flow tracers trajectories (500 nm diameter fluorescent polystyrene nanospheres). Videos of the trajectories of the flow tracers following the rectified EO pattern are recorded and then analysed to extract the fluid velocity field shown in the figure on the right. The colour map represents the magnitude of the flow velocity. In this particular case the electrolyte conductivity was 1.75 mS/m, the applied voltage 1000 Vpp and the frequency 70 Hz.

A quantitative characterisation of the flow magnitude was performed as a function of the electric field frequency and for different electrolyte conductivities to gain further insight on the origin of the EO quadrupolar rolls around dielectric pillars occurring at low frequencies and explore their role on the low frequency deviation inside DLD devices.

For that purpose, 500 nm fluorescent nanospheres were used as flow tracers and their trajectories under the influence of the EO rectified flow were analysed using microparticle image velocimetry (μPIV)[257]. This technique evaluates sequences of images to extract the trajectories of single particles and compute the velocity on each position. Each frame is compared to the previous frame so that, if the pixel-to-distance ratio and the time interval between frames are known, the velocity of the particles can be calculated. From this analysis it is then possible to derive a velocity field within the examined Region-of-Interest (ROI) by examining a large enough number of frames.

Videos of the behaviour of 500 nm nanospheres around the 20 μm dielectric PDMS posts were recorded and then analysed using an open source PIV software tool[258]. The videos were taken in the region of the devices with a periodic array of pillars spaced 20 μm apart from each other (the gap was equal to the post diameter). The ROI contained a sub-array of 2 x 3 pillars in the central section of the channel (see Figure 6-18a). Prior to the μPIV analysis, the images were pre-processed to ensure robust measurements. The area occupied by the posts was removed, the background light was subtracted, and the contrast and brightness of the images were enhanced to allow the software to easily identify single particles. Finally, the ROI was divided into six identical windows or unit cells, each containing a single post in the centre, which were then analysed independently. From each sequence of images, six different velocity fields such as that shown in Figure 6-18b were obtained.

6.4.3.2 Results and discussion

Figure 6-19 shows measurements of the mean fluid velocity in the unit cell, averaged between the six different unit cells analysed on each sequence of images, as a function of the applied electric field frequency for three different electrolyte conductivities (1.75 mS/m, 5.01 mS/m and 11.23 mS/m). The error bars correspond to the standard deviation between the measurements on the six different unit cells. This plot shows a decay of the magnitude of the rectified EO flows with the frequency of the electric field approximately as $f^{-0.5}$; the slopes of the curves were -0.45, -0.51 and -0.55 for electrolyte conductivities of 1.75 mS/m, 5.01 mS/m and 11.23 mS/m respectively.

Classical Electroosmosis predicts an oscillating slip velocity with zero-time average for AC electric fields. However, as explained in section 3.3 of Chapter 3 there are other mechanisms that can give rise to a net AC electroosmotic flow. In Induce-Charge EO, for example, the net EO flow arises from the interaction of the electric field with the charges the same field induces at the interface between the dielectric liquid and a conducting surface. Non-zero time average EO flows around dielectric surfaces, similar to the stationary quadrupolar EO rolls described in this section, have been recently attributed to ICEO mechanisms[219,259–261].

Nevertheless, ICEO cannot explain the experimental results in Figure 6-19. First, ICEO predicts a decay of the rectified flow around the relaxation frequency of the electrolyte $f_{\mathrm{ICEO}} = \sigma/2\pi\varepsilon$, which have typical values around $\sim 10^6$ Hz[261,262]. In these experiments, instead, the relaxation frequency was found to be much lower (< 1 kHz). Furthermore, the dependence of the rectified EO with the frequency of the electric field, which was empirically found to be close to $f^{-0.5}$, does not agree with the predictions of the ICEO theory[261,262].

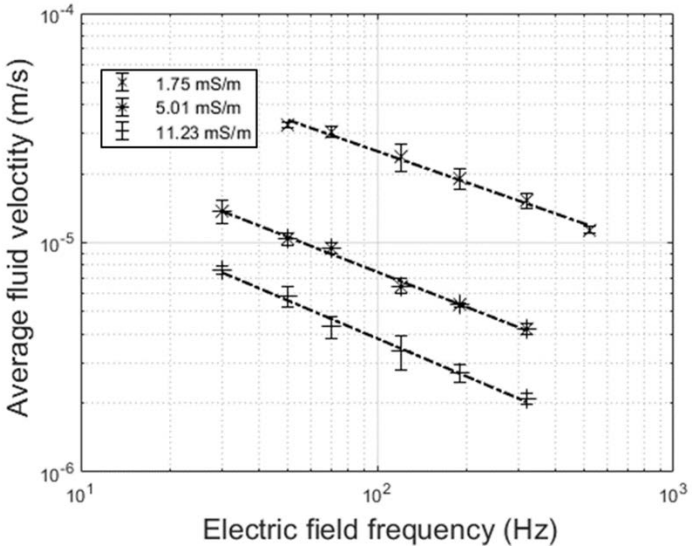

Figure 6-19. Experimentally measured mean fluid flow velocity of the quadrupolar EO rolls around insulating 20 µm diameter pillars as a function of the frequency of the AC electric field for three different electrolyte conductivities and a constant peak-to-peak voltage of 1600 V.

Although the physical mechanism underlying the stationary quadrupolar EO flows around the dielectric pillars is not yet understood, they exhibit a similar dependence of with the AC electric field frequency and the electrolyte conductivity. To explore the role they could have in the low frequency deviation, these flows can be included "ad hoc" in the numerical simulations. Assuming they have the same patterns as classical ICEO flows, a slip velocity is added at the post surface which, in polar coordinates with origin at the centre of the post, depends on angle φ, as defined in Figure 6-20a, as $v_{rolls}(\varphi) = U_{max} \sin(2\varphi)$, with U_{max} the maximum value of the slip velocity. The resulting flow profile is shown in Figure 6-20a, for a value of U_{max} equal to 200 µm/s. The white lines represent the quadrupolar flows streamlines around the insulating posts and the black arrows indicate the direction of the flow.

The effect of these flows on the low frequency particle trajectories can then be calculated by adding an extra component to the particle velocity:

$$\boldsymbol{v}_p = \boldsymbol{v}_f + \boldsymbol{v}_{\mathrm{DEP}} + \boldsymbol{v}_{\mathrm{EP}} + \boldsymbol{v}_{\mathrm{rolls}} \tag{6.32}$$

Figure 6-20b shows an example of the particle trajectories under the action of a low frequency EP oscillation but also affected by the existence of the quadrupolar rolls with U_{max} equal to 200 µm/s. As shown in the figure, including the EK rolls does not result in an induced bumping mode and the particles zig-zag around the posts. The value of 200 µm/s for U_{max} was chosen as a realistic value taken from the maximum fluid flow velocities observed experimentally in the EK quadrupolar rolls. For values of U_{max} below 200 µm/s, the effect is even less pronounced, so the trajectories are more alike those obtained when only a low frequency EP acts on the particles. For values beyond 200 µm/s, an induced displacement of the particles is still not observed and the increase of the strength of the rolls eventually leads to the particles getting trapped in the fluid vortices. A wide range of parameters was studied (electric field magnitude, frequency and U_{max}) and a low frequency induced lateral displacement was never observed. The inclusion of DEP into these simulations did not result in a significant modification of the particle trajectories and did not force them to switch to the bumping mode.

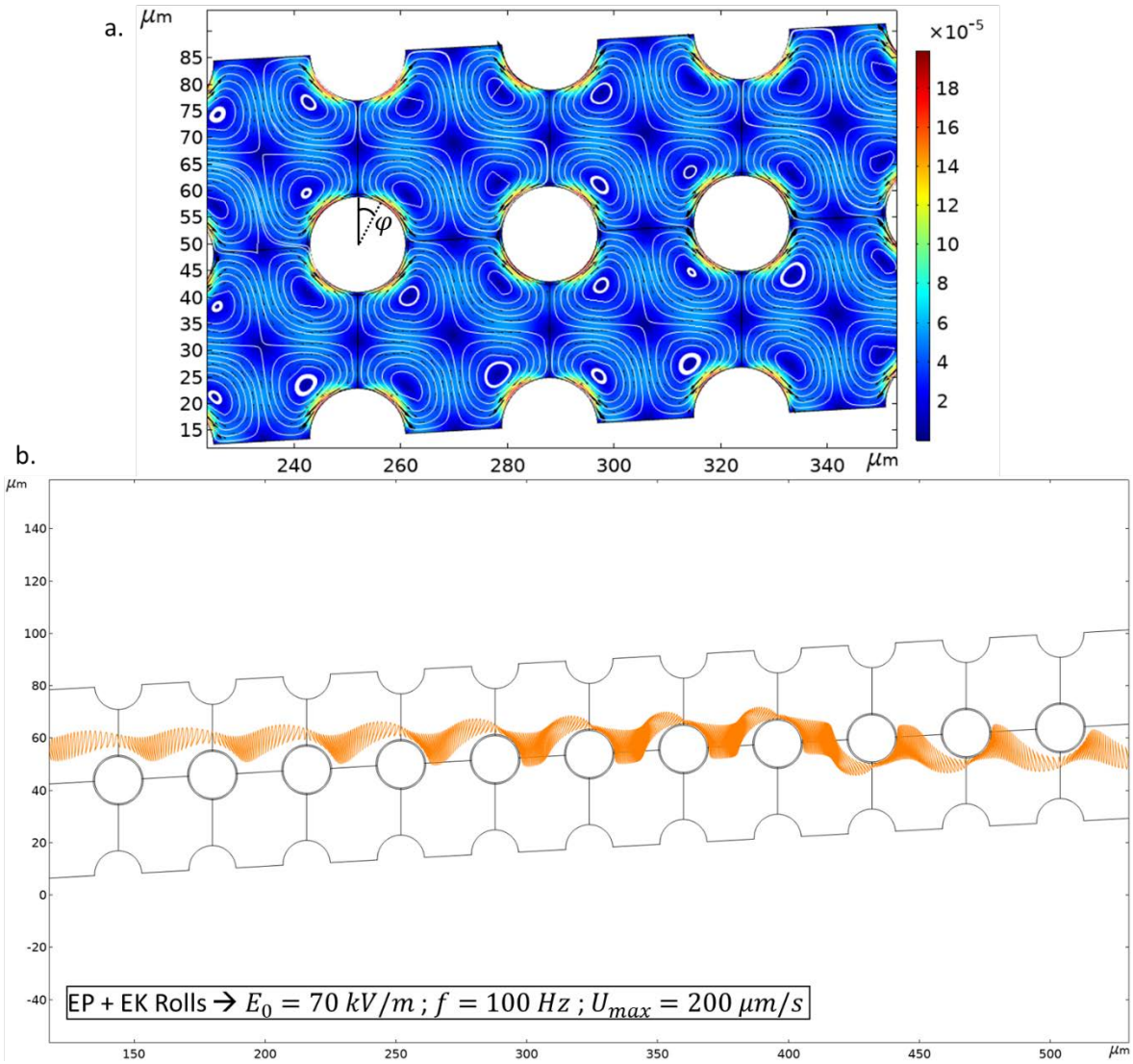

Figure 6-20. (a) Quadrupolar flow profile around the DLD pillars included "ad hoc" to the low frequency simulations as $v_{rolls}(\varphi) = U_{max} \sin(2\varphi)$ – with origin at the centre of each pillar and for $U_{max} = 200\ \mu m/s$. The white lines represent the flow streamlines, the black arrows indicate the direction and the colour map the fluid velocity magnitude. (b) Effect of the quadrupolar EK vortices on the trajectories of the particles, which also undergo a low frequency electrophoretic oscillation along the electric field lines.

The existence of these rolls around the DLD pillars would not satisfactorily explain the size dependence of the low frequency deflection. A valid hypothesis for the size dependence would be that these flows also occur around the surface of the particles as they flow through the DLD channels when a low frequency field is applied, and lead to an additional repulsion from the DLD pillars due to a hydrodynamic interaction, forcing the particles to switch to displacement mode.

6.5 Conclusions

In the previous chapter, a novel technique that combines DLD with electrokinetics to achieve tunable particle separation using AC electric fields applied orthogonal to the fluid flow was described. The experimental characterisation with respect to the electric field frequency showed two distinct regimes, one at high frequencies and another at low frequencies, with a transition around 1 kHz. In this chapter further experimental characterisation as a function of different parameters (flow rate, field magnitude, medium conductivity, particle size, …) is presented. This served to identify scaling laws governing the induced deflection of both separation mechanisms (at low and high frequencies).

For the high frequencies a theoretical framework was established that postulate nDEP as the force responsible for the induced deviation. This theory matches qualitatively well with the scaling laws derived from the experimental results. To perform a quantitative comparison, a numerical model was developed which provided excellent agreement between the experimental results and the predictions from the simulations. These findings provide strong support to the hypothesis that nDEP causes the deviation observed at high frequencies and demonstrate that the developed numerical method is a powerful tool for the design of new separation devices for specialised purposes.

At low frequencies the scaling laws of the induced deflection were also characterised. Interestingly, the scaling laws for low frequencies are very similar to the nDEP induced deviation, although two key facts lead to the exclusion of DEP as the governing force causing the deflection. First, the field magnitude threshold at which particles are forced to switch from the zig-zag to bumping mode are significantly lower at low frequencies. Secondly and more important, deflection was found for both particles experiencing nDEP and pDEP, forces that point in opposition directions.

Even though the scaling laws have been experimentally identified, the underlying mechanism causing the deviation is still unclear. The results in this chapter show that the EP oscillation and the EDL polarisation are not crucial, and that the deviation does not depend directly on the oscillation amplitude. Numerical simulations did not provide any further comprehension on the mechanism behind the induced deflection at low frequencies indicating that new physics not included in the numerical model is missing.

Rectified Electroosmotic quadrupolar flows were observed and characterised in the vicinity of the insulating PDMS pillars when low frequency fields were applied. These rolls had a very similar pattern to classical ICEO flows around conducting pillars and show a similar trend to the low frequency induced deviation, where the strength decreased with conductivity and field frequency.

However, they cannot account for the size dependence of the low frequency deviation mechanism and numerical simulations showed that they neither can explain the low frequency behaviour.

Future work will focus on a deeper exploration of the particle behaviour at low frequencies, and near insulating structures. This should focus on the possibility of similar non-zero time average AC Electroosmosis at the surface of the particles which could repel the particles away from the DLD posts leading to particle deviation. Future research should also include investigations on the origin of the rectified EO flows at the surface of dielectrics which would bring a deeper understanding on the non-linear electrokinetic phenomena. In addition, a valid theoretical model will enable these flows to be successfully used for real applications such as pumping or mixing, same as ICEO but eliminating the need for the fabrication of conducting microstructures.

Chapter 7 Combining DC and AC electric fields with DLD for micro- and nano-particle separation

7.1 Introduction

Previous chapters described how DLD devices can be combined with AC electric fields to achieve tunable particle separation by exerting EK forces on the particles to modify their paths through the microfluidic channels. Many EK separation techniques use DC fields to sort particles according to their electrical response (see section 3.4 Electrokinetics for particle separation). DC fields can be used independently or in combination with AC signals to further improve DLD particle sorting, achieving a greater degree of tunability, expanding the range of properties that can be exploited for separation and reducing the minimum size of the particles that can be targeted by the technique.

Nowadays there is a huge interest in techniques for isolation and separation of nanoparticles such as extracellular vesicles (EVs) or exosomes. However, the separation of such small particles poses an important challenge. Due to their very small size, nanoparticles require either very strong forces or weaker forces applied for longer times to ensure efficient extraction from the rest of the sample – in other words, they require a huge amount of energy to be manipulated. Thus, to achieve nanoparticle separation by DLD, narrow microfluidic channels are necessary to achieve a small enough critical diameter. This leads to an increased hydrodynamic resistance and therefore reduced sample throughput[92]. This limitation can be compensated by device parallelisation, running several DLD devices at the same time, but this brings serious complications in terms of device design, fabrication and operation[12].

The motion of nanoparticles is also largely affected by Brownian motion (which leads to diffusion), producing unpredictable trajectories and the widening of particle streams. The result is an important obstacle on the separation efficiency and resolution.

One advantage of using DC electric fields is that the EK forces exerted on the particles are several orders of magnitude stronger than those arising when AC fields are used. EP and EO are first order forces which originate from the interaction of the electric field with charges at the surfaces of particles and walls, in opposition to DEP which depends on the gradients of the electric field. This implies that the field magnitude (and thus the applied voltage) needed to induce deflection using a DC field inside the DLD devices is significantly lower. In addition, DC fields enable much smaller particles to be targeted, where stronger forces are required to deflect them. This chapter describes

how a combination of classical DLD or AC-tuned DLD with orthogonal DC electric fields achieves successful charge-based separation and sorting/fractionation of nanoparticles (smaller than 1 μm) whilst, at the same time, reversing the effects of diffusion. This latter effect is caused through the generation of conductivity gradients near the electrodes that create gradients in the electric field, depending on the distance from the electrodes.

7.2 Experimental methods

The DLD devices used for the experiments in this chapter were devices #1 from DLD Design A, with $D_c = 6.3\ \mu\text{m}$ and $D_c = 5.0\ \mu\text{m}$ (see section 4.1 Device design). In all experiments a negative DC voltage was applied to the electrode closer to the sample inlet (bottom electrode or electrode A in Figure 7-1a) whilst the other electrode was grounded (top electrode or electrode B in Figure 7-1a).

As explained in the previous chapter, the fluid flow velocity is an important parameter that plays a role in the induced deflection. This chapter does not include a characterisation of the DC induced deflection as a function of the flow rate but focuses only on the DC electrokinetic behaviour inside DLD devices. Nevertheless, the role of the fluid velocity is expected to be very similar to the situation for AC electric fields, i.e. the induced deflection reduces with increasing flow rates.

The following particles of different sizes and different zeta potentials were used in the experiments: 100 nm, 200 nm, 500 nm, 1 μm and 3 μm fluorescent carboxylate microspheres from Fluoresbrite and 3 μm plain polystyrene microspheres from Sigma-Aldrich. The values of the zeta potential are given in Table 4-4 (Chapter 4). The particles were suspended in dilute KCl of two different conductivities: 6.6 mS/m and 12.8 mS/m.

Quantification of the lateral displacement was done slightly differently to previous chapters. The experiments did not focus on the characterisation of induced deflection (as in Chapter 5 and Chapter 6) but on the separation and fractionation of particle populations. Hence, the experiments were performed using several different particle types at the same time so that the separation between distinct populations could be observed. The fact that different particle streams were present, restricted analysis of the data as previously, and the lateral displacement was thus estimated manually. The particle populations were different enough to be distinguished by the human eye with help from video processing software. As a result, the data in this chapter is presented in terms of lateral displacement, with the data points corresponding to the mean lateral displacement and vertical bars on each point representing the particle stream width. Furthermore, the particle trajectories did not follow the traditional DLD paths of zig-zag or displacement mode so that quantifying the deflection in terms of a deviation angle was difficult. Therefore, the

behaviour was determined via the quantification of the net lateral displacement throughout the DLD channel with respect to the mean entry lateral position, which was more consistent.

7.3 Results and discussion

7.3.1 Size-based tunable separation combining DC and AC electric fields

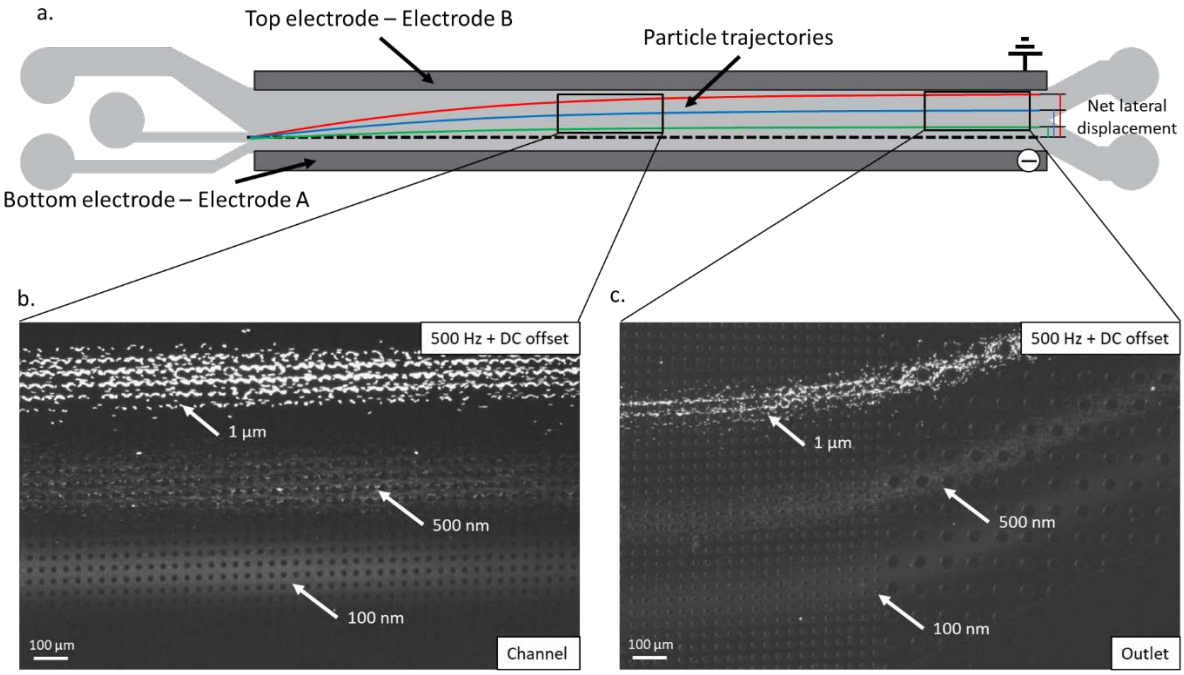

Figure 7-1. (a) Diagram of DC driven deflection in DLD devices. (b) Image of fractionation of a mixture of 1 µm, 500 nm and 100 nm fluorescent negatively charged (carboxylate) particles in a 12.8 mS/m suspending medium inside a 6.3 µm D_c DLD device using an AC electric field of 500 Hz and 320 Vpp with a DC offset of -0.25 V applied to the bottom electrode (or electrode A) - The particles move upwards and create different bands corresponding to different particle populations which flow almost parallel to the microchannel and electrodes. (c) The particle bands maintain a constant lateral separation all the way to the channel outlet. The average particle velocity was approximately 50 µm/s.

Figure 7-1 shows how a DC electric field applied orthogonal to the fluid flow can lead to a successful fractionation of particles in the range of nanometres inside a DLD. This figure shows the separation of 1 µm, 500 nm and 100 nm particles within a 6.3 µm D_c DLD, created through the combined action of an AC voltage of 500 Hz and 320 Vpp combined with a DC potential of -0.25 V. The pressure drop at the microchannel created a flow rate of approximately 50 µm/s. The particles enter together in the DLD channel via the sample inlet and displace laterally with respect to the entry position due to the action of the orthogonal electric field. If a DC voltage is applied, the particles stop deflecting

when they achieve a maximum lateral displacement that depends on the particle size and charge and then start to flow in an almost straight line parallel to the electrodes (Figure 7-1b). As a result, the different components in the sample are separated into different streams, and this separation maintained until they reach the outlet (Figure 7-1c). Note that the curved trajectories in Figure 7-1c are caused by an artifact due to the geometry of the outlet channels – the two outlets channels placed at the end of the devices are tilted at an angle which distorts the flow profile corresponding to an straight DLD microchannel.

The results shown in Figure 7-1 also indicate that the effect electrode polarisation on the DC signals can be neglected since the particle trajectories are significantly altered for DC offsets as low as -0.25 V. Therefore, the voltage drop in the EDL at the electrodes must lower than -0.25 V so that the voltage drop across the channel is substantial to lead to an observable response on the particle motion.

Three main advantages of combining a DC electric field with classic DLD or AC tuned DLD can be inferred from the results in Figure 7-1. The addition of a tiny DC voltage serves to tune the induced AC binary separation and turns the system into an effective particle fractionation platform. As shown in the previous chapters, the action of an AC field is only able to force particles smaller than the D_c to switch from the zig-zag mode to the bumping mode, i.e. it only allows two possible trajectories thus separating the sample into maximum two different populations. However, the DC component establishes a maximum induced lateral displacement that depends on the particle characteristics, which enables fractionation of the sample into several streams, each corresponding to a specific particle type.

Another important advantage is that a DC field enables manipulation of much smaller particles. The fact that the DC electrophoretic force does not vary with the particle size, translates into a significant induced deflection of particles even in the range of nanometres. Previous chapters showed that particles of 500 nm and below did not deviate under the action of an AC electric field. However, Figure 7-1 shows a significant deflection of 500 nm and 100 nm particles. Furthermore, as particles deviate, they were observed to focus into tight streams that were even narrower than the sample inlet channel. In other words, the DC field creates conditions where the particles overcome diffusion, which is an important obstacle to nanoparticle sorting.

To explore the physical mechanisms by which the combined action of a DC and AC electric field lead to the behaviour described above, separation of 3 µm, 1 µm and 500 nm carboxylate particles inside a 5.0 µm D_c DLD was investigated for different experimental conditions. The data is summarised in Figure 7-2. The particle size was increased and the DLD array dimensions were reduced to improve the experiments and enable a faster flow rate to be used.

Figure 7-2a depicts the effects of applying a DC electric field only. The data shows similar behaviour for the three types of particles; all of them are deflected and the lateral displacement increases with the voltage. The similarity in the behaviour is expected since the only force acting on the particles is electrophoresis and they are all made of the same material and suspended in the same electrolyte, i.e. they bear a very similar zeta potential (see Table 4-4).

However, successful separation of the 3 µm particle particles from the rest (1 µm and 500 nm) is achieved at voltages between -0.5 V and -1 V but no significant separation of the 1 µm and 500 nm particles is observed. This result cannot be attributed solely to the difference in the zeta potentials since the difference between ζ of the 3 µm (-78 ± 6 mV) and the 1 µm particles (-71 ± 4 mV) is very close to the difference between the ζ of the latter and the ζ of the 500 nm particles (-63 ± 3 mV). This implies that the particle size influences the net DC induced lateral displacement, probably due to the presence of the DLD posts. The fact that the particle streams of the 1 µm and the 500 nm particles overlap for any applied voltage suggests that the DLD array has a similar effect on both types of particles and that the effect is more important the closer the particle size is to the critical diameter.

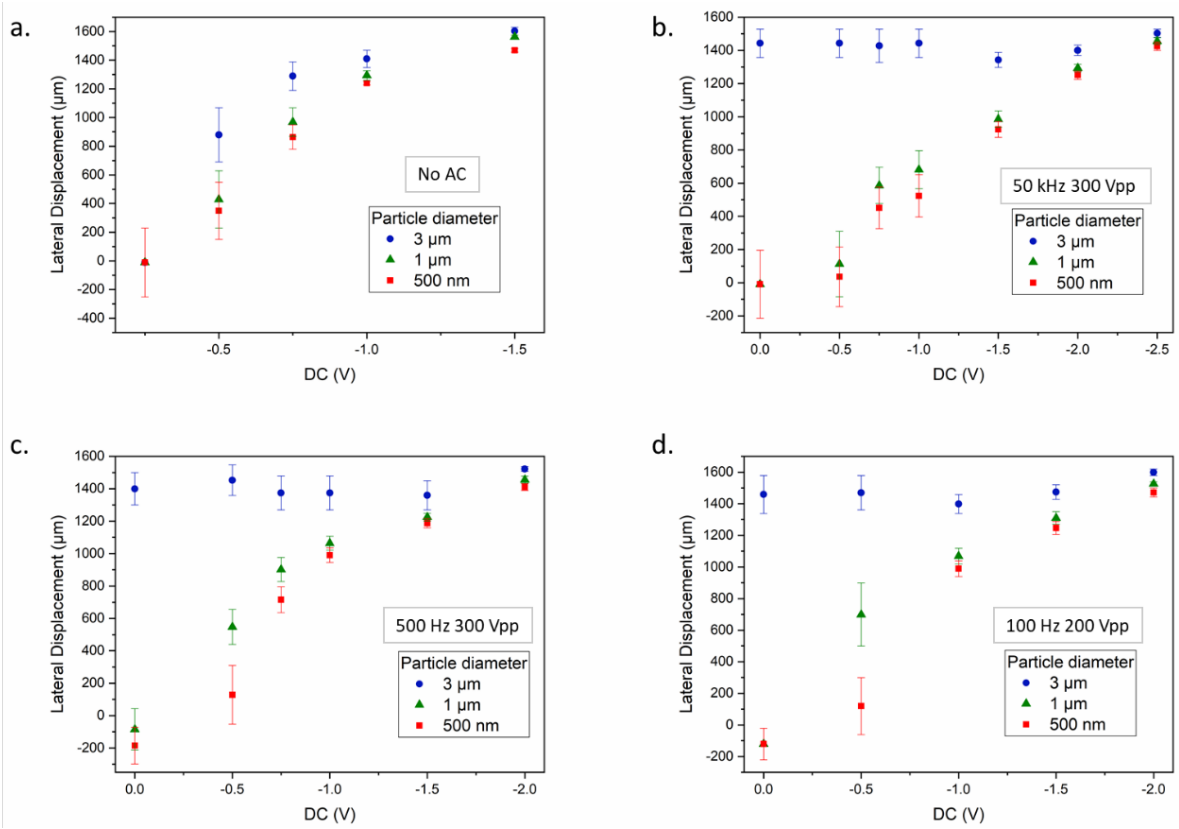

Figure 7-2. DC tuned DLD and AC biased DLD separation of 3 µm, 1 µm and 500 nm carboxylate particles inside a 5.0 µm D_c DLD as a function of the applied DC voltage. The data is represented in terms of the induced lateral displacement at the measured outlet; the data points correspond to the mean lateral displacement while the vertical

bars represent the particle stream width. The fluid flow velocity was approximately 120 µm/s while the suspending medium had an electrical conductivity of 6.6 mS/m. (a) DC signal only applied. (b) DC in combination with an AC signal of 50 kHz and 300 Vpp. (c) DC in combination with an AC signal of 500 Hz and 300 Vpp. (d) DC in combination with an AC signal of 100 Hz and 200 Vpp.

For more negative DC voltages beyond -1 V, the net lateral displacement is almost independent of the particle size and the aforementioned separation becomes marginal, i.e. all three particle streams overlap. This matches perfectly with the electrophoretic behaviour – all particles have a high enough electrophoretic velocity for the size influence to be minimal and all three achieve approximately the same lateral displacement.

However, the experimental data shows that the induced deflection does not scale linearly with the applied DC voltage as predicted from the Helmholtz-Smoluchowski equation for the EP force. At a constant flow rate, a uniform and orthogonal DC electric field is expected to induce a lateral displacement caused by EP that is proportional to the applied voltage. Nevertheless, the plot in Figure 7-2a reveal a different trend. The deflection increases approximately linearly for small applied DC voltages and this translates into lateral displacements smaller than 1000 µm. But this linearity is lost for larger displacements where the induced Electrophoretic deflection exhibits a sublinear increase with the electric field magnitude. As the particles approach the top electrode (electrode B) the electrophoretic velocity reduced, resulting in a decrease in the net lateral displacement. This dependence on the proximity to the electrode can be attributed to a non-uniform electric field which creates a non-uniform EP velocity along the channel section.

Figure 7-2b, Figure 7-2c and Figure 7-2d illustrate how the AC biased DLD separation can be improved when combined with an orthogonal DC electric field; these figures summarise the experimental data for the lateral displacement as a function of the applied DC voltage applied on top of alternating fields of different frequencies.

Figure 7-2b shows that, in the absence of a DC, the high frequency AC electric field is only capable of deflecting the biggest particles (3 µm) that experience a strong enough nDEP force to overcome the fluid drag and bump on the posts (as explained in previous chapters). The paths followed by the 1 µm and 500 nm particles remained unchanged until a DC voltage was applied. The non-uniform electrophoretic velocity gave rise to a lateral displacement of the smallest particles but no substantial separation was observed between the two populations at any applied DC voltage, as in the case where only a DC was applied (Figure 7-2a).

The DC tuned separation improves significantly when coupled with a low frequency AC electric field. Figure 7-2c and Figure 7-2d demonstrate how a DC field is coupled with the low frequency (<1 kHz) deviation mechanism (described in the previous chapters) to achieve successful particle fractionation within the DLD devices, separating not only the 3 µm from the smaller particles but also sorting the 1 µm and 500 nm particles from each other. The optimal DC voltage that led to the biggest separation between the three different populations was found to be -0.5 V in both cases; for an AC signal of 500 Hz and 300 Vpp and for an AC signal of 100 Hz and 200 Vpp. Under such conditions, the DC was strong enough to help the low frequency mechanism displace the 1 µm particles but not sufficient to cause a notable deflection of the 500 nm nanospheres; the low frequency deviation strongly depends on the particle size as demonstrated in Chapter 6. For more negative applied DC voltages, the lateral displacement becomes almost independent of the underlying AC electric field and the behaviour resembles the case where there is no AC field (Figure 7-2a), i.e. for DC voltages that are too high, the effects of applying an AC electric field become negligible and the induced lateral displacement solely depends on the DC behaviour.

The results shown in Figure 7-2 demonstrate another important effect where the particles are focused into tight streams, as shown Figure 7-1, apparently overcoming diffusion. The particle stream width is represented in the plots as vertical bars on each data point. This corresponds to the stream width when they reach the DLD outlet. These bars show that as the negative DC voltage magnitude increases, the negatively charged particles focus into tighter and tighter streams that flow closer and closer to the top (grounded) electrode (electrode B), which is assumed to be due to a non-uniform electrophoretic velocity along the channel section that reduces as the particles approach the electrode.

7.3.2 DC induced nanoparticle focusing and deflection

Further experiments using 200 nm carboxylate particles were conducted to explore the effects of applying a DC electric field on the particle behaviour in the DLD. For consistency, the same pressure was applied to the microfluidic channels, delivering a flow rate of around 120 µm/s and a particle stream width very close to the sample inlet width (300 µm) as shown in Figure 7-3a. The suspending medium conductivity was reduced to 1.4 mS/m to enable higher voltages to be applied.

In the absence of any external force, such small particles flow almost unperturbed by the presence of the DLD post array in straight trajectories from the inlet to the outlet, zigzagging around the posts and experiencing a widening of the stream due to diffusion. According to the Stokes-Einstein equation (see section 2.1.3 Diffusion) this is around 80 µm.

Figure 7-3 depicts the effects of applying a DC electric field to the particles flowing within the DLD channel. Figure 7-3a shows the stream of 200 nm spheres immediately after they have entered the channel while Figure 7-3b shows the same particles when they arrive at the channel outlet after being deflected and focused by a DC electric field created by applying -3 V to the bottom electrode (electrode A). A comparison between both pictures clearly exemplifies the influence of the DC voltage on particle behaviour. The negative DC applied to the bottom electrode (electrode A) creates an electric field from the top part of the channels to the bottom; from electrode B to electrode A. Thus, the negatively charged 200 nm particles are pushed towards the top part of the device (towards electrode B) and are, therefore, displaced laterally by an amount dependent on the applied DC voltage. At the same time, the particle stream reaches the channel outlet with a substantially reduced width, although a widening of the stream would be expected due to the impact of diffusion. Figure 7-3c illustrates qualitatively the particle trajectories observed experimentally. As soon as the particles are affected by the electric field, they start deflecting, approaching electrode B, with an electrophoretic velocity v_{EP} that depends on the proximity to the grounded electrode. v_{EP} reduces as the particles displace laterally, forcing them to agglomerate in a tight band that flows almost parallel to the electrode. These trajectories are different from those expected for a uniform v_{EP} (see Figure 7-3c) and demonstrate that the v_{EP} and, hence the electric field, is not uniform along the channel section.

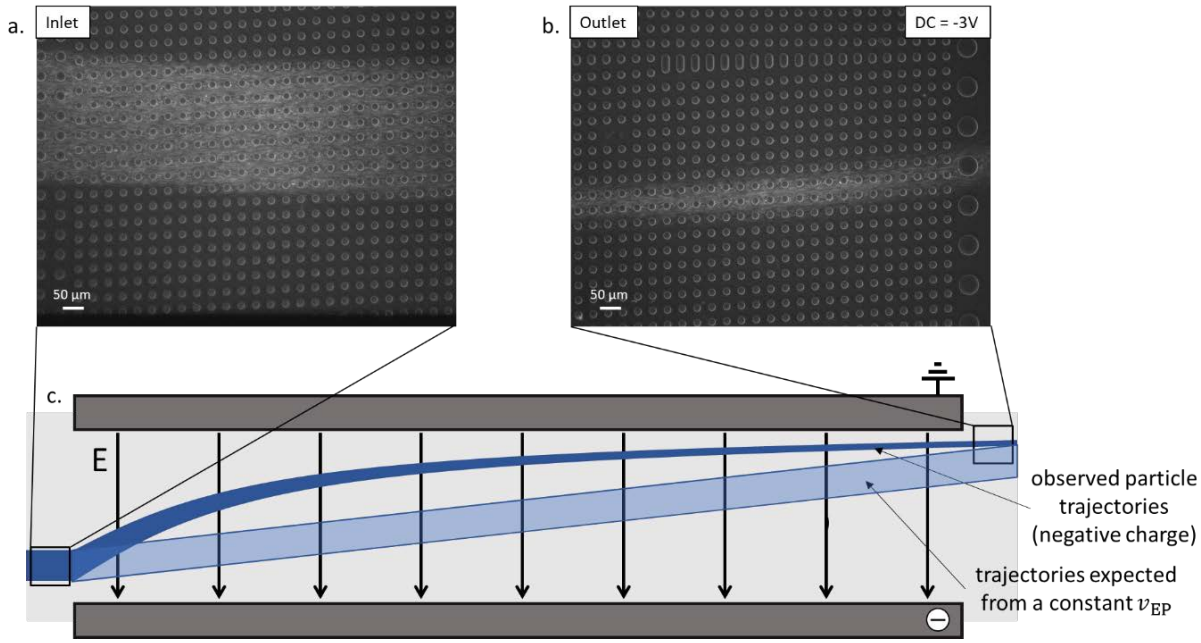

Figure 7-3. Behaviour of 200 nm carboxylate fluorescent nanospheres inside a DLD device. Particles are suspended in a 1.4 mS/m KCl solution and move in the presence of an orthogonal DC electric field. (a) At the channel inlet, the particle stream width is very similar to the width of the sample inlet channel, 300 µm. (b) At the outlet, after being displaced laterally closer to electrode B (top of the image) by the DC electric field

(-3 V DC voltage applied to electrode A, bottom of the image), they are focused into a much narrower particle stream. (c) Diagram showing the average trajectories of negatively charged particles inside a DLD under the action of a DC electric field applied from top to bottom. The diagram compares the trajectories observed in the experiments with the trajectories expected from a uniform electrophoretic velocity.

Figure 7-4 describe quantitatively the dependence of the DC induced lateral displacement and particle focusing as a function of the applied voltage. Figure 7-4a shows that the overall lateral displacement increases as the voltage increases but not linearly as expected from the linear dependence of the v_{EP} with the electric field magnitude given by the Helmholtz-Smoluchowski equation. Instead, it shows a sublinear increase in accordance with measurements for larger particles given in Figure 7-2. Figure 7-4b, as well as the vertical bars in Figure 7-4a, provide measurements of the particle stream width at the outlet and shows how it is significantly reduced for all applied negative voltages beyond -0.25 V. This is probably because for such negative voltages the particles are displaced close enough to the electrodes so that they reach regions of low electric field and thus low v_{EP}, leading to the formation of the narrow bands.

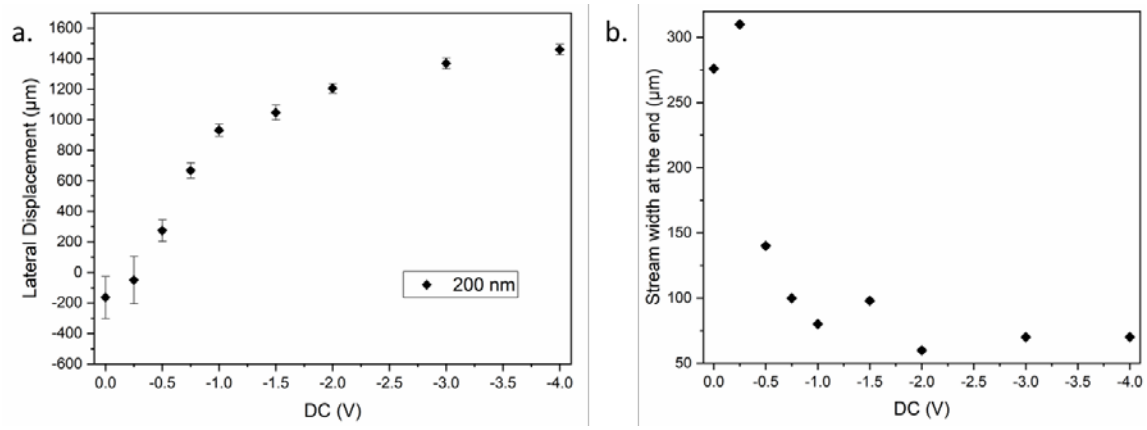

Figure 7-4. (a) DC induced lateral displacement of 200 nm carboxylate particles inside the DLD device as a function of the DC voltage. (b) Reduction in the particle stream width measured at the channel outlet as a function of the DC voltage.

7.3.3 Zeta potential based separation

The addition of a DC component to the electric field not only improved the size-based separation, but also allowed zeta-potential based separation. Experiments with two types of particles of the same size (3 µm diameter) but different zeta potentials were performed. The carboxylate particles had a zeta potential of $\zeta_{carb} = -78 \pm 6\ \mathrm{mV}$ while the plain polystyrene particles had a much lower zeta potential $\zeta_{plain} = -15 \pm 3\ \mathrm{mV}$. According to the classical theory of EP, this should lead to a much stronger electrophoretic force on the carboxylate particles, which in turn translates into a

much larger lateral displacement inside the DLD device. The results of the experiments are summarised in Figure 7-5 and Figure 7-6.

As expected, experiments showed that when only an AC electric field was applied, both populations had the same behaviour and deflection was induced under the same conditions, at high as well as at low frequencies. Therefore, separation was not achieved. This result is not surprising for the high frequency regime since both types of particles were expected to experience nDEP, with a minimum value of the CM factor, with the magnitude of this force independent of the particle surface charge. More unexpected was the fact that no separation was observed when a low frequency AC electric field was applied. This suggests that the role of EP is even less relevant than expected and demonstrates again that the low frequency induced deviation mechanism is independent of the electrophoretic oscillation amplitude (as explained in Chapter 6).

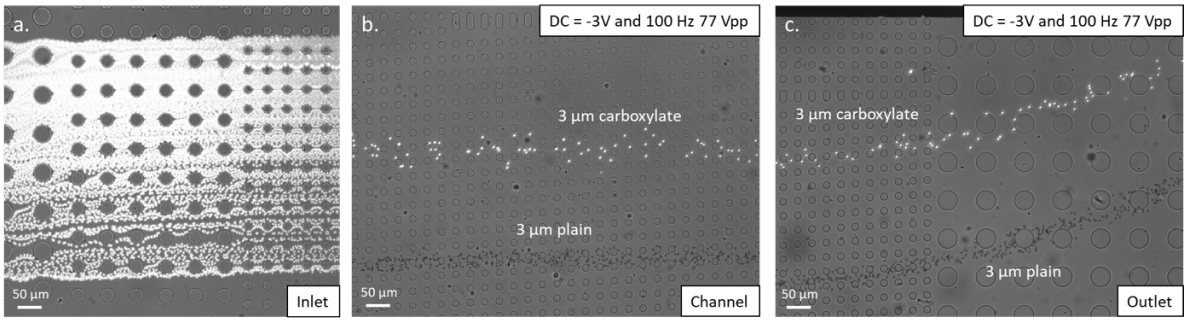

Figure 7-5. Zeta-potential based separation of 3 µm diameter fluorescent carboxylate (white particles in the figure) and 3 µm diameter plain (not fluorescent – dark particles in the figure) microspheres suspended in a 6.6 mS/m KCl solution in a 5.0 µm D_c DLD with a DC (-3 V applied to electrode A) and AC electric field (100 Hz and 77 Vpp). (a) The mixture of particles enters the channel in a stream with a similar width to the sample inlet channel. (b) The particles are deflected by the electric field and separate into distinct and narrower streams. (c) Particles of the same size reach the outlet but separated depending on their zeta-potential. Those with a more negative zeta potential, the carboxylate particles, experience a greater electrically-induced lateral displacement.

When a DC electric field was applied the behaviour changed completely. Figure 7-5 illustrates the particle behaviour and induced deflection under the action of a DC voltage (-3V applied to electrode A) combined with a low frequency electric field of 100 Hz and 77 Vpp. This figure shows three different pictures taken along the DLD channel. Figure 7-5a shows the particles entering the device with a stream width that is very similar to the sample inlet channel. As the particles flow through the device, they are deflected by the electric field and separate into two different particle streams corresponding to each of the particle types. The carboxylate particles are subjected to a stronger

electrophoretic force, which translates into a faster electrophoretic velocity and hence into a greater lateral displacement (see Figure 7-5b). The distance between both populations is maintained until the particles reach the outlet, resulting in successful charge based particle separation (see Figure 7-5c). In this case, the particles were also concentrated in bands which were narrower than the width at which they entered the channel.

To characterise the zeta-potential based separation, the induced lateral displacement and the stream narrowing were measured as a function of the DC applied voltage, always negative and applied to the bottom electrode (electrode A). This was done for only DC or in combination with AC electric fields of high and low frequencies. The data is presented in Figure 7-6. For a DC electric field (see Figure 7-6a), the separation between the charged and the uncharged particles is clear only at the highest applied voltages (beyond -2 V). At lower field magnitudes, the carboxylate particles experience a larger deflection but there is an overlap between both populations.

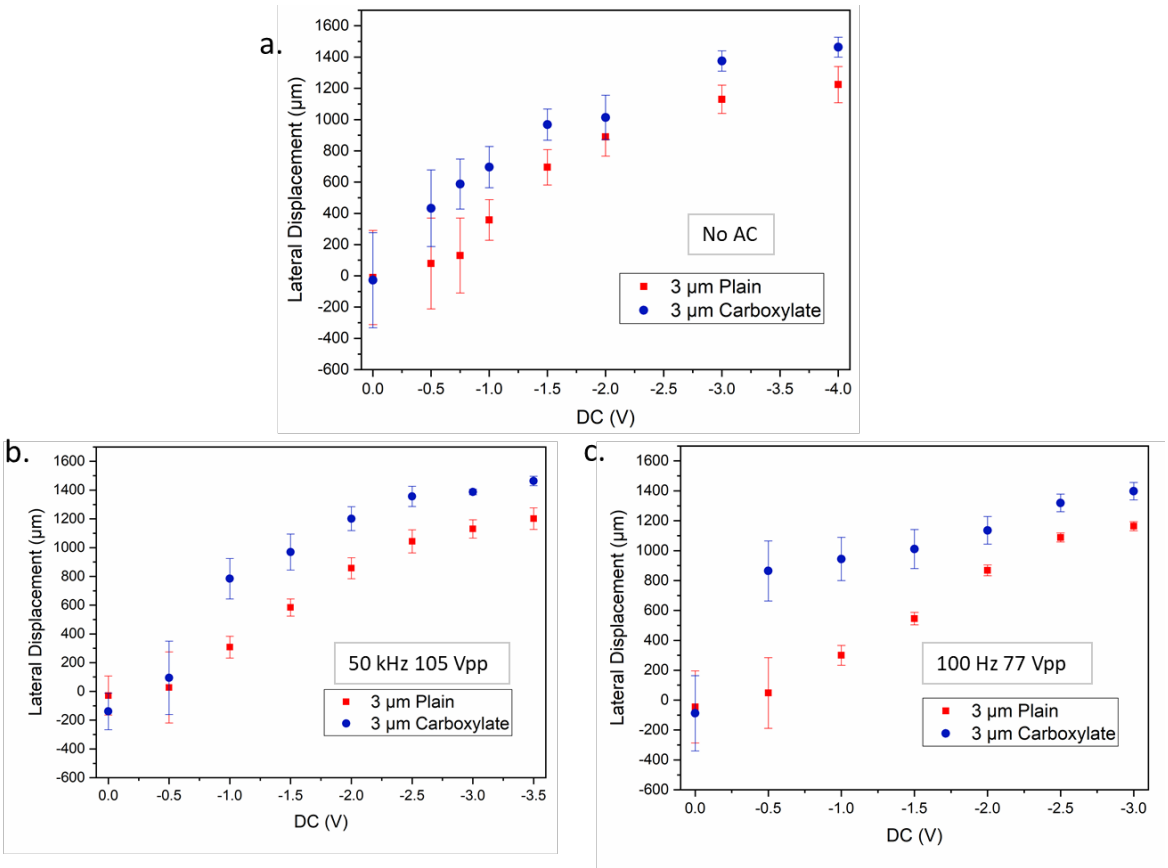

Figure 7-6. DC assisted sorting of particles of the same size, 3 µm diameter, but with different zeta-potentials: carboxylate ($\zeta_{carb} = -78 \pm 6$ mV) versus plain ($\zeta_{plain} = -15 \pm 3$ mV) in a 5.0 µm D_c DLD device with a suspending medium conductivity of 6.6 mS/m as function of the DC voltage applied to electrode A. The vertical bars represent the width of the particle stream. (a) Negative DC only. (b) DC and a high frequency AC: 50 kHz 105 Vpp. (c) DC and a low frequency AC: 100 kHz 77 Vpp.

With the addition of an AC electric field, separation is significantly improved and a clear distinction is achieved for voltages beyond -1 V for a high frequency AC (50 kHz – Figure 7-6b), and for -0.5 V for a low frequency AC (100 Hz – Figure 7-6c). At high frequencies the same DEP is expected for both particle types, however the stronger EP acting on the carboxylate particles results in a larger deflection. The most relevant effect of the low frequency field can be appreciated for the data corresponding to -0.5 V DC. For such low DC fields, no significant deflection and definitely no clear separation was achieved with either only DC or DC in combination with a high frequency AC was applied. Yet, when combined with a 100 Hz AC, the biggest separation was observed. For more negative voltages, the deflection of the plain PS particles grows while that of the carboxylate particles does not increase very much because they concentrate in the region near the electrodes where a much lower electric field magnitude occurs.

Note that in both cases the magnitude of the AC electric field is very low so that it is not capable of deviating the particles without the assistance of the DC field (see the data points for the 0 V DC). In addition, these plots show same the nonlinear dependence of the DC induced deviation and the reduction of the particle stream widths as the lateral displacement increases, as discussed in the previous sections.

7.3.4 Electric field gradients and particle banding

To further investigate the role of the DC in the separation technique described in this chapter, experiments in the absence of a pressure driven flow were performed. The pictures in Figure 7-7 illustrate the particle behaviour in the presence of a DC electric field created by applying a negative voltage to electrode A (bottom of the pictures) with electrode B (top of the pictures) grounded. Under these conditions, given the electrode geometry (coplanar parallel electrodes), a uniform electric field is expected within the microfluidic channels. Therefore, the negatively charged particles were expected to move away from electrode A towards electrode B at a constant speed, as predicted by the Helmholtz-Smoluchowski equation.

Instead, the particles showed an unexpected behaviour. They moved away from the negative electrode but with a velocity that depended on their proximity to the electrodes, i.e. a velocity gradient was established across the channel section: particles in the centre of the channel had a much larger velocity than those close to any of the electrodes. Since the particles slow down as they approach the grounded electrode, they concentrate into narrow bands which form parallel to the electrode; particles move quickly from the channel centre arriving at the leading front of the particle band near the electrode which displace at a much slower speed.

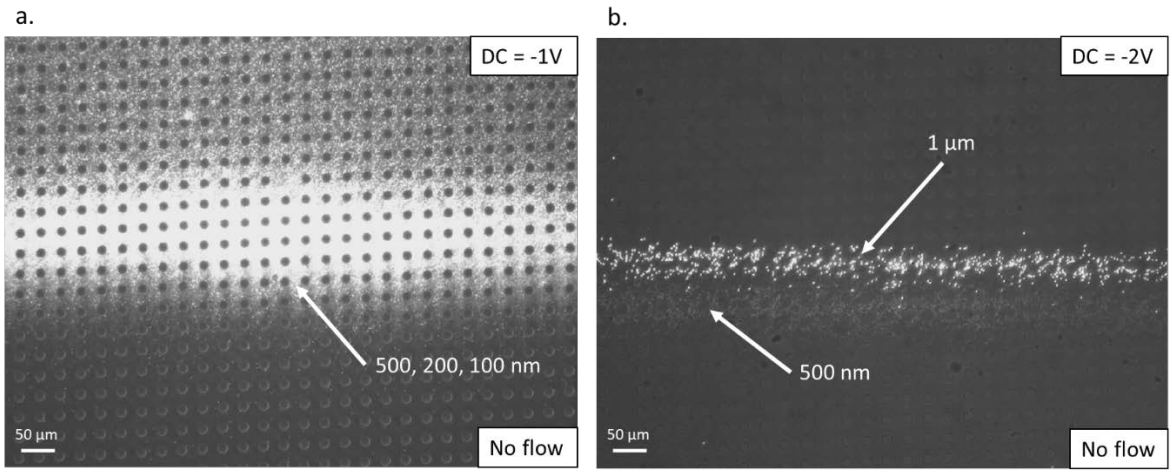

Figure 7-7. Pictures of particles aggregating in bands running parallel to the electrodes upon the application of a DC voltage due to the existence of a non-uniform electric field. The width of the bands depends on the proximity to the electrode. (a) Band formed by the accumulation of 500 nm, 200 nm and 100 nm carboxylate fluorescent particles that were initially spread uniformly over the channel section following the application of a -1 V DC voltage applied to electrode A (towards the bottom of the figure). (b) Two distinct bands for the 1 µm and 500 nm fluorescent carboxylate particles upon the application of -2 V DC signal to electrode A. The particles were initially close to the bottom electrode (bottom of the figure) and were then displaced by different amounts when the field was applied, probably due to their slightly different electrophoretic mobilities.

Figure 7-7a shows the bands created from a mixture of 500 nm, 200 nm and 100 nm particles which accumulate upon the application of -1 V DC signal to electrode A. These particles were initially uniformly distributed all over the channel section. When the field was applied, the particles repel from electrode A and move towards electrode B forming well defined bands parallel to this electrode due to the velocity gradient. Particles near the grounded electrode are almost unperturbed by the field – they sit in a region of very small electrophoretic velocity with no force pushing them away from the electrode. In contrast, even though particles close to the negative electrode also experience a very small electrophoretic force, this grows as they move away (up) from the electrode and in the end they join the particles that were in the middle of the channel centre, concentrating in the band shown in Figure 7-7a.

Figure 7-7b shows a similar pattern emerging from a mixture of 1 µm and 500 nm particles that in this case were initially located close to electrode A. When a -2 V DC was applied to that electrode, all the particles moved away but concentrated into distinct bands corresponding to each particle type, i.e. they experienced a degree of displacement that depended on their size. Such behaviour

may arise from the small differences in the zeta potential of the particles and also from their interaction with the posts as they displace laterally towards the grounded electrode.

The dependence of the electrophoretic velocity on particle position indicates that the DC electric field created inside the channel is not uniform and that an electric field gradient is established. This gradient is created from local changes in the electrolyte conductivity in the region near the electrodes. Similar to the technique reported by Yang *et al.*[263] where the AC electrokinetic behaviour of a microfluidic system is biased using a DC component, the application of a DC voltage gives rise to electrochemical reactions at the electrode surface that release ions into the electrolyte and increase the local electrical conductivity. The regions of increased conductivity are regions of reduced resistivity and thus the voltage drop across those regions is also reduced. As a result, the electric field magnitude, which is proportional to the voltage difference, decreases and so does the electrophoretic velocity that the particles exhibit.

This mechanism is similar to the principles of isotachophoresis[58,241] although, for the above case the conductivity gradients are not created deliberately but result from electrochemical reactions at the electrodes when a voltage is applied. In the presence of a pressure driven flow, the particles enter the channel at a lateral position with a high electric field which translates into a fast-lateral electrophoretic movement. As the particles displace laterally, they reach the region of minimum electric field where they concentrate in tight streams almost parallel to the electrodes. The position of this stream depends on the electrophoretic mobility of the particles and the diffusion of the species generated at the electrodes. The faster the particles move the farther they displace until they reach the front of the diffusing ions.

Even though the electric field magnitude decreases enormously near the grounded electrode (electrode B), it does not disappear and thus the particles keep displacing until they reach the outlet. This behaviour maintains a focused stream, overcoming the effects of diffusion. Particles are not allowed to diffuse towards the negative electrode (electrode A) due to the fast EP velocity that pushes them back into the band. At the same time, when particles diffuse towards the grounded electrode, they move to a region with a slower v_{EP}. This means that the particles left behind in the main stream quickly reach that lateral position leaving no observable effect of the diffusion. Warnick *et al*. [61] reported a very similar focusing mechanism using a non-uniform electric field along a single spatial dimension. Here, the focusing of the particles is performed in the dimension perpendicular to the fluid flow in the microchannel, enabling continuous flow separation.

A final qualitative observation that demonstrates the non-uniformity of the electric field inside the DLD channel was made using a low frequency AC electric field applied on top of the DC. The amplitude of the electrophoretic oscillation induced by the AC field, which is proportional to the

electric field magnitude, was notably smaller close to electrodes with respect to the oscillation observed in the central area of the microchannel. This confirms the fact that the magnitude of the DC field is reduced near the electrodes

7.4 Conclusions

This chapter described a new improved DLD microfluidic particle separation method using electrokinetics. Previous chapters described how classical DLD separation can be significantly improved by applying AC electric fields orthogonal to the fluid flow. In this chapter, both classical DLD and AC-tuned DLD were combined with DC electric fields (applied perpendicular to the flow), to deliver an even more powerful and tunable separation technique.

Experimental characterisation revealed several advantages in adding a DC component to electrokinetic biased DLD systems. The action of a DC electric field turns the original DC binary separation into particle fractionation, i.e. a mixture made of more than two types of particles can be successfully sorted into several different components; something that was never achieved when DLD was combined only with AC electrokinetics. In addition, as the different populations are sorted, they are also focused into tight streams narrower than when they entered the channel. In other words, the effect of diffusion is reduced. The separation possibilities are also increased: when a DC signal is applied, zeta-potential based sorting can be performed and the minimum particle size that this technique can target is considerably reduced. These characteristics make the DC-DLD separation technique suitable for addressing the separation of nanoparticles.

All the DC induced effects are driven by a non-uniform electric field along the channel section, in a direction perpendicular to the fluid flow. When a voltage is applied electrochemical reactions at the electrodes generate ionic species that diffuse into the electrolyte and modify the local conductivity. This creates an electric field gradient perpendicular to the flow: the field magnitude is reduced near the electrodes and increased in the central region of the channel. This approach is similar to other techniques which also use conductivity gradients to control de spatial dependence of the electrokinetic forces acting over the particles in separation systems[229,264,265].

In the experiments presented here the conductivity gradients and hence the non-uniform electric fields are generated accidentally and in an uncontrolled way. Future work should focus on a redesign of the devices and experimental setup so that the changes in the local conductivity and the field spatial dependence can be controlled. The use of gel electrodes or semipermeable membranes would allow to control the diffusion of species into de channel. For example, with gel electrodes the metal electrodes can be placed in reservoirs far from the channels so that the generated species do not diffuse into the devices. This enables to then create the concentration

gradients in a controlled manner, by placing extra side-channels at the edges of the devices (carrying medium with a different concentration) separated from the main DLD channels by ion selective membranes. This would allow methodical characterisation of the behaviour as a function of changes in the electrical conductivity leading to a deeper understanding of the underlying principles of the DC-DLD particle sorting.

Chapter 8 Electrokinetics integrated DLD for nanoparticle separation

8.1 Introduction

The separation of particles in the range of nanometres is challenging. The role of nanobioparticles is becoming more apparent as research develops and they are known to play an important role in mechanisms like cell signalling and communication. Extracellular vesicles (EVs) and exosomes are two examples of such particles and are believed to carry useful information on several key biological aspects about the tissue from where they originated. For example, they can contain information from undetected tumours and serve as a diagnostic biomarker[5,266]. New research also shows that exosomes, in particular those found in breastmilk, are responsible for the development of the immune system of the new-borns[267,268].

Unfortunately the size of these particles ranges from tens to a few hundred nanometres in diameter making them very hard to extract from biological samples like blood or milk[252,269]. This is an obstacle for further research and the development of diagnostics and therapies based on the detection, analysis and manipulation of these particles. Current protocols to extract and purify exosomes and other nanoparticles are mainly based on ultracentrifugation, precipitation and filtration, which use huge pieces of equipment, are expensive and take a long time, often several days[4,270].

Microfluidic techniques are capable of significantly reducing the cost and time of the separation process whilst also increasing the quality of the separation. However, most existing microfluidic sorting techniques focus on separation of larger micron-sized particles like cells and bacteria. A few attempts have been reported for nanoparticle separation but most fail in one or more key separation aspects such as resolution, precision or throughput. High-throughput techniques often fail to resolve the particle sizes in the sample leading to a poor-quality separation. Meanwhile, very precise techniques with a high resolution are normally characterised by high fluidic resistances which limit enormously the sample throughput in a given time[36,41,252]. DLD nanoparticle separation approaches are examples of these low-throughput techniques: to target very small particles of ~50-200 nm diameter, the channel and post array dimensions need to be extremely small[92].

Chapter 7 of this thesis described how separation of nanoparticles inside a DLD can be achieved by using a combination of DC and AC electric fields applied perpendicular to the fluid flow. This technique depended on the creation of field-driven electrical conductivity gradients that generate a spatially non-uniform electric field. Under the action of an electric force with a magnitude

gradient in the direction perpendicular to the flow, from low strength near the electrodes to a maximum in the channel central region, the different sample components concentrate in distinct bands depending on their electrical response (size, charge, polarisability, …). However, these gradients arise “accidentally” and cannot be controlled or characterised.

To resolve this issue this chapter presents a more reliable and well understood DLD biased AC electrokinetic system that addresses the problem of nanoparticle separation. It is based on the mechanisms described in Chapter 5 and Chapter 6 with an improved design of DLD devices. Although the technique presented here requires further refinement, the experiments show promising results which indicate that a standard and easy to use AC tuned DLD system might be capable of large-scale extraction of purified exosomes and EVs.

8.2 Device optimisation using numerical model

The previous DLD design (DLD design A, see Chapter 4) used in combination with an orthogonal AC electric field was not capable of inducing a significant deflection of particles smaller than 1 µm. To reduce the target size and separate particles in the range of nanometres the DLD devices had to be redesigned so that the AC electrokinetic forces acting on the particles were much stronger. Since deviation at high frequencies caused by nDEP is a well understood mechanism, the device redesign focused on increasing the magnitude of the DEP force inside the DLD devices. To achieve this, the post array and microchannel dimensions were reduced. The new modifications were also expected to increase the strength of the low frequency deviation forces.

The numerical model introduced in Chapter 6 was used to explore the dependence of the nDEP induced deviation with the geometry of the DLD array and to determine the most suitable design to target nanoparticle separation. The results from the simulations are summarised in Figure 8-1. The particles in the simulations were 1 µm in diameter and experienced a nDEP with the real part of the CM factor set to the minimum ($\mathrm{Re}[f_{CM}] = -0.5$). Virtual walls were used to account for the size of the particles which did not allow the simulated particles to approach the posts closer than a distance equal to the particle radius. This did not affect the electric field or fluid flow distribution. Since the electric field was applied orthogonal to the fluid flow (in the lateral direction), the horizontal gap between the posts (the gap in the direction perpendicular to the posts) was reduced in order to increase the electric field gradient generated between posts of the same row. This significantly reduced the electric field magnitude necessary to achieve maximum deflection of the particles (see Figure 8-1a). The results showed that the smaller the horizontal gap the lower the field necessary to force the particle to switch to bumping mode due to larger electric field gradient arising between the posts.

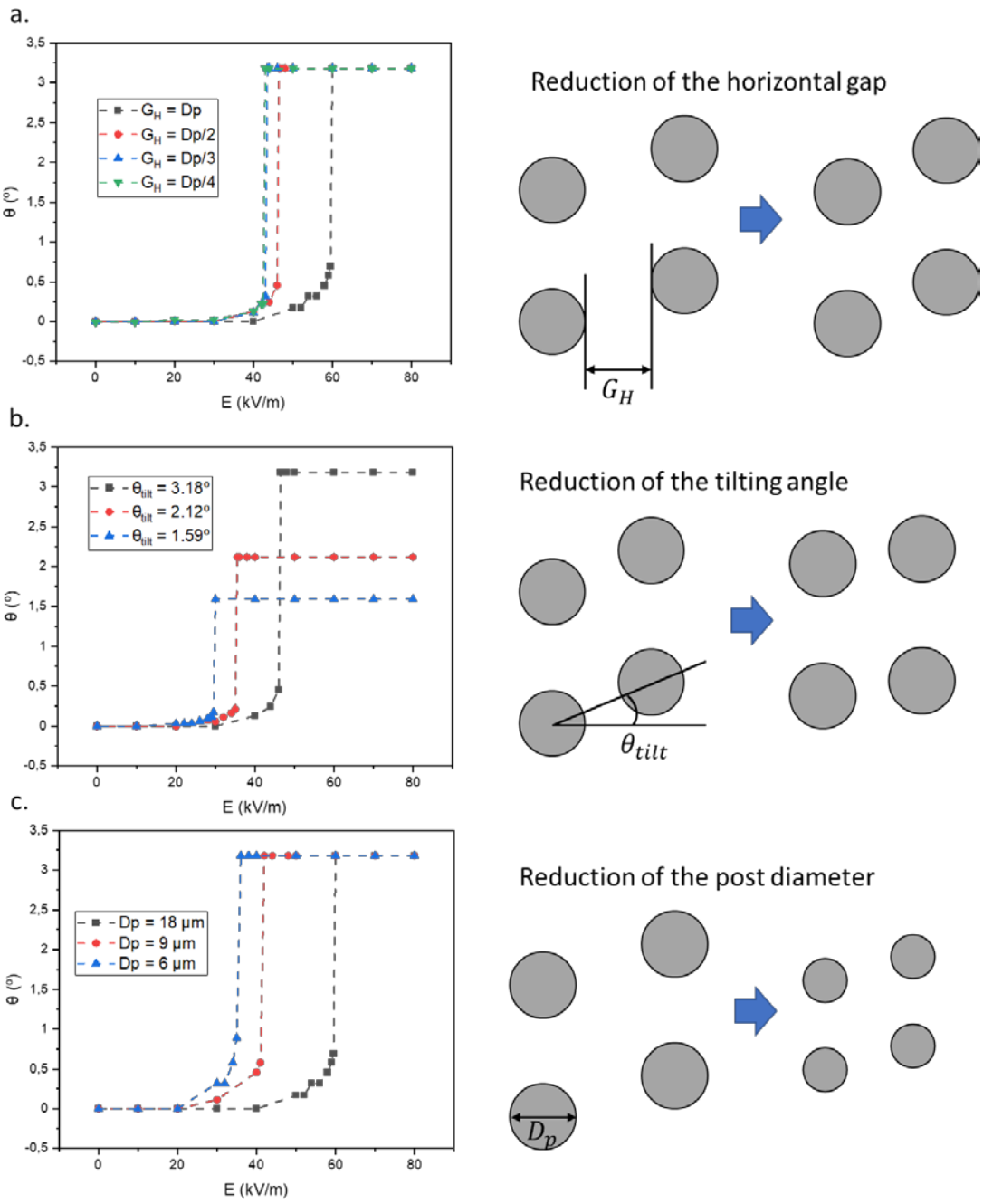

Figure 8-1. Results from the simulations used to investigate the dependence of the nDEP induced deviation angle with DLD post array geometry, as a function of the electric field magnitude. In all cases, particles were 1 µm diameter and the nDEP force was set to maximum (i.e. $\mathrm{Re}[f_{CM}] = -0.5$). (a) Dependence on the horizontal gap (G_H). The lateral gap was equal the post diameter lateral gap ($G_L = D_p$). (b) Dependence on the tilt angle of the posts (θ_{tilt}). The gaps between the posts were $G_L = D_p$ and $G_H = D_p/2$. (c) Dependence on the post diameter (D_p) with gaps between the posts $G_H = G_L = D_p$.

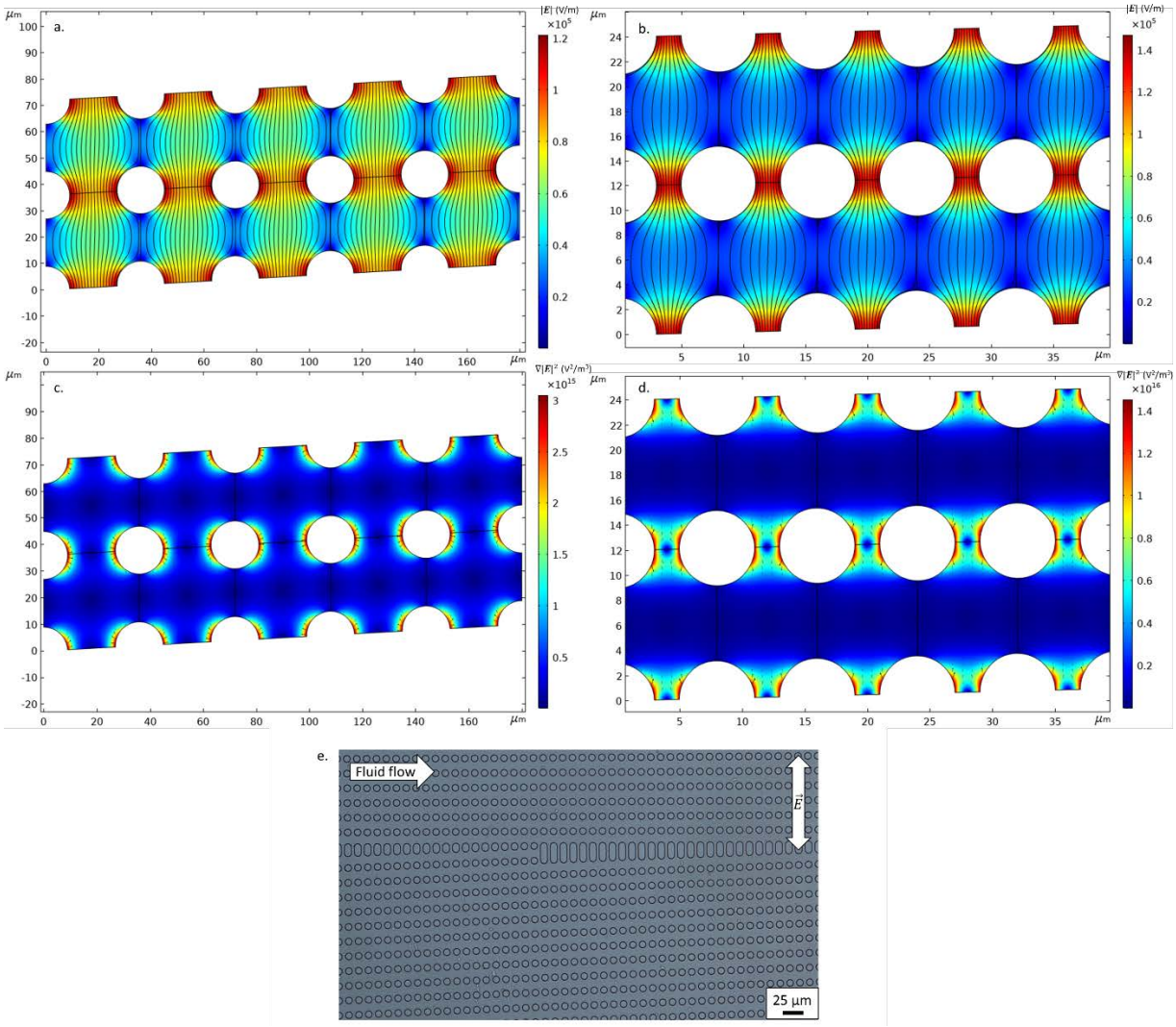

Figure 8-2. Comparison of the electric field and spatial distributions of the DEP for two different types AC electrokinetic tuned DLD devices. (a) Electric field distribution for DLD design A. The colour map represents the field magnitude for an applied voltage of 320 Vpp, while the black lines represent the electric field lines. (b) Electric field distribution for DLD design B. The colour map represents the field magnitude for the same field as in Figure 8-3a and the black lines represent the electric field lines. (c) Spatial dependence of $\nabla|\boldsymbol{E}|^2$ (proportional to the DEP force) for DLD design A. (d) Spatial dependence of $\nabla|\boldsymbol{E}|^2$ for DLD design B. (e) Picture of a DLD Design B device used for nanoparticle separation with $D_p = 9\ \mu\text{m}$.

Figure 8-1b shows the effects of reducing the offset between consecutive columns of posts. This is analogous to reducing the tilt angle of the rows and increasing the periodicity of the array. The reduced angle translates into a much weaker fluid drag force pushing the particles to flow in the zig-zag mode. This means that a weaker nDEP force is necessary to overcome the reduced fluid drag and force the particles to bump on the posts. However, in practice this geometric modification has an inconvenience: a device with a smaller angle needs to be longer to produce a large enough lateral

separation between the different populations in the sample. In addition, Figure 8-1c demonstrates that a reduced post diameter (and a reduction of the DLD array geometry accordingly) decreases the field magnitude threshold for maximum nDEP induced deviation, also due to an increase in the electric field gradient around the posts.

In light of these results, all three modifications – reduction of the horizontal gap, the tilt angle and the post diameter – were incorporated in the new DLD devices (see Figure 8-2). The design is described in detail in section 4.1.2 Design B – Nanoparticle Electrokinetic DLD separation in Chapter 4. The new design (DLD Design B) had smaller posts placed in an array with asymmetric horizontal and lateral gaps, $G_H \neq G_L$, of sizes $G_L = D_p$ and $G_H = D_p/3$, and, in general, a much smaller offset ($\Delta\lambda$) between consecutive pillar columns. These devices also had narrower channels so that the distance between the coplanar parallel electrodes could be reduced, thus increasing the magnitude of the electric field that could be applied.

8.3 Experiments and data analysis

To investigate the performance of the new devices, separation experiments with particles of different sizes were carried out, first without an applied electric field (2 µm carboxylate, 1.5 µm plain, 1 µm carboxylate and 500 nm carboxylate particles) to estimate the DLD array critical diameter, and then with an orthogonal AC field using only carboxylate fluorescent nanoparticles of 500 nm, 200 nm and 100 nm diameter.

As explained in section 4.1.2 of Chapter 4, these devices had a single outlet connected to the main channel through 24 channels which were 35 µm wide and were spaced 20 µm apart from each other. The net displacement of each particle subpopulation was then given in terms of the outlet channel exit number (instead of the total lateral displacement). The average exit channel was estimated manually by eye from processed pre-recorded videos; the data points displayed on the experimental plots represent the average exit channel while the vertical bars on each data point show the particle stream width at the outlet.

Preliminary experiments indicated that, as expected, the devices with smaller tilt angles and post diameters performed best at separating nanoparticles. Since all devices had very similar throughput and precision, in the experiments described in this chapter only device #6 from Table 4-2 was used (see section 4.1.2 Design B – Nanoparticle Electrokinetic DLD separation in Chapter 4) which had a DLD post array with the following geometrical parameters: $D_p = 6\ \mu\text{m}, \lambda_L = 12\ \mu\text{m}, \lambda_H = 8\ \mu\text{m}, \Delta\lambda = 0.3\ \mu\text{m}, N = 40, \theta = 1.43°$.

8.4 Results and discussion

8.4.1 Behaviour without electric field

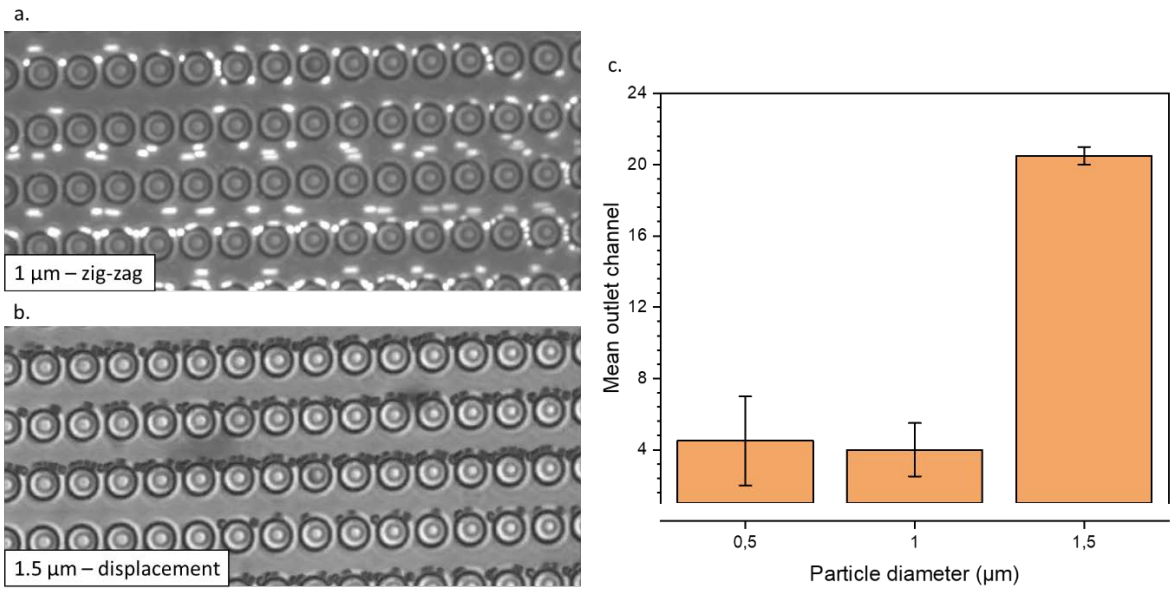

Figure 8-4. Performance in the absence of electric field of a nano-DLD device (DLD Design B) with an array of 6 µm posts, a horizontal gap of 2 µm and a periodicity equal to 40. (a) 1 µm diameter particles travelling in zig-zag mode. (b) 1.5 µm diameter particles bumping in displacement mode. (c) Mean exit outlet for 500 nm, 1 µm and 1.5 µm particles without an applied electric field. The vertical bars represent the particle stream width at which they reach the outlet. The results indicate that the value of D_c for these devices is between 1 and 1.5 µm.

Experiments using the aforementioned DLD devices (DLD array with $D_p = 6\ \mu\text{m}$ and $N = 40$) were performed without an orthogonal electric field, to characterise particle behaviour as a function of size, and estimate the critical diameter (D_c). The results are shown in Figure 8-4. The picture in Figure 8-4a shows 1 µm diameter PS fluorescent particles zigzagging around the posts following trajectories with zero net lateral displacement through the DLD devices, whereas Figure 8-4b shows the behaviour of slightly bigger particles (1.5 µm diameter) bumping on the posts and deflecting in the array. Figure 8-4c shows the mean exit channel for different particle sizes. Given that the inlet channel causes all the particles to enter at the same lateral position as the fourth outlet channel (starting from the bottom edge of the device), these results show that particles of diameter equal or smaller than 1 µm travel in zig-zag mode and do not exhibit any lateral deflection, whilst the 1.5 µm diameter particles are displaced laterally by the DLD array (maximum lateral displacement corresponds to outlet number 21). The experimental results in Figure 8-4 enable an estimate of D_c for these devices of between 1 µm and 1.5 µm.

8.4.2 High frequency regime

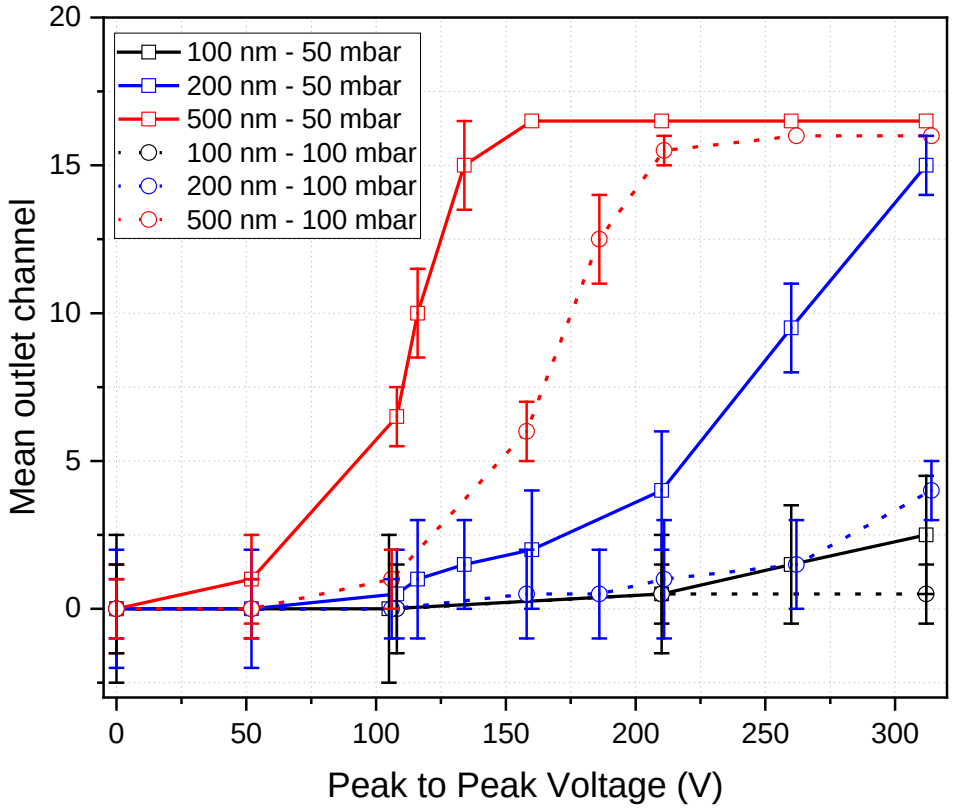

Figure 8-5. nDEP induced deviation of 100 nm, 200 nm and 500 nm diameter nanoparticles inside DLD devices of Design B with $D_p = 6\ \mu\text{m}$ and $N = 40$ for two different applied pressures. The applied AC electric field had a frequency of 100 kHz (DEP was the only EK force acting on the particles) and the suspending medium had an electrical conductivity of 105 mS/m to ensure that the particles experienced negative DEP ($\text{Re}[f_{CM}] \approx -0.5$).

Experiments with 500 nm, 200 nm and 100 nm diameter carboxylate fluorescent nanoparticles were performed to investigate the nDEP induced deflection inside these devices. The particles were suspended in a 105 mS/m conductivity electrolyte to ensure they always experienced nDEP, and an AC electric field of 100 kHz was applied so that the particle electrokinetic behaviour could be attributed solely to DEP, i.e. DEP was the only relevant force acting on the particles. The data for this nDEP driven deflection as a function of the applied voltage, in terms of the mean exit channel and for two different values of applied pressure (and therefore flow rate), is summarised in Figure 8-5.

In this plot, outlet channel number zero corresponds to the same lateral position as the sample inlet channel, thus particles exiting through this outlet experience zero net displacement. The outlet corresponding to maximum deflection is channel number 16. Beyond that, the outlet channels are located within the straight post array located at the top of the device (the

concentration region), a region that the particles in bump mode never reach since they stop deviating in the transition region between the tilted array and the straight array (this part of the device is shown in Figure 8-2e). The vertical bars at each data point represent the width of the particle stream at the outlet.

This figure depicts a behaviour of the nanoparticles very similar to that observed for microparticles described in Chapter 5 and Chapter 6. Above a given voltage threshold, the induced deviation rises quickly and reaches a plateau corresponding to the maximum lateral displacement, i.e. the particles in displacement mode reach the concentration region of the DLD arrays. This threshold reduces with particle size and increases with the mean fluid flow velocity, in agreement with the data presented in Chapter 6. The figure shows that, for the two flow rates used in the experiments, the 500 nm particles are easily deflected by a high frequency AC electric field inside these DLD devices at relatively low applied voltages whereas higher field magnitudes are necessary to induce the deviation of smaller particles. A significant nDEP deflection of 200 nm particles is achieved at low flow rates, but for an applied pressure of 100 mbar the deviation is minor. The 100 nm nanospheres require even stronger fields than could be applied with the current setup to be deflected and therefore no deflection was observed even for the slower flow rates (within the range of applied voltages available experimentally).

Figure 8-5 clearly depicts the potential of this new EK biased nano-DLD devices for performing nDEP based nanoparticle separation. Any particle of 500 nm diameter or bigger can be easily separated from smaller particles at low applied voltages. Furthermore, stronger electric fields enable successful separation of 200 nm and 100 nm particles, demonstrating the very high precision and resolution of this technique.

8.4.3 Low frequency regime

The experimental characterisation showed that the nanoparticle behaviour under the action of low frequency AC electric field was more unpredictable. In this case, the experiments were performed with the same particles (500 nm, 200 nm and 100 nm diameter) but using a 100 Hz AC field, and suspended in an electrolyte with a much lower conductivity of 1.75 mS/m, to avoid Faradaic reactions at the electrodes (which arise when a high voltage and low frequency AC electric field is applied). The reduction of the medium conductivity was also done in accordance to the experimental results presented in Chapter 6 which demonstrate that the mechanism leading to the low frequency induced deviation is stronger at lower conductivities.

The experimental results of the low frequency induced nanoparticle deviation are summarised in Figure 8-6. As expected, the low frequency behaviour differs enormously from the behaviour at

high frequencies which is solely attributed to DEP. However, the plots show some unexpected results which differ from the behaviour observed for microparticles described in Chapter 6.

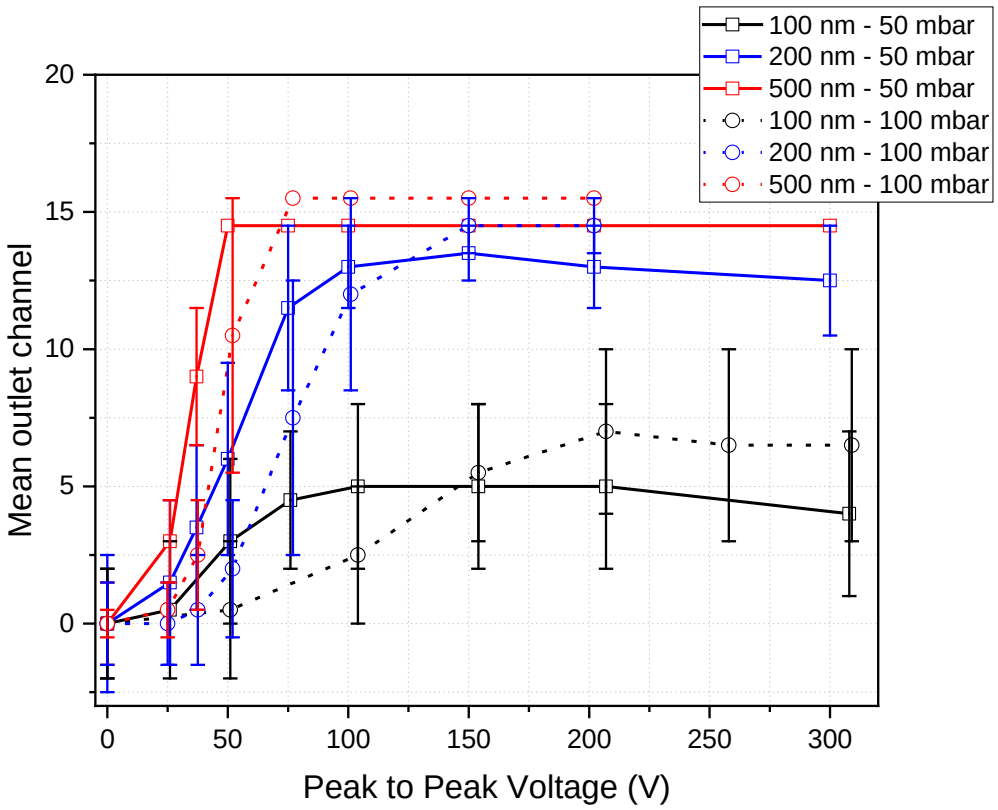

Figure 8-6. Low frequency induced deviation of 100 nm, 200 nm and 500 nm diameter nanoparticles inside DLD devices from Design B with $D_p = 6$ μm and $N = 40$ for two different applied inlet pressures. The applied AC electric field had a frequency of 100 Hz (the deflection mechanism was not dominated by DEP) and the suspending medium had an electrical conductivity of 1.75 mS/m.

Previous experiments showed that at low frequencies the electric field magnitude required to induce a significant deflection is reduced with respect to the high frequency case. This results was also observed in the nanoparticle electrokinetic DLD separation devices - as the field magnitude increases, the particles exhibit a sharp transition from zig-zag to bump mode at an electric field magnitude threshold significantly lower than at high electric field frequencies (compare the curves for the induced deviation of 500 nm particles in Figure 8-5 and Figure 8-6). In practice, this allows faster flow rates to be used with reduced voltages, increasing the separation throughput.

However, in this devices with a scaled down geometry, the benefits of the low frequency induced deviation (lower field magnitude and enhanced throughput) come at the expense of an erratic behaviour that leads to a poor size resolution and precision with wide particle distributions, which are significantly larger than those predicted by the diffusion mechanism.

The wide particle distributions observed when low frequency AC electric fields were applied can be observed in the error bars in the curves for 200 nm and 100 nm particles in Figure 8-6 which represent the nanoparticle stream width at the outlet. This fact is not observed in the case of the 500 nm diameter particles since they experience full deflection and focus in the concentration region of the channels. Nevertheless, comparison of the curves for the 500 nm and 200 nm particles show that clean separation is never fully achieved and that both particle populations overlap in most cases mainly due to the wide distributions of the 200 nm particle streams.

An important result is that for the highest flow rate the maximum lateral displacement increases for the three different particle sizes. This effect is most important for the 100 nm particles which also show a maximum lateral displacement far away from the concentration region. These unexpected observations cannot be explained in terms of the current theory for electrokinetic induced separation inside DLD devices (described in Chapter 6) and are not understood yet.

Qualitative inspection of the particle trajectories and the behaviour near the electrodes suggest that the low frequency electric fields could induce the generation of ionic species at the electrodes, leading to perturbation of the local electrolyte conductivity and thus the creation of electric field gradients (in a similar way to the experiments described in Chapter 7). This effect could be important in this case, although it was negligible for devices from DLD Design A – the fact that the nano-DLD devices are much smaller (only ~4 μm tall) and therefore contain smaller volumes of liquid combined with stronger electric fields and lower flow rates imply that the conductivity of the liquid bulk is perturbed more easily in this devices with respect the devices from the previous design

A perturbed conductivity could lead to a focusing position far from the channels such as that measured for the 100 nm particles but still cannot account for the wide particle distributions observed or a larger maximum lateral deflection at higher flow rates. To clarify these experimental results, a complete theory on the effects of the low frequency electric field on the particle trajectories inside the DLD devices is necessary.

8.5 Conclusions

This chapter described how AC electrokinetic biased DLD systems can be scaled down to address the problem of nanoparticle sorting. The design of the DLD devices was optimized to reduce the minimum particle size for separation, and the design performance was characterised as a function of different parameters.

At high frequencies, the nDEP induced deviation was capable of separating 500 nm, 200 nm and 100 nm diameter PS nanospheres. The sorting is selectively controlled via the applied electric field

magnitude and flow rate and showed a high degree of precision and resolution in size enabling deflection of 200 nm diameter particles, separating them from 100 nm particles. However, the reduced dimensions of these DLD devices imply a high fluidic resistance that significantly limits the throughput and thus the volume of sample that can be processed in a given time frame (~1 µL/h). In addition, the smaller the target size, the lower flow rate needs to be and thus the throughput reduces even further.

Device parallelisation could be used to overcome this problem with several devices operating at the same time. However, this would bring complications in terms of fabrication and operation, and an increase in costs, making the technique unfeasible for real world applications. On the contrary, improvements in the current fabrication process might allow the microchannels to be expanded, for example making them wider and taller, to reduce the fluidic resistance and increase the separation throughput. This would require higher resolution in the photolithography fabrication process so that the thin narrow gaps between the small posts could be resolved with an increased aspect ratio.

The experiments at low frequencies showed a more complicated behaviour. Although the separation mechanism was stronger and lower applied voltages were necessary to achieve nanoparticle separation, the separation quality was much reduced with respect to the high frequency regime. The low frequency field causes very wide particle streams, in most cases wide enough to overlap with the other populations in the samples, so that the size resolution of the separation is reduced. Furthermore, the particle trajectories showed unexpected behaviour that is not understood. Qualitative analysis indicates uncontrolled changes in the suspending medium conductivity that perturbs the net induced lateral displacement and decreases the separation quality at low frequencies. Future work should include an improved experimental setup to control and prevent such disruptions with further characterisation experiments to achieve a full understanding of the mechanism driving the separation when low frequency AC electric fields are applied.

Chapter 9 Conclusion and outlook

This thesis has presented a novel label-free continuous-flow particle separation technique in which Deterministic Lateral Displacement (DLD) devices are combined with Electrokinetic particle manipulation. Coplanar parallel electrodes are integrated within DLD channels in order to apply electric fields orthogonal to the fluid flow. This adds extra forces acting on the particles that serve to control their behaviour depending on their electrical response. This turns DLD into a tunable technique capable of performing separation based not only on the particle size but also on other structural and electrical properties.

Classical DLD particle sorting is a very robust size-based technique which has demonstrated a high level of precision and resolution. However, this technique still has some important flaws which inhibit DLD from becoming viable for real world applications. DLD devices can only perform size-based separation and are not tunable; once fabricated they can be used only to separate particles above and below a given size threshold, the critical diameter, which depends only on the device geometry and cannot be modified. Also, these devices only allow for binary separation, i.e. the sample can only be divided into two different populations. If more than two subpopulations need to be extracted from a given sample, several DLD devices need to be combined and run sequentially. In addition, the smaller the target particles are, the smaller the channel dimensions must be to achieve a small enough the critical diameter, resulting in a throughput that is too low for DLD to be feasible for processing real biologically relevant samples.

Nevertheless, as described throughout this thesis, combining DLD with electrokinetics significantly enhances the separation capability, and alleviate many of these deficiencies. In Chapter 5, proof-of-principle experiments first showed that it is possible to control the behaviour inside DLD devices of particles smaller than the critical diameter using AC electric fields, and force these particles to deflect with the tilt angle of the posts. This provides a means of choosing which particles in a mixture are displaced laterally within the DLD microchannel, so that they can be separated from the rest of the particles in the sample that flow with no net deviation, only by controlling the electric signal applied to the system. This is a significant improvement over classical size-based passive DLD separation where the critical diameter is fixed by the array geometry, limiting enormously the separation capabilities. On the contrary, the results in Chapter 5 illustrated how the electrokinetic biased DLD systems can be used to separate particles depending on their electrical response using externally applied forces which can be actively controlled.

The experimental frequency characterisation showed two main modes of operation. At high frequencies (> 500 Hz), the particle behaviour and the induced lateral deflection are governed by

their dielectrophoretic response. Similarly to iDEP devices (extensively studied in the literature), the DLD insulating posts disturb the field distribution around them creating a spatially non-uniform electric field which then gives rise to a DEP force acting on the particles flowing through the DLD microchannels. Since the DEP depends on parameters which can be manually and actively controlled - electric field frequency and magnitude and medium conductivity - such force allows direct control on the particle trajectories and therefore in the separation.

Amongst the two possible directions of the DEP force (positive – attracted the high electric field gradient regions; or negative – repelled from high electric field gradient regions) the experiments showed that only particles experiencing a strong negative DEP force are forced to switch from the zig-zag to the displacement mode. The nDEP force creates repulsive regions between the DLD post rows which the particles experiencing nDEP cannot enter to cross between two posts and continue in a zig-zag motion. As a result, they are forced to follow displacing trajectories following the tilting angle of the DLD rows of posts.

At low frequencies (< 500 Hz), the particles exhibit an electrophoretic oscillation, on top of the DEP force, along the electric field lines which are perturbed by the presence of the posts. The experimental characterisation showed that the particles are also forced to deflect by the low frequency electric field in a mechanism, different from the nDEP induced deviation but not yet fully understood. Two main results led to the conclusion that DEP was not responsible for the behaviour at low frequencies. Firstly, the field magnitude threshold to induce deviation is significantly lower at this frequency regime and secondly, both, particles experiencing pDEP and nDEP, can be deflected by a low frequency electric field.

In Chapter 6, the scaling laws governing particle deviation at each frequency regime were identified as a function of different parameters: particle size, flow rate and applied electric field magnitude. These scaling laws were then tested against the electrokinetic behaviour expected from theory by means of a numerical model. This comparison showed an excellent agreement between theory and experiments in the high frequency regime where the particle electrokinetic motion is dominated by DEP and led to the confirmation that nDEP was in fact, the force responsible for the induced deviation at high frequencies. By contrast, the numerical simulations did not provide further insight into the mechanism responsible for separation in the low frequency regime. This remains unclear even though the dependence with respect the most relevant parameters (field magnitude and frequency, flow rate and particle size) was experimentally characterised.

The possibility that the polarisation of the EDL and therefore a change in the dielectrophoretic behaviour at low frequencies could account for the behaviour at low frequencies was also evaluated. The current theory of EDL polarisation predicts a relaxation, the α-relaxation, at lower

frequencies than the Maxwell-Wagner relaxation which reduces the overall magnitude of the induced dipole on the particles. However, this mechanism cannot account for the reduced electric field magnitude deviation threshold observed at low frequencies or the fact that particles experiencing pDEP are also forced to deflect. This possibility was also tested using the numerical model presented in Chapter 6 and the simulations showed no difference with the high frequency case, i.e. the deviation only depended on the magnitude and direction of the DEP force and not on the mechanism responsible for the induced dipole on the particles.

Furthermore, experiments performed with low frequency electric fields revealed the presence of quadrupolar rectified electroosmotic flows in the vicinity of the insulating DLD posts. This novel non-linear electrokinetic phenomenon was explored as a function of the applied field frequency and medium conductivity, showing a dependence very similar to that of the low frequency induced deviation. Although these EO flows are unable to explain the experimental behaviour since they cannot account for the size dependence of the low frequency induced deviation, these results suggest that the quadrupolar rectified flows around the insulating posts and the low frequency deviation could have a common origin related to non-linear electrokinetic phenomena.

The thesis also describes how orthogonal DC electric fields (Chapter 7), by themselves and combined with AC electric fields can improve DLD separation. Upon the application of a DC voltage, electrically induced conductivity gradients were observed near the electrodes, leading to a spatially non-uniform DC electric field magnitude along the channel cross-section. This spatial dependence gives rise to non-uniform electrophoresis which displaces the particles laterally while concentrating them into tight bands, overcoming particle diffusion. Experiments showed that such behaviour, also in combination with AC electric fields, can be used to separate particles of much smaller sizes (in the range of nanometres) into distinct narrow bands depending on their charge and size, and turns the DLD binary separation into a particle fractionation device.

Finally, Chapter 8 introduces a refined device design to reduce the minimum particle size that could be targeted by the electrokinetic biased DLD separation system. For that purpose, and given that the mechanisms driving the separation scale with the particle size, the dimensions of the DLD devices were scaled down and the geometry of the DLD post array was reduced and modified so that the strength of the electrical forces acting on the particles increased. Specifically, the gap between the posts, the post diameter, the DLD tilting angle and the distance between the electrodes were reduced. Although only proof-of-principle experiments with polystyrene nanospheres were performed, the results showed potential in terms of precision and resolution, and demonstrate that this technique is suitable for targeting the separation of biological nanoparticles such as EVs and exosomes.

In summary, this thesis describes how classic DLD can be improved when combined with Electrokinetic phenomena. The existence of easy-to-control electrical forces acting on the particles as they flow through the micropillar array, turns DLD size-based binary separation devices with a fixed critical diameter, into tunable systems capable of performing micro and nano-particle sorting and fractionation exploiting the electrokinetic response of the particles. However, there are several open questions that must be addressed in future research.

The mechanism driving particle induced deflection inside DLD devices in the presence of low frequency AC electric fields is still unclear. The scaling laws were empirically derived but the physical principles behind this behaviour is not understood yet. The existence of quadrupolar rectified EO flows around the insulating PDMS DLD posts indicate that non-linear electrokinetic phenomena is important when low frequency AC fields are used; indicating that the deviation at low frequencies could have a similar origin.

Future experiments should explore the role of non-linear electrokinetics inside DLD microchannels, combined with effects such as concentration polarisation near dielectric surfaces, diffusiophoresis or electrokinetic wall-particle repulsion. Examples of these future experiments include studying the behaviour of micrometre and nanometre particles near insulating straight walls and posts under the action of low frequency electric fields to study possible low frequency AC wall-repulsion effects and experimentally characterise of the quadrupolar rectified EO flows. The observation of concentration polarisation effects near posts using fluorescent dyes like Rhodamine 6G or fluorescein, which map the electrolyte concentration, due to the existence of surface conductance at the insulating post walls would indicate the existence of rectified electric fields which would give play an important role in the low frequency behaviour and could provide a theoretical framework to explain the existence of the rectified EO flows.

The arising of the quadrupolar rolls around the insulating obstacles is an interesting phenomenon by itself. Although similar flows around dielectric objects have been already reported and attributed to Induced-Charge Electrokinetic (ICEK) phenomena[261,271], the preliminary experiments presented in this thesis suggest that these flows arise from a different mechanism. Future research would focus on testing such hypothesis, with the aim of establishing a well-founded theoretical model of non-linear Electroosmosis (EO) near dielectric surfaces. Moreover, if the quadrupolar rectified EO flows described here have its origin on a concentration polarisation arising around the posts due to a surface conductance at the insulating walls, this mechanism would also take place around the micro- and nano-spheres used for the experiments in this thesis, generating flows around them and therefore a hydrodynamic lift force from any nearby walls. Such lift happening inside the DLD

channels could then lead to and induced deflection, caused by the low frequency AC electric field. This hypothesis will be tested as part of the future work.

Finally, the thesis also describes two further improvements to AC biased DLD that target nanoparticle separation. Adding a DC component to the electric field has demonstrated nanoparticle fractionation within a DLD system. However, this method relies on concentration gradients generated accidentally due to Faradaic reactions at the electrodes triggered by the DC voltages. For this approach to be reliable and suitable for real world applications, future designs should find ways of creating such concentration gradients in a controlled manner, for example by using a combination of gel-electrodes, which allow to place the electrodes in reservoirs far from the channels, and ion-selective membranes, which would enable control of the diffusion of species into the bulk liquid. The second approach relies on reducing the dimensions of the devices to increase the magnitude of the electric forces acting on the nanoparticles but compromising the throughput of the separation. Experiments with polystyrene nanospheres were promising, but the separation performance must be characterised with biologically relevant particles such as EVs or exosomes and the throughput must be increased, for example, via device parallelisation.

Particle sorting is a crucial step in almost any analytical technologies and the development of microfluidic and electrokinetic techniques for particle manipulation and separation will lead to a revolution in the way samples are tested worldwide. Building on to previous research this thesis presents and characterises a novel and promising separation technique which combines microfluidics and electrokinetics. The results demonstrated the capabilities for high-quality sorting of particles from a sample with broad size distribution, from micrometres to hundreds of nanometres, with a wide range of potential applications. This technique adds to a far-reaching family of microfluidic separation techniques that will reshape how particle separation is carried out, contributing to the development of Lab-on-a-Chip and Point-of-Care systems.

References

1. Sajeesh, P. & Sen, A. K. Particle separation and sorting in microfluidic devices: A review. *Microfluid. Nanofluidics* **17**, 1–52 (2014).

2. Jackson, E. L. & Lu, H. Advances in microfluidic cell separation and manipulation. *Curr. Opin. Chem. Eng.* **2**, 398–404 (2013).

3. Yu, M., Stott, S., Toner, M., Maheswaran, S. & Haber, D. A. Circulating tumor cells: approaches to isolation and characterization. *J. Cell Biol.* **192**, 373–382 (2011).

4. Théry, C., Amigorena, S., Raposo, G. & Clayton, A. Isolation and Characterization of Exosomes from Cell Culture Supernatants and Biological Fluids. *Curr. Protoc. Cell Biol.* **30**, 3.22.1-3.22.29 (2006).

5. Soung, Y. H., Ford, S., Zhang, V. & Chung, J. Exosomes in cancer diagnostics. *Cancers (Basel).* **9**, (2017).

6. Parks, D. R. & Herzenberg, L. A. Fluorescence-activated cell sorting: Theory, experimental optimization, and applications in lymphoid cell biology. in *Immunochemical Techniques, Part G* (eds. Di Sabato, G., Langone, J. J. & Van Vunakis, H. B. T.-M. in E.) **108**, 197–241 (Academic Press, 1984).

7. Bonner, W. A., Hulett, H. R., Sweet, R. G. & Herzenberg, L. A. Fluorescence activated cell sorting. *Rev. Sci. Instrum.* **43**, 404–409 (1972).

8. Miltenyi, S., Müller, W., Weichel, W. & Radbruch, A. High gradient magnetic cell separation with MACS. *Cytometry* **11**, 231–238 (1990).

9. Gravesen, P., Branebjerg, J. & Jensen, O. S. Microfluidics-a review. *J. Micromechanics Microengineering* **3**, 168–182 (1993).

10. Stone, H. A. & Kim, S. Microfluidics: Basic issues, applications, and challenges. *Am. Inst. Chem. Eng. AIChE J.* **47**, 1250 (2001).

11. Dalili, A., Samiei, E. & Hoorfar, M. A review of sorting, separation and isolation of cells and microbeads for biomedical applications: microfluidic approaches. *Analyst* **144**, 87–113 (2019).

12. Smith, J. T. *et al.* Integrated nanoscale deterministic lateral displacement arrays for separation of extracellular vesicles from clinically-relevant volumes of biological samples.

Lab Chip **18**, 3913–3925 (2018).

13. Reece, A. *et al.* Microfluidic techniques for high throughput single cell analysis. *Curr. Opin. Biotechnol.* **40**, 90–96 (2016).

14. Gossett, D. R. *et al.* Label-free cell separation and sorting in microfluidic systems. *Anal. Bioanal. Chem.* **397**, 3249–3267 (2010).

15. Reyes, D. R., Iossifidis, D., Auroux, P.-A. & Manz, A. Micro Total Analysis Systems. 1. Introduction, Theory, and Technology. *Anal. Chem.* **74**, 2623–2636 (2002).

16. Toner, M. & Irimia, D. Blood-on-a-Chip. *Annu. Rev. Biomed. Eng.* **7**, 77–103 (2005).

17. Figeys, D. & Pinto, D. Lab-on-a-chip: A revolution in biological and medical sciences. *Anal. Chem.* **72**, 330–335 (2000).

18. Dittrich, P. S. & Manz, A. Lab-on-a-chip: microfluidics in drug discovery. *Nat. Rev. Drug Discov.* **5**, 210–218 (2006).

19. Mark, D., Haeberle, S., Roth, G., Von Stetten, F. & Zengerle, R. Microfluidic Lab-on-a-Chip Platforms: Requirements, Characteristics and Applications BT - Microfluidics Based Microsystems. in (eds. Kakaç, S., Kosoy, B., Li, D. & Pramuanjaroenkij, A.) 305–376 (Springer Netherlands, 2010).

20. Sia, S. K. & Kricka, L. J. Microfluidics and point-of-care testing. *Lab Chip* **8**, 1982–1983 (2008).

21. Yager, P., Domingo, G. J. & Gerdes, J. Point-of-Care Diagnostics for Global Health. *Annu. Rev. Biomed. Eng.* **10**, 107–144 (2008).

22. Gubala, V., Harris, L. F., Ricco, A. J., Tan, M. X. & Williams, D. E. Point of Care Diagnostics: Status and Future. *Anal. Chem.* **84**, 487–515 (2012).

23. Happel, J. & Brenner, H. *Low Reynolds number hydrodynamics: with special applications to particulate media*. **1**, (Springer Science & Business Media, 2012).

24. Bruus, H. *Theoretical microfluidics*. **18**, (Oxford university press Oxford, 2008).

25. Yin, H. & Marshall, D. Microfluidics for single cell analysis. *Curr. Opin. Biotechnol.* **23**, 110–119 (2012).

26. Sun, T. & Morgan, H. Single-cell microfluidic Impedance cytometry: A review. *Microfluid. Nanofluidics* **8**, 423–443 (2010).

27. Wheeler, A. R. *et al.* Microfluidic device for single-cell analysis. *Anal. Chem.* **75**, 3581–3586 (2003).

28. Chin, C. D., Linder, V. & Sia, S. K. Commercialization of microfluidic point-of-care diagnostic devices. *Lab Chip* **12**, 2118–2134 (2012).

29. Volpatti, L. R. & Yetisen, A. K. Commercialization of microfluidic devices. *Trends Biotechnol.* **32**, 347–350 (2014).

30. Squires, T. M. & Quake, S. R. Microfluidics: Fluid physics at the nanoliter scale. *Rev. Mod. Phys.* **77**, 977–1026 (2005).

31. Einstein, A. On the movement of small particles suspended in a stationary liquid demanded by the molecular-kinetic theory of heart. *Ann. Phys.* **17**, 549–560 (1905).

32. Miller, C. C. The Stokes-Einstein law for diffusion in solution. *Proc. R. Soc. London. Ser. A, Contain. Pap. a Math. Phys. Character* **106**, 724–749 (1924).

33. Manz, A. *et al.* Planar chips technology for miniaturization and integration of separation techniques into monitoring systems: Capillary electrophoresis on a chip. *J. Chromatogr. A* **593**, 253–258 (1992).

34. Toner, M. & Irimia, D. Blood-on-a-chip. *Annu. Rev. Biomed. Eng.* **7**, 77–103 (2005).

35. Bhagat, A. A. S. *et al.* Microfluidics for cell separation. *Med. Biol. Eng. Comput.* **48**, 999–1014 (2010).

36. Salafi, T., Zeming, K. K. & Zhang, Y. Advancements in microfluidics for nanoparticle separation. *Lab Chip* **17**, 11–33 (2017).

37. Lenshof, A. & Laurell, T. Continuous separation of cells and particles in microfluidic systems. *Chem. Soc. Rev.* **39**, 1203–1217 (2010).

38. Bayareh, M. An updated review on particle separation in passive microfluidic devices. *Chem. Eng. Process. - Process Intensif.* **153**, 107984 (2020).

39. Fiedler, S., Shirley, S. G., Schnelle, T. & Fuhr, G. Dielectrophoretic Sorting of Particles and Cells in a Microsystem. *Anal. Chem.* **70**, 1909–1915 (1998).

40. Furlani, E. P. Magnetophoretic separation of blood cells at the microscale. *J. Phys. D. Appl. Phys.* **40**, 1313–1319 (2007).

41. Wu, M. *et al.* Isolation of exosomes from whole blood by integrating acoustics and

microfluidics. *Proc. Natl. Acad. Sci.* **114**, 10584–10589 (2017).

42. Pamme, N. Magnetism and microfluidics. *Lab Chip* **6**, 24–38 (2006).

43. Pamme, N. & Wilhelm, C. Continuous sorting of magnetic cells via on-chip free-flow magnetophoresis. *Lab Chip* **6**, 974–980 (2006).

44. Pamme, N., Eijkel, J. C. T. & Manz, A. On-chip free-flow magnetophoresis: Separation and detection of mixtures of magnetic particles in continuous flow. *J. Magn. Magn. Mater.* **307**, 237–244 (2006).

45. Kim, K. S. & Park, J. K. Magnetic force-based multiplexed immunoassay using superparamagnetic nanoparticles in microfluidic channel. *Lab Chip* **5**, 657–664 (2005).

46. Laurell, T., Petersson, F. & Nilsson, A. Chip integrated strategies for acoustic separation and manipulation of cells and particles. *Chem. Soc. Rev.* **36**, 492–506 (2007).

47. Lin, S. C. S., Mao, X. & Huang, T. J. Surface acoustic wave (SAW) acoustophoresis: Now and beyond. *Lab Chip* **12**, 2766–2770 (2012).

48. Lenshof, A., Magnusson, C. & Laurell, T. Acoustofluidics 8: Applications of acoustophoresis in continuous flow microsystems. *Lab Chip* **12**, 1210–1223 (2012).

49. Petersson, F., Åberg, L., Swärd-Nilsson, A. M. & Laurell, T. Free flow acoustophoresis: Microfluidic-based mode of particle and cell separation. *Anal. Chem.* **79**, 5117–5123 (2007).

50. Pamme, N. Continuous flow separations in microfluidic devices. *Lab Chip* **7**, 1644–1659 (2007).

51. Petersson, F., Nilsson, A., Holm, C., Jönsson, H. & Laurell, T. Continuous separation of lipid particles from erythrocytes by means of laminar flow and acoustic standing wave forces. *Lab Chip* **5**, 20–22 (2005).

52. Augustsson, P., Magnusson, C., Nordin, M., Lilja, H. & Laurell, T. Microfluidic, label-free enrichment of prostate cancer cells in blood based on acoustophoresis. *Anal. Chem.* **84**, 7954–7962 (2012).

53. Antfolk, M., Muller, P. B., Augustsson, P., Bruus, H. & Laurell, T. Focusing of sub-micrometer particles and bacteria enabled by two-dimensional acoustophoresis. *Lab Chip* **14**, 2791–2799 (2014).

54. Wu, M. *et al.* Separating extracellular vesicles and lipoproteins via acoustofluidics. *Lab Chip*

19, 1174–1182 (2019).

55. Lee, K., Shao, H., Weissleder, R. & Lee, H. Acoustic Purification of Extracellular Microvesicles. *ACS Nano* **9**, 2321–2327 (2015).

56. Nilsson, A., Petersson, F., Jönsson, H. & Laurell, T. Acoustic control of suspended particles in micro fluidic chips. *Lab Chip* **4**, 131–135 (2004).

57. Wong, P. K., Wang, T. H., Deval, J. H. & Ho, C. M. Electrokinetics in micro devices for biotechnology applications. *IEEE/ASME Trans. Mechatronics* **9**, 366–376 (2004).

58. Bahga, S. S. & Santiago, J. G. Coupling isotachophoresis and capillary electrophoresis: A review and comparison of methods. *Analyst* **138**, 735–754 (2013).

59. Smejkal, P. *et al.* Microfluidic isotachophoresis: A review. *Electrophoresis* **34**, 1493–1509 (2013).

60. Hlushkou, D., Perdue, R. K., Dhopeshwarkar, R., Crooks, R. M. & Tallarek, U. Electric field gradient focusing in microchannels with embedded bipolar electrode. *Lab Chip* **9**, 1903–1913 (2009).

61. Warnick, K. F. *et al.* Field gradient electrophoresis. *Electrophoresis* **26**, 405–414 (2005).

62. Huang, Z. & Ivory, C. F. Digitally controlled electrophoretic focusing. *Anal. Chem.* **71**, 1628–1632 (1999).

63. Pethig, R. Dielectrophoresis: Status of the theory, technology, and applications. *Biomicrofluidics* **4**, 22811 (2010).

64. Çetin, B. & Li, D. Dielectrophoresis in microfluidics technology. *Electrophoresis* **32**, 2410–2427 (2011).

65. Lapizco-Encinas, B. H., Simmons, B. A., Cummings, E. B. & Fintschenko, Y. Insulator-based dielectrophoresis for the selective concentration and separation of live bacteria in water. *Anal. Chem.* **76**, 1571–1579 (2004).

66. Čemažar, J., Douglas, T. A., Schmelz, E. M. & Davalos, R. V. Enhanced contactless dielectrophoresis enrichment and isolation platform via cell-scale microstructures. *Biomicrofluidics* **10**, (2016).

67. Xing, X., Ng, C. N., Chau, M. L. & Yobas, L. Railing cells along 3D microelectrode tracks for continuous-flow dielectrophoretic sorting. *Lab Chip* **18**, 3760–3769 (2018).

68. Hawkins, B. G., Smith, A. E., Syed, Y. A. & Kirby, B. J. Continuous-Flow Particle Separation by 3D Insulative Dielectrophoresis Using Coherently Shaped, dc-Biased, ac Electric Fields. *Anal. Chem.* **79**, 7291–7300 (2007).

69. Kang, Y., Cetin, B., Wu, Z. & Li, D. Continuous particle separation with localized AC-dielectrophoresis using embedded electrodes and an insulating hurdle. *Electrochim. Acta* **54**, 1715–1720 (2009).

70. Yamada, M., Nakashima, M. & Seki, M. Pinched flow fractionation: Continuous size separation of particles utilizing a laminar flow profile in a pinched microchannel. *Anal. Chem.* **76**, 5465–5471 (2004).

71. Jain, A. & Posner, J. D. Particle dispersion and separation resolution of pinched flow fractionation. *Anal. Chem.* **80**, 1641–1648 (2008).

72. Zhang, J. *et al.* Fundamentals and applications of inertial microfluidics: A review. *Lab Chip* **16**, 10–34 (2016).

73. Di Carlo, D. Inertial microfluidics. *Lab Chip* **9**, 3038 (2009).

74. Martel, J. M. & Toner, M. Inertial focusing in microfluidics. *Annu. Rev. Biomed. Eng.* **16**, 371–96 (2014).

75. Lee, M. G., Shin, J. H., Bae, C. Y., Choi, S. & Park, J. K. Label-free cancer cell separation from human whole blood using inertial microfluidics at low shear stress. *Anal. Chem.* **85**, 6213–6218 (2013).

76. Kuntaegowdanahalli, S. S., Bhagat, A. A. S., Kumar, G. & Papautsky, I. Inertial microfluidics for continuous particle separation in spiral microchannels. *Lab Chip* **9**, 2973–2980 (2009).

77. Di Carlo, D., Irimia, D., Tompkins, R. G. & Toner, M. Continuous inertial focusing, ordering, and separation of particles in microchannels. *Proc. Natl. Acad. Sci.* **104**, 18892–18897 (2007).

78. Romeo, G., D'Avino, G., Greco, F., Netti, P. A. & Maffettone, P. L. Viscoelastic flow-focusing in microchannels: Scaling properties of the particle radial distributions. *Lab Chip* **13**, 2802–2807 (2013).

79. Leshansky, A. M., Bransky, A., Korin, N. & Dinnar, U. Tunable nonlinear viscoelastic 'focusing' in a microfluidic device. *Phys. Rev. Lett.* **98**, 1–4 (2007).

80. Liu, C. *et al.* Field-Free Isolation of Exosomes from Extracellular Vesicles by Microfluidic Viscoelastic Flows. *ACS Nano* **11**, 6968–6976 (2017).

81. Lu, X. & Xuan, X. Continuous Microfluidic Particle Separation via Elasto-Inertial Pinched Flow Fractionation. *Anal. Chem.* **87**, 6389–6396 (2015).

82. Li, Y. *et al.* Dynamic control of particle separation in deterministic lateral displacement separator with viscoelastic fluids. *Sci. Rep.* **8**, 3618 (2018).

83. Huang, L. R., Cox, E. C., Austin, R. H. & Sturm, J. C. Continuous Particle Separation Through Deterministic Lateral Displacement. *Science (80-.).* **304**, 987–990 (2004).

84. McGrath, J., Jimenez, M. & Bridle, H. Deterministic lateral displacement for particle separation: A review. *Lab Chip* **14**, 4139–4158 (2014).

85. Salafi, T., Zhang, Y. & Zhang, Y. *A Review on Deterministic Lateral Displacement for Particle Separation and Detection*. *Nano-Micro Letters* (Springer Singapore, 2019). doi:10.1007/s40820-019-0308-7

86. Inglis, D. W., Davis, J. A., Austin, R. H. & Sturm, J. C. Critical particle size for fractionation by deterministic lateral displacement. *Lab Chip* **6**, 655–658 (2006).

87. Davis, J. A. Microfluidic Separation of Blood Components through Deterministic Lateral Displacement. *PhD Thesis* (Princeton University, 2008).

88. Davis, J. A. *et al.* Deterministic hydrodynamics: Taking blood apart. *Proc. Natl. Acad. Sci.* **103**, 14779–14784 (2006).

89. Liu, Z. *et al.* Rapid isolation of cancer cells using microfluidic deterministic lateral displacement structure. *Biomicrofluidics* **7**, (2013).

90. Xavier, M. *et al.* Label-free enrichment of primary human skeletal progenitor cells using deterministic lateral displacement. *Lab Chip* **19**, 513–523 (2019).

91. Santana, S. M., Antonyak, M. A., Cerione, R. A. & Kirby, B. J. Microfluidic isolation of cancer-cell-derived microvesicles from hetergeneous extracellular shed vesicle populations. *Biomed. Microdevices* **16**, 869–877 (2014).

92. Wunsch, B. H. *et al.* Nanoscale lateral displacement arrays for the separation of exosomes and colloids down to 20nm. *Nat. Nanotechnol.* **11**, 936–940 (2016).

93. Holm, S. H., Beech, J. P., Barrett, M. P. & Tegenfeldt, J. O. Separation of parasites from human blood using deterministic lateral displacement. *Lab Chip* **11**, 1326–1332 (2011).

94. Beech, J. P. *et al.* Separation of pathogenic bacteria by chain length. *Anal. Chim. Acta* **1000**,

223–231 (2018).

95. Inglis, D. W., Herman, N. & Vesey, G. Highly accurate deterministic lateral displacement device and its application to purification of fungal spores. *Biomicrofluidics* **4**, (2010).

96. Holmes, D. *et al.* Separation of blood cells with differing deformability using deterministic lateral displacement. *Interface Focus* **4**, (2014).

97. Beech, J. P., Holm, S. H., Adolfsson, K. & Tegenfeldt, J. O. Sorting cells by size, shape and deformability. *Lab Chip* **12**, 1048–1051 (2012).

98. Zeming, K. K., Ranjan, S. & Zhang, Y. Rotational separation of non-spherical bioparticles using I-shaped pillar arrays in a microfluidic device. *Nat. Commun.* **4**, 1625–1628 (2013).

99. Beech, J. P., Jönsson, P. & Tegenfeldt, J. O. Tipping the balance of deterministic lateral displacement devices using dielectrophoresisY. *Lab Chip* **9**, 2698–2706 (2009).

100. Loutherback, K. *et al.* Improved performance of deterministic lateral displacement arrays with triangular posts. *Microfluid. Nanofluidics* **9**, 1143–1149 (2010).

101. Ranjan, S., Zeming, K. K., Jureen, R., Fisher, D. & Zhang, Y. DLD pillar shape design for efficient separation of spherical and non-spherical bioparticles. *Lab Chip* **14**, 4250–4262 (2014).

102. Al-Fandi, M., Al-Rousan, M., Jaradat, M. A. K. & Al-Ebbini, L. New design for the separation of microorganisms using microfluidic deterministic lateral displacement. *Robot. Comput. Integr. Manuf.* **27**, 237–244 (2011).

103. Au, S. H. *et al.* Microfluidic isolation of circulating tumor cell clusters by size and asymmetry. *Sci. Rep.* **7**, 1–10 (2017).

104. Zeming, K. K., Salafi, T., Chen, C. H. & Zhang, Y. Asymmetrical Deterministic Lateral Displacement Gaps for Dual Functions of Enhanced Separation and Throughput of Red Blood Cells. *Sci. Rep.* **6**, 1–10 (2016).

105. Calero, V., Garcia-Sanchez, P., Honrado, C., Ramos, A. & Morgan, H. AC electrokinetic biased deterministic lateral displacement for tunable particle separation. *Lab Chip* **19**, 1386–1396 (2019).

106. Zeming, K. K., Thakor, N. V., Zhang, Y. & Chen, C. H. Real-time modulated nanoparticle separation with an ultra-large dynamic range. *Lab Chip* **16**, 75–85 (2016).

107. Devendra, R. & Drazer, G. Gravity Driven Deterministic Lateral Displacement for Particle

Separation in Microfluidic Devices. *Anal. Chem.* **84**, 10621–10627 (2012).

108. Delgado, A. V., González-Caballero, F., Hunter, R. J., Koopal, L. K. & Lyklema, J. Measurement and interpretation of electrokinetic phenomena. *J. Colloid Interface Sci.* **309**, 194–224 (2007).

109. Morgan, H. & Green, N. G. *AC electrokinetics*. (Research Studies Press, 2003).

110. Ramos, A. *Electrokinetics and electrohydrodynamics in microsystems*. **530**, (Springer Science & Business Media, 2011).

111. Hughes, M. P. AC electrokinetics: Applications for nanotechnology. *Nanotechnology* **11**, 124–132 (2000).

112. Parsons, R. Electrical Double Layer: Recent Experimental and Theoretical Developments. *Chem. Rev.* **90**, 813–826 (1990).

113. Ramos, A., Morgan, H., Green, N. G. & Castellanos, A. The role of electrohydrodynamic forces in the dielectrophoretic manipulation and separation of particles. *J. Electrostat.* **47**, 71–81 (1999).

114. Castellanos, A., Ramos, A., González, A., Green, N. G. & Morgan, H. Electrohydrodynamics and dielectrophoresis in microsystems: scaling laws. *J. Phys. D. Appl. Phys.* **36**, 2584–2597 (2003).

115. Voldman, J. Electrical Forces for Microscale Cell Manipulation. *Annu. Rev. Biomed. Eng.* **8**, 425–454 (2006).

116. Talary, M. S., Burt, J. P. H., Tame, J. A. & Pethig, R. Electromanipulation and separation of cells using travelling electric fields. *J. Phys. D. Appl. Phys.* **29**, 2198–2203 (1996).

117. Ramos, A., Morgan, H., Green, N. G. & Castellanos, A. Ac electrokinetics: a review of forces in microelectrode structures Dielectrophoretic investigations of sub- micrometre latex spheres N G Green and H Morgan - Ac electrokinetics: a survey of sub- micrometre particle dynamics. *J. Phys. D. Appl. Phys.* **31**, 2338–2353 (1998).

118. Chang, C. C. & Yang, R. J. Electrokinetic mixing in microfluidic systems. *Microfluid. Nanofluidics* **3**, 501–525 (2007).

119. Bousse, L. *et al.* Electrokinetically Controlled Microfluidic Analysis Systems. *Annu. Rev. Biophys. Biomol. Struct.* **29**, 155–181 (2000).

120. Bazant, M. Z. & Squires, T. M. Induced-Charge Electrokinetic Phenomena: Theory and Microfluidic Applications. *Phys. Rev. Lett.* **92**, 1–4 (2004).

121. Griffiths, D. J. Introduction to electrodynamics. (2005).

122. Bunget, I. & Popescu, M. Physics of solid dielectrics. *Mater. Sci. Monogr.* **19**, (1984).

123. Jones, T. B. *Electromechanics of Particles*. (Cambridge University Press, 1995).

124. Hanai, T., Koizumi, N. & Irimajiri, A. A method for determining the dielectric constant and the conductivity of membrane-bounded particles of biological relevance. *Biophys. Struct. Mech.* **1**, 285–294 (1975).

125. Zhang, H. Z., Sekine, K., Hanai, T. & Koizumi, N. Dielectric observations on polystyrene microcapsules and the theoretical analysis with reference to interfacial polarization. *Colloid Polym. Sci.* **261**, 381–389 (1983).

126. Huang, Y., Holzel, R., Pethig, R. & Xiao-B.Wang. Differences in the AC electrodynamics of viable and non-viable yeast cells determined through combined dielectrophoresis and electrorotation studies. *Phys. Med. Biol.* **37**, 1499–1517 (1992).

127. Gimsa, J., Marszalek, P., Loewe, U. & Tsong, T. Y. Dielectrophoresis and electrorotation of neurospora slime and murine myeloma cells. *Biophys. J.* **60**, 749–760 (1991).

128. Jones, T. B. Basic theory of dielectrophoresis and electrorotation. *IEEE Eng. Med. Biol. Mag.* **22**, 33–42 (2003).

129. Dukhin, S. S., Shilov, V. N. & Bikerman, J. J. Dielectric phenomena and double layer in disperse systems and polyelectrolytes. *J. Electrochem. Soc.* **121**, 154C-154C (1974).

130. López-García, J. J., Horno, J. & Grosse, C. Poisson-Boltzmann description of the electrical double layer including ion size effects. *Langmuir* **27**, 13970–13974 (2011).

131. Lyklema, J., Springer, M. M., Shilov, V. N. & Dukhin, S. S. The relaxation of the double layer around colloidal particles and the low-frequency dielectric dispersion. Part III. Application of theory to experiments. *J. Electroanal. Chem.* **198**, 19–26 (1986).

132. Bikerman, J. J. XXXIX. Structure and capacity of electrical double layer. *London, Edinburgh, Dublin Philos. Mag. J. Sci.* **33**, 384–397 (1942).

133. Grahame, D. C. The electrical double layer and the theory of electrocapillarity. *Chem. Rev.* **41**, 441–501 (1947).

134. Lyklema, J. *Fundamentals of Interface and Colloid Science Vol II*. (Academic Press London, 1995).

135. Hunter, R. J. *Introduction to modern colloid science*. **7**, (Oxford University Press Oxford, 1993).

136. Ermolina, I. & Morgan, H. The electrokinetic properties of latex particles: Comparison of electrophoresis and dielectrophoresis. *J. Colloid Interface Sci.* **285**, 419–428 (2005).

137. Arnold, W. M., Schwan, H. P. & Zimmermann, U. Surface conductance and other properties of latex particles measured by electrorotation. *J. Phys. Chem.* **91**, 5093–5098 (1987).

138. Shilov, V. N. *et al.* Polarization of the electrical double layer. Time evolution after application of an electric field. *J. Colloid Interface Sci.* **232**, 141–148 (2000).

139. López-García, J. J., Horno, J., González-Caballero, F., Grosse, C. & Delgado, A. V. Dynamics of the electric double layer: Analysis in the frequency and time domains. *J. Colloid Interface Sci.* **228**, 95–104 (2000).

140. Zhao, H. Double-layer polarization of a non-conducting particle in an alternating current field with applications to dielectrophoresis. *Electrophoresis* **32**, 2232–2244 (2011).

141. Schwarz, G. A theory of the low-frequency dielectric dispersion of colloidal particles in electrolyte solution. *J. Phys. Chem.* **66**, 2636–2642 (1962).

142. Sasaki, S., Ishikawa, A., Hanai, T. DIELECTRIC PROPERTIES OF SPHERICAL MACROION SUSPENSIONS I. STUDY ON MONODISPERSE POLYSTYRENE LATEX. *Biophys. Chem.* **14**, 45–53 (1981).

143. Schwan, H. P., Schwarz, G., Maczuk, J. & Pauly, H. On the low-frequency dielectric dispersion of colloidal particles in electrolyte solution. *J. Phys. Chem.* **66**, 2626–2635 (1962).

144. Schurr, J. M. On the theory of the dielectric dispersion of spherical colloidal particles in electrolyte solution. *J. Phys. Chem.* **68**, 2407–2413 (1964).

145. Hölzel, R. & Pethig, R. Protein dielectrophoresis: Key dielectric parameters and evolving theory. *Electrophoresis* (2020). doi:10.1002/elps.202000255

146. Hunter, R. J. *Foundations of Colloidal Science*. (Oxford University Press, 2000).

147. Shilov, V., Barany, S., Grosse, C. & Shramko, O. Field-induced disturbance of the double layer electro-neutrality and non-linear electrophoresis. *Adv. Colloid Interface Sci.* (2003).

doi:10.1016/S0001-8686(03)00040-X

148. Delgado, A. V., González-Caballero, F., Hunter, R. J., Koopal, L. K. & Lyklema, J. Measurement and interpretation of electrokinetic phenomena: (IUPAC technical report). *Pure Appl. Chem.* **77**, 1753–1805 (2005).

149. Schnitzer, O. & Yariv, E. Nonlinear electrophoresis at arbitrary field strengths: Small-Dukhin-number analysis. *Phys. Fluids* **26**, (2014).

150. Mishchuk, N. A. Concentration polarization of interface and non-linear electrokinetic phenomena. *Adv. Colloid Interface Sci.* **160**, 16–39 (2010).

151. O'Brien, R. W. & White, L. R. Electrophoretic mobility of a spherical colloidal particle. *J. Chem. Soc. Faraday Trans. 2 Mol. Chem. Phys.* **74**, 1607–1626 (1978).

152. Peltor, R. H., Pelton, H. M., Morphesis, A. & Rowell, R. L. Particle Sizes and Electrophoretic Mobilities of Poly(N-isopropylacrylamide) Latex. *Langmuir* **5**, 816–818 (1989).

153. Nichols, S. C., Loewenberg, M. & Davis, R. H. Electrophoretic Particle Aggregation. *J. Colloid Interface Sci.* **176**, 342–351 (1995).

154. Hjerten, S., Jerstedt, S. & Tiselius, A. Electrophoretic "particle sieving" in polyacrylamide gels as applied to ribosomes. *Anal. Biochem.* **11**, 211–218 (1965).

155. Pohl, H. A. *Dielectrophoresis: The behavior of neutral matter in nonuniform electric fields (Cambridge Monographs on physics)*. (Cambridge/New York: Cambridge University Press, 1978).

156. Abraham, M., Becker, R. & Dougall, J. *The classical theory of electricity and magnetism*. (Blackie London, 1932).

157. Green, N. G. & Morgan, H. Dielectrophoresis of Submicrometer Latex Spheres. 1. Experimental Results. *J. Phys. Chem. B* **103**, 41–50 (1999).

158. Green, N. G. & Morgan, H. Dielectrophoretic investigations of sub-micrometre latex spheres. *J. Phys. D. Appl. Phys.* **30**, 2626–2633 (1997).

159. Mernier, G., Piacentini, N., Braschler, T., Demierre, N. & Renaud, P. Continuous-flow electrical lysis device with integrated control by dielectrophoretic cell sorting. *Lab Chip* **10**, 2077–2082 (2010).

160. Nascimento, E. M. *et al.* Dielectrophoretic sorting on a microfabricated flow cytometer:

Label free separation of Babesia bovis infected erythrocytes. *Bioelectrochemistry* **73**, 123–128 (2008).

161. Demierre, N., Braschler, T., Muller, R. & Renaud, P. Focusing and continuous separation of cells in a microfluidic device using lateral dielectrophoresis. *TRANSDUCERS EUROSENSORS '07 - 4th Int. Conf. Solid-State Sensors, Actuators Microsystems* **132**, 1777–1780 (2007).

162. Auerswald, J. & Knapp, H. F. Quantitative assessment of dielectrophoresis as a micro fluidic retention and separation technique for beads and human blood erythrocytes. *Microelectron. Eng.* **67**–**68**, 879–886 (2003).

163. Markx, G. H. & Pethig, R. Dielectrophoretic separation of cells: Continuous separation. *Biotechnol. Bioeng.* **45**, 337–343 (1995).

164. Grilli, S. & Ferraro, P. Dielectrophoretic trapping of suspended particles by selective pyroelectric effect in lithium niobate crystals. *Appl. Phys. Lett.* **92**, 2–5 (2008).

165. Sebastian, A., Buckle, A. M. & Markx, G. H. Formation of multilayer aggregates of mammalian cells by dielectrophoresis. *J. Micromechanics Microengineering* **16**, 1769–1777 (2006).

166. Barsotti, R. J. *et al.* Assembly of metal nanoparticles into nanogaps. *Small* **3**, 488–499 (2007).

167. Velev, O. D. & Kaler, E. W. In situ assembly of colloidal particles into miniaturized biosensors. *Langmuir* **15**, 3693–3698 (1999).

168. Lapizco-Encinas, B. H., Davalos, R. V., Simmons, B. A., Cummings, E. B. & Fintschenko, Y. An insulator-based (electrodeless) dielectrophoretic concentrator for microbes in water. *J. Microbiol. Methods* **62**, 317–326 (2005).

169. Hughes, M. P. & Morgan, H. Dielectrophoretic trapping of single sub-micrometre scale bioparticles. *J. Phys. D. Appl. Phys.* **31**, 2205–2210 (1998).

170. Asbury, C. L. & Van Den Engh, G. Trapping of DNA in nonuniform oscillating electric fields. *Biophys. J.* **74**, 1024–1030 (1998).

171. Lapizco-Encinas, B. H., Ozuna-Chacón, S. & Rito-Palomares, M. Protein manipulation with insulator-based dielectrophoresis and direct current electric fields. *J. Chromatogr. A* **1206**, 45–51 (2008).

172. Regtmeier, J., Duong, T. T., Eichhorn, R., Anselmetti, D. & Ros, A. Dielectrophoretic manipulation of DNA: Separation and polarizability: Analytical Chemistry. (2007).

173. Kawabata, T. & Washizu, M. Dielectrophoretic detection of molecular bindings. *IEEE Trans. Ind. Appl.* **37**, 1625–1633 (2001).

174. Jones, T. B. & Washizu, M. Multipolar dielectrophoretic and electrorotation theory. *J. Electrostat.* **37**, 121–134 (1996).

175. Ren, Y. K., Morganti, D., Jiang, H. Y., Ramos, A. & Morgan, H. Electrorotation of metallic microspheres. *Langmuir* **27**, 2128–2131 (2011).

176. Rodríguez-Sánchez, L., Ramos, A. & García-Sánchez, P. Electrorotation of semiconducting microspheres. *Phys. Rev. E* **100**, 1–8 (2019).

177. Lin, Y.-Y., Lo, Y.-J. & Lei, U. Measurement of the Imaginary Part of the Clausius-Mossotti Factor of Particle/Cell via Dual Frequency Electrorotation. *Micromachines* **11**, 329 (2020).

178. Arnold, W. M. & Zimmermann, U. Electro-rotation: development of a technique for dielectric measurements on individual cells and particles. *J. Electrostat.* **21**, 151–191 (1988).

179. Harden, V. P. & Harris, J. O. The isoelectric point of bacterial cells. *J. Bacteriol.* **65**, 198–202 (1953).

180. Rijnaarts, H. H. M., Norde, W., Lyklema, J. & Zehnder, A. J. B. The isoelectric point of bacteria as an indicator for the presence of cell surface polymers that inhibit adhesion. *Colloids Surfaces B Biointerfaces* **4**, 191–197 (1995).

181. Ramos, A., Morgan, H., Green, N. G. & Castellanos, A. AC Electric-Field-Induced Fluid Flow in Microelectrodes. *J. Colloid Interface Sci.* **217**, 420–422 (1999).

182. Ramos, A., Morgan, H., Green, N. G. & Castellanos, A. Ac electrokinetics: a review of forces in microelectrode structures. *J. Phys. D. Appl. Phys.* **31**, 2338–2353 (1998).

183. Fluri, A. M. and C. S. E. and N. B. and D. J. H. and K. S. and K. Electroosmotic pumping and electrophoretic separations for miniaturized chemical analysis systems. *J. Micromechanics Microengineering* **4**, 257 (1994).

184. Lazar, I. M. & Karger, B. L. Multiple open-channel electroosmotic pumping system for microfluidic sample handling. *Anal. Chem.* **74**, 6259–6268 (2002).

185. Glasgow, I., Batton, J. & Aubry, N. Electroosmotic mixing in microchannels. *Lab Chip* **4**, 558–562 (2004).

186. Brask, A., Kutter, J. P. & Bruus, H. Long-term stable electroosmotic pump with ion exchange

membranes. *Lab Chip* **5**, 730–738 (2005).

187. Sasaki, N., Kitamori, T. & Kim, H. B. AC electroosmotic micromixer for chemical processing in a microchannel. *Lab Chip* **6**, 550–554 (2006).

188. Salimi-Moosavi, H., Tang, T. & Harrison, D. J. Electroosmotic pumping of organic solvents and reagents in microfabricated reactor chips. *J. Am. Chem. Soc.* **119**, 8716–8717 (1997).

189. Pu, Q. & Liu, S. Microfabricated electroosmotic pump for capillary-based sequential injection analysis. *Anal. Chim. Acta* **511**, 105–112 (2004).

190. Green, N. G., Ramos, A., González, A., Castellanos, A. & Morgan, H. Electrothermally induced fluid flow on microelectrodes. *J. Electrostat.* **53**, 71–87 (2001).

191. González, A., Ramos, A., Morgan, H., Green, N. G. & Castellanos, A. Electrothermal flows generated by alternating and rotating electric fields in microsystems. *J. Fluid Mech.* **564**, 415–433 (2006).

192. Sigurdson, M., Wang, D. & Meinhart, C. D. Electrothermal stirring for heterogeneous immunoassays. *Lab Chip* **5**, 1366–1373 (2005).

193. Kunti, G., Bhattacharya, A. & Chakraborty, S. Analysis of micromixing of non-Newtonian fluids driven by alternating current electrothermal flow. *J. Nonnewton. Fluid Mech.* **247**, 123–131 (2017).

194. Ramos, A., García-Sánchez, P. & Morgan, H. AC electrokinetics of conducting microparticles: A review. *Curr. Opin. Colloid Interface Sci.* **24**, 79–90 (2016).

195. Garc, P. *et al.* Alternating current electrokinetic properties of gold-coated microspheres. *Langmuir* **28**, 13861–13870 (2012).

196. Arcenegui, J. J., Ramos, A., García-Sánchez, P. & Morgan, H. Electrorotation of titanium microspheres. *Electrophoresis* **34**, 979–986 (2013).

197. Squires, T. M. & Bazant, M. Z. Induced-charge electro-osmosis. *J. Fluid Mech.* **509**, 217–252 (2004).

198. Squires, T. M. & Bazant, M. Z. *Breaking symmetries in induced-charge electro-osmosis and electrophoresis*. *Journal of Fluid Mechanics* **560**, (2006).

199. Gangwal, S., Cayre, O. J., Bazant, M. Z. & Velev, O. D. Induced-charge electrophoresis of metallodielectric particles. *Phys. Rev. Lett.* **100**, 1–4 (2008).

200. Daghighi, Y., Sinn, I., Kopelman, R. & Li, D. Experimental validation of induced-charge electrokinetic motion of electrically conducting particles Yasaman. *Electrochim. Acta* **87**, 270–276 (2013).

201. Squires, T. M. Induced-charge electrokinetics: Fundamental challenges and opportunities. *Lab Chip* **9**, 2477–2483 (2009).

202. Wu, Z. & Li, D. Micromixing using induced-charge electrokinetic flow. *Electrochim. Acta* **53**, 5827–5835 (2008).

203. Wu, Z. & Li, D. Mixing and flow regulating by induced-charge electrokinetic flow in a microchannel with a pair of conducting triangle hurdles. *Microfluid. Nanofluidics* **5**, 65–76 (2008).

204. Paustian, J. S., Pascall, A. J., Wilson, N. M. & Squires, T. M. Induced charge electroosmosis micropumps using arrays of Janus micropillars. *Lab Chip* **14**, 3300–3312 (2014).

205. Sugioka, H. Suppression of reverse flows in pumping by induced-charge electro-osmosis using asymmetrically stacked elliptical metal posts. *Phys. Rev. E - Stat. Nonlinear, Soft Matter Phys.* **78**, 2–5 (2008).

206. Gregersen, M. M., Okkels, F., Bazant, M. Z. & Bruus, H. Topology and shape optimization of induced-charge electro-osmotic micropumps. *New J. Phys.* **11**, 0–21 (2009).

207. Mishchuk, N. A. & Takhistov, P. V. Electroosmosis of the second kind. *Colloids Surfaces A Physicochem. Eng. Asp.* **95**, 119–131 (1995).

208. Rubinstein, I., Zaltzman, B. & Lerman, I. Electroconvective instability in concentration polarization and nonequilibrium electro-osmotic slip. *Phys. Rev. E - Stat. Nonlinear, Soft Matter Phys.* **72**, (2005).

209. Mishchuk, N. A. & Dukhin, S. S. Electrophoresis of solid particles at large Peclet numbers. *Electrophoresis* **23**, 2012–2022 (2002).

210. Manzanares, J. A., Murphy, W. D., Mafé, S. & Reiss, H. Numerical simulation of the nonequilibrium diffuse double layer in ion-exchange membranes. *J. Phys. Chem.* **97**, 8524–8530 (1993).

211. Rubinstein, I. & Zaltzman, B. Electro-osmotically induced convection at a permselective membrane. *Phys. Rev. E - Stat. Physics, Plasmas, Fluids, Relat. Interdiscip. Top.* **62**, 2238–2251 (2000).

212. Kijlstra, J., Van Leeuwen, H. P. & Lyklema, J. Effects of surface conduction on the electrokinetic properties of colloids. *J. Chem. Soc. Faraday Trans.* **88**, 3441–3449 (1992).

213. Dukhin, S. S. Electrochemical characterization of the surface of a small particle and nonequilibrium electric surface phenomena. *Adv. Colloid Interface Sci.* **61**, 17–49 (1995).

214. Grzegorczyn, S. & Ślezak, A. Kinetics of concentration boundary layers buildup in the system consisted of microbial cellulose biomembrane and electrolyte solutions. *J. Memb. Sci.* **304**, 148–155 (2007).

215. Bosio, B., Arato, E. & Costa, P. Concentration polarisation in heterogeneous electrochemical reactions: A consistent kinetic evaluation and its application to molten carbonate fuel cells. *J. Power Sources* **115**, 189–193 (2003).

216. Shaposhnik, V. A., Vasil'eva, V. I. & Praslov, D. B. Concentration fields of solutions under electrodialysis with ion-exchange membranes. *J. Memb. Sci.* **101**, 23–30 (1995).

217. Wang, S. C., Lai, Y. W., Ben, Y. & Chang, H. C. Microfluidic mixing by dc and ac nonlinear electrokinetic vortex flows. *Ind. Eng. Chem. Res.* **43**, 2902–2911 (2004).

218. Mishchuk, N. A., Heldal, T., Volden, T., Auerswald, J. & Knapp, H. Micropump based on electroosmosis of the second kind. *Electrophoresis* **30**, 3499–3506 (2009).

219. Takhistov, P., Duginova, K. & Chang, H. C. Electrokinetic mixing vortices due to electrolyte depletion at microchannel junctions. *J. Colloid Interface Sci.* **263**, 133–143 (2003).

220. Stol, R., Kok, W. T. & Poppe, H. Size-exclusion electrochromatography with controlled pore flow. *J. Chromatogr. A* **914**, 201–209 (2001).

221. Li, M. & Anand, R. K. Recent advancements in ion concentration polarization. *Analyst* **141**, 3496–3510 (2016).

222. Ben, Y., Demekhin, E. A. & Chang, H. C. Nonlinear electrokinetics and 'superfast' electrophoresis. *J. Colloid Interface Sci.* **276**, 483–497 (2004).

223. Jeon, H., Lee, H., Kang, K. H. & Lim, G. Ion concentration polarization-based continuous separation device using electrical repulsion in the depletion region. *Sci. Rep.* **3**, 3483 (2013).

224. Kwak, R., Kim, S. J. & Han, J. Continuous-flow biomolecule and cell concentrator by ion concentration polarization. *Anal. Chem.* **83**, 7348–7355 (2011).

225. Choi, S. & Park, J. K. Microfluidic system for dielectrophoretic separation based on a

trapezoidal electrode array. *Lab Chip* **5**, 1161–1167 (2005).

226. Rousselet, J., Markx, G. H. & Pethig, R. Separation of erythrocytes and latex beads by dielectrophoretic levitation and hyperlayer field-flow fractionation. *Colloids Surfaces A Physicochem. Eng. Asp.* **140**, 209–216 (1998).

227. Dürr, M., Kentsch, J., Müller, T., Schnelle, T. & Stelzle, M. Microdevices for manipulation and accumulation of micro- and nanoparticles by dielectrophoresis. *Electrophoresis* **24**, 722–731 (2003).

228. Wang, X. B. *et al.* Cell separation by dielectrophoretic field-flow-fractionation. *Anal. Chem.* **72**, 832–839 (2000).

229. Markx, G. H., Dyda, P. A. & Pethig, R. Dielectrophoretic separation of bacteria using a conductivity gradient. *J. Biotechnol.* **51**, 175–180 (1996).

230. Masuda, S., Washizu, M. & Nanba, T. Novel method of cell fusion in field constriction area in fluid integration circuit. *IEEE Trans. Ind. Appl.* **25**, 732–737 (1989).

231. Lapizco-Encinas, B. H. On the recent developments of insulator-based dielectrophoresis: A review. *Electrophoresis* 1–18 (2018). doi:10.1002/elps.201800285

232. Hill, N. & Lapizco-Encinas, B. H. Continuous flow separation of particles with insulator-based dielectrophoresis chromatography. *Anal. Bioanal. Chem.* (2020). doi:10.1007/s00216-019-02308-w

233. Cummings, E. B. & Singh, A. K. Dielectrophoresis in microchips containing arrays of insulating posts: Theoretical and experimental results. *Anal. Chem.* **75**, 4724–4731 (2003).

234. Pesch, G. R., Du, F., Baune, M. & Thöming, J. Influence of geometry and material of insulating posts on particle trapping using positive dielectrophoresis. *J. Chromatogr. A* **1483**, 127–137 (2017).

235. Saucedo-Espinosa, M. A. & Lapizco-Encinas, B. H. Experimental and theoretical study of dielectrophoretic particle trapping in arrays of insulating structures: Effect of particle size and shape. *Electrophoresis* **36**, 1086–1097 (2015).

236. LaLonde, A., Gencoglu, A., Romero-Creel, M. F., Koppula, K. S. & Lapizco-Encinas, B. H. Effect of insulating posts geometry on particle manipulation in insulator based dielectrophoretic devices. *J. Chromatogr. A* **1344**, 99–108 (2014).

237. Abdallah, B. G., Chao, T.-C., Kupitz, C., Fromme, P. & Ros, A. Dielectrophoretic Sorting of

Membrane Protein Nanocrystals. *ACS Nano* **7**, 9129–9137 (2013).

238. Kang, Y., Li, D., Kalams, S. A. & Eid, J. E. DC-Dielectrophoretic separation of biological cells by size. *Biomed. Microdevices* **10**, 243–249 (2008).

239. Dolník, V., Liu, S. & Jovanovich, S. Capillary electrophoresis on microchip. *Electrophoresis* **21**, 41–54 (2000).

240. Turgeon, R. T. & Bowser, M. T. Micro free-flow electrophoresis: Theory and applications. *Anal. Bioanal. Chem.* **394**, 187–198 (2009).

241. Jung, B., Bharadwaj, R. & Santiago, J. G. On-chip millionfold sample stacking using transient isotachophoresis. *Anal. Chem.* **78**, 2319–2327 (2006).

242. Křivánková, L., Pantůčková, P. & Boček, P. Isotachophoresis in zone electrophoresis. *J. Chromatogr. A* **838**, 55–70 (1999).

243. Liu, J., Sun, X., Farnsworth, P. B. & Lee, M. L. Fabrication of conductive membrane in a polymeric electric field gradient focusing microdevice. *Anal. Chem.* **78**, 4654–4662 (2006).

244. Kohlheyer, D., Besselink, G. A. J., Schlautmann, S. & Schasfoort, R. B. M. Free-flow zone electrophoresis and isoelectric focusing using a microfabricated glass device with ion permeable membranes. *Lab Chip* **6**, 374–380 (2006).

245. Inglis, D. W. Efficient microfluidic particle separation arrays. *Appl. Phys. Lett.* **94**, 013510 (2009).

246. Bhattacharya, S., Datta, A., Berg, J. M. & Gangopadhyay, S. Studies on surface wettability of poly(dimethyl) siloxane (PDMS) and glass under oxygen-plasma treatment and correlation with bond strength. *J. Microelectromechanical Syst.* **14**, 590–597 (2005).

247. Xiong, L., Chen, P. & Zhou, Q. Adhesion promotion between PDMS and glass by oxygen plasma pre-treatment. *J. Adhes. Sci. Technol.* **28**, 1046–1054 (2014).

248. Davalos, R. V. *et al.* Performance impact of dynamic surface coatings on polymeric insulator-based dielectrophoretic particle separators. *Anal. Bioanal. Chem.* **390**, 847–855 (2008).

249. Viefhues, M. *et al.* Physisorbed surface coatings for poly(dimethylsiloxane) and quartz microfluidic devices. *Anal. Bioanal. Chem.* **401**, 2113–2122 (2011).

250. Hellmich, W. *et al.* Poly(oxyethylene) Based Surface Coatings for Poly(dimethylsiloxane) Microchannels. *Langmuir* **21**, 7551–7557 (2005).

251. Schneider, C. A., Rasband, W. S. & Eliceiri, K. W. NIH Image to ImageJ: 25 years of image analysis. *Nat. Methods* **9**, 671–675 (2012).

252. Contreras-Naranjo, J. C., Wu, H. J. & Ugaz, V. M. Microfluidics for exosome isolation and analysis: Enabling liquid biopsy for personalized medicine. *Lab Chip* **17**, 3558–3577 (2017).

253. Zhang, H. *et al.* Deterministic Lateral Displacement-Based Separation of Magnetic Beads and Its Applications of Antibody Recognition. *Sensors* **20**, 2846 (2020).

254. Hochstetter, A. *et al.* Deterministic Lateral Displacement : Challenges and Perspectives. doi:10.1021/acsnano.0c05186

255. Kim, S. *et al.* Broken flow symmetry explains the dynamics of small particles in deterministic lateral displacement arrays - Supplementary Information Appendix. *Proc. Natl. Acad. Sci.* (2017).

256. Beech, J. P. Tuneable separation in Deterministic Lateral Displacement devices. *PhD Thesis* (2009).

257. Lindken, R., Rossi, M., Große, S. & Westerweel, J. Micro-Particle Image Velocimetry (PIV): Recent developments, applications, and guidelines. *Lab Chip* **9**, 2551–2567 (2009).

258. Thielicke, W. & Stamhuis, E. J. PIVlab – Towards User-friendly, Affordable and Accurate Digital Particle Image Velocimetry in MATLAB. *J. Open Res. Softw.* **2**, (2014).

259. Eckstein, Y., Yossifon, G., Seifert, A. & Miloh, T. Nonlinear electrokinetic phenomena around nearly insulated sharp tips in microflows. *J. Colloid Interface Sci.* **338**, 243–249 (2009).

260. Thamida, S. K. & Chang, H. C. Nonlinear electrokinetic ejection and entrainment due to polarization at nearly insulated wedges. *Phys. Fluids* **14**, 4315–4328 (2002).

261. Zehavi, M., Boymelgreen, A. & Yossifon, G. Competition between Induced-Charge Electro-Osmosis and Electrothermal Effects at Low Frequencies around a Weakly Polarizable Microchannel Corner. *Phys. Rev. Appl.* **5**, 1–13 (2016).

262. Yossifon, G., Frankel, I. & Miloh, T. Macro-scale description of transient electro-kinetic phenomena over polarizable dielectric solids. *J. Fluid Mech.* **620**, 241–262 (2009).

263. Ng, W. Y., Ramos, A., Lam, Y. C., Mahendra Wijaya, I. P. & Rodriguez, I. DC-biased AC-electrokinetics: A conductivity gradient driven fluid flow. *Lab Chip* **11**, 4241–4247 (2011).

264. Vahey, M. D. & Voldman, J. An equilibrium method for continuous-flow cell sorting using

dielectrophoresis. *Anal. Chem.* **80**, 3135–3143 (2008).

265. Markx, G. H., Rousselet, J. & Pethig, R. DEP-FFF: Field-Flow Fractionation Using Non-Uniform Electric Fields. *J. Liq. Chromatogr. Relat. Technol.* **20**, 2857–2872 (1997).

266. Jalalian, S. H., Ramezani, M., Jalalian, S. A., Abnous, K. & Taghdisi, S. M. Exosomes, new biomarkers in early cancer detection. *Anal. Biochem.* **571**, 1–13 (2019).

267. Admyre, C. *et al.* Exosomes with Immune Modulatory Features Are Present in Human Breast Milk. *J. Immunol.* **179**, 1969–1978 (2007).

268. Zhou, Q. *et al.* Immune-related microRNAs are abundant in breast milk exosomes. *Int. J. Biol. Sci.* **8**, 118–123 (2011).

269. Abramowicz, A., Widlak, P. & Pietrowska, M. Proteomic analysis of exosomal cargo: The challenge of high purity vesicle isolation. *Mol. Biosyst.* **12**, 1407–1419 (2016).

270. Momen-Heravi, F. *et al.* Current methods for the isolation of extracellular vesicles. *Biol. Chem.* **394**, 1253–1262 (2013).

271. Wang, Q., Dingari, N. N. & Buie, C. R. Nonlinear electrokinetic effects in insulator-based dielectrophoretic systems. *Electrophoresis* **38**, 2576–2586 (2017).